UNIVERSITÀ DEGLI STUDI DI UDINE
hic sunt futura
www.uniud.it

PhD Course:

"Environmental and Energy Engineering Science"

XXXIII cycle

Title of thesis:

Localized Corrosion Mechanisms on Micro-and Nano devices in Biomedical Field

PhD student
Ehsan Rahimi

Supervisor
Dr. Maria Lekka

Co-supervisor
Prof. Lorenzo Fedrizzi

2021

Preface

This Ph.D. thesis is the result of 3 years research performed under the project "Localized Corrosion Mechanism on Micro-and Nano devices in Biomedical Field", at Polytechnic Department of Engineering and Architecture of University of Udine. This research was realized within the framework of the Innovative Training Network mCBEEs (Advanced integrative solutions to **C**orrosion problems beyond **m**icro-scale: towards longterm durability of miniaturized **B**iomedical, **E**lectronic and **E**nergy **s**ystems).

mCBEEs Innovative Training Network is a joint venture between academia and industry with a primary goal to train young researchers in the field of corrosion and corrosion protection of micro- and nanodevices. The network focuses on the study of corrosion mechanisms beyond microscale of components in miniaturized systems in different environments using localized techniques, and the development of multifunctional protective coatings to increase the long-term durability of such components. The ITN brought together 15 Early-Stage Researchers (ESRs) enrolled by 9 Universities, 3 Research Centers and 3 Companies belonging to 11 Countries.

Withing the mCBEEs network I was contracted by University of Udine and enrolled in the PhD school of Environmental and Energy Engineering Science. The majority of my research activities were undertaken at the Polytechnic Department of Engineering and Architecture of University of Udine under the supervision of Dr. Maria Lekka and Prof. Fedrizzi. Parts of research work were performed in secondment periods to partner institutions of the mCBBEs network.

Fabrication process of NiCo and NiCo/Au coated micropillars and cobalt ferrite ($CoFe_2O_4$ (CFO)) and cobalt ferrite@bismuth ferrite ($CoFe_2O_4$@$BiFeO_3$ (CFO@BFO)) ceramic

nanoparticles was performed at the Institute of Robotics and Intelligent Systems (IRIS), ETH Zurich University, under the supervision of prof. Salvador Pané, in Zurich, Switzerland. The XPS surface analysis and in-situ AFM of both CoCrMo and Ti6Al4V alloy were performed in collaboration with Research Group Electrochemical and Surface Engineering in VUB University, under the supervision of Prof. Herman Terryn, Brussels, Belgium.

This project has received funding by the European Union's Horizon 2020 research and innovation programme under the Marie Sklodowska-Curie grant agreement No. 76977.

Abstract

Thus far, both Ti6Al4V and CoCrMo alloys are the most common implant materials in the biomedical field, mainly used in orthopaedic, dental, cardiovascular, and fixing fracture components. The significant capability of these implant materials is due to high corrosion resistance or resistance to metal ion release and specific mechanical properties. However, during implantation in human body media as a complex corrosive environment with various types of ions (phosphate, calcium, chloride, fluoride, etc.), proteins (albumin, fibronectin, globulin, ferritin, etc.), and cells, all these species significantly can influence on implants corrosion behaviour during the lifetime performance.

The same story can be described for micro and nanomaterials as innovative and intelligent materials to be used in biological fields for targeted drug delivery, nanosurgery, cancer therapy, and isolation of biological targets. In this research, we employed NiCo and NiCo/Au metallic micropillars and cobalt ferrite ($CoFe_2O_4$ (CFO)) and cobalt ferrite@bismuth ferrite ($CoFe_2O_4$@$BiFeO_3$ (CFO@BFO)) ceramic nanoparticles. These micro and nano magnetic materials present good chemical stability (especially ceramic nanoparticles), low production cost and can be driven using external magnetic field to the target. However, these tiny smart devices can gradually miss the swimming efficiency, speed, and controllability due to their degradation accelerated by the protein nano-biofilm formation.

Protein molecules adsorbed on the surface of biomaterials can control the dynamic physicochemical interactions, on the surfaces of biological components. Depending on the different parts of human body where the biomaterials can be used, different protein species exist with particular biological behaviour which affect the metal ion release such as serum

albumin, commonly found in blood plasma, or ferritin and apoferritin (ferritin without iron core), presented in spleen, liver, and inflammatory macrophages.

To investigate the protein adsorption, morphology, and its influence on degradation mechanisms in the surgical implants or large-scale materials (CoCrMo and Ti6Al4V alloys), bovine serum albumin (BSA) protein with various concentrations was added in phosphate-buffered saline (PBS) solution. In addition, in micro-scale materials or NiCo and NiCo/Au micropillars, BSA protein was selected to monitor the metal ion releasing process in PBS media and its effect on the degradation mechanism for a long-term period. In the nano-scale materials or CFO and CFO@BFO nanoparticles, which due to their chemical nature are stable in PBS environment containing albumin protein, apoferritin was used to monitor the protein molecule role on both metal ion releasing and up-taking processes of nanoparticles in PBS media during immersion for a long-term period.

A multi-technique characterization based on electrochemical measurements, microscopy, and spectroscopy analyses was used to visualize the electrochemical interactions at electrolyte/protein/solid interfaces, the protein adsorption morphology and its impact on chemical stability of passive film (CoCrMo, Ti6Al4V, NiCo micropillar) and oxide surface (ceramic nanoparticles). We believe that the combination of findings in our research can provide new insight into the protein adsorption and its effect on the metal ion releasing process of all metallic and ceramic biomaterials during the performance in the human body as a complex biological environment.

Contents

Preface i
Abstract iii
List of symbols viii
List of Acronyms xi
List of chemical formula xiv
Chapter 1: Introduction 1
1.1 Metallic biomaterials used for implants 1
1.1.1 Mechanical properties 1
1.1.2 Biocompatibility 3
1.1.3 High wear resistance 3
1.1.4 Osseointegration 3
1.1.5 Long fatigue life 3
1.1.6 High corrosion resistance 4
1.2 Micro and nano-devices in human body 4
1.3 Corrosion of metallic implants in human body fluids 8
1.3.1 Pitting Corrosion 9
1.3.2 Galvanic corrosion 12
1.3.3 Intergranular corrosion 14
1.3.4 Crevice corrosion 15
1.3.5 Fretting corrosion 16
1.4 Protein adsorption and its influence on corrosion behaviour of metallic implants 19
1.4.1 Adsorption of protein on biomaterial surface 19
1.4.2 Protein effect on corrosion mechanisms 25
1.4.3 Protein effect on Tribo-corrosion mechanism 27
1.4.4 Protein effect on the corrosion behaviour of SS316, Co-based and Ti-based alloys 29
1.4.4.1 SS 316L 29
1.4.4.2 Co-based alloy 31
1.4.4.3 Ti-based alloys 34
1.5 Corrosion phenomena on ferromagnetic micro- and nano-devices in biological environment 37
Chapter 2: Research project layout 40

2.1 Ti6Al4V and CoCrMo alloys 40
2.2 NiCo and NiCo/Au micropillars, CFO and CFO@BFO nanoparticles 43
Chapter 3: Experimental procedures and methodology 45
3.1 Ti6Al4V and CoCrMo alloys 45
3.1.1 Materials and sample preparation 45
3.1.2 Electrolytes and electrochemical measurements 45
3.1.3 Microstructural characterisation and AFM/SKPFM measurements 47
3.1.4 X-ray photoelectron spectroscopy (XPS) 49
3.2 NiCo and NiCo/Au micropillars 50
3.2.1 NiCo and NiCo/Au micropillar fabrication 50
3.2.2 Microscopy characterizations 52
3.2.3 Sample preparation for electrochemical measurements 52
3.2.4 Electrolyte and electrochemical measurements 54
3.2.5 Long-time free immersion tests 55
3.3 CFO and CFO@BFO nanoparticles 56
3.3.1 Fabrication of core-shell $CoFe_2O_4$-$BiFeO_3$ nanoparticles 56
3.3.2 Sample preparation for electrochemical measurement 56
3.3.3 Electrolyte and electrochemical measurements 58
3.3.4 Microscopy characterizations 60
Chapter 4: Role of phosphate, calcium species and hydrogen peroxide on albumin protein adsorption on surface oxide of Ti6Al4V alloy 61
4.1 PDP and EIS measurements of the complex surface layer 62
4.2 Mott–Schottky analysis of complex surface layer 66
4.3 Protein–oxide surface complex analysis by XPS 70
4.4 Surface potential and protein conformational arrangement 74
4.4.1 Analysis of the as-polished alloy 74
4.4.2 Effect of BSA protein under polarisation in different environments 76
4.4.3 Effect of the polarisation in the different environment containing BSA+H_2O_2 80
4.5 Degradation occurrence on complex oxide layer 81
4.6 Partial conclusions 83
Chapter 5: A visualizing on Albumin protein adsorption, electrochemical and surface potential evaluation on oxide layer of CoCrMo implant alloy 85
5.1 OCP, PDP and EIS measurements of the complex surface layer 86
5.2 Protein–oxide surface complex analysis by XPS 91

5.3 Surface potential and protein conformational arrangements 95
5.4 Degradation phenomena on the complex oxide layer 102
5.5 Partial Conclusions 104
Chapter 6: Degradation mechanisms of magnetic microrobotic platforms in protein media 106
6.1 Microstructure and electronic properties of NiCo and NiCo/Au-MPs 107
6.2 Electrochemical study of NiCo and NiCo/Au-MPs in PBS with and without BSA 111
6.3 Long-term immersion tests 116
6.3.1 EIS measurements 116
6.3.2 Metal ions release and morphological evaluation of the degradation 119
6.4 Partial Conclusions 123
Chapter 7: apoferritin protein impact on the electrochemical behaviour and degradation process of $CoFe_2O_4$ and $CoFe_2O_4$-$BiFeO_3$ nanoparticles 125
7.1 Surface potential of nanoparticles oxide surface by SKPFM 126
7.2. Electrochemical behaviour of nanoparticles in PBS at different pH and apoferritin concentrations 129
7.3. Electronic properties evaluations during interaction with apoferritin protein 135
7.4 ICP-AES analysis 139
7.5 Partial Conclusions 140
Chapter 8: Final Remarks and suggestion for future work 142
8.1 Final Remarks 142
8.2 Suggestions for future work 146
List of publications and conferences: 147
Acknowledgment 149
References 150

List of symbols

°C	Degree Celsius
Å	Angstrom
A	Surface area of measured field
C	Capacitance (F)
C_H	Capacitance of the Helmholtz double-layer (μF)
cm	Centimetre
cm	Centimetre
CPE	Constant phase element ($\mu F.S^{-1}.cm^{-2}$)
CPE_{ads}	Constant phase element of adsorbed layer ($\mu F.S^{-1}.cm^{-2}$)
CPE_{com}	Constant phase element of complex layer ($\mu F.S^{-1}.cm^{-2}$)
CPE_{dl}	Constant phase element of double layer ($\mu F.S^{-1}.cm^{-2}$)
CPE_{oxide}	Constant phase element of oxide layer ($\mu F.S^{-1}.cm^{-2}$)
C_{SC}	Space charge capacitance (μF)
e	Electron charge (1.6×10^{-19} C)
E	Applied potential (V vs. Ag/AgCl)
E_c	Conduction band energy
E_{corr}	Corrosion potential (mV vs. Ag/AgCl)
E_{fb}	Flat band potential (mV vs. Ag/AgCl)
E_g	Band gap energy
E_{OCP}	Open circuit potential (mV vs. Ag/AgCl)
E_v	Valance band energy
eV	Electron Volt
exp	Exponential
f	Spatial frequency (μm^{-1})
Hz	Hertz
i_{corr}	Corrosion current density ($A.cm^{-2}$)
i_{pass}	Passivity current density ($A.cm^{-2}$)

i_{tunnel}	Tunneling current
j	Imaginary unit
k	Boltzmann constant
L	Liter
mL	Mililiter
n	Constant phase element component
N_a	Acceptor density (cm^{-3})
N_d	Donor density (cm^{-3})
nm	Nanometer
r	Position vector
R_{ads}	Resistance of adsorbed layer ($\Omega.cm^2$)
R_{com}	Complex layer resistance ($\Omega.cm^2$)
R_{ct}	Charge transfer resistance ($\Omega.cm^2$)
R_{oxide}	Oxide layer resistance ($\Omega.cm^2$)
R_s	Solution resistance ($\Omega.cm^2$)
R_{total}	Complex layer resistance ($\Omega.cm^2$)
T	Absolute temperature (°K)
V_{bias}	Voltage bias
W	Watt
Y	Counts number
Y_0	Modulus
α	Alpha
β	Beta
ΔP	Volta or surface potential diference
ε	Dielectric constant of the oxide film
ε_0	Vacuum permittivity (8.854×10^{-14} $F.cm^{-1}$)
ζ	Zeta potential
μ	Micro
Π	Pi

Φ	Work function energy
ω	Angular frequency
$z(r)$	Surface Volta potential data of the surface roughness
μ	Mean value of surface Volta potential (mV)
σ	Standard deviation of surface Volta potential (mV)

List of Acronyms

AC	Amplitude current
AES	Auger electron spectroscopy
AFM	Atomic force microscopy
AgQRE	Silver wire quasi-reference electrode
ATR	Attenuated total reflection spectroscopy
BR	Bacteriorhodopsin
BSA	Bovine serum albumin
BSE	Back-scattered electrons
CAFM	Conductive atomic force microscopy
CP	Commercial pure
DC	Direct current
EC-AFM	In situ electrochemical atomic force microscopy
ECSTM	In situ electrochemical scanning tunneling microscopy
EDXS	Energy-dispersive X-ray spectroscopy
EEC	Equivalent electrical circuit (EEC)
EIS	Electrochemical Impedance spectroscopy
ET	Electronic transport
FFT	Fast Fourier transform
FT-IRRAS	Fourier transform infrared reflection–adsorption spectra
FWHM	Full width at half maximum
HOPG	Highly ordered pyrolytic graphite
HSA	Human serum albumin
ICP-AES	Inductively coupled plasma-atomic emission spectroscopy
ICP-MS	Inductively coupled plasma-mass spectroscopy
ICP-MS	Inductively coupled plasma-mass spectroscopy
IEP	Isoelectric point
IR	Infrared spectroscopy

IRRAS	IR-reflection-absorption spectroscopy
ITO	Indium tin oxide
MGD	Multimodal Gaussian distributions
MP	Micropillar
MS	Mott-Schottky
OCP	Open circuit potential
OER	Oxygen evolution reaction
PBS	Phosphate-buffered saline
PDB	Protein data bank
PDP	Potentiodynamic polarization
PREN	Pitting resistance equivalent number
PSD	Power spectral density
Pt–Ir	Platinum-Iridium
PVD	physical vapor deposition
QCM	Quartz crystal microbalance
RH	Relative humidity
RHE	Reversible hydrogen electrode
ROS	Reactive oxygen species
SAXS	Small-angle X-ray scattering
SE	Secondary electrons
SECM	Scanning electrochemical microscopy
SEM	Scanning electron microscopy
SFG	Sum-frequency generation
SHE	Standard Hydrogen Electrode
SKP	Scanning Kelvin probe
SKPFM	Scanning Kelvin probe force microscopy
SPM	Scanning probe microscopy
SS	Stainless steel
STM	Scanning tunneling microscopy

SVET	Scanning vibrating electrode technique
TDLW	Three-dimensional direct laser writing
TEM	Transmission electron microscopy
UME	Ultramicroelectrode
UV	Ultraviolet
WFE	Work function energy
XPS	X-ray photo electron spectroscopy

List of chemical formula

Ag	Silver
Al	Aluminium
Al_2O_3	Aluminium(III) oxide
Au	Gold
Bi	Bismuth
BiFeO3 (BFO)	Bismuth ferrite oxide
C	Carbon
Ca^{2+}	Calcium ion
$CaHPO_4$	Calcium phosphate
CaO	Calcium oxide
CeO	Cerium oxide
Cl-	Chloride ion
Co	Cobalt
Co^{2+}	Cobalt (II) ion
Co^{3+}	Cobalt (II) ion
CoCrMo	Cobalt-Chromium-Molybdenum
CoF_2O_4 (CFO)	Cobalt ferrite oxide
CoF_2O_4@ $BiFeO_3$ (CFO@BFO)	Cobalt Ferrite@Bismuth Ferrite
CoO	Cobalt (II) oxide
Cr	Chromium
Cr_2O_3	Chromium (III) oxide
$CrOH_3$	Chromium (III) hydroxide
CrPO4	Chromium(III) phosphate
CTAB	Hexadecyltrimethylammonium bromide
Cu_2O	Copper(I) oxide or cuprous oxide
F^-	Fluoride ion
Fe	Iron

Fe^{2+}	Ferrous ion
Fe_2O_3	Iron(III) oxide or ferric oxide
Fe^{3+}	Ferric ion
H^+	Hydrogen ion
H_2	Hydrogen gas
H_2O_2	Hydrogen peroxide
Ir^-	Iridium
Li	Lithium
$Mg(OH)_2$	Magnesium hydroxide
Mo	Molybdenum
$Mo(PO_3)_3$	Molybdenum(III) metaphosphate
MoO_3	Molybdenum trioxide
N	Nitrogen
N	Nitrogen
Na_2HPO_4	Sodium hydrogen phosphate
Na_3PO_4	Trisodium phosphate
NH_2 or $–NH_2$	Azanide
Ni	Nickel
O_2	Oxygen gas
O^{2-}	Superoxide
OH^-	Hydroxide
P	Phosphorus
Pt	Platinum
Si	Silicon
Ti	Titanium
Ti_2O_3	Titanium (III) oxide
Ti^{3+}	Titanium (III) ion
Ti6Al4V	Titanium-6%Aluminium-4%Vanadium
TiO_2	Titanium dioxide

V	Vanadium
ZnO	Zinc oxide

Chapter 1: Introduction

1.1 Metallic biomaterials used for implants

Biomaterials science and engineering are concerned with the application of biomaterials science in the design and engineering aspects in order to fabricate medical devices. Among a large biomaterial's classification, metallic biomaterials are still used widely to replace different human structural components because they surpass polymeric and ceramic materials in terms of tensile strength, fatigue strength, and fracture toughness [1]. They are used extensively for the fabrication of surgical orthopaedic implants such as artificial hip, knee joint, elbows, bone fixation, dental implant; and medical devices such artificial heart valves, blood conduits and other components of heart assist devices, vascular stents [1, 2]. Likewise, metals' particular electrical conductivity led to their use for producing neuromuscular stimulation devices such as cardiac pacemakers [3, 4]. The unique combination of mechanical properties, wear resistance and corrosion resistance of metallic biomaterials extended their use in different orthopaedic parts in the human body. Generally, a metallic biomaterial must comply some crucial properties to replace structural body components: 1. mechanical properties close to those of the bone, 2. Biocompatibility, 3. High wear resistance, 4. Osseointegration capacity, 5. Nontoxicity, 6. Long fatigue life, 7. High corrosion resistance [5]. A short description of these important key factors is reported below.

1.1.1 Mechanical properties

Metallic biomaterials with stiffness close to the bone and reasonable strength are required to prohibit stress shielding and fatigue failure [3]. Diverse geometries with different mechanical strengths have been designed to achieve the ideal scaffolds with suitable

mechanical behaviour. The chemical composition and mechanical properties of the most common metallic biomaterials are shown in the following into **Table 1.1 and 1.2**.

Table 1.1. The approximate weight percent of different metals within popular orthopaedic alloys [6].

Alloy	Ni	N	Co	Cr	Ti	Mo	Al	Fe	Mn	Cu	W	C	Si	V
Stainless steel (ASTM F138)	10–15.5	<0.5	*	17–19	*	2–4	*	61–68	*	<0.5	<2.0	<0.06	<1.0	*
CoCrMo alloys														
(ASTM F75)	<2.0	*	61–66	27–30	*	4.5–7.0	*	<1.5	<1.0	*	*	<0.35	<1.0	*
(ASTM F90)	9–11	*	46–51	19–20	*	*	*	<3.0	<2.5	*	14–16	<0.15	<1.0	*
(ASTM F562)	33–37	*	35	19–21	<1	9.0–11	*	<1	<0.15	*	*	*	<0.15	*
Ti alloys														
CPTi (ASTM F67)	*	*	*	*	99	*	*	0.2–0.5	*	*	*	<0.1	*	*
Ti-6Al-4V (ASTM F136)	*	*	*	*	89–91	*	5.5–6.5	*	*	*	*	<0.08	*	3.5–4.5
45TiNi	55	*	*	*	45	*	*	*	*	*	*	*	*	*
Zr alloy														
(95% Zr, 5% Nb)	*	*	*	*	*	*	*	*	*	*	*	*	*	*

*Indicates less than 0.05%.
Note: Alloy compositions are standardized by the American Society for Testing and Materials (ASTM vol. 13.01).

Table 1.2. Mechanical properties of dominant metallic orthopaedic biomaterials [6].

Orthopedic biomaterial	ASTM designation	Trade name and company (examples)	Elastic modulus (Young's modulus) (GPa)	Yield strength (elastic limit) (MPa)	Ultimate strength (MPa)	Fatigue strength (endurance limit) (MPa)	Hardness HVN	Elongation at fracture (%)
Cortical bone[a]								
Low strain			15.2	114t	150c/90t	30–45	—	—
High strain			40.8	—	400c–270t	—	—	—
Metals								
Stainless steels	ASTM F138	Protusul S30-Sulzer	190	792	930t	241–820	130–180	43–45
Co–Cr alloys								
	ASTM F75	Alivium-Biomet CoCrMo-Biomet Endocast SlL-Krupp Francobal-Benoist Girard Orthochrome- DePuy Protosul 2-Sultzer Vinertia-Deloro Vitallium C-Howmedica VitalliumFHS-Howmedica Zimaloy-Zimmer Zimalloy Micrograin	210–253	448–841	655–1277t	207–950	300–400	4–14
	ASTM F90	Vitallium W-Howdmedica	210	448–1606	1896t	586–1220	300–400	10–22
	ASTM F562	HS25l-Haynes Stellite MP35N-Std Pressed Steel Corp.	200–230	300–2000	800–2068t	340–520	8–50 (RC)	10–40
	ASTM 1537	TJA 1537-Allvac Metasul - Sulzer	200–300	960	1300t	200–300	41 (RC)	20
Ti alloys								
CPTi	ASTM F67	CSTi-Sulzer	110	485	760t	300	120–200	14–18
Ti-6Al-4V	ASTM 136	Isotan-Aesculap Werke Protosul 64WF-Sulzer Tilastan-Waldemar Link Tivaloy 12-Biomet Tivanium-Zimmer	116	897–1034	965–1103t	620–689	310	8

[a] Cortical bone is both anisotropic and viscoelastic thus properties listed are generalized.
c, compression; t, tension; *, no current ASTM standard; RC, Rockwell Hardness Scale; HVN, Vickers Hardness Number, kg/mm.

1.1.2 Biocompatibility

Metallic biomaterials after implantation process in human body media must not surpass normal cells' activity and should be non-toxic [7]. This can be achieved by selected a proper chemical composition of the bulk materials or by applying coatings to create a barrier between the toxic substrate and the human body environment [5]. Likewise, they should also provide specific conditions for protein adsorption, cell adhesion, and healthy cell growth on their surfaces in the human complex media [8].

1.1.3 High wear resistance

A low friction coefficient and high wear resistance are assigned to a perfect metallic biomaterial during sliding over the various body tissues and metal-on-metal or bone. The wear debris created during the contact between tissues and/or bone and biomaterials interface can lead to the destruction of the bone supporting the implant [9, 10].

1.1.4 Osseointegration

A perfect attachment and connection between the living bone and surface of a load-carrying implanted biomaterial is defined as osseointegration. Some crucial parameters such as chemical composition, surface chemistry, roughness, and topography of biomaterials surface are serious concerns for osseointegration [11]. Therefore, the loosening of the implanted biomaterials is due to a non-perfect connection between the biomaterials surface and nearby bone [12].

1.1.5 Long fatigue life

A metallic biomaterial during the lifetime performance is under the effect of the abundant cyclic loadings in the human body that can lead to progressive and localized

structural damage and growth of cracks. Therefore, the appropriate metallic biomaterials should demonstrate high mechanical resistance and stress shielding behaviour [7].

1.1.6 High corrosion resistance

The most common metallic biomaterials (in this thesis, metallic implants), as presented in **Table 1.2**, represent an outstanding resistance to degradation, with low metal ion release than in turn decreases the toxic reaction [2]. Therefore, a metallic implant with superior corrosion resistance can decline some interconnected critical problems such as the toxicity of corrosion products arising from localized corrosion, wear, and fretting debris [13-15]; fracture due to the low corrosion fatigue and fretting corrosion fatigue [1].

1.2 Micro and nano-devices in human body

Small-scale swimmers, which comprise motors and robots, are tiny machines capable of moving and operating at the micro- and nano realms. These motile micro- and nanodevices have been proposed for a large variety of applications including manufacturing, material removal, environmental remediation, targeted drug delivery, nanosurgery, and isolation of biological targets [16-19]. As such these newly developed tiny devices can be considered a novel class of biomaterials.

The controlled locomotion of small-scale swimmers in liquid environments has been the object of study for at least two decades, as motion at low Reynolds numbers requires the execution of non-reciprocal motions for achieving translational displacement (at least for Newtonian fluids) [20]. To this end, researchers have investigated several strategies to provide the energy necessary for the motion of micro- and nanostructures [21, 22]. Efforts have been made to develop tiny machines that can display one or more locomotion mechanisms including tumbling, rolling, corkscrewing, crawling, shuttling, and contraction

[23]. Two main approaches exist for providing a driving force necessary for the motion of small-scale swimmers. In the first, the micro- or nanostructure acts as a platform for triggering a chemical or an electrochemical reaction, which results in the propulsion of the structure (**Figure 1.1A**) [24]. These reactions take place on the swimmer's surface, which serves as a reactant or as a catalyst for the transformation of the chemical species present in the surrounding media [25, 26]. In this situation, swimmers are motors (not robots) because their directionality and speed cannot be controlled. The second approach consists of using small-scale structures that are responsive to an external source of energy, such as magnetic or electric fields, ultrasound, light or combinations of these, which causes the structure to move [22, 27]. The swimmers that are controlled by external sources of energy are known as robots, because their speed and directionality can be externally controlled by tuning the energy of the source (**Figure 1.1B**) [28]. In both approaches, not only the components but also their geometry are key for their optimal motion or manipulation [29]. However, as swimmers are ultimately designed for the realization of tasks, it might be necessary to incorporate additional components in the final swimmer architecture [18].

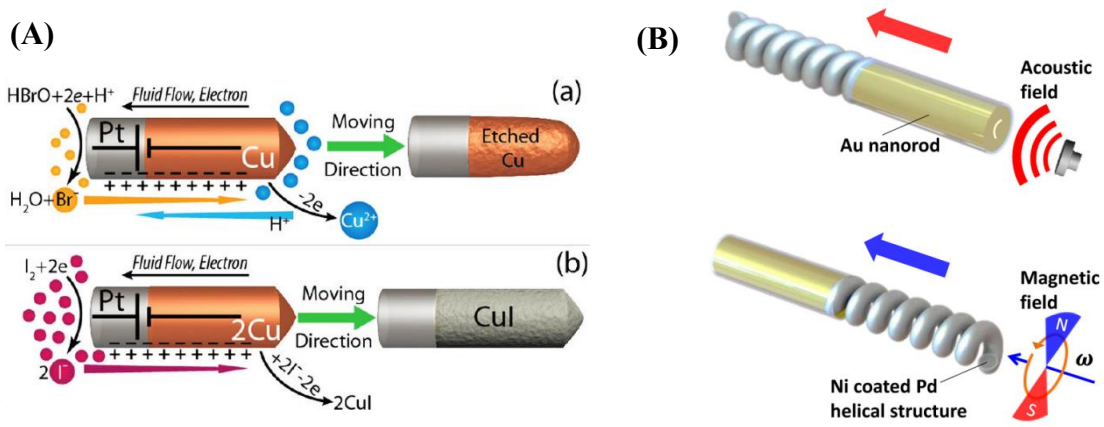

Figure 1.1. (A) Schematic representation of the mechanism of self-powered nanomotor motion in (a) Aqueous Br_2 and (b) Aqueous I_2 [24], (B) Schematic illustration of the design of the magneto–acoustic hybrid nanomotor and its dual propulsion modes under the acoustic and magnetic fields [28].

Arguably, the use of external magnetic fields is one of the most versatile approaches for the manipulation of magnetic micro- and nanorobots, as a wide variety of swimming mechanisms can be achieved by changing the way magnetic fields are applied (i.e. rotating, oscillating, gradients or combinations thereof) [30]. Additionally, considering that some of the most sought applications are in the biomedical area, magnetic fields are suitable for biomedical purposes owing to their high biocompatibility characteristics towards biological tissues [30, 31]. Most magnetic micro- and nanorobots are fabricated of ferro- and ferrimagnetic metals, alloys or ceramic oxides containing at least one of the following elements: Fe, Ni, and Co [30, 32, 33]. Note that the manipulation of diamagnetic and paramagnetic small-scale robots has also been investigated, but few examples are available in comparison to ferro- and ferrimagnetic devices.

Magnetic micro- and nanorobots can be produced using different techniques such as physical vapor deposition (PVD), three-dimensional direct laser writing (TDLW), assembly of materials, and template-assisted electrodeposition [29]. The latest has attracted many researchers as it is a low-cost method that does not require special equipment and allows the formation of several micro- and nanoarchitectures made of different materials ranging from metals to polymers [29, 34-36].

Over the last decades, the great insight and studies have been considered on the performance of magnetic nanomaterials in biomedical field with varieties application including target drug delivery [37, 38], tissue engineering [39, 40], magnetic hyperthermia treatment [41-44], magnetic resonance imaging [45, 46] etc. The type of application, chemical composition, shape, size, and multifunctionality of magnetic nanoparticles play a determined step in improving the efficiency of them during their performance.

Spinel ferrites as cobalt ferrite ($CoFe_2O_4$, CFO) nanoparticles with special scientific and technological interest have been extensively used in all branches of engineering, medicine, and subdisciplines due to their properties including magnetic, mechanical hardness, suitable catalytic properties and desirable chemical stability [47-50]. The combination of these outstanding properties triggers using $CoFe_2O_4$ for a wide range of applications such as high-density storage devices, ferrofluids, catalysts, magnetic separation, magnetic resonance imaging, drug targeting, and gas sensors [51-56]. Moreover, by covering the CFO particles with other multiferroic materials such as bismuth ferrite ($BiFeO_3$, BFO), creating core-shell structures, new functionalities could be achieved such as magnetoelectric, magnetooptic, and photocatalytic properties [57, 58] together with an enhanced resistance to degradation.

In terms of motion and processability, ferromagnetic metals, alloys and ceramics are very attractive for the construction of magnetic micro- and nanorobots [59]. Additionally, these materials exhibit optimal properties for magnetic manipulation, such as high saturation magnetization and high magnetic susceptibility. Furthermore, their magnetic softness/hardness can be modulated by tailoring their crystal structure and/or by alloying with other magnetic and nonmagnetic elements [60].

1.3 Corrosion of metallic implants in human body fluids

The high resistance to corrosion or metal ions releasing of metallic biomaterials is one of the most important factors to be considered in selecting metals or alloys for the implant. [61]. Few metallic biomaterials are considered acceptable as suitable surgical and dental implants for applications in different human body parts (**Table 1.2**). The average lifetime of the implanted metallic prosthesis is approximately close to 15 years [2]. Recently, the lifetime average of metallic orthopaedics has been increased due to the significant progress of biomaterials science in surgical techniques, treatment, material manufacturing, and quality control [62-68]. Therefore, understanding the corrosion behaviour of metallic implants in vitro and in vivo can help estimating their lifetime performances.

Nowadays, with numerous innovations on new metallic biomaterials, still titanium-based alloy (CP-Ti and Ti6Al4V), stainless steel, and CoCrMo alloys are the most popular medical implants, especially for orthopaedic applications [69, 70]. The high corrosion resistance and biocompatibility of these metallic implants are related to their ability to form well-adhered, dense, protective oxide surface layers (passive oxide films typically 5–10 nm thick) that are retained in vivo [3, 71]. The characteristic of the simple or complex passive film on metallic implants and their relative stability can act as a barrier to electron and metal ions transfer at electrolyte/solid interface [72].

As stated earlier, forming a compact and stable passive film on metallic implants during exposure to natural and alkaline environments can significantly reduce the corrosion rate to a very low level [73]. However, during a long-term performance in human body media, this protective passive films are susceptible to metal ion release, even if at low rate. Under particular critical conditions, the passive films can undergo severe damage and

electrochemical breakdown (as called passive film breakdown) [74]. The passive film's breakdown and corrosion attacks on metallic implants can occur under various circumstances in different parts of the human body undegoing pitting corrosion, galvanic corrosion, crevice corrosion, intergranular corrosion, fretting corrosion, stress corrosion cracking. The following discussion will be related to different corrosion mechanisms on the three most common metallic implants such as Ti6Al4V, CoCrMo, and stainless-steel (SS) alloys in real or simulated human body fluid.

1.3.1 Pitting Corrosion

The local dissolution rate of the passive film on metallic implants in the presence of aggressive ions e.g., Cl^- significantly increases due to the initiation and propagation of corrosion pits [75]. The possibility of pitting corrosion can significantly increase by increasing the concentration of aggressive ions, lowering the pH, and increasing the concentration of biological species (proteins and reactive oxygen species (ROS)) [73, 76], as presented in **Figure 1.2**.

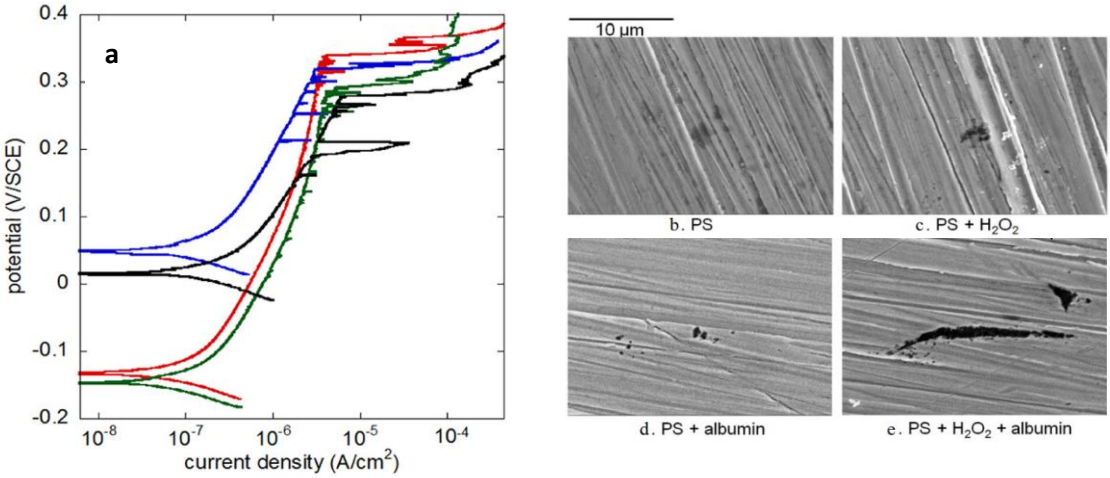

Figure 1.2. (a) Plots of anodic polarization curves of 316L stainless steel in physiological saline with or without 100 µM H_2O_2 and/or 0.1% albumin at 37 °, sweep rate 1 mV/s, SEM images of 316L stainless steel discs after 16 weeks immersion in (b) physiological saline

(PS), (c) PS and 100 μM H_2O_2, (d) PS and albumin, and (e) PS with both H_2O_2 and albumin after 16 weeks immersion at 37 °C [76].

It should be considered that the pit sits on the passive film of metallic implants in the presence of the different applied stress in the human body can serve as sites for the initiation of stress corrosion cracking. Pits initiation and their propagation through the passive film on the metallic implant can occur after short or long-term implantation in human body media [76].

Pitting corrosion is a common problem of stainless-steel implants, mainly grade 304. However, the use of SS 316L with 2-3% Mo, importantly decreases the number of failures due to pitting corrosion. Considering the pitting resistance equivalent number (PREN= %Cr + 3.3Mo + 16%N), a PREN value higher than 26 is required to prevent in vivo pitting corrosion [1, 77, 78]. By increasing the Ni content in SS 316L, the PREN value can slightly exceed the threshold of 26 (SS316L PREN=32 and high-N SS PREN=35). Moreover, by changing the microstructure, chemical composition, or surface treatment on SS316L can improve its resistance to pitting corrosion due to the modifications of the passive film chemical composition.

For example, Mold Talha et al. [79] used different SS316L with different chemical compositions, cold working, and annealing processes (at 1050 °C for 15 min followed by water quenching), as shown in **Table 1.3**. Their results (**Figure 1.3**) showed that increasing nitrogen content significantly increased the pitting corrosion resistance of all SS316L samples in the annealed condition (0% cold worked). As the cold working of the alloys increased from 0% to 20%, an improvement in pitting resistance was noticed. Moreover, the cold-rolled samples showed lower passive current density than the annealed materials. Another study by M.K. Lei et al. [80] using plasma source ion nitriding as surface treatment

on SS316L showed that no-pitting corrosion was detected on the treated sample in the Ringer's solutions in pH 7.2 and 5.5 at 37 °C.

Table 1.3. Composition of stainless steels (wt.%) [79].

Sample	C	Cr	Mn	Ni	Si	Mo	S	P	N	Fe
316LVM	0.02	17.24	1.68	14.42	0.24	2.83	0.004	0.007	0.07	Bal.
$316MnN_1$	0.48	19.32	12.77	0.05	0.26	3.32	0.006	0.009	0.34	Bal.
$316MnN_2$	0.08	19.11	11.85	0.08	0.25	3.02	0.004	0.010	0.43	Bal.
$316MnN_3$	0.017	18.28	11.92	0.04	0.07	3.24	0.003	0.008	0.52	Bal.

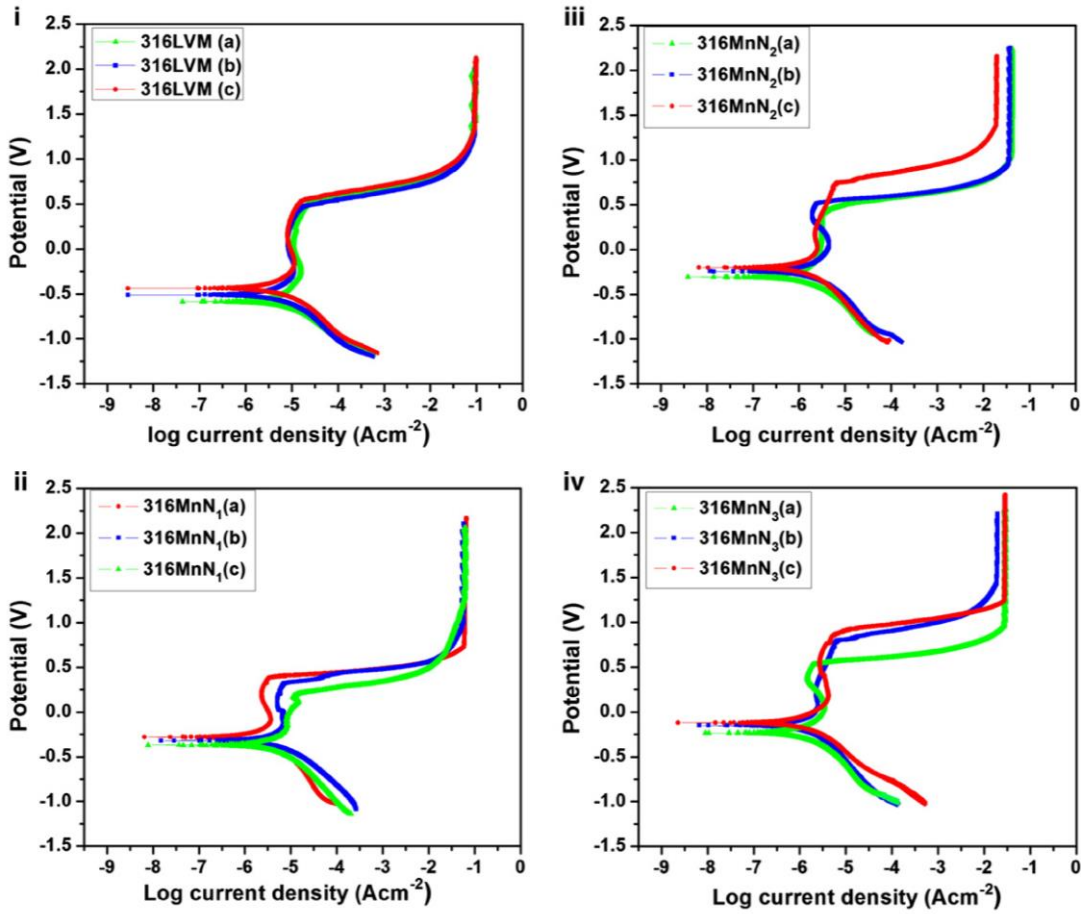

Figure 1.3. Polarization curves in Hank's solution at 37 °C for (i) 316LVM, (ii) 316MnN1, (iii) 316MnN2, and (iv) 316MnN3. *a = annealed, b = 10% c.w., and c= 20% c.w [79].

However, the story for Co-based alloys is different. Most of the research works report that these alloys (especially CoCrMo alloy with low carbon (0.03%)) are resistant to pitting corrosion attack under static conditions [62, 74, 81]. However, CoCrMo alloys with a high carbon (0.24%) are susceptible to pitting corrosion due to the formation of chromium carbides which leads to a local Cr depletion as well as the galvanic coupling between the carbides and the matrix [82].

The Cp-Ti and Ti-based alloys are considered as an immune metallic implant to pitting corrosion attacks in any in vivo environments [83, 84]. Nevertheless, some in vitro research studies indicated that Ti alloys suffer to nominal pitting corrosion at a potential value higher than 1.3 or 1.5 V vs. SCE [1, 85, 86]. These results are not contradictory as according to [87] a range between +400 to +500 mV vs. Ag/AgCl is representative of the human body environment under normal conditions and the Ti alloys passive film does not suffer pitting in this potential range.

1.3.2 Galvanic corrosion

Galvanic corrosion can occur when two different metals or alloys with different nobility are electrically connected together [73]. In this condition, two separate regions will be established with the less noble metal acting as anode and the more noble metal acting as cathode. The galvanic coupling can also occur internally between various phases of multi-phases alloys [88, 89]. Most metallic biomaterials are in the passive state, and the galvanic coupling process cannot expect to trigger any significant changes in the corrosion rate of joined metallic implants [90, 91]. However, because of the dynamic conditions of the human body alongside with the presence of various biological species, a shifting of the potential to higher values can occur , which in turn could increase the probability of localized corrosion

attacks [92]. Alex Lanzutti et al. [93] showed that high carbon CoCrMo is susceptible to preferential dissolution due to galvanic coupling between carbides and matrix, which increases the intergranular corrosion rate (**Figure 1.4**). In a particular condition that titanium and Co-based alloys are joined together, the titanium oxide layer act as a cathode and Co-based alloy behave as an anodic site. However, the low kinetics of the oxygen and water reduction reactions on the titanium oxide layer can significantly reduce this type of localized corrosion.

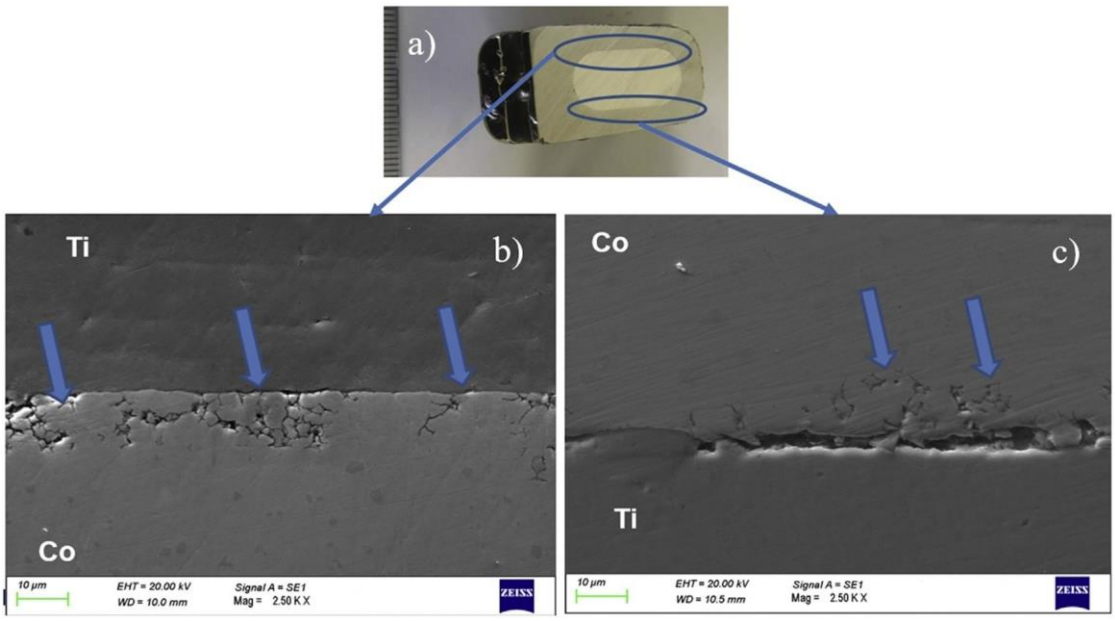

Figure 1.4. Corrosion morphologies at the interface of the conical joint between the CoCrMo alloy neck and the Ti alloy stem. The failed component was extracted from a patient (66-year-old man with 90 Kg weight and 180 cm height) after a 3 years and 9 months implantation [93].

1.3.3 Intergranular corrosion

Grain boundaries are high energy sites with more reactive nature and thus intergranular corrosion is a phenomenon that occurs adjacent to grain boundaries with relatively low corrosion of grains [94]. The presence of carbon element in stainless steel and some Co-based alloys in order to improve their strength can lead to the formation of chromium carbides during different heat treatments as a secondary phase [93, 95]. Therefore, the grain boundaries around these secondary phases are chromium depleted. Hence, the passive protective film with a higher distribution of atomic defects around these regions is significantly susceptible to breakdown and localized corrosion attacks [95]. Emily E. Hoffman et al., [96] using transmission electron microscopy (TEM) showed that both the chromium depletion at nanoscale regions in high-carbon CoCrMo alloy and the grain boundaries can act as preferential sites for corrosion initiation (**Figure 1.5**). Moreover increased release of toxic Co and Cr ions from CoCrMo in patients has been reported as a result of selective dissolution around carbides [97]. Another study by Alex Lin et al. [98] indicated that the low-Σ coincident site lattice boundaries in high-carbon CoCrMo presented carbides precipitation and a lower degree of sensitization, which in turn, made them more resistant to intergranular corrosion attacks. In fact, higher presence of carbide precipitates and larger Cr depletion was detected at high-energy boundaries, where corrosion initiation and propagation were more intense.

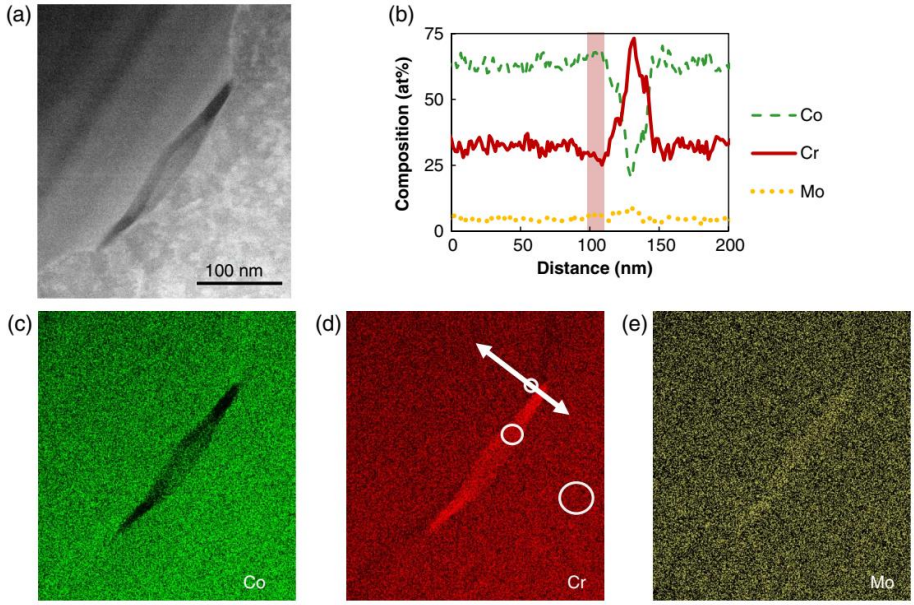

Figure 1.5. The chromium depleted region around a chromium-rich carbide, with (a) the annular dark field-TEM image, (b) an extracted line scan to show the Cr-depleted zone, (c) cobalt, (d) chromium, and (e) molybdenum. The arrow indicates where the line scan was taken [96].

1.3.4 Crevice corrosion

When two surfaces come together, make a thin layer trapping of electrolyte between them. Therefore, crevice corrosion initiates due to the operation of a differential oxygen concentration between the bulk electrolyte and crevice region [1, 73]. Based on the Nernst equation [73], the crevice region with lower oxygen concentration presents a more negative potential than bulk electrolyte with higher oxygen content (oxygen concentration cell). Also, the limiting current density for O_2 reduction reaction within the crevice decreases with respect to the bulk electrolyte region. Both effects simultaneously concentrate the anodic reactions in the crevice zone and the supporting cathodic reaction on the large surface outside the crevice. The complex shapes of metallic prosthesis often present crevices and could suffer from crevice corrosion. The various species in the human body environments can penetrate into the narrow gap or crevice region and strongly alter the crevice solution

chemistry and the rate of metal ion releasing. In fact, the possible acidification of the body fluids inside the crevice is due to differential hydrolysis favoured by the presence of aggressive Cl^- ion [93]. Typical examples of crevice corrosion event in biomedical application are CoCrMo stem from a metal-on-polyethylene implant [99, 100] (**Figure 1.6**) ,Ti6Al4V and Co-based alloys head-neck tapers [101-103], Co-Cr/Co-Cr [104], and dental implants [92, 105] and CoCrMo grain boundary assisted to crevice corrosion [96].

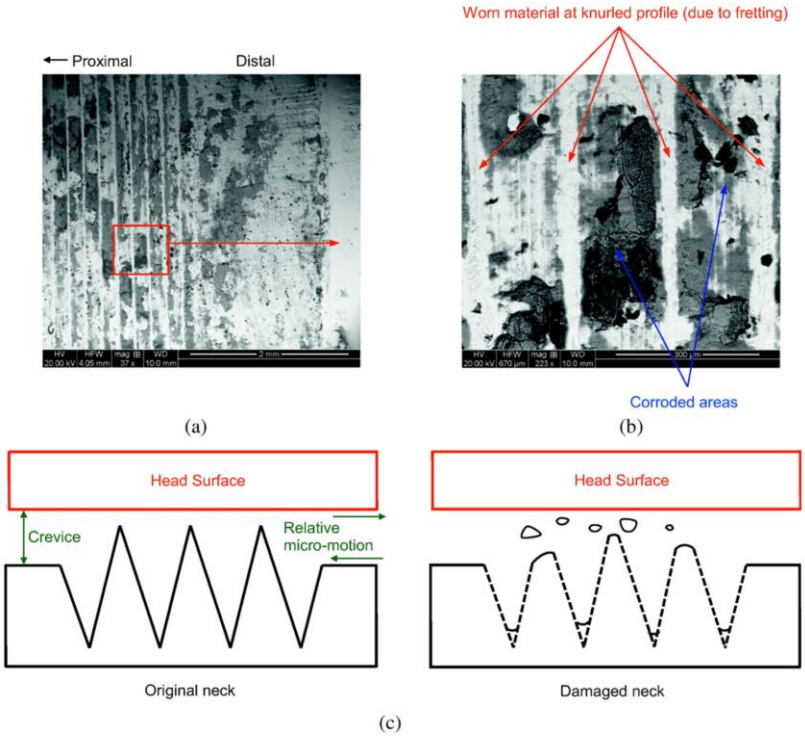

Figure 1.6. (a) Surface damage to the CoCrMo neck, mainly in the distal medial area; (b) SEM image with a higher magnification showing both mechanical fretting wear and crevice corrosion damage; and (c) a schematic mechanism showing material removal from the knurled profile over the neck surface in contact with the head surface, corrosion channels are also shown between the lines of the profile [99].

1.3.5 Fretting corrosion

Fretting is a special type of tribological contact which involves a mutual motion of prosthesis parts in a small amplitude (a few micrometers) into sliding joints [2]. This mechanical sliding causes damaging the protective passive film, and then the bulk material

immediately undergo the active corrosion attack, called fretting corrosion [6]. The fretting corrosion process at joints can generate a serious problem, not only related to metal ion releasing but also changes in the dimensions of the prosthesis joint, thus causing fixation problems [1]. On the other side, the mechanical wear at joints can trigger to loss of the surrounding cement or bone, leading to further movement of the implant, thereby enhancing the susceptibility of implants to fatigue corrosion [93, 106]. The three most common surgical metallic implants, including Ti-based, Co-based alloys, and stainless steel, suffer from fretting corrosion. Also, surgical implants' fretting corrosion can significantly affect both solution chemistry and potential [107].

The combined effects of multiple factors, including surface potential, contact pressure, fretting amplitude and protein content, strongly influence the intensity of the fretting corrosion process [108]. Viswanathan Swaminathan et al. [109] reposted that among different metallic implant combinations, Ti6Al4V/Ti6Al4V couple exhibited the higher fretting currents, higher friction, and lowest work done per cycle compared to CoCrMo/CoCrMo and Ti6Al4V/CoCrMo couples (**Figure 1.7**). Likewise, the Ti6Al4V/CoCrMo couple fretting corrosion behaviour was similar to that of the CoCrMo/CoCrMo couple.

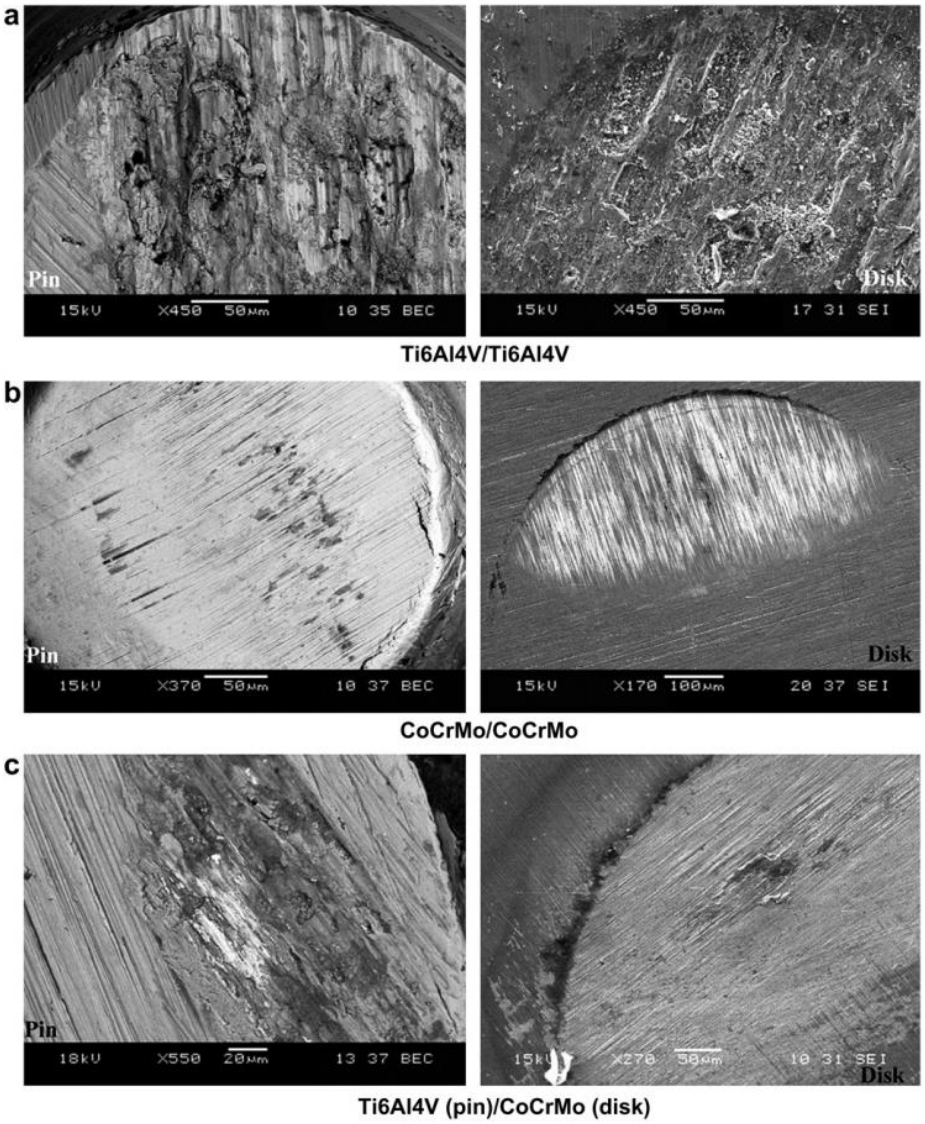

Figure 1.7. Back-scatter (BS) and secondary electron (SE) mode SEM micrographs of pin and disk surfaces of different material combinations obtained at the end of fretting corrosion testing. Note the severity of plastic deformation associated with Ti6Al4V surfaces (a and c) as a result of fretting corrosion. The dark grayish regions in the BS micrographs (a,b, and c) indicate the corrosion debris that is mostly composed of oxides. CoCrMo surfaces (b and c) show much less plastic deformation, but the fretting scars are clearly visible [109].

1.4 Protein adsorption and its influence on corrosion behaviour of metallic implants

1.4.1 Adsorption of protein on biomaterial surface

When any type of biomaterial is transplanted into the human body, adsorption of protein molecules on its surface is the first stage that directly determines the subsequent events [110]. Protein adsorption can significantly control the subsequent cell-surface interaction and greatly influence the life of the implanted biomaterials [111]. From the biomaterial's aspect, the instantaneous adsorption of protein remarkably influences implants' biocompatibility [112, 113]. The adsorbed protein layer enhances osteoblast cell attachment, proliferation, differentiation, and bone tissue regeneration [111]. It has been proved that the adsorbed protein layer plays a critical role in further physiological results of implanted biomaterials in biological media, including coagulation, thrombogenesis, and inflammatory responses [114]. In addition, protein's denaturation, fragmentation, and conformational arrangement during adsorption on biomaterials surface may influence the host body's function [1]. A schematic presentation of successive events on biomaterial surfaces after the implantation is shown in Figure 1.8 [115].

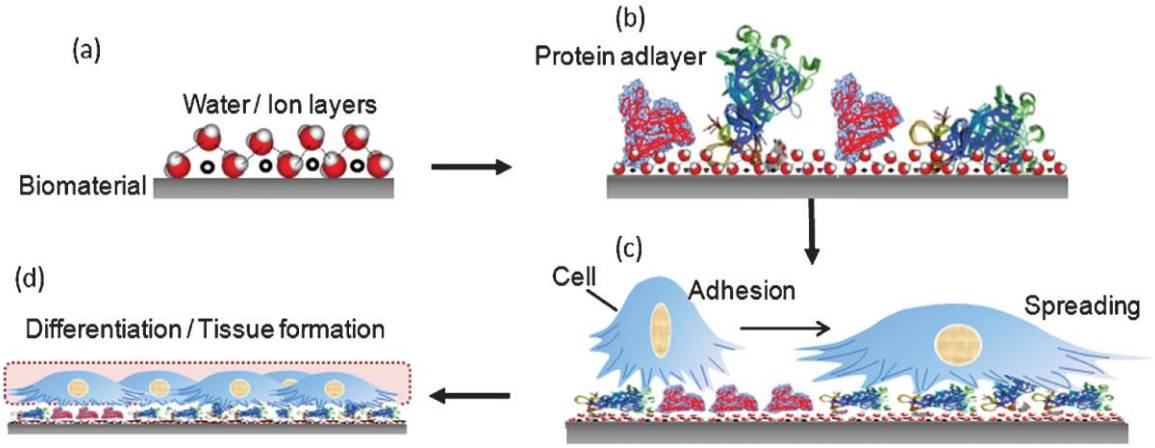

Figure 1.8. Scheme of the successive events on biomaterial surfaces after the implantation; (a) formation of water and ion layer, (b) protein adsorption, (c) cell adhesion/spreading, and (d) differentiation/tissue formation [115].

The kinetics of the protein adsorption and its morphology in a complex media with various species are greatly affected by the implanted biomaterials surface properties such as surface energy, net charge distribution, roughness, hydrophobic/hydrophilic character of the surface, and surface oxide thickness [116]. Likewise, protein molecule properties such as protein size, charge, hydrophobicity and concentration alongside with the solution properties such as ionic strength, pH, shear rates and agitation determine the type and amount of the protein adsorption on solid surfaces [117]. One of the important factors in the kinetics of protein adsorption is assigned to the sequence of amino acids as primary structure of proteins. In fact, the amino acids bonds act as active zones of protein molecule to create the interaction with surface [111] [118].

Several models have been postulated for protein adsorption on solid surfaces based on the surface covering and the adsorbed protein morphology such as Langmuir isotherm and cooperative adsorption [119-121]. Isotherm adsorption defines the various mechanisms relating to the adsorption in equilibrium conditions such as Langmuir, Freundlich, and Temkin equations [111]. The Langmuir-isotherm adsorption (protein adsorbate) assumes the formation of a monolayer protein over a homogeneous surface. Most studies on the protein adsorption on metallic biomaterials surfaces such as SS316 [122, 123], CoCrMo [114, 124], Ti alloys [125-127] and gold [128] have been explained based on Langmuir isotherm. In the other side, the cooperative protein adsorption model describes the preferential adsorption of proteins in the vicinity of preabsorbed proteins forming protein aggregates or two-dimensional clusters on the surface [129, 130].

Some proteins such as fibronectin and vitronectin as extracellular matrix adhesion proteins is expected to enhance the cell adhesion [131]. Although, the adsorption of other protein species such as albumin protein plays a key role as cell adhesion inhibitor, biofouling

the implant surface [132]. Albumin protein is generally found in blood plasma and extracellular fluid with a unique behaviour among the plasma proteins [122]. Human serum albumin (HSA) protein is the most abundant protein in human blood plasma [2, 133]. In comparison with other proteins in blood plasma, HAS protein is mainly responsible for the preservation of blood pH and osmotic pressure [134, 135]. **Table 1.4** and **Table 1.5** show the ionic concentrations in blood plasma and extracellular fluid as well as the major proteins and other species, respectively.

Table 1.4. Ionic concentrations in blood plasma and extracellular fluid [6].

Anion, cation	Blood plasma (m*M*)	Extracellular fluid (m*M*)
Cl^-	96–111	112–120
HCO_3^-	16–31	25.3–29.7
HPO_4^{2-}	1–1.5	193–102
SO_4^{2-}	0.35–1	0.4
$H_2PO_4^-$	2	—
Na^+	131–155	141–15
Mg^{2+}	0.7–1.9	1.3
Ca^{2+}	1.9–3	1.4–1.55
K^+	35–5.6	3.5–4

Table 1.5. Major proteins and other organic constituents of blood plasma [6].

Major proteins and organic molecules in blood plasma (gl^{-1} unless stated otherwise)	
Albumin	30–55
α-Globulins	5–10
β-Globulins	6–12
γ-Globulins	6.6–15
α-Lipoproteins	3.5–4.5
Fibrinogen	1.7–4.3
Total cholesterol	1.2–2.5
Fatty acids	1.9–4.5
Glucose	0.65–1.1
Lactate	0.5–2.2 m*M*
Urea	3–7 m*M*

The most outstanding albumin protein property is assigned to its ability to reversibly bond with an incredible variety of ligands such as fatty acids, hematin, bilirubin, charged aromatic compounds, and cysteine glutathione, and various metals [2]. Based on these abilities, bovine serum albumin (BSA) is considered as a model protein in biocompatibility studies, especially protein adsorption on metallic implants. BSA is a globular protein (average MW 66 kDa) that consists of 580 amino acid residues with 17 intrachain disulfide bonds and one free thiol group at residue 34 [136]. Likewise, BSA's secondary structure consists of approximately 54% R-helix and 40% β-structure and contains three binding domains [136]. According to the literature [91, 92], BSA dimensions are 4 × 4 × 14 nm, which presents an ellipsoidal shape. BSA protein isoelectric point (IEP) based on experimental and theoretical (simulation method) is in the range value of 4.7 - 5.5 in NaCl solution (ionic strength 10 mM) at 25 °C [137]. In addition, at these experimental conditions, BSA protein has a negative zeta potential, which is approximately close to -10 mV. The BSA molecular structure, charge distribution, and its hydrophobicity is presented in **Figure 1.9** based on a molecular simulation study.

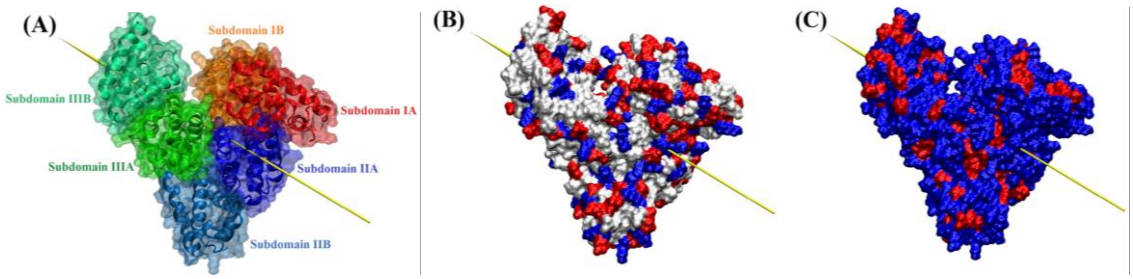

Figure 1.9. BSA structure (A), and the distribution of charge (B) and hydrophobicity (C) on its surface. In Fig. (A) the protein "ghost" surface is shown alongside the secondary structure elements represented by "cartoon" as defined in VMD.13 Domain I is indicated by red-related colors (IA – red, IB – orange), domain II by blue-related colors (IIA – blue, IIB – light blue) and domain III by green-related colors (IIIA – green, IIIB – lime). All subdomains are annotated, and the yellow arrow indicates the protein dipole moment. In (B) and (C) the protein surface is solid and colored by residues' total charge (positive-blue, negative-red, neutral-white) and hydrophobicity (hydrophobic-red, hydrophilic-blue), respectively [138].

Ferritin is a major iron storage protein that can store up to 4500 iron atoms within the protein shell [139]. Iron is sequestered as a hydrous ferric oxide phosphate mineral that is structurally similar to ferrihydrite ($5Fe_2O_3$. $9H_2O$). The ferritin protein without bound iron is called apoferritin and is composed of 24 structurally homologous subunits. Two types of subunits are present, heavy (H) and light (L) subunits, classified according to the subunit molecular weight, 21 and 19 kDa, respectively. The ratio of the two types of subunits in apoferritin is species- and tissue-specific because each subunit carries out a different function. In horses, liver and heart apoferritins are composed of 4050 wt % H subunits and 8590 wt % H subunits, whereas spleen apoferritin contains 90 wt % L subunits [140]. The H subunits play a major role in iron oxidation, and the L subunits are involved in the efficient nucleation and mineralization of iron. These subunits assemble as a hollow rhombic dodecahedron protein shell with 4-3-2 symmetry that forms intersubunit channels along the three- and four-fold axes to accommodate iron [140].

The crystal structure of apoferritin was found to have a ferritin core (i.e., a ferrihydrite core), as determined by transmission electron microscopy (TEM). The structures of apoferritin and the ferritin core in solution were investigated by small-angle X-ray scattering (SAXS). The general structural models that reconstructed from the experimental SAXS data by molecular simulation programs are presented in **Figure 1.10.**

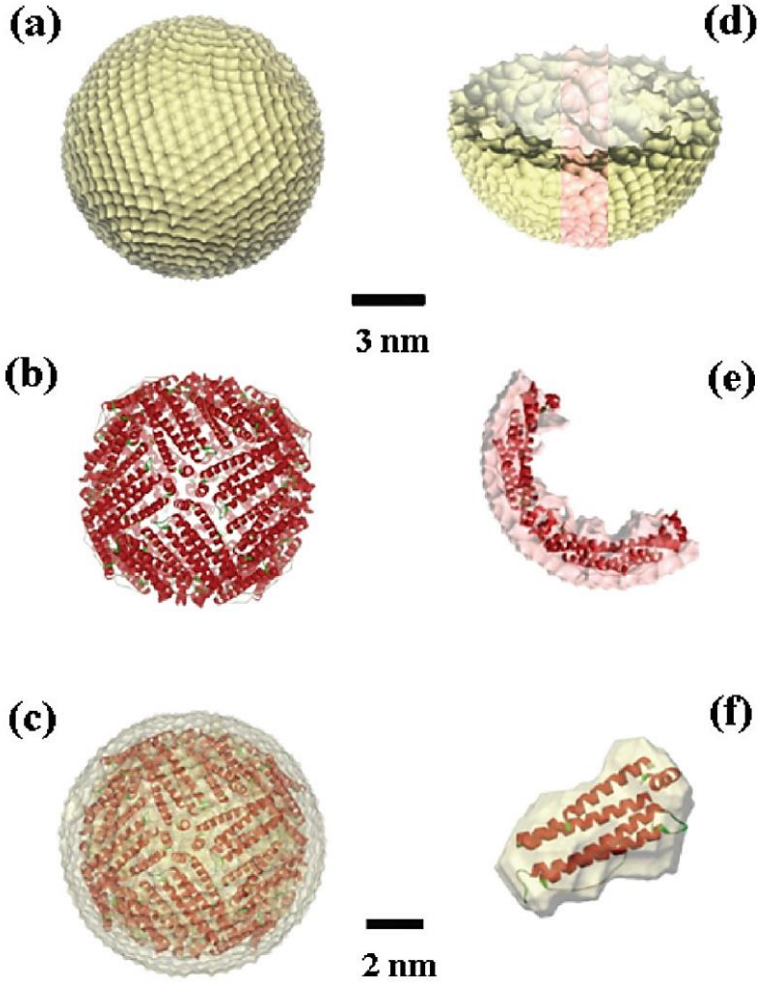

Figure 1.10. Structural models reconstructed from the experimental small-angle X-ray scattering (SAXS) data for apoferritin in neutral solution: (a) structural model of apoferritin in solution of pH 7.30; (b) ribbon diagram for the crystal structure of apoferritin (protein data bank (PDB) code 3F32); (c) ribbon diagram for the crystal structure of apoferritin in part b was superimposed on the reconstructed structural model of apoferritin at pH 7.30 using SUPCOMB program to compare overall shape and dimension as well as to reconfirm the hollow sphere structure; (d) structural model cut into half of apoferritin structure in part a; (e) structural model of the domain highlighted with pink color in part b, where ribbon diagram for the crystal structure of apoferritin subunits is superimposed on the structural model; and (f) ribbon diagram for the crystal structure of apoferritin subunit, which is superimposed on the structural model reconstructed from the theoretical SAXS curve calculated from the subunit crystal using the CRYSOL program [140] .

1.4.2 Protein effect on corrosion mechanisms

As discussed earlier, most of the metallic implants are covered with a protective and compact oxide film. In this condition, protein interactions are only limited to oxide film and not to the underneath metal. As a result, protein adsorption on the native oxide film of most metallic implants can be associated with the oxide film's surface chemistry and physical properties such as chemical composition, the local density of states, and bandgap energy etc. [141, 142]. Corrosion of metallic implants in human body media is a complex process involving various ions, proteins, etc. [117]. However, understanding the type of protein adsorption on a solid surface is an important parameter for estimating the degradation process. Protein adsorption on a solid surface can occur lonely or as a combination of different interactions including hydrophobic, electrostatic, hydrogen-bonding, and Van der Waals interactions [110].

Regarding the metallic implants, the adsorption of protein molecules can affect the corrosion performance during the lifetime [143, 144]. The synergetic effect of both electrochemical dissolution (e.g., pitting corrosion, galvanic corrosion, crevice corrosion, etc.) and chemical dissolution by protein molecules can accelerate the degradation of metallic implants. Many studies have shown that protein adsorption on metallic implants can either decrease the metal ions release or increase the degradation process, depending on the type of protein and metallic implant, protein concentration, solution condition, and short or long-term experimental results [111, 145, 146].

Protein binding to various metal atoms in the oxide layer of metallic implants is strongly dependent on the chemical and physical properties of the surface oxide film. A metal-protein detachment or an increase of metal ion release due to protein-metal bond will occur if metal-oxide or metal-hydroxide bonds have weak bonding[117]. Different

degradation mechanisms can be explained based on the protein effect on the biomaterial surface (in this case, metallic implants) such as shielding effect, lubrication effect, the attraction of counterions, complex action effects, Vroman effect, metal-protein conjugates as reported in **Figure 1.11**[117].

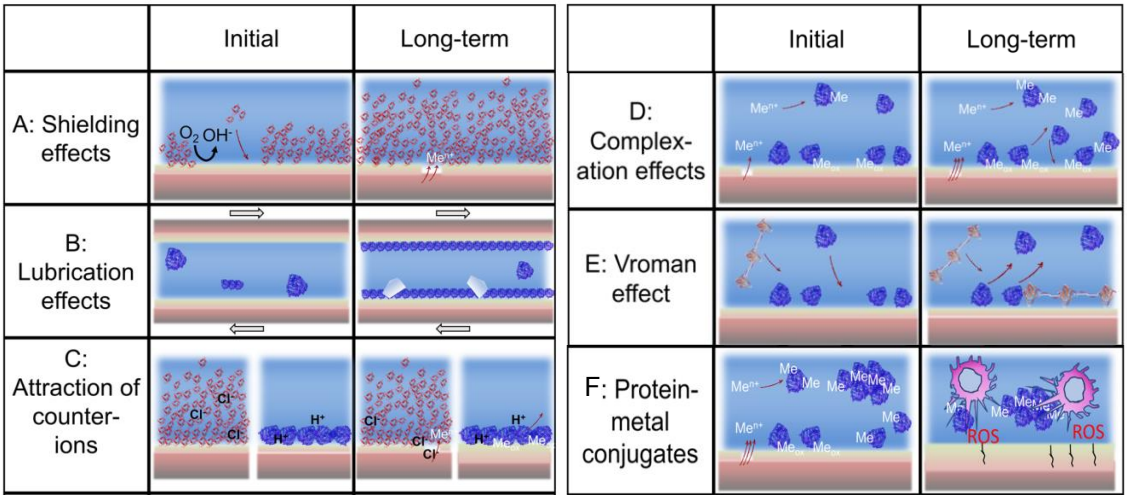

Figure 1.11. Schematic representation of the effect of proteins on material degradation in physiological media as a function of time [117].

In the shielding effect, the adsorbed protein regions on the biomaterial surface initially can decrease the degradation process by inhibiting the cathodic reactions [117]. However, after a long-term immersion, it can provide a condition for localized corrosion attacks. The lubricant effect of adsorbed protein initially can decrease the friction process on a solid surface. Although, the trapping of wear particles in the aggregated protein region or metal-protein complex region with the passing time may accelerate the friction process [147, 148]. The attraction of counterions, especially Cl^- and F^- on oxide film of metallic implants, significantly demolish the oxide and then localized corrosion can take place[149]. Complexation of released metal ions in human media with the protein species at protein/metal (metal oxide) interface can increase the corrosion process leading to the

detachment or metal-protein conjugates. In the Vroman effect, the abundant exchanges of adsorbed protein on solid surface increase the dissolution rate by detaching metal-bound proteins [150]. Metal protein conjugates can be defined as the formation of large-sized protein aggregates (between hundred nanometer to micrometer size) which can cause immunological and inflammatory reactions and eventually enhance the degradation process on biomaterial surfaces [117].

1.4.3 Protein effect on Tribo-corrosion mechanism

The mechanically assisted corrosion processes such as fretting corrosion, tribo-corrosion and etc., in metallic biomaterials, is one of the crucial issues which should be considered especially in highly loaded medical implants [109]. In addition, this type of mechanical sliding between the similar or dissimilar metallic implant's surfaces (e.g. knee and hip joint replacement), especially in the presence of biological species such as cells and protein molecules, can significantly affect the mechanism of passive film removing and its re-passivation process [151]. M.J. Runa et al. [151] studied the bio-tribocorrosion behaviour of Ti6Al4V in the presence of MG63 osteoblastic-like cells and fetal albumin protein . Based on this research, the presence of an osteoblastic cell layer seeded on the implant surface remarkably influences the tribocorrosion resistance of Ti6Al4V alloys. Likewise, they presented that in a culture medium with protein and cell species, the corrosion resistance of Ti6Al4V increased under the specific testing conditions.

According to previous studies [117, 152, 153], the adsorbed proteins molecules influence the formation mechanism of the protective oxide film on the metallic materials, forming initially a shielding layer, which under sliding inhibits the passive film re-formation. Also, M.J. Runa et al. [151] reported that the adsorbed protein layer accelerated the

passivation and re-formation of a new layer with a quick recovery of potential towards more positive values and higher total polarization resistance values after sliding (**Figure 1.12**). Another study performed by S. Hiromoto and S. Mischler [154] on collagen and albumin's effects on the fretting–corrosion behaviour of a Ti6Al4V alloy in PBS solution reports that the albumin proteins do not significantly influence wear rate, friction, and the wear-accelerated corrosion of the Ti6Al4V alloy. The wear rate increased by increasing the normal load and overpotential, which is independent on the presence of proteins. Consequently, the presence of the adsorbed protein layer on the implant's surface can prevent the mechanical degradation of metallic implants. In fact, a thin layer of adsorbed protein can protect the metallic implants from wear under fretting corrosion against other soft (polymer) or hard materials [117, 155]. Summarizing, the presence of BSA protein does not seem to negatively influence the tribo-corrosion or fretting corrosion behavior of passive metallic alloys.

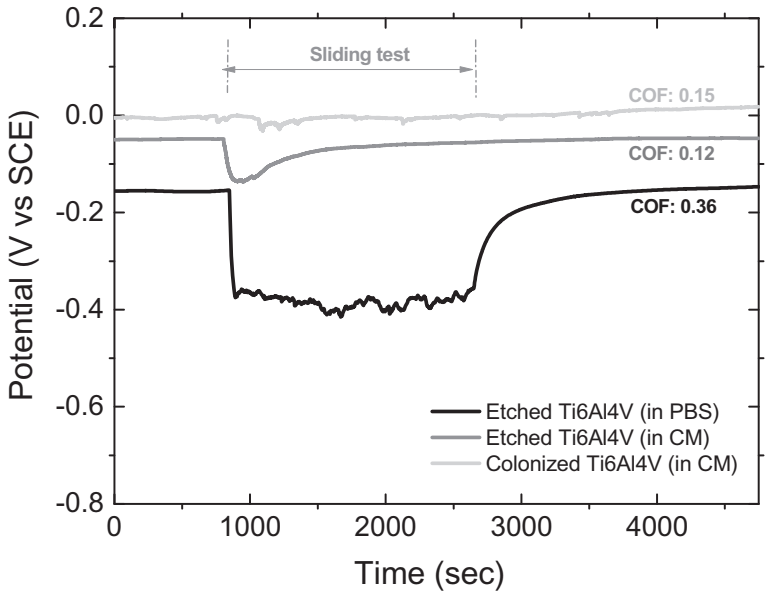

Figure 1.12. Evolution of the potential during tribocorrosion experiment for the different surfaces tested: etched Ti6Al4V immersed in PBS, etched Ti6Al4V immersed in CM, and etched Ti6Al4V colonized with osteoblastic cells [151].

1.4.4 Protein effect on the corrosion behaviour of SS316, Co-based and Ti-based alloys

In the following discussion, the effect of albumin protein molecules on the corrosion behaviour of the most common metallic implants such as SS316L, Co-based alloys, and Ti-based alloys in various solutions such as physiological saline (0.9 %wt NaCl), phosphate-buffered saline (PBS), Hanks, and Ringer's solutions will be presented.

1.4.4.1 SS 316L

The electrochemical interaction on the surface of orthopaedic SS 316L was studied by Shima Karimi et al. [70] at different BSA protein concentrations in PBS media. The open-circuit potential (OCP) and potentiodynamic polarization (PDP) results showed that the gradual increase in the BSA concentration from 0 up to 4 $g.L^{-1}$ lead to OCP and corrosion potential (E_{corr}) decrease [70] (Figure 1.13).

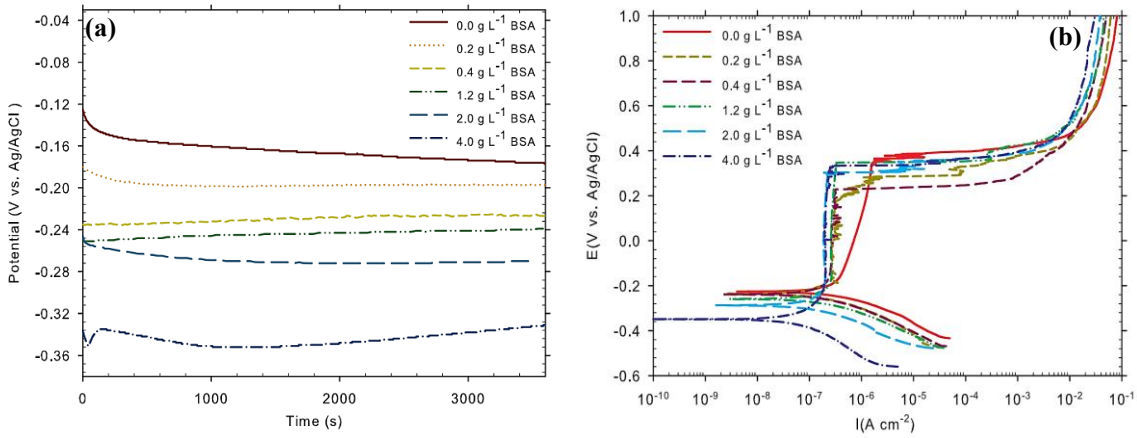

Figure 1.13. (a) Open circuit potential and (b) potentiodynamic polarization curves of 316L in PBS solutions and various BSA concentrations (0– 4 $g.L^{-1}$) from 0.25 V vs. OCP to 1 V vs. Ag/AgCl with a scan rate of 0.167 $mV.s^{-1}$ in aerated conditions at 37 °C and pH of 7.4 [70].

In addition, PDP and electrochemical impedance spectroscopy (EIS) results showed a decrease on the corrosion current density (i_{corr}) and increase to the charge transfer resistance by increasing the BSA protein concentration after 1-hour immersion in PBS media. Therefore, based on these results, BSA could act as a cathodic inhibitor at higher concentrations. The same results approximately were observed on corrosion behaviour of SS316 in the presence of HSA protein in PBS media[149]. Based on cyclic voltammetry results, BSA adsorption is greater than that of HSA protein due to the lowest passivity current density (i_{pass}) value not only on SS316L but also on CoCrMo alloy [149]. This means that there is a lower Fe dissolution rate in BSA protein environment than in HSA media. It is known that BSA and HSA are homologous proteins having a similar sequence and conformation, whereas HSA and BSA contain 585 and 583 amino acid residues, respectively [156-158]. These structural differences could influence human and animal serum adsorption on the alloy's surface. The previous research indicated that the amount of adsorbed BSA protein on stainless steel surface is higher than that of HSA protein under the same conditions [159].

The synergetic effects of BSA protein, immersion time, and nitrogen on corrosion behaviour of SS316L in PBS media were studied by Mohd Talha et al. [160]. They report that the BSA protein had a significant inhibition effect on the corrosion of SS316L and the corrosion resistance increased for BSA concentrations up to 2 $g.L^{-1}$. However, at higher protein concentration (4 $g.L^{-1}$) and long immersion times (24 hours), the chelating effect of BSA with the corrosion products, destroyed the protective film, accelerating the corrosion process [160].

Moreover inflammatory conditions, simulated by adding reactive oxygen species (ROS) such as hydrogen peroxide (H_2O_2) in the protein environment can strongly accelerate

the degradation process of SS316L as reported by Weichen Xu et al.[76] using the electrochemical tests and X-ray photoelectron spectroscopy (XPS) surface analysis. Based on the electrochemical tests results, they showed that BSA protein accelerated the anodic dissolution reaction and suppressed the cathodic reaction, whereas, in the presence of H_2O_2 agent, a promotion was observed on the cathodic reaction. Likewise, both BSA protein and H_2O_2 agents significantly enhanced the meta-stable and stable pitting corrosion and decreased the charge transfer resistance [76]. Based on XPS results, the higher dissolution rate of SS316L in the presence of BSA protein and H_2O_2 agent is attributed to the increased Fe oxides and CrOOH formation by the H_2O_2 agent. Then the BSA molecules interact with these oxides promoting Fe and Cr ions release.

1.4.4.2 Co-based alloy

A. Igual Muñoz and S. Mischler [61] investigated the interaction of albumin protein and phosphates species present in the body fluids on the passive film of the CoCrMo alloy by electrochemical measurements, XPS and Auger electron spectroscopy (AES) surface analysis. They reported that the CoCrMo alloy in the presence of phosphate species in PBS solution with respect to the 0.14M NaCl solution shows a lower i_{corr} and i_{pass} alongside with an increase in E_{corr}. Moreover, the passive film in PBS media with respect to 0.14M NaCl solution is more stable without any anodic current density fluctuations during sweeping to higher anodic potential. Based on AES and XPS results, the passive film on CoCrMo in PBS+BSA demonstrated the higher Cr distribution and lower adsorbed protein amount than 0.14M NaCl+BSA (**Figure 1.14**) [61].

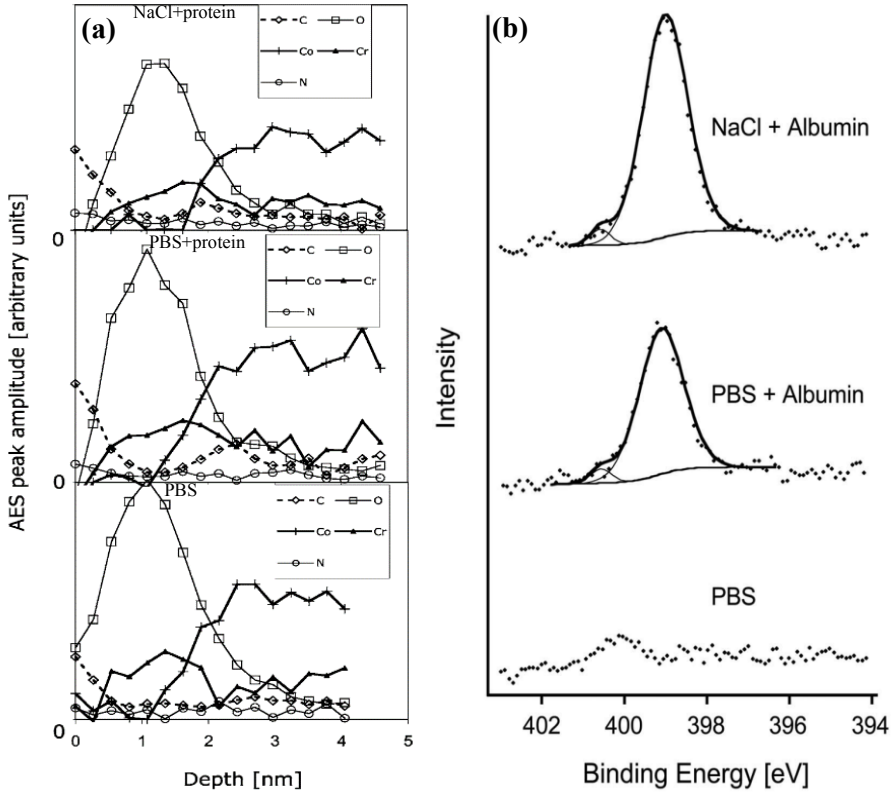

Figure 1.14. (a) AES sputter depth profiles after correction for the electron escape depth measured on samples polarized at -0.1 V in a NaCl + albumin solution, PBS + albumin solution, and PBS solution, (b) Fitting of XPS N 1s peaks measured on the samples polarized at -0.1 V SCE in different solutions pH 7.4 and 37°C [61].

It is known that the albumin protein acts as a cathodic inhibitor due to its adsorption which prohibit the easy access of oxidant species to the metal surface [2]. Also, phosphate species behave as an anodic inhibitor creating a barrier film on the surface. The protein molecules compete with the phosphate species (having both a negative charge) on adsorbing on the metal surface and can accelerate the anodic reaction rate [61]. In fact, it is possible that the BSA protein with a negative charge can act as a barrier preventing the adsorption of anions such as chloride and phosphate on the solid surface [161].

The adsorption of protein on the passive film of stainless steel and CoCrMo alloys leads to the formation of complexes with metal ions from the passive film and thus enhance the corrosion of metallic implants [2]. In fact, the effect of adsorbed protein on decreasing corrosion activation energy of stainless steel and CoCrMo alloys is accompanied by charge transfer [162]. According to M.L.C.A. Afonso et al.[163] the lower BSA protein concentration, the complexing behaviour of BSA protein is predominant, which leads to a higher degradation of metallic implants, while the higher BSA concentrations lead to a formation of a protective film covering the metal surface.

As already discussed, the surface properties such as hydrophobicity or hydrophilicity and positive or negative surface charge can strongly control the type and amount of protein adsorption. It is found that the protein adsorbs on the hydrophobic surface with higher stability than on hydrophilic surfaces [116]. However, on hydrophilic surfaces, protein can adsorb by electrostatic interactions [2]. Another study by YuYan et al. [110] on the corrosion behaviour of CoCrMo alloy in PBS solution at different pHs with BSA protein presented that when the substrate was positively charged (anodic polarization), the maximum protein adsorption observed in IEP condition (pH 4.7).

Further results by scanning Kelvin probe force microscopy (SKPFM) showed that the adsorption of BSA protein can increase the corrosion rate of CoCrMo alloy by inducing the free electron to escape from the surface. However, this findings are contradictory with the study of Izhar Ron et al. [164] which showed that the BSA protein behaved with the lowest electrical charge transporting (lower electron transfer) than other protein molecules such as azurin, a blue-copper ET protein and bacteriorhodopsin.

The role of solution chemistry on BSA protein adsorption on Cr and Mo metals was studied by C.M. Pradier et al. [118] in two different solutions, including pure water and PBS solution. Based on the Fourier transform infrared reflection–adsorption spectra (FT-IRRAS) results, they detected the BSA protein tends to adsorb more on Cr surface than Mo during a short time immersion (a few minutes) in pure water. In addition, a rigorous decrease was observed in the intensity of amide bands on Cr and Mo surfaces in PBS solution compared to pure water due to an increase in the ionic force of the solution, which may reduce the electrostatic interactions between proteins and metal surfaces [118]. In fact, these results revealed that in the presence of phosphate species, the BSA protein adsorption strongly diminished because the adsorbed phosphates film hinders BSA adsorption.

1.4.4.3 Ti-based alloys

The stability of passive film on metallic implants and its perfect protecting behaviour to prevent corrosion phenomena, especially in complex biological media, strongly depend on the microstructure of bulk material. Arash Fattah-Alhosseini et al. [83] reported the electrochemical behaviour and semiconductor properties of the passive film formed on two different commercial pure titanium (CP-Ti) in Hanks solution at 37 °C including annealed CP-Ti (grain size 45 ± 1 μm) and nano-grained CP-Ti (grain size 80 ± 5 nm). Based on PDP measurement results, nano-grained CP-Ti presented a lower i_{corr} and i_{pass} value in comparison with annealed CP-Ti. In addition, the Mott-Schottky (MT) analysis showed that the grain refinement process led to a reduction on the donor densities distribution within the passive film formed on CP-Ti, which significantly improved the stability of passive film and the corrosion performance [83].

Albumin protein can also in this case influence the corrosion resistance of Ti alloys, especially in presence of ROS, such as H_2O_2 [165]. A research work by Fei Yu et al. [144] showed that a physiological saline solution (0.15 M NaCl) containing albumin and H_2O_2 enhances the degradation process of Ti6Al4V alloy (**Figure 1.15**). They stated that two events could occur parallelly, H_2O_2 complexation with Ti which increases the anodic reaction rate and a suppression of the cathodic reactions by the BSA protein. Moreover, another study demonstrated that BSA protein, inhibiting the cathodic reactions, lead to a slight increase in Ti release during the long-term immersion due to an increase in the dissolution rate of Ti6Al4V in the active region [144]. A mechanistic study was performed by Yolanda S. Hedberg et al. [166] on the combined effect of albumin and H_2O_2 on the surface oxide layer and metal ions releasing process of Ti6Al4V alloy in PBS solution. They reported that the PBS solution combining BSA and H_2O_2 greatly increased the metals releasing rate from Ti6Al4V at all investigated conditions (10 µM–30 mM H_2O_2; 1–40 g/L BSA; PBS at pH 7.3, 37 °C, 4 h – 2 weeks).

A complexation-induced metal release process and a metal depletion process from the surface oxide, most probably induced by H_2O_2-Ti and/or albumin-Al interactions was proposed [166]. The corrosion behaviour of CP-Ti was also investigated in the physiological solution containing the albumin protein (0.1 or 1 $g.L^{-1}$) and fluorides (2 $g.L^{-1}$) by Shinji Takemoto et al. [167] using PDP and XPS surface analysis. Results showed that the presence of F^- decreased the corrosion resistance of CP-Ti. In addition, adding BSA protein in the fluorides containing solution prevented the F^- ions to adsorb on the oxide surface of titanium slightly increasing on the corrosion resistance.

From all the above, we could state that the presence of albumin protein can increase or decrease the electrochemical interactions on a metal surface and the metal ions release

depending on its concentration in a physiological environment, the chemical composition and surface properties of metallic implants and the solution properties (ions, biological species, temperature and pH etc.).

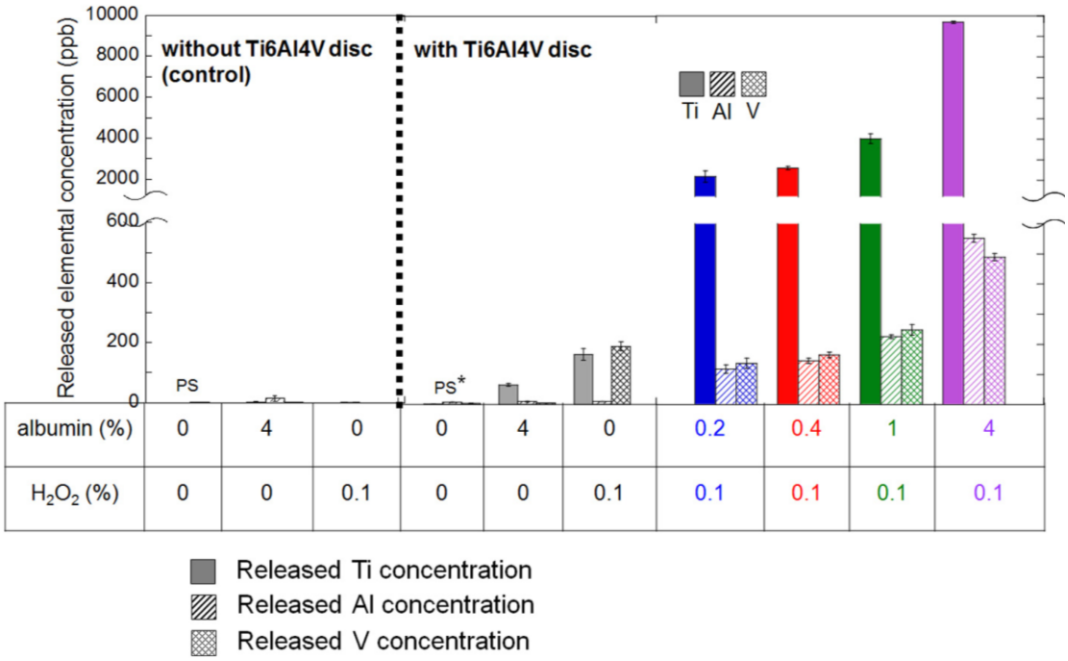

Figure 1.15. The mean concentrations and standard deviations (ppb) measured with ICP-MS of Ti, Al and V released from mirror-polished Ti6Al4V following immersion in physiological saline (0.15 M NaCl) with and without H_2O_2 and albumin for 2 weeks at 37 °C (n = 3) [144].

1.5 Corrosion phenomena on ferromagnetic micro- and nano-devices in biological environment

Ferromagnetic micro- and nano-devices can exhibit similar degradation mechanisms in the human body as the larger components used for implants. Due to the tiny dimensions the degradation can strongly impact on their functionality. Indeed, corrosion phenomena occurring in micro- and nanodimensional components can develop in a completely different path than in their bulk counterparts. Unfortunately, most ferromagnetic metals and alloys degrade (except ceramic materials such as CFO and CFO@BFO with more insulating behaviour), especially when they are in contact with fluids, which can result in the release of toxic ions into the surrounding media [88, 89].

Among the three ferromagnetic elements of the periodic table, Fe is the only one that displays biocompatible characteristics as most of the surrounding tissues can uptake iron ions via transferrin [168]. While iron is highly prone to degrade and can be remediated by the body, can also be cytotoxic to certain cells, such as the retinal tissue [169]. Other alloys, such as NiCo, present a good corrosion resistance in different environments thanks to their ability to create a stable passive film. However, media such as biological fluids can result in their slow degradation and the release of metal ions, which can accumulate in cells and tissues and ultimately affect the human immune system [170]. Finally, degradation of ferromagnetic materials also implies a deterioration of their magnetic and mechanical properties, which can severely impair their swimming performance, speed, and controllability.

Considering all these facts, magnetic small-scale robots can be designed as fully degradable, or composed of an inert part that prevents any deleterious effect to the

performance of the device or to the surrounding environment. If designed in a degradable form, swimmers must contain metals that exhibit biocompatibility characteristics (i.e. non-toxic, non-carcinogenic, non-allergenic, and non-inflammatory) [171, 172]. Additionally, the biodegradability should be programmed so that swimmers have a sufficient lifetime to perform the tasks for which they are designed [173]. Combinations of magnetic iron or iron-based alloys containing elements such as Zn, Mn, or additional layers containing these elements, are suitable candidates for biodegradable swimmers. If swimmers are composed of magnetic parts containing toxic elements (i.e.: Ni, Co), protective films against their degradation in the specific working environment should be incorporated. Inert metals, such as Au, Pt, Ag or metals exhibiting a passive behaviour like Ti, are appropriate for building non-degradable magnetic swimmers. Surface protection can improve the biocompatibility characteristics of magnetic swimmers and limit the release of toxic ions from magnetic components [25, 35]. For example, noble metals are a widely adopted option for preventing the metal ion release process [174]. However, from the corrosion point of view, the small dimensions of micro- and nanorobotic architectures and the complexity of the human body environment (interaction with proteins, cells, and tissues) should be carefully considered [175-177].

Besides, the integration of several materials being in physical or electrical contact might lead to galvanic coupling, which could cause degradation of the less noble material or its complete dissolution due to its small dimensions. Another widely unexplored issue is how the shape of a small-scale structure influences the corrosion. Certain geometries can critically favour corrosion processes (crevice corrosion, pitting etc.), which have not been yet clearly defined for small scales, and whose mechanisms remain unknown at such dimensions. The presence of micro- or nanoscale defects in protective coatings, which could

be considered negligible in large scale components, can become dramatically relevant at the micro-and nanoscale dimensions. Specially, the galvanic coupling of metals with a marked difference in nobility can become significantly exacerbated in small-scale swimmers composed of different metal segments, or on those metallic designs coaxially coated by other metals or alloys [176, 178]. Additionally, some materials such as ceramics can lose their protecting attributes, as at nanoscale, they become semiconductors due to defects [176].

Corrosion thus can have a dramatic impact on small-scale swimmers. To date there are only a few works that have addressed the corrosion phenomena on micro- or nano-devices [174, 176, 177]. However, corrosion has been studied with indirect methods, such as morphological analyses, to observe the degradation after a certain period of immersion in the corrosive fluid [174, 177], chemical analyses of the corrosive media to measure ions release [176, 177], or through the deterioration of the performances [174].

Chapter 2: Research project layout

This research work focuses on the degradation of different materials used in the biomedical field and in particular on the corrosion mechanisms in micro- or nanoscale. Human body is a highly corrosive environment containing various types of ions (phosphate, calcium, chloride, fluoride, etc.), proteins (albumin, fibronectin, globulin, ferritin, etc.), and cells. All these species can influence significantly on implants corrosion behaviour during the lifetime.

The research work layout can be divided in two main routes:

A) Study of the corrosion mechanisms of bulk, passive alloys commonly used for biomedical implants, such as Ti6Al4V and CoCrMo. The study focuses on the effect of protein adsorption and the formation of the nano-bio interface on their surface and its influence on the passive film formation and corrosion resistance.

B) Study of the corrosion mechanisms of micro- and nano-devices which can be used for targeted drug delivery, cancer therapy and isolation of biological targets. In particular, the degradation mechanisms of NiCo and NiCo/Au coated micropillars and cobalt ferrite ($CoFe_2O_4$ (CFO)) and cobalt ferrite@bismuth ferrite ($CoFe_2O_4$@$BiFeO_3$ (CFO@BFO)) ceramic nanoparticles in human body simulated solutions containing different proteins were investigated.

2.1 Ti6Al4V and CoCrMo alloys

A multi-characterisation approach was followed using electrochemical measurements, especially Mott– Schottky analysis, SEM-EDXS, XPS, AFM, and SKPFM to reveal and establish the BSA protein interaction mechanism with the most important ions or inorganic species in different human body simulating solutions and its role in corrosion

phenomena occurring on a heterogeneous surface. The main goals of these research study can summarize into:

1. Influence of BSA protein adsorption on charge carriers distribution on the complex oxide layer of Ti6Al4V alloy in various simulated body fluids including 0.9% NaCl, PBS and Hanks solutions.

2. The role of H_2O_2 and H_2O_2 + BSA on the corrosion resistance, protein adsorption morphology and local surface potential on Ti6Al4V surface.

3. Influence of the different protein concentrations (0, 0.5, 1 and 2 $g.L^{-1}$) and applied overpotentials (OCP, 0.1V and 0.3V vs. Ag/AgCl) on the electrochemical response, local surface potential (SKPFM) and elemental distribution (XPS) on the surface of CoCrMo alloy.

4. Investigation of the conformational arrangements of adsorbed BSA protein and its influence on the local surface potential (SKPFM) and elemental distribution (XPS) on the complex oxide layer of both Ti6Al4V and CoCrMo alloys in OCP and different applied overpotentials.

5. The visualizing the localized corrosion mechanisms in the regions with absorbed BSA proteins and the BSA protein/substrate interface.

A scheme that summarizes the research activity for the Ti6Al4V and CoCrMo alloys is reported in Figure 2.1.

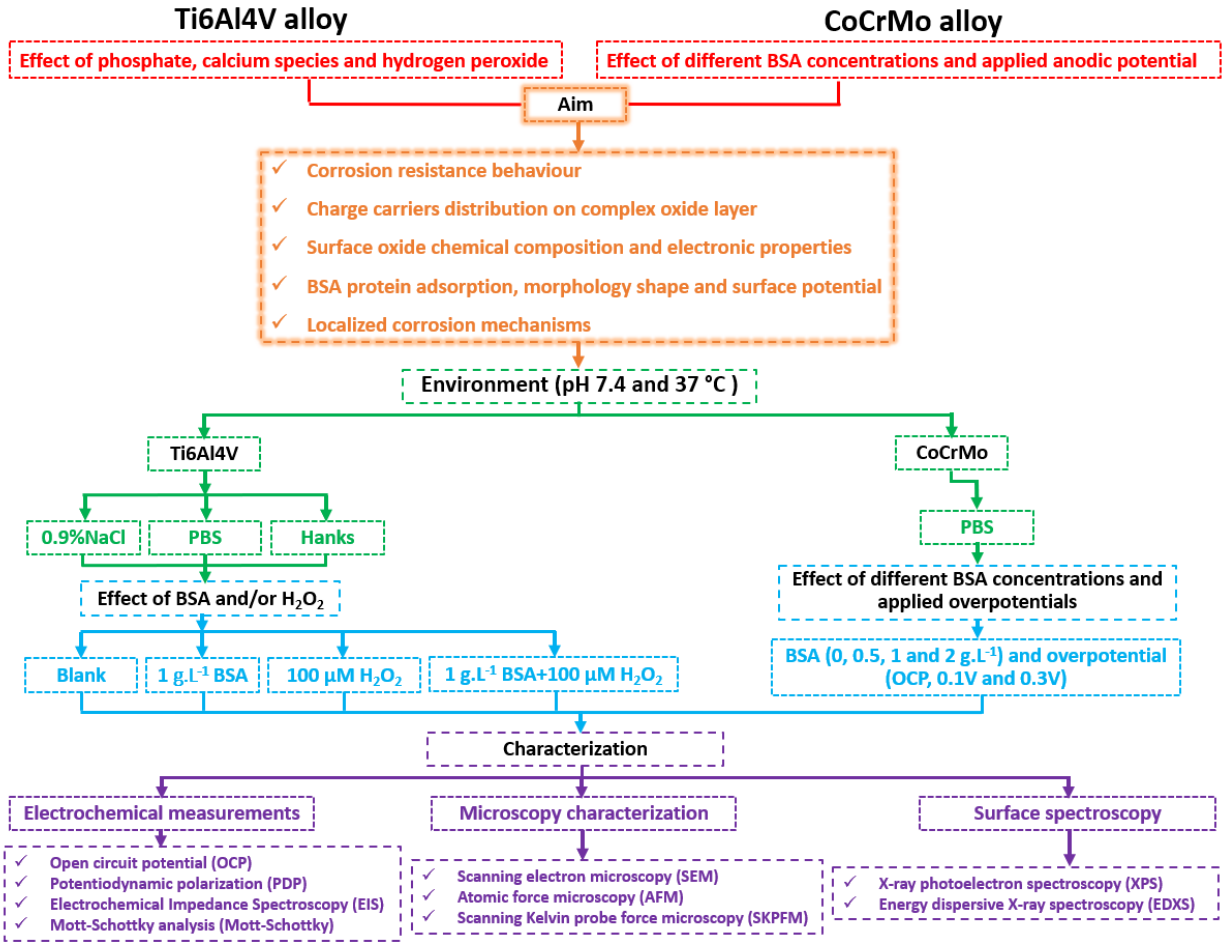

Figure 2.1. A schematic presentation of the research activity related to BSA protein interactions on Ti6Al4V and CoCrMo alloys.

2.2 NiCo and NiCo/Au micropillars, CFO and CFO@BFO nanoparticles

The field of biomedical small-scale swimmers has made major progress during the last two decades. While their locomotion aspects and functionalities have been demonstrated, there are key aspects that have been often overlooked such as their service live durability, which difficult their translation to the clinics. Several swimmers consist of combinations of metals and alloys that, while they excel in their functionalities, they fail in their stability due to corrosion in highly aggressive complex body fluids. A systematic approach by combining electrochemical and surface analysis techniques has been followed, which shed light on the degradation mechanisms of these systems in simulated body fluids. In particular BSA protein was selected to investigating the corrosion and biodegradation process in PBS media for a short and long-term periods of NiCo and NiCo/Au micropillars. On the other hand, the role of apoferritin on the degradation of CFO and CFO@BFO nanoparticles was studied as the ceramic particles cannot undergo "traditional" corrosion. A scheme that summarizes the research activity for the NiCo and NiCo/Au micropillars, CFO and CFO@BFO nanoparticles is reported in **Figure 2.2**.

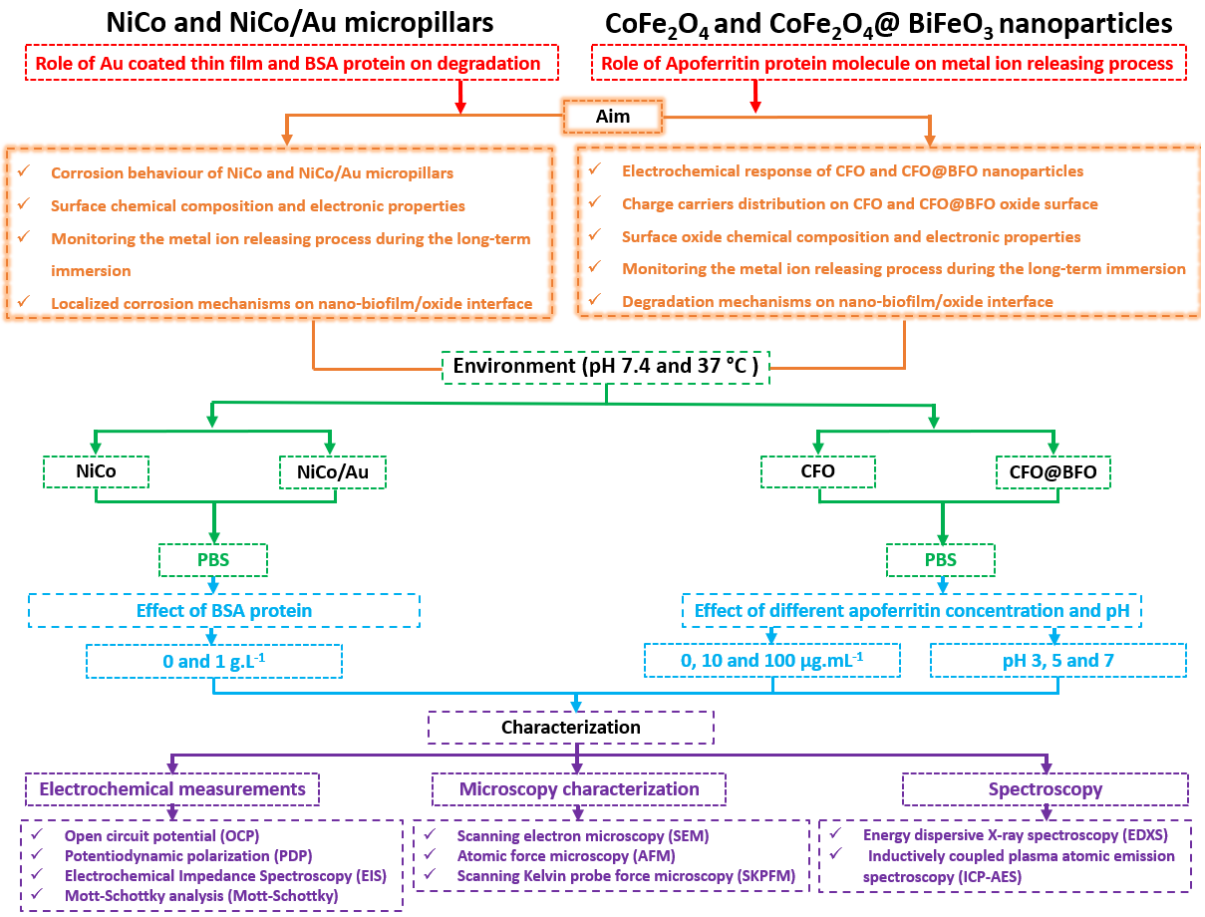

Figure 2.2. A schematic presentation of the research activity related to corrosion and biodegradation mechanisms of NiCo and NiCo/Au micropillars as well as CFO and CFO@BFO nanoparticles in different body fluid simulating environments.

Chapter 3: Experimental procedures and methodology

3.1 Ti6Al4V and CoCrMo alloys

3.1.1 Materials and sample preparation

Specimens with surface areas of 5 cm^2 both for Ti6Al4V and CoCrMo alloys have been used for electrochemical measurements and specimens with surface areas of 0.8 cm^2 have been used for microstructural characterisation and AFM and SKPFM measurements. All specimens were cut from Ti6Al4V ASTM F1472 and CoCrMo-low carbon ASTM F1537 bars which chemical compositions (wt.%) are provided in Table 3.1. The samples were mechanically ground using SiC paper from 500-grit up to 2000-grit and then polished to a mirror-like surface using an alumina slurry suspension. The polished samples were washed with ethanol, ultrasonicated in acetone for 30 min, finally dried by air blowing before characterisation. All samples for surface analysis and microscopic measurements were stored in a desiccator at room temperature.

Table 3.1. The chemical composition distribution (wt%) in Ti6Al4V and CoCrMo alloys.

Alloys	Al	C	Fe	H	N	O	V	Y	Ti	Co	Cr	Mo	Si	Mn	P	S	Ni
Ti6Al4V	6.25	0.065	0.23	0.003	0.01	0.185	4.45	0.001	Bla.								
CoCrMo		0.05	0.38		0.22				0.005	Bla.	27.77	5.08	0.39	0.45	0.004	0.001	0.25

3.1.2 Electrolytes and electrochemical measurements

The electrochemical behaviour of the Ti6Al4V alloy was studied in different physiological environments to reveal the effect of the solution chemistry on protein adsorption, morphology, surface potential, donor density, and corrosion initiation sites on the oxide layer of the Ti6Al4V alloy. Thus, NaCl, PBS (different salts were purchased

from Sigma-Aldrich), and Hanks' solutions (H 8264, Sigma-Aldrich) were prepared as shown in Table 3.2.

Table 3.2. Chemical composition and parameters of the NaCl, PBS and Hanks' solutions.

Solution	$CaCl_2 \cdot 2H_2O$	$MgSO_4$	KCl	KH_2PO_4	$NaHCO_3$	NaCl	Na_2HPO_4	pH	Temperature (°C)
NaCl	-	-	-	-	-	9	-	7.4	37
PBS	-	-	0.2	0.2	-	8	1.15	7.4	37
Hanks	0.185	0.097	0.4	0.06	0.35	8	0.047	7.4	37

To investigate the electrochemical interaction and morphological arrangements of BSA protein on the Ti6Al4V alloy surface, 1 $g \cdot L^{-1}$ of BSA protein (lyophilised powder; ≥96% agarose gel electrophoresis, Sigma-Aldrich) was dissolved in the abovementioned solutions and the pH was adjusted to approximately 7.4. 100 µM H_2O_2 (PanReac Applichem, 30% w/v) was also added to some solutions to simulate inflammation conditions [76]. On the other hand, the electrochemical measurements of CoCrMo alloy were studied only in PBS solution with considering ASTM Standard (F2129) [179], as reported in Table 3.2. To investigate the BSA protein adsorption and its interactions with the alloy, BSA was added to the PBS solution at different concentrations: 0.5, 1, and 2 $g.L^{-1}$.

Electrochemical measurements of both Ti6Al4V and CoCrMo alloys were carried out using an Avesta cell according to the method of Qvarfort [180] and a conventional three-electrode electrochemical cell to reduce the crevice corrosion around the specimen holder and to control the temperature at 37 °C. The measurements were conducted using an AUTOLAB PGSTAT 30 potentiostat, a $Ag/AgCl/KCl_{3M}$ electrode (+222 vs. SHE) as the

reference electrode, and a platinum wire as the counter electrode. All electrochemical measurements related to both alloys were performed after 1-h immersion in the solutions to stabilise the open-circuit potential (OCP) and reach the steady-state conditions. The potentiodynamic polarisation (PDP) measurements were carried out at a scan rate of 1 $mV \cdot s^{-1}$ from cathodic to anodic potentials. Electrochemical impedance spectroscopy (EIS) measurements were performed in the frequency range of 100 kHz to 10 mHz by applying a sinusoidal excitation signal of ±10 mV. The electronic properties of the passive film on Ti6Al4V and CoCrMo alloys were investigated by MS analysis at 1 kHz frequency in the potential range from -1 to 1 V vs. Ag/AgCl with an amplitude of ±10 mV in all selected solutions.

3.1.3 Microstructural characterisation and AFM/SKPFM measurements

The protein adsorption on the passive film of the Ti6Al4V and CoCrMo alloy were studied using FESEM and AFM/SKPFM techniques. The microscopy observations related to Ti6Al4V alloy were performed after polarising the specimens to +0.2 V vs. Ag/AgCl (in the passivity region) immersed in different physiological environments (NaCl, PBS and Hanks) with or without the addition of BSA protein or H_2O_2 for 1h. The microstructural examinations of CoCrMo surface were carried out after the exposure to only PBS solution containing 0.5 and 2 $g.L^{-1}$ BSA after polarizing to OCP, +0.1V and +0.3V vs. Ag/AgCl.

The SEM was a field- emission FE-SEM JEOL, 7610FPlus instrument equipped with an Oxford X-MAX20 energy-dispersive X-ray spectrometer (EDXS) and the observations have been performed at a working distance of 15 mm, an accelerating voltage of 5 kV, and secondary electron (SE) mode. The AFM device was a Nanoscope IIIa Multimode with an n-type doped silicon pyramid single-crystal tip coated with PtIr5 (SCM-Pit probe). The surface potential images were captured in dual-scan mode. In the first scan,

topography data were obtained using tapping mode, and in the second scan, the surface potential was detected by lifting the tip 100 nm. Topographic and surface potential images were obtained in air atmosphere at 27 °C with an approximate relative humidity (RH) of 28%, a pixel resolution of 512 × 512, zero-bias voltage, and a scan frequency rate of 0.2 Hz.

The histogram and power spectral density (PSD) analysis based on the multimodal Gaussian distributions (MGD) and fast Fourier transform (FFT), respectively, were used to interpret the surface potential on the heterogeneous surface affected by the differential BSA protein shape, morphology, and WFE. The histogram plots were deconvoluted based on MGD in the form of multi-peaks using the following equation [88]:

$$Y=\frac{1}{\sigma\sqrt{\frac{\pi}{2}}}\,exp\left[-\frac{2(x-\mu)^2}{\sigma^2}\right], \tag{3.1}$$

where Y represents the count number, σ is the standard deviation, and μ is the mean value of the surface potential values. Moreover, PSD analysis provided both lateral and longitudinal information about the surface Volta potential distribution of BSA proteins with different morphologies as compared to other statistical treatments of AFM/SKPFM images, such as root-mean-square, mean value, and peak-to-peak analysis [181]. The PSD analysis information related to the surface potential components as a function of spatial frequency were calculated by the following equation [182]:

$$PSD(f) = \lim_{A\to\infty}\frac{1}{A}\left|\int_A z(r)exp\,(-2\pi i f.r)dr\right|^2, \tag{3.2}$$

where $z(r)$ represents the height data of the surface roughness, A is the surface area of the measuring field, r is the position vector, and f is the spatial frequency vector in the $x-y$ plane.

3.1.4 X-ray photoelectron spectroscopy (XPS)

The chemical composition of the surface layers on Ti6Al4V and CoCrMo alloys was analysed by a PHI-5000 Versaprobe II (Physical Electronics) using a monochromatic Al Kα X-ray source (1486.71 eV photon energy) and a spot diameter of 100 μm to measure surface compositions up to ca. 10 nm in depth. The irradiation power of the X-ray beam was 25 W. The kinetic energy of the photoelectrons was measured with a take-off angle of 45°. The vacuum in the analysis chamber was approximately 1×10^{-9} Torr. The XPS results were analysed using the PHI Multipak software (V9.0). High-resolution scans of C 1s, N 1s, O 1s, Ti 2p, Al 2p, Co 2p, Cr 2p, Mo 3d, P 2p, and Ca 2p were obtained with a pass energy of 23.5 eV and a 0.05 eV energy step size.

3.2 NiCo and NiCo/Au micropillars

3.2.1 NiCo and NiCo/Au micropillar fabrication

The fabrication steps for the production of NiCo and NiCo/Au-MPs are reported in Figure 3.1.

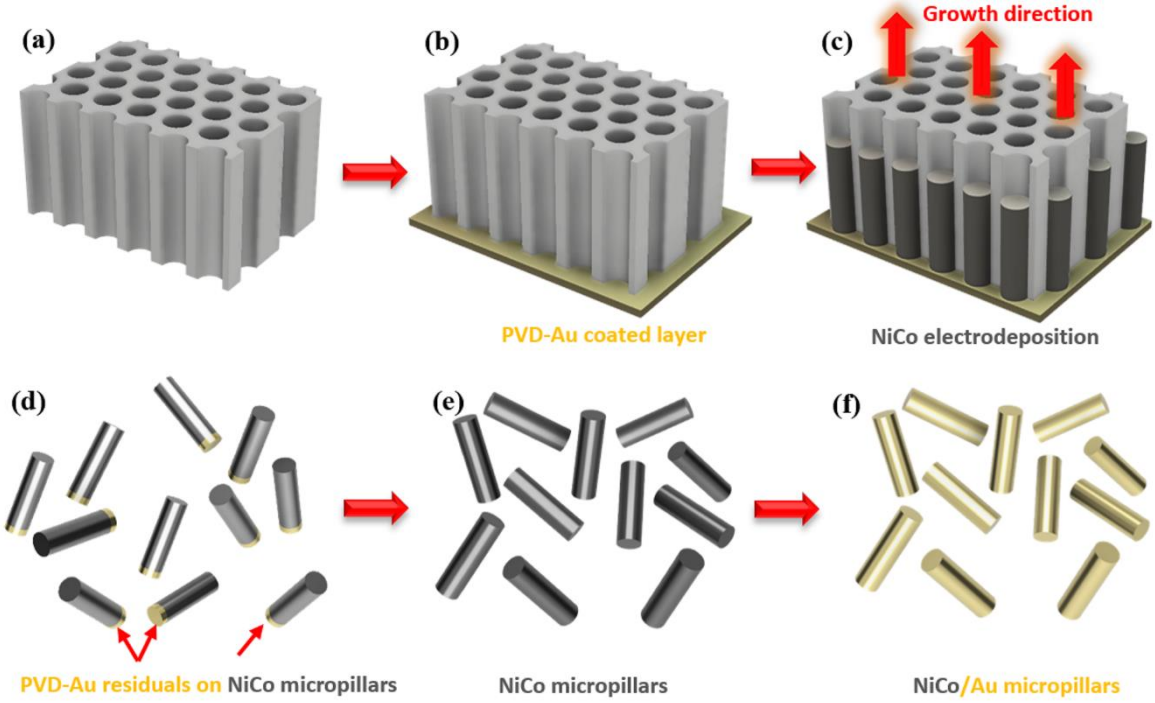

Figure 3.1. A schematic representation of the NiCo and NiCo/Au-MP fabrication process, (a) organic membrane template (MT) with 1 µm pore diameter and 100µm length, (b) Physical vapour deposition of Au on one side of the MT, (c) NiCo electrodeposition within the pores, (d) Detachment of the formed NiCo-MPs by dissolving the MT, (e) Dissolving of the PVD Au coated layer, (f) Au thin layer coated on NiCo-MPs by electroless deposition.

The technique is based on template-assisted electrodeposition using commercially available membranes (PVP-Free Nuclepore Hydrophobic Membrane from Whatman, with a pore size of 1µm and pore length of 10 µm). A thin layer of Au (~100 nm) was deposited on the membrane by PVD. This thin conductive layer acted as a cathode for the nucleation and growth of NiCo pillars. The electrodeposition process was performed with the three-electrode cell using an Autolab potentiostat (Metrohm, PGSTAT204). The Au coated MT, a Pt plate, and an Ag/AgCl/Na_2SO_4 electrode were arranged as cathode, anode, and the reference electrode, respectively. The chemical composition and parameters of the Ni-Co electrolyte are reported in Table 3.3.

Table 3.3 Plating bath chemical composition and parameters.

Plating bath chemical composition	
Nickel sulfate hexahydrate ($NiSO_4(H_2O)_6$)	300 g/L
Nickel chloride hexahydrate ($NiCl_2.6H_2O$)	30 g/L
Cobalt sulfate hexahydrate ($CoSO_4.7H_2O$)	40 g/L
Boric acid (H_3BO_3)	20 g/L
Citric acid	40 g/L
Saccharin	2 g/L
Tergitol 08	3mL/L
Bath parametrs	
Temperature (°C)	35°C
pH	5.8
Stirring rate	100 rpm

To obtain the NiCo MPs, a potentiostatic polarization was applied at -1.1V vs. Ag/AgCl/Na_2SO_4 for approximately 150 seconds. The membrane was then dissolved by immersion in Chloroform (Sigma–Aldrich) for 1 hour to obtain the separated NiCo-MPs. The sputtered Au layer was removed by etching in Gold etchant, nickel compatible (Sigma-Aldrich). Finally, the NiCo-MPs were cleaned in an ultrasound bath in acetone, ethanol, and de-ionized (DI) water. To improve the biocompatibility characteristics and prevent the metal

ions release, a thin layer of Au was deposited on the NiCo-MPs using an immersion Au commercial bath (TRANSENE INC). The deposition was carried out at 90°C for 20 minutes, maintaining the NiCo-MPs in suspension by stirring. Consequently, the NiCo/Au-MPs were cleaned by ultrasonication in acetone for 20 minutes and rinsed with DI water several times.

3.2.2 Microscopy characterizations

The MPs have been characterized using FE-SEM, AFM, and SKPFM techniques. For the analysis, both NiCo and NiCo/Au-MPs were mixed with ethanol and then spread onto a glassy carbon plate (C000502, Goodfellow). The microstructure and the chemical composition of the MPs both prior to and after immersion in the corrosive environment was evaluated using an FE-SEM (JEOL, JSM-7610FPlus) equipped with an EDXS (OXFORD X-MAX 20) analysis system. AFM and SKPFM mappings were obtained to evaluate the topography and surface Volta potential differences of NiCo and NiCo/Au-MPs. The scanning probe microscope (SPM) was a Digital Instruments Nanoscope IIIa Multimode with an n-type doped silicon pyramid single crystal tip coated with PtIr5 (SCM-Pit probe). The surface Volta potential mappings were carried out using the dual-scan mode. In the first scan, topography data was obtained using the tapping mode, and the second scan surface Volta potential was captured by lifting the tip up to 100nm. Topography and Volta potential mappings were obtained in air at 25 C^{o} with an approximate relative humidity of 28%, a pixel resolution of 512×512, a zero-bias voltage, and a scan frequency rate of 0.2 Hz.

3.2.3 Sample preparation for electrochemical measurements

In order to obtain a suitable working electrode for the electrochemical measurements, 2x2cm^2 indium tin oxide coated glass (ITO,18-20 ohms/sq, techinstro) was coated with a conductive polymer (Nafion® 117, Sigma–Aldrich) in which the MPs had been previously

dispersed. Nafion® was used to ensure the electrical connection between the MPs and the ITO glass [183-185]. Nafion® as a perfluorinated anionic polyelectrolyte has been extensively used in recent years for the fabrication of redox polymer-modified electrodes with high chemical stability and good biocompatibility, particularly for the detection of protein adsorption [186, 187].

The procedure was optimized to achieve samples where part of the pillars are not fully embedded in Nafion®, ensuring enough exposed metallic area to the electrolyte. Several attempts were made to achieve this aim, and the obtained specimens were controlled by FE-SEM. The optimized preparation procedure is as follows: first, 40 mg of either NiCo or NiCo/Au-MPs were gently mixed with 150µL of ethanol and 20µL of Nafion® (as also reported in other studies [188, 189]). The obtained solution was uniformly spread on the ITO glass by a spin coater (Ossila, UK) using a spin speed of 500rpm for 20 seconds. Under these conditions, only the first layer of MPs was embedded fully in Nafion®, while the top layer was composed of partially embedded MPs leaving part of their surface in direct contact with the electrolyte during the electrochemical measurements as shown in **Figure 3.2**. Finally, the MPs coated ITO glass was dried at 60 C° for 1 hour in the air-oven. An optical microscope and image analysis method (ImageJ software [190]) was used to estimate the percentage of the ITO glass surface occupied by MPs during exposure in the solution for all electrodes, as shown in **Figure 3.3.**

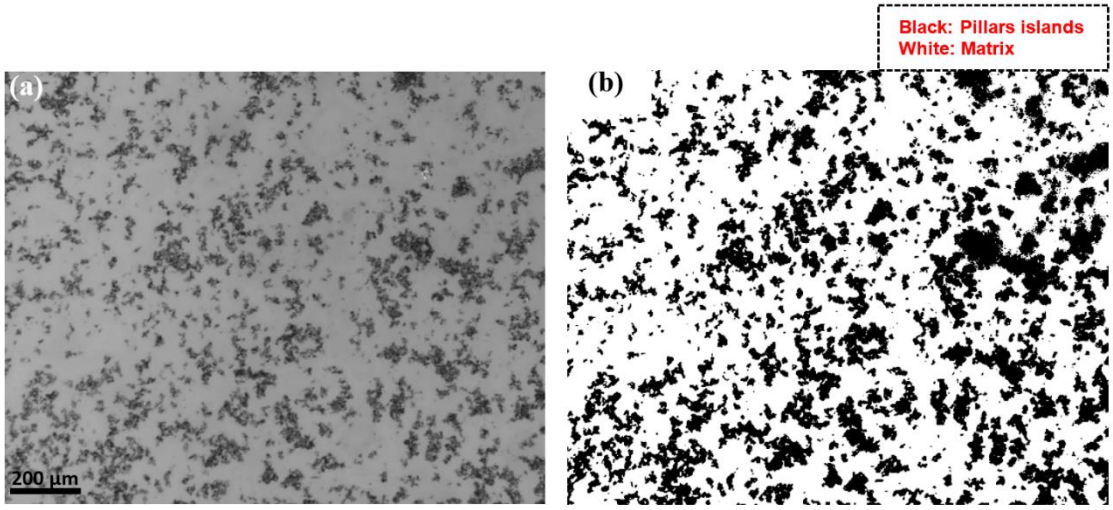

Figure 3.2. SEM images of collective (a) NiCo and (b) NiCo/Au-MPs supported on ITO glass with Nafion.

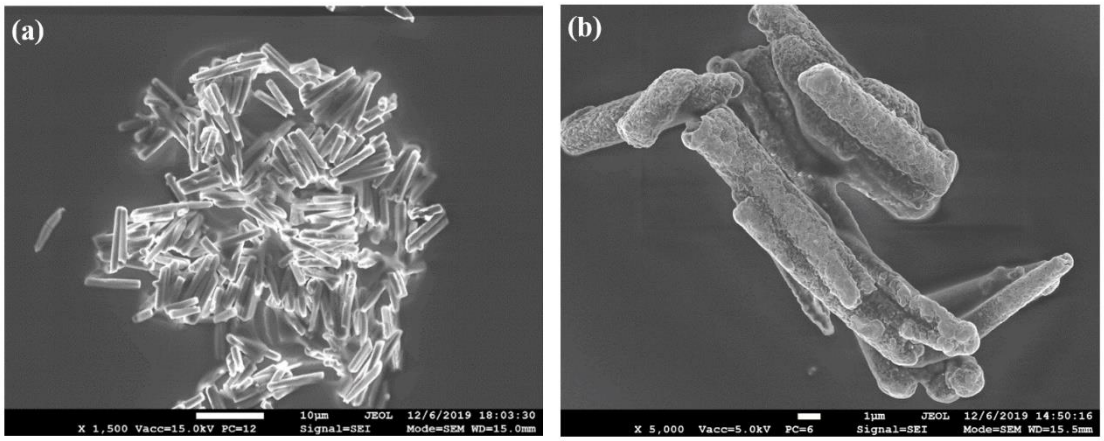

Figure 3.3. (a) Optical microscope image of ITO/Nafio/NiCo-MPs electrode, (b) image analysis of NiCo-MPs occupied regions to determine the contact-surface area for electrochemical measurements.

3.2.4 Electrolyte and electrochemical measurements

PBS solution was used as a base electrolyte to perform all electrochemical measurements. 1g/L of BSA protein (lyophilized powder, ≥96% agarose gel electrophoresis, Sigma–Aldrich) was added to the PBS solution (Table 3.2) to obtain conditions closer to those of the human body to evaluate its influence on the MPs degradation.

All electrochemical measurements were performed at 25C° and pH 7.4±1 using an AUTOLAB PGSTAT 30 potentiostat in a three electrodes conventional cell. The coated ITO glass was used as a working electrode, an Ag/AgCl/KCl_{3M} electrode (+222 vs. SHE) as a reference, and a Pt wire as the counter electrode. The potentiodynamic polarization (PDP) measurements were carried out at a scan rate of 1 $mV.s^{-1}$ from cathodic (- 200 mV vs. OCP)) to anodic potentials up to 1200 mV vs. Ag/AgCl/KCl_{3M}, if no breakdown was observed earlier. PDP measurements were done after 1 hour immersion in the electrolyte to stabilize the OCP. The long-term degradation of NiCo and NiCo/Au-MPs was investigated by OCP and EIS measurements in both PBS and PBS+1 $g.L^{-1}$ BSA environments for 30 days and the following "control-times": 1h, 2h, 4h, 8h, 12h, 1day, 2days, 4days, 8days, 18days, and 30days. EIS measurements were performed in a frequency range of 10 mHz to 10 kHz by applying a sinusoidal excitation signal of ±10 mV vs. OCP.

3.2.5 Long-time free immersion tests

NiCo and NiCo/Au MPs (not supported onto ITO glass) were also immersed in PBS and PBS+BSA environments at pH 7.4 and 25 °C for a period of up to 140 days. The solutions were appropriately prepared after 7, 56, and 140 days and analysed using inductively coupled plasma-atomic emission spectrometry (ICP-AES, Agilent 5800) to determine the released Ni and Co ions. The calibration was done using an ICP-standard 23 elements solution in 5% nitric acid (Merck solution IV). Before ICP-AES analysis, the whole PBS and PBS+BSA solutions containing released Ni and Co ions were digested in acidic media [69]. The ICP-AES analyses were performed at ppm (mg/L) concentration for all solutions. The MPs were collected, cleaned in ethanol and DI water with ultrasound, and analysed by FE-SEM to control the morphology and the extent of the corrosion attack.

3.3 CFO and CFO@BFO nanoparticles

3.3.1 Fabrication of core-shell $CoFe_2O_4$-$BiFeO_3$ nanoparticles

A hydrothermal synthesis procedure was used in order to fabricate $CoFe_2O_4$ (CFO) nanoparticles [57]. The nanoparticles have been produced by Multi-Scale Robotics Lab (MSRL), Institute of Robotics & Intelligent Systems (IRIS), ETH Zurich. In the first step, 0.14 M hexadecyltrimethylammonium bromide (CTAB), 0.092 M $FeCl_3 \cdot 6H_2O$, and 0.046 M $CoCl_2$ were dissolved in DI water alongside mechanical stirring. Then, a 6M NaOH solution was added to the above prepared solution under intensive mechanical stirring followed by ultrasonic agitation. Finally, the prepared solution was poured to Teflon-lined steel autoclave and heated at 180 °C for 24 hours. At the end, the obtained black powder was washed several times with DI and ethanol and dried 12 hours at 80 °C. Likewise, a precursor of $BiFeO_3$ (BFO) was prepared by dissolving 0.011 M $Bi(NO_3) \cdot 5H_2O$ and 0.01 M $Fe(NO_3) \cdot 9H_2O$ in ethylene glycol. To fabrication of core-shell $CoFe_2O_4$-$BiFeO_3$ (CFO@BFO) nanoparticles, 0.1 g dried-CFO nanoparticles were added in 60 mL of BFO precursor solution followed by sonication for 2h. Following, this solution was dried at 80 °C overnight and the dried powder was annealed at 600 °C for 2 hours.

3.3.2 Sample preparation for electrochemical measurement

The preparation procedure of CFO and CFO@BFO nanoparticles for electrochemical measurements was as follows: in the first, 20 mg of CFO or CFO@BFO were gently mixed by the 150 µL of ethanol and 20 µL of Nafion (Nafion® 117, Sigma–Aldrich) according to previous researches [188, 189]. To decline the influence of Nafion on total electrochemical signal and protein adsorption on nanoparticles, a higher ethanol content was considered than Nafion, as stated above. Then, the suspension uniformly was coated on indium thin oxide (ITO,18-20 ohms/sq, techinstro) coated glass using a spin coater (Ossila,

UK) with spin speed 800 rpm and spin time 20 seconds. In this condition, the most of top layers or surfaces of nanoparticles are with the lowest influence of Nafion, while the bottom coated layers of nanoparticles are embedded in Nafion mixture, as shown in **Figure 3.4 and 3.5**.

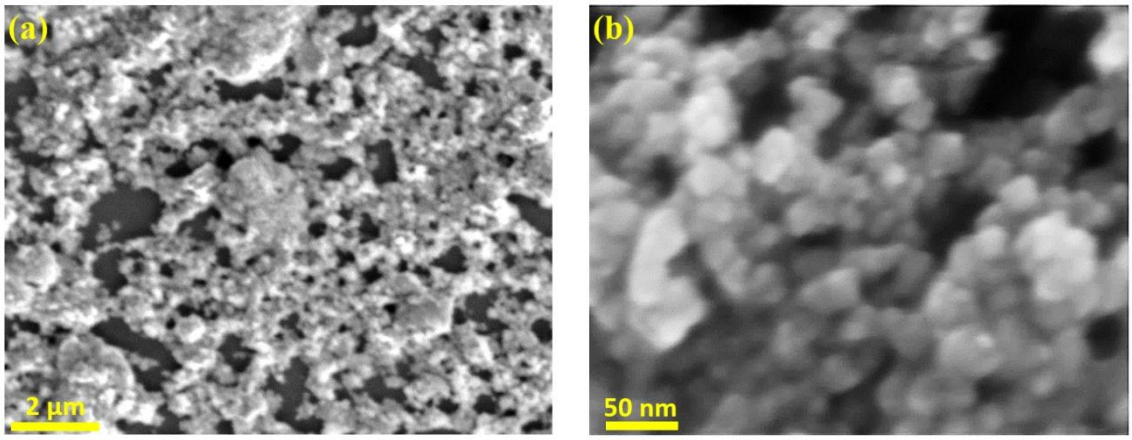

Figure 3.4. A schematic presentation of nanoparticles+ Nafion distribution spin-coated on ITO glass

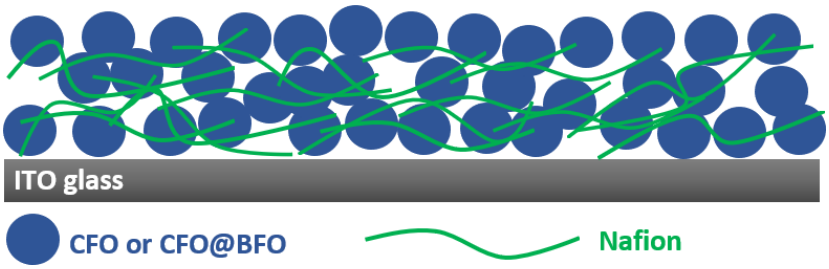

Figure 3.5. Low (a) and high (b) magnification SEM images of CFO nanoparticles +Nafion spin-coated on ITO glass.

The surface area of ITO glass was 2×2cm^2. Finally, the ITO glass/nanoparticle coated samples were dried at 60 C° for 1 hour in oven. The thickness of nanoparticles coated layer was approximatly 400 nm based on AFM analysis (**Figure 3.6**). The ITO glass has been used as conductive support to perform the electrical connection necessary to build up the electrochemical cell. The conductive polymer film (Nafion) has been used to embed partially

the nanoparticles in order to ensure the electrical connection between nanoparticles and the ITO glass[183-185]. Nafion as a perfluorinated anionic polyelectrolyte has been attractively utilized in recent years for fabrication of redox polymer-modified electrodes with high chemical stability and good biocompatibility especially detection of protein adsorption [186, 187].

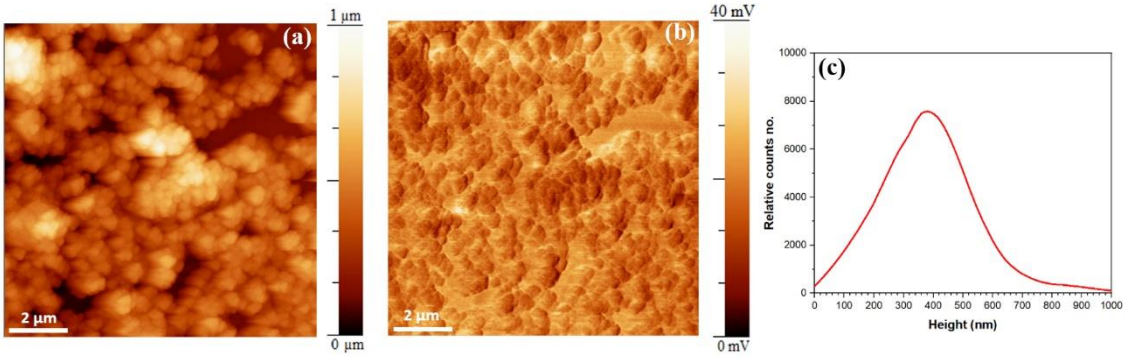

Figure 3.6. (a) Topography, (b) surface potential, and (c) height histogram analysis of CFO nanoparticles which spin-coated on glassy carbon at 25 °C and RH 28%, respectively.

3.3.3 Electrolyte and electrochemical measurements

The electrochemical interaction and degradation behavior (or metal ion releasing) of CFO and CFO@BFO nanoparticles were investigated in PBS solution (**Table 3.2**) as simulated body solution [179]. Likewise, apoferritin (apoferritin from equine spleen, with concentration 100mg/mL, 0.2µm filtered, Sigma–Aldrich) was added to the PBS solution at three different concentrations:0, 10 and 100 µg/mL to provide inflammatory conditions and to evaluate its impact on metal ion releasing and up-taking process. Since the solution pH can significantly influence the metal ion releasing process and the surface charge of both apoferritin protein and nanoparticles oxide surface, three different pH conditions were considered:pH 7, 5, and 3. The pH was controlled by a pH meter (GLP 21, CRISON) and adjusted with the addition of hydrochloric acid (HCl 37%, Sigma–Aldrich) [140].

All electrochemical measurements were performed at 25C° and aerated conditions. A AUTOLAB PGSTAT 30 potentiostat was used in a three electrodes configuration using Ag/AgCl/KCl_{3M} electrode (+222 vs. SHE) as reference electrode and a platinum wire as counter electrode. The surface area of all exposed samples was 0.3 cm^2. All electrochemical measurements were done after 1-hour immersion in the different solutions to stabilize the OCP. The I-E measurements were carried out at a scan rate of 1 $mV.s^{-1}$ at anodic potentials in order to reveal the oxidation or anodic reaction on the oxide surface of both CFO and CFO-BFO nanoparticles.

The electronic properties of the surface oxide of CFO and CFO@BFO nanoparticles including donor and/or acceptor flat band potential (E_{fb}) were evaluated in the different solutions by the capacitance (space charge region and Helmholtz double layer)/solution interface respect to the applied potential. Mott-Schottky analysis can be explained by the following equation [191]:

$$\frac{1}{C^2} = \frac{1}{C_{SCR}^2} + \frac{1}{C_H^2} = \pm\frac{2}{\varepsilon\varepsilon_0 e N_{d\ or\ a}}\left(E - E_{fb} - \frac{kT}{e}\right) \quad (3.3)$$

where C_{SCR} is the capacitance of the Space Charge Region (SCR), C_H is the capacitance of the Helmholtz double-layer, E is applied potential, ε is the dielectric constant of the oxide layer, ε_0 is the vacuum permittivity (8.854×10^{-14} $F.cm^{-1}$), e is the electron charge (1.6×10^{-19} C), N_d is the donor density, N_a is the acceptor density, k and T are Boltzmann constant and the absolute temperature. According to a previous study [192], ε value for CFO and BFO@CFO nanoparticle at 10MHz are considered 25 and 40, respectively. The intersection point of the fitted straight line (in the approximate linear region of Mott-Schottky curve) with the potential axis was considered as E_{fb}. MS analysis was performed at 1 kHz frequency in the potential range of -1 to 1.2 V vs. Ag/AgCl with the amplitude value of ±10 mV. This

range of potential was considered for the following reasons: (a) the different applied potentials (negative and positive) can strongly affect the slops of MS plots due to the fact that different potentials trigger the formation of passive films with different semiconductor characters, (b) to detect any difference on MS slops (e.g p-type or n-type semiconductor characters) due to the presence of H_2O_2 and BSA in a wide range of potential. As mentioned above, the C^{-2} magnitude is a reflection of total capacitance value at the oxide surface/electrolyte interface into space charge region, Helmholtz layer, and non-uniform or heterogenous protein adsorbed layer (only in protein environment). Since the physicochemical interactions by protein molecules such as adsorption and detachment is a dynamic process, the different potential sweeping on MS can affect significantly these interactions [193, 194].

3.3.4 Microscopy characterizations

To evaluate the topography and surface potential or work function energy (WFE) distribution on the oxide surface of CFO and CFO@BFO nanoparticles, AFM and SKPFM techniques were used. AFM/SKPFM was a Digital Instruments Nanoscope IIIa Multimode with n-type doped silicon pyramid single crystal tip, which coated with PtIr5 (SCM-Pit probe). Before AFM and SKPFM analysis, both CFO and CFO@BFO nanoparticles mixed in ethanol solution and then uniformly were distributed on glassy carbon plate (VC000502, Goodfellow). The surface potential mappings were carried out using the dual-scan mode. In the first scan, topography data was obtained using tapping mode and then second scan surface potential was captured with lifting the tip up to 100nm. Topography and surface potential mappings were performed in the air atmosphere at 25 C° with an approximate relative humidity of 28%, a pixel resolution of 512 × 512, a zero-bias voltage, and a scan frequency rate of 0.2 Hz.

Chapter 4: Role of phosphate, calcium species and hydrogen peroxide on albumin protein adsorption on surface oxide of Ti6Al4V alloy

In this chapter the effect of different simulated physiological solutions, including a 0.9%wt. NaCl solution, phosphate-buffered saline (PBS) solution, and Hanks' solution, along with an inflammatory condition simulated by the addition of hydrogen peroxide (H_2O_2), on bovine serum albumin (BSA) protein adsorption, conformational arrangement, and surface potential distribution on a Ti6Al4V alloy are presented. A direct comparison of the three most used solutions to simulate body fluids, highlighting the role of the most important ions or inorganic species of the solutions, on the corrosion resistance and on the passive film formation on the Ti6Al4V alloy is performed for the first time also in presence of compounds like BSA and H_2O_2 simulating inflammatory conditions. A multi-characterisation approach was followed using electrochemical measurements, especially Mott–Schottky (MS) analysis, FESEM, XPS, AFM, and SKPFM to reveal and establish the BSA protein interaction mechanism with the above mentioned species and its role in corrosion phenomena occurring on a heterogeneous surface. MS analysis is used to reveal the semiconductive properties of the passive film and correlate them to the degradation mechanisms.

4.1 PDP and EIS measurements of the complex surface layer

The influence of phosphate and calcium species, as well as of BSA protein and H_2O_2, on the resistivity of the oxide layer was investigated, and the BSA protein adsorption and conformational changes during interaction with the oxide layer on the Ti6Al4V alloy were evaluated. The PDP curves of the Ti6Al4V alloy in NaCl, PBS, and Hanks' solution are shown in **Figures 4.1a, b, and c**, respectively. The key electrochemical parameters such as the corrosion potential (E_{corr}) and corrosion current density (i_{corr}) calculated by Tafel extrapolation, along with passive current density (i_{pass}), are shown in **Figures 4.1d, e, and f**, respectively.

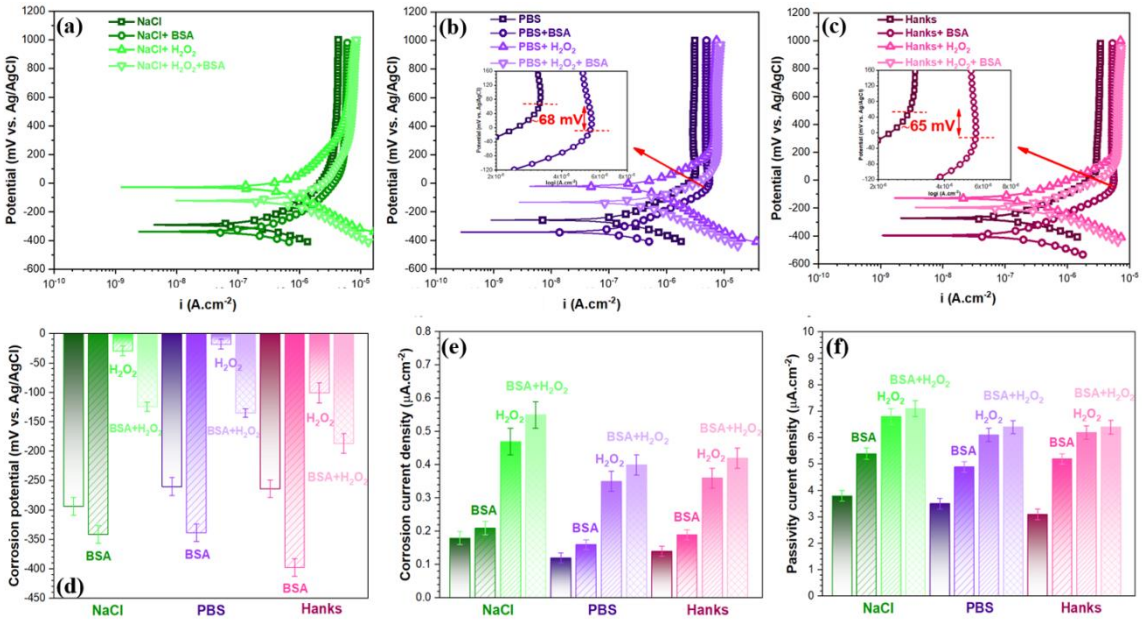

Figure.4.1. PDP plots of Ti6Al4V alloy after 1-h immersion in (a) NaCl, (b) PBS, and (c) Hanks physiological solutions with the addition of either BSA or H_2O_2 or both at 37 °C, pH 7.4, and aerated conditions, (d) E_{corr}, (e) i_{corr} and (f) $i_{passive}$ values as calculated from the PDP curves.

The addition of 1 g.L^{-1} of BSA protein led to a decrease in E_{corr} (of about 80 mV vs. Ag/AgCl) and a slight increase in i_{corr} (of about 0.04 μA.cm^{-2}) in all three physiological solutions. Likewise, a slight decrease in the cathodic current was detected upon adding BSA protein. The BSA protein could have inhibited the cathodic reactions (hydrogen or oxygen evolution) by covering the active sites on the heterogeneous surface with chemisorbed bonds [76, 149, 195]. An increase in both the passivity region and i_{pass} (of about 1.5 μA.cm^{-2}) in the presence of BSA protein was observed in the PDP curves of all solutions. This can be attributed to the BSA protein molecules or complexes that control the kinetics of metal ion release and reduction reactions [2]. A similar effect has been observed for other implant materials, such as CoCrMo and stainless steel 316L, in various physiological solutions [61, 70, 110]. This mechanism can be explained by the external donation of hydrogen atoms through protonation to protein amino groups on the Ti oxide layer that could trigger protein adsorption and covering according to the following equation [149]:

$$\mathrm{Ti{-}OH} + \mathrm{NH_3^+} \rightarrow \mathrm{Ti-OH_2^+ : NH_2{-}R} \qquad (4.1)$$

Moreover, the i_{corr} of the Ti6Al4V alloy in the PBS media presented a slightly lower value than that in the Hanks' or NaCl solutions ($0.18_{NaCl} > 0.14_{Hanks} > 0.12_{PBS}$ μA.cm^{-2}), as presented in **Figure 4.1e**. It can be supposed that the phosphate species, which has a higher concentration in PBS than in Hanks' solution, can adsorb onto the TiO_2 oxide layer with the formation of a thin and compact film, thus reducing the activity or charge transfer through the TiO_2 oxide layer [2, 111]. In fact, the Ti–OH bond is replaced by a Ti–OP bond, changing the basic hydroxyl group into $H_2PO_4^-$ $HPO_4^{2-}$and leading to the formation of a strong complexation bond with Ti on the passive film [195]. When a Ti6Al4V alloy is immersed in Hanks' solution, the first stage is the formation of calcium-phosphate, which occurs by preferential adsorption of phosphate ions on the TiO_2 oxide layer [196]. The

growth of the TiO_2 oxide layer is accompanied by hydration, creating TiOH groups at the oxidised surface, which leads to the binding of calcium ions (Ca^{2+}) to the hydrated oxide layer or electrostatic interaction with O^{-1} [197, 198].

The Ti6Al4V alloy showed a very small active/passive peak in the PDP curves obtained in both the PBS and Hanks' solution environments owing to the formation of Ti^{3+} [144]. The addition of BSA protein to PBS and Hanks' solution led to a decrease in the active/passive potential peaks (inserted images in **Figures 4.1b and c**) from 69 to 1 mV vs. Ag/AgCl and from 56 to -9 mV vs. Ag/AgCl, respectively. The addition of H_2O_2 to all environments led to an increase in both E_{corr} (of about 200 mV vs. Ag/AgCl) and i_{corr}, (of about 0.2 $\mu A.cm^{-2}$) as shown in **Figures 4.1d and e**, respectively. The most marked effect was the increase in i_{pass} compared to that of the base solutions. Because H_2O_2 has a high standard electrode potential (1.54 V vs. SCE), its reduction provides a more positive E_{corr} and higher cathodic current densities [144]. According to previous studies [165, 199-201], H_2O_2 has a negative effect on the corrosion resistance of Ti implant materials, creating rough surfaces because of the selective dissolution of the β-phase. Under harsh inflammatory conditions, which were simulated by adding BSA+H_2O_2 to the three different solutions, a decrease in the cathodic current density and E_{corr} with respect to the addition of only H_2O_2 was detected owing to the role of BSA protein as a complex agent with oxides or corrosion products on the TiO_2 film.

Figures 4.2a, b, and c represent the Bode phase and Bode magnitude diagrams of the Ti6Al4V alloy in NaCl, PBS, and Hanks' solutions, respectively. The Ti6Al4V samples in the three physiological solutions show only a one-time constant in the frequency range of 0.01 to 100 kHz. The fitting process of the EIS measurements was carried out using the ZView software package and the results are presented in **Table 4.1.** The equivalent

electrical circuit includes R_s as the solution resistance, R_{Com} as the resistance of the complex layer (protein–passive film), and CPE_{dl} as the constant-phase element of the double layer or the complex layer. CPE is used instead of a capacitor because the capacitive elements have non-ideal behaviour owing to surface roughness and heterogeneity during BSA molecule or complex interactions [61]. According to the literature [195], a Ti alloy is composed of two oxide layers, with a porous outer layer and a barrier inner layer. However, the outer layer in this study was not clear and integrated into a complex layer with phosphate, calcium-phosphate, protein, and protein–metal species or in the form of an inhomogeneous region.

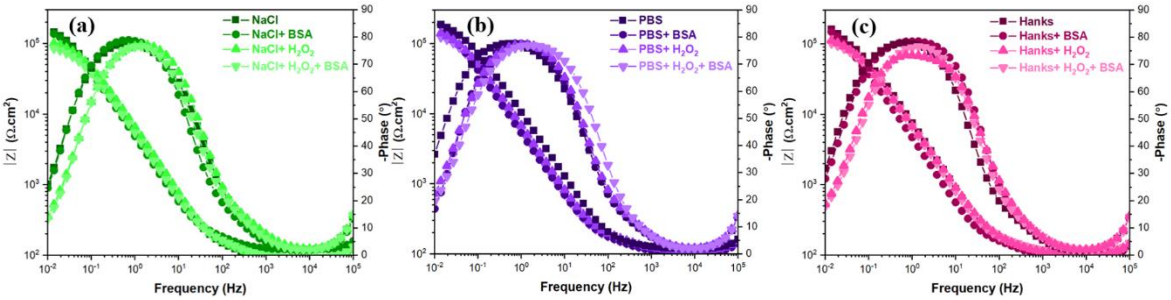

Figure 4.2. EIS spectra of Ti6Al4V alloy after 1-h immersion in (a) NaCl, (b) PBS, and (c) Hanks physiological solutions with the addition of either BSA or H_2O_2 or both at 37 °C, pH 7.4, and aerated conditions.

Table 4.1. Fitting data obtained from EIS measurements in Figure 4.2 using an R(RCPE) equivalent electrical circuit.

Condition	R_s ($\Omega.cm^2$)	R_{ct} ($K\Omega.cm^2$)	CPE_{dl} ($\mu F\ S^{-1}\ cm^{-2}$)	n_{ads}
NaCl				
NaCl	86 ± 5	159 ± 6	34 ± 2	0.92 ± 0.02
NaCl+ BSA	128 ± 5	147 ± 10	29 ± 3	0.91 ± 0.02
NaCl+ H_2O_2	87 ± 8	104 ± 6	30 ± 4	0.88 ± 0.01
NaCl+ BSA+ H_2O_2	95 ± 6	91 ± 12	35 ± 6	0.88 ± 0.02
PBS				
PBS	119 ± 8	221 ± 8	35 ± 4	0.90 ± 0.02
PBS + BSA	106 ± 4	200 ± 4	20 ± 8	0.88 ± 0.03
PBS + H_2O_2	109 ± 3	151 ± 8	31 ± 2	0.89 ± 0.02
PBS + BSA+ H_2O_2	118 ± 5	129 ± 5	28 ± 6	0.88 ± 0.03
Hanks				
Hanks	126 ± 4	212 ± 11	38 ± 4	0.89 ± 0.02
Hanks + BSA	104 ± 7	168 ± 10	25 ± 7	0.90 ± 0.01
Hanks + H_2O_2	115 ± 8	119 ± 8	29 ± 3	0.88 ± 0.02
Hanks + BSA+ H_2O_2	107 ± 5	106 ± 11	28 ± 3	0.86 ± 0.02

The Bode modulus diagrams in NaCl solutoin, PBS, and Hanks' solution revealed that the inflammatory condition simulated by BSA proteins and H_2O_2 led to a slight decrease in the corrosion resistance of the Ti6Al4V sample. It should be considered that BSA strongly adsorbs onto the TiO_2 oxide layer by chemisorption through a carboxylate-amino acid group with electrostatic or hydrophobic interactions and that it controls the kinetics of electrochemical reactions [144]. Therefore, the Ti6Al4V samples in the BSA/H_2O_2 solutions showed the lowest corrosion resistance and were more susceptible to metal ion release. Likewise, a slight shift in the magnitude of the phase angle from 80° to 75° can be seen in the BSA/H_2O_2 integrated inflammatory condition in all environments owing to the decrease in the dielectric properties and their effect on the capacitance of the oxide layer.

4.2 Mott–Schottky analysis of complex surface layer

The semiconductor characteristics of the passive film on Ti6Al4V alloy and the donor or acceptor density were measured in the different physiological environments by the capacitance (space charge region and Helmholtz double-layer)/solution interface with respect to the applied potential at 37 °C, pH 7.4. The MS analysis is explained by the following equation [191]:

$$\frac{1}{C_{SC}^2} + \frac{1}{C_H^2} = \pm \frac{2}{\varepsilon\varepsilon_0 e N_{d\ or\ a}} (E - E_{fb} - \frac{kT}{e}) \ , \tag{4.2}$$

where C_{SC} is the space charge capacitance, C_H is the capacitance of the Helmholtz double-layer, E is the applied potential, ε is the dielectric constant of the passive film, ε_0 is the vacuum permittivity (8.854×10^{-14} F·cm^{-1}), e is the electron charge (1.6×10^{-19} C), N_d is the donor density, N_a is the acceptor density, E_{fb} is the flat band potential, and k and T are the Boltzmann constant and absolute temperature, respectively. As mentioned above, the C^{-2} magnitude is a reflection of the total capacitance value at the oxide surface/electrolyte interface into the space charge region, the Helmholtz layer, and the non-uniform or heterogeneous protein adsorbed layer (only in the protein environment). Because the physicochemical interactions of protein molecules such as adsorption and detachment are dynamic processes, the different potential sweeping on MS can significantly affect these interactions [193, 202]. Hence, we can state that the major part of the C^{-2} magnitude is related to the space charge capacitance of the oxide layer.

According to previous studies [83, 144, 197, 203], the passive film on Ti and its alloys is a mixture of TiO (close to the metallic substrate), TiO_2, and Ti_2O_3 (on the top of the passive film), which can affect protein adsorption, conformational alternation, and electron transfer for electrochemical reactions. The low donor density value explains the electrochemical reactions at the TiO_2 passive film/solution interface, which can be inhibited by reducing the charge transfer. The intensity of donor density is related to the density of

the oxygen vacancies or the interstitial distribution of Ti or Al in the passive film region [204]. Thus, the decrease in the formation rate and transfer velocity of oxygen vacancies along with Ti interstitials enhances the stability and protective behaviour of the passive film with low mass transfer [205]. As shown in **Figure 4.3**, all three basic solutions demonstrated an increasing trend in the C^{-2} magnitude (decline in space charge region) at the approximate potential of 0 V vs. Ag/AgCl owing to the transfer from the active region to the passive region. The linear region with a positive slope represents the n-type character of the semiconductor properties of the passive film [83]. The BSA protein slightly decreased the C^{-2} magnitude in the potential range of -1 to 0.1 V vs. Ag/AgCl in all tested environments. After 0.1 V vs. Ag/AgCl, in the BSA protein environments, there was a slight decrease in the C^{-2} magnitude, which can be attributed to the effect of BSA protein adsorption on the passive film and especially on the distribution of charge carrier densities. To calculate the N_d value, ε was considered to be 80 in agreement with previous studies [206]. N_d was calculated by fitting a straight line on the positive slope into the following equation (with considering the standard deviation during the fitting process (error bar)) [207]:

$$\alpha = \frac{-2}{N_d\, e\varepsilon\varepsilon_0} \quad , \tag{4.3}$$

where α is the slope in C^{-2} versus the applied potential. The results of the fitting process on the Mott–Schottky curves are shown in **Figure 4.3d**. It is important to notice that the fitting process and the calculation of N_d value is based on the flatness of the passive regions which is different in each proposed simulated solution (**Figure 4.3a, 4.3b and 4.3c**). This is due to the different chemical composition of the base solutions as well as the presence of H_2O_2 and BSA. All these factors strongly influence the C^{-2} magnitude, positive slope region, and its shape.

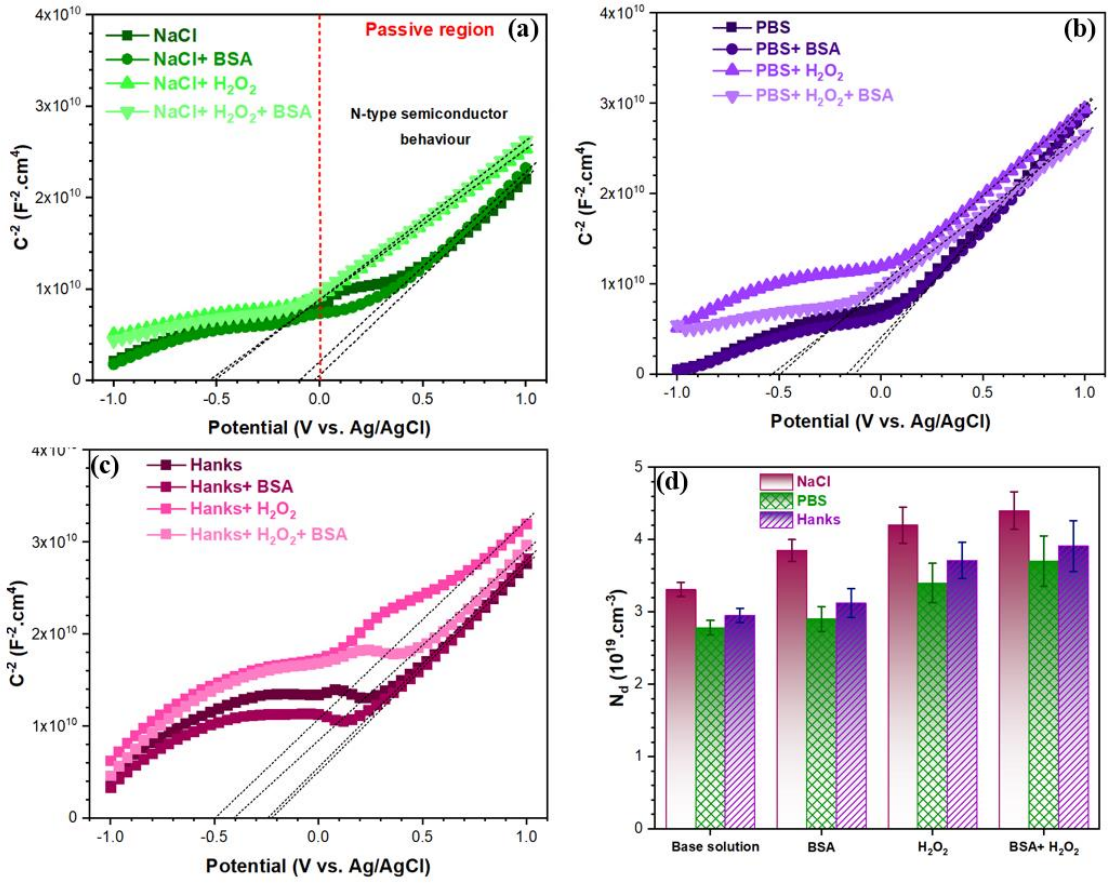

Figure 4.3. Mott-Schottky analysis of Ti6Al4V alloy after 1-h immersion in (a) NaCl, (b) PBS, and (c) Hanks physiological solutions with the addition of either BSA or H_2O_2 or both at 37 °C, pH 7.4, and aerated conditions, (d) Donor carrier density in the passive film of Ti6Al4V alloy in the different physiological solutions.

Adding H_2O_2 triggered an increase in the C^{-2} magnitude in all three solutions and at all applied potentials. H_2O_2 in the presence of phosphate or calcium-phosphate could modify the TiO_2 oxide layer and thicken it [208]. Protein molecules with complex effects could damage the TiO_2 oxide layer during the interaction with H_2O_2, increasing the material degradation [117]. The adsorbed protein on TiO_2 oxide can shift the E_{fb} to more negative values and increase N_d owing to local alkalisation of the (hydr)oxide surface groups on TiO_2 [209]. In fact, the adsorbed layer of BSA proteins can strongly affect the space charge region, which is directly related to the charge carrier density in the conduction band [209]. The donor

density of the film formed on the Ti6Al4V in the three tested base solutions follows the order PBS<Hanks's <NaCl in all conditions. Adding BSA and H_2O_2 in NaCl solution increased N_d, as shown in **Figure 4.3d.** Although, this increase was not more intensive in PBS and Hanks solutions. As a result, we can state that both BSA protein and BSA/H_2O_2 environments provide a higher dissolution rate owing to the increase in the number of defect sites and the higher rate of mass transport through the oxide region, which decreases the protective properties in accordance with the PDP and EIS results.

Throughout the range of applied potentials, especially between -1 V and 0.1 V vs. Ag/AgCl, specimens immersed in Hanks' solution showed a higher C^{-2} magnitude than those immersed in PBS and the NaCl solution. This is due to the calcium-phosphate complex layer formed on the TiO_2 oxide layer, which acted as a protective layer that inhibited the electrochemical reactions and blocked the mass transportation of oxygen or reaction products on passive film [210]. Likewise, BSA proteins tended to bind with the calcium-phosphate complex layer. Moreover, the phosphate compounds absorbed on the passive film and formed metal–phosphate complexes, which led to a decrease in i_{corr} or acted as an anodic inhibitor, shifting E_{corr} to more positive values.

4.3 Protein–oxide surface complex analysis by XPS

A complementary study was carried out by XPS surface analysis to reveal the significant role of phosphate and calcium species, BSA protein adsorption, and H_2O_2 interaction on the complex oxide layer on the Ti6Al4V alloy. The individual high-resolution spectra of elements are shown in **Figure 4.4** to highlight the the BSA protein adsorption and the H_2O_2 influence on the metal ion release and chemical composition distribution of the surface layer. Moreover, the element content distribution in the surface layer calculated from XPS results is shown in **Figure 4.4h**. Two separate Ti peaks were detected on the Ti

spectrum at binding energies of 464.8 ± 0.4 eV and 459.1 ± 0.8 eV, which are attributed to Ti^{4+} $2p_{1/2}$ and Ti^{4+} $2p_{3/2}$, respectively, in form of TiO_2 oxide [69]. Likewise, at a binding energy of 74.8 ± 0.6 eV, a sharp peak of the Al 2p spectrum was distinguished for the Al oxide [166]. The O 1s spectrum showed two dominant individual peaks that originated from oxide (O^{2-}) at 530.4 ± 0.8 eV and hydroxide or hydroxyl groups at 532.1 ± 0.4 eV arising from metal oxides and oxidised surface carbon [211].

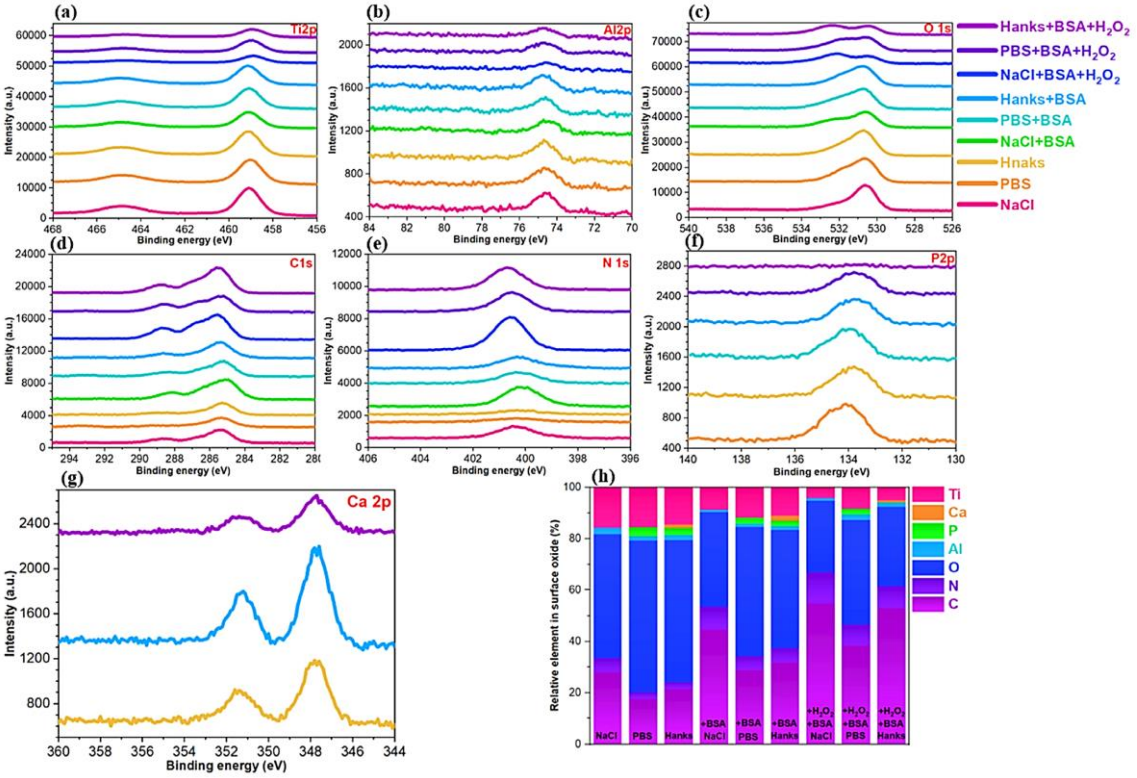

Figure 4.4. XPS spectra of (a)Ti 2p, (b) Al 2p, (c) O 1s, (d) C 1s, (e) N 1s, (f) P 2p, and (g) Ca 2p electron energy regions on Ti6Al4V alloy after polarising at 0.2 V vs. Ag/AgCl for 1-h in NaCl, PBS, and Hanks solutions with or without BSA and H_2O_2, (h) Relative % of elements in the surface oxide calculated from XPS spectra.

The main content of the C spectrum originated from airborne carbon or contamination. According to previous studies [69, 167], BSA protein is included in CO–NH peptides and in amino ($–NH_2$) and carboxyl (–COOH) groups. Thus, the C 1s peaks can be deconvoluted into three peaks at 284.5 ± 0.9 eV, 285.8 ± 0.8 eV, and 287.7 ± 0.9 eV, which

are related to mainly C–C and C–H bonds, peptidic residues or C–O and C–N bonds, and N–C=O bonds, respectively [145, 212]. Therefore, we can conclude that the higher C and N intensity peaks on the surface layer in all BSA solutions are due to BSA protein adsorption on the surface oxide. Ca spectrum peaks only appeared in Hanks' basic solution with two individual peaks at 347.6 ± 0.1 eV and 351.6 ± 0.2 eV, which are attributed to Ca^{2+} $2p_{3/2}$ and Ca^{2+} $2p_{1/2}$, respectively [213]. P spectrum peaks (P 2p3 peak) were well distinguished for PBS and Hanks' basic solution at a binding energy of 133.6 ± 0.5 eV [214].

By changing the solution chemistry from NaCl to PBS and Hanks' solutions, the Ti and Al spectra represented the same approximate Ti and Al contents on the surface layer, whereas the O spectrum increased on the surface oxide (**Figure 4.4h**). However, with the addition of BSA protein to the three basic solutions, the amount of Ti on the surface oxide decreased and finally reached the lowest value in BSA+H_2O_2-containing solutions. However, the Al in the PBS+BSA solution showed a lower value than that in PBS, and again the content increased slightly in the PBS+BSA+H_2O_2 solution owing to the preferential dissolution of Ti [166]. A higher amount of Ti on the surface layer in both PBS and Hanks' solutions under BSA and BSA+H_2O_2 conditions was observed in comparison with the NaCl solution. Likewise, a decrease in the P and Ca contents by adding BSA and BSA+H_2O_2 to PBS and Hanks' solutions was observed. Comparing the three base solutions with BSA protein, the C and N contents followed the order NaCl > Hanks' > PBS. The C and N contents in the surface layer increased by adding H_2O_2 to the solutions containing BSA, indicating higher protein adsorption [166]. As a result, for all solutions with BSA+H_2O_2, the lowest Ti and Al contents and the highest C and N contents were observed. This is because H_2O_2 as an oxidising agent leads to the formation of a TiOOH defective complex or a H_2O_2–TiO_2

complex, which enhances the Ti and Al release process, especially from phosphate and calcium complexes that are bonded to Ti oxides [166, 215].

In the PBS environment, HPO_4^{2-} and $H_2PO_4^-$ are dominant species that can easily adsorb onto TiO_2 oxide to form a thin phosphate-complex film. However, CaO and Na_3PO_4 or Na_2HPO_4 in Hanks' media tend to adsorb onto the TiO_2 oxide [214]. According to previous studies, we can deduce that the presence of Ca 2p3 at a binding energy of 347.6 eV is attributed to $CaHPO_4$ [216], whereas P 2p3 at a binding energy of 133.6 eV originates from HPO_4^{2-} or Na_2HPO_4 [217]. Therefore, the thin and rich layer of phosphate species formed in the PBS solution on the TiO_2 oxide offers better protection, hindering the release of Ti and Al ions or blocking the mass transport as compared to the NaCl and Hanks' solutions with $CaHPO_4$ [2]. The BSA protein in the NaCl solution had a higher adsorption rate than that in PBS and Hanks' solutions, which is related to the competition between the protein and the phosphate and calcium species. However, it should be noted that both BSA molecules and phosphate species have negative zeta potentials [70]. In fact, the phosphate and calcium species are smaller and move faster, thus bonding to the surface oxide better than the large protein molecules. This decreases the amount of protein on the surface layer due to the shielding or repulsing of protein molecules.

Likewise, the PBS solution showed slightly lower C and N contents (adsorbed proteins) than the Hanks' solution arising from the surface chemistry and electronic properties of the adsorbed phosphate species (discussed in the next section). Therefore, the formation of metal–protein complexes and not compact films is more probable on the surface layer in the Hanks' solution. Consequently, the higher the i_{corr} value, the lower the resistance to charge transfer. The higher density of charge carriers on the Ti surface oxide in NaCl solution is attributed to the high amount of adsorbed BSA protein on the surface oxide, which

can lead to protein–metal complex detachment. A schematic representation of the different phenomena occurring on the surface of the Ti alloy immersed in different environments is shown in Figure 4.5.

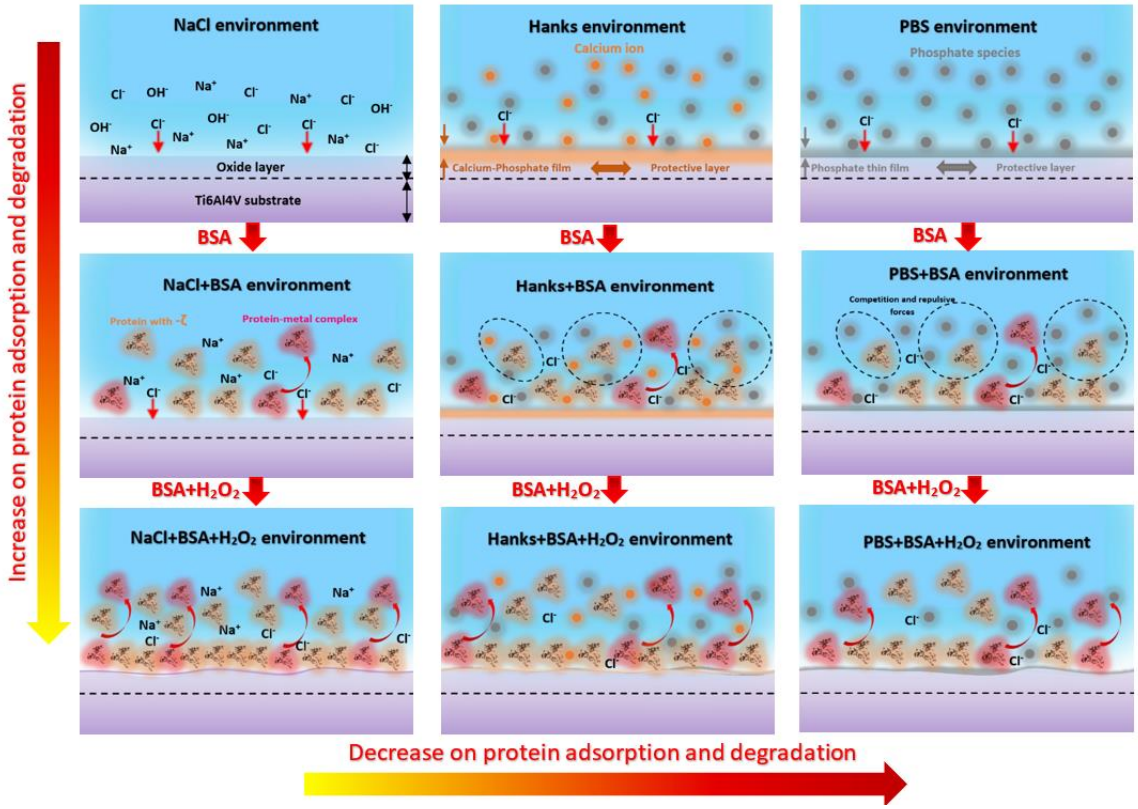

Figure 4.5. Schematic representation of the role of the different species present in the tested environments and their influence on the BSA protein adsorption on the surface of Ti6Al4V and metal ion release.

4.4 Surface potential and protein conformational arrangement

4.4.1 Analysis of the as-polished alloy

The heterogeneous surface of Ti6Al4V with α- and β-phases during exposure to the simulated environment can show different adsorption mechanisms of the various ions and protein species, protein conformations, and metal ion release processes. This is because the oxide layer on the different metal phases could have different chemical compositions, nanometric roughness, and WFEs with occupied and unoccupied densities of state, which can control the abovementioned parameters [89]. Therefore, SKPFM measurements were

used to measure and correlate the morphology and surface potential of individual α- and β-phases according to different adsorption contents of protein and metal ion species.

Figure 4.6 show the topography and surface potential, respectively, of the air-formed passive film on the as-polished surface of the Ti6Al4V alloy. The surface potential image clearly distinguishes the α- and β-phases as separate regions with different WFEs as the nobility criterion. The diverse nobility of the α- and β-phases is related to the different elemental distributions and WFEs. According to the literature [218, 219], the β-phase, which has a higher vanadium content, has a higher relative surface potential and acts as a nobler phase than the α-phase, which has a higher aluminium content. Vanadium has a higher WFE, 4.3 eV, in comparison to aluminium, which has a WFE of 4.26 eV in the polycrystalline condition [220]. According to EDX analysis, the β-phase contained 13.38% V and 4.79% Al, whereas the α-phase contained 2.28% V and 6.87% Al.

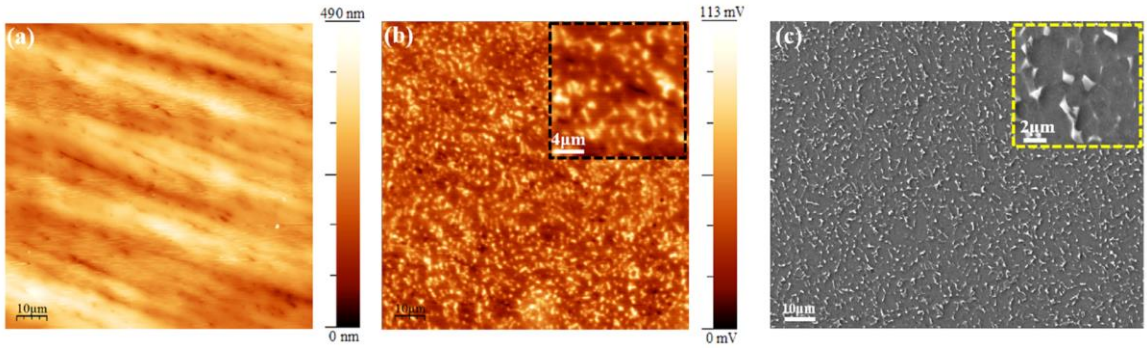

Figure 4.6. (a) topography and (b) surface potential maps of polished Ti6Al4V alloy, (c) FESEM image of etched Ti6Al4V alloy.

Therefore, the α- and β-phases have different tendencies to transfer the valance electrons to electrochemical reactions at the passive film/solution interface, which in turn leads to a microgalvanic driving force for corrosion attack with active (anode) and noble (cathode) sites. Al and V ions released from Ti6Al4V surfaces can diminish normal bone healing processes, which leads to a negative effect on osteoblast cell behaviour [221]. It must

be noted that vanadium stabilises the β-phase, and its oxide layer is harmful to the human body [203].

4.4.2 Effect of BSA protein under polarisation in different environments

The SKPFM and SEM micrographs of the Ti6Al4V specimens after 1-h polarisation at 0.2 V vs. Ag/AgCl in the three base solutions containing BSA protein at 37 °C are shown in Figure 4.7.

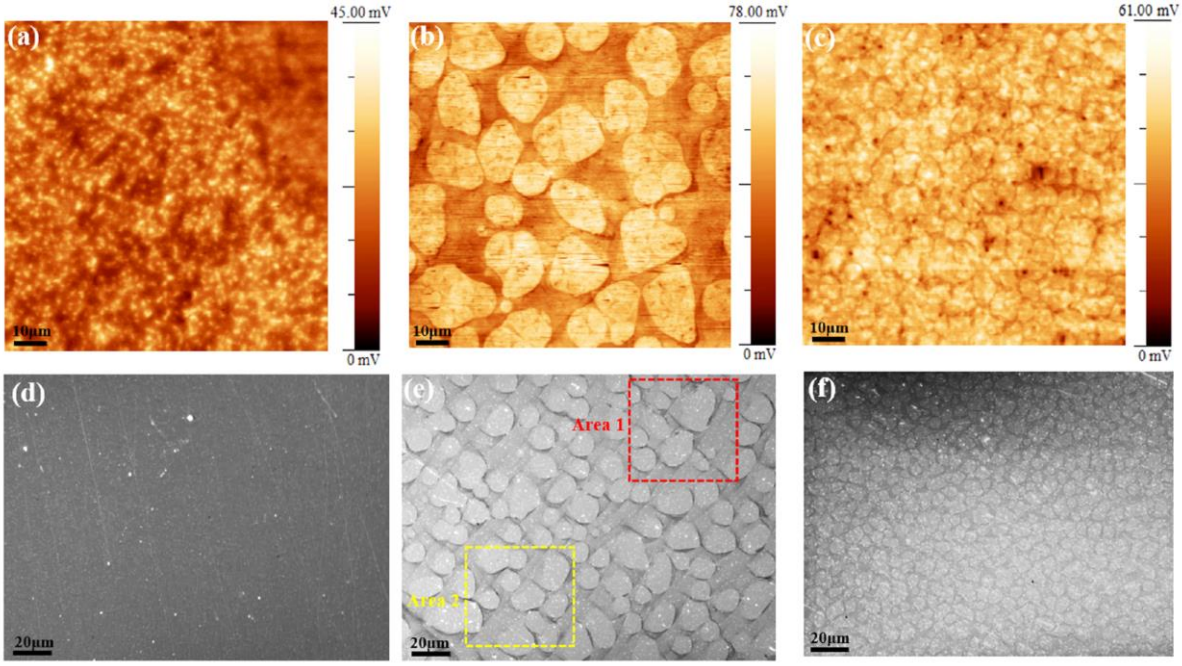

Figure 4.7. Surface potential maps and SEM images of Ti6Al4V alloy polarized at 0.2 V vs. Ag/AgCl for 1-h in (a, d) 0.9% NaCl, (b, e) PBS, and (c, f) Hanks physiological solutions with 1 g L^{-1} BSA protein.

The presence of BSA protein in both the PBS and Hanks' solution led to a particular conformational arrangement of BSA protein with a fibrillar or network morphology on the surface layer in comparison with the NaCl solution, as shown in Figures 4.7b and c. In the NaCl solution, individual α- and β-phases were detected with a new Volta potential distribution (Table 4.2), with no evidence of protein cluster morphology, as observed in PBS and Hanks' conditions. In PBS and Hank's solutions, no differences between the α- and β-

phases could be distinguished and the BSA was adsorbed on the surface in the form of a dense network or cluster shape, as shown in both the SKPFM maps (darker regions) and SEM images. Additionally, two separate regions were detected, including protein-enriched regions and matrices (including both α- and β-phases), which were deconvoluted in the form of bimodal peaks in the histogram curves in **Figure 4.8a**.

The protein enrichment region in PBS solution clearly exhibits a low surface potential or surface charge (as a criterion for electronic conductivity), with a mean value of 40.5 mV, as compared to the matrix or passivated film at 52.2 mV (**Table 4.2**). According to the literature [164], BSA protein (known as a low-conductive protein) exhibits low charge transport or electronic transport (ET) efficiency in comparison with other proteins such as azurin and bacteriorhodopsin (BR), with a high ET bias bandgap in the current–voltage curve (*I–V*).

Table 4.2 Extracted Gaussian distribution parameters from the surface potential histograms in **Figure 4.8.**

Region label	Constituents*	Mean value of surface potential (μ,mV)+ standard deviation (σ,mV)
Ti6Al4V alloy	α-phase	34.3 ± 12.5
	β-phase	48.5 ± 34.6
PBS+BSA	Protein cluster	40.5 ± 16.5
	Matrix (α and β-phase)	52.2 ± 9.4
Hanks+BSA	Protein+ α-phase	32.4 ± 11.8
	β-phase	39.6 ± 6.4
NaCl+BSA	α-phase	14.6 ± 7.1
	β-phase	18.7 ± 8.3
PBS+BSA+H_2O_2	α-phase	46.5 ± 12.2
	β-phase	54.1 ± 21.3
Hanks+BSA+H_2O_2	α-phase	34.7 ± 8.9
	β-phase	45.6 ± 8.5
NaCl+BSA+H_2O_2	α-phase	15.5 ± 6.5
	β-phase	19.8 ± 7.8

* The surface potential of α and β phases in BSA and BSA+H_2O_2 conditions is influenced by the adsorbed BSA.

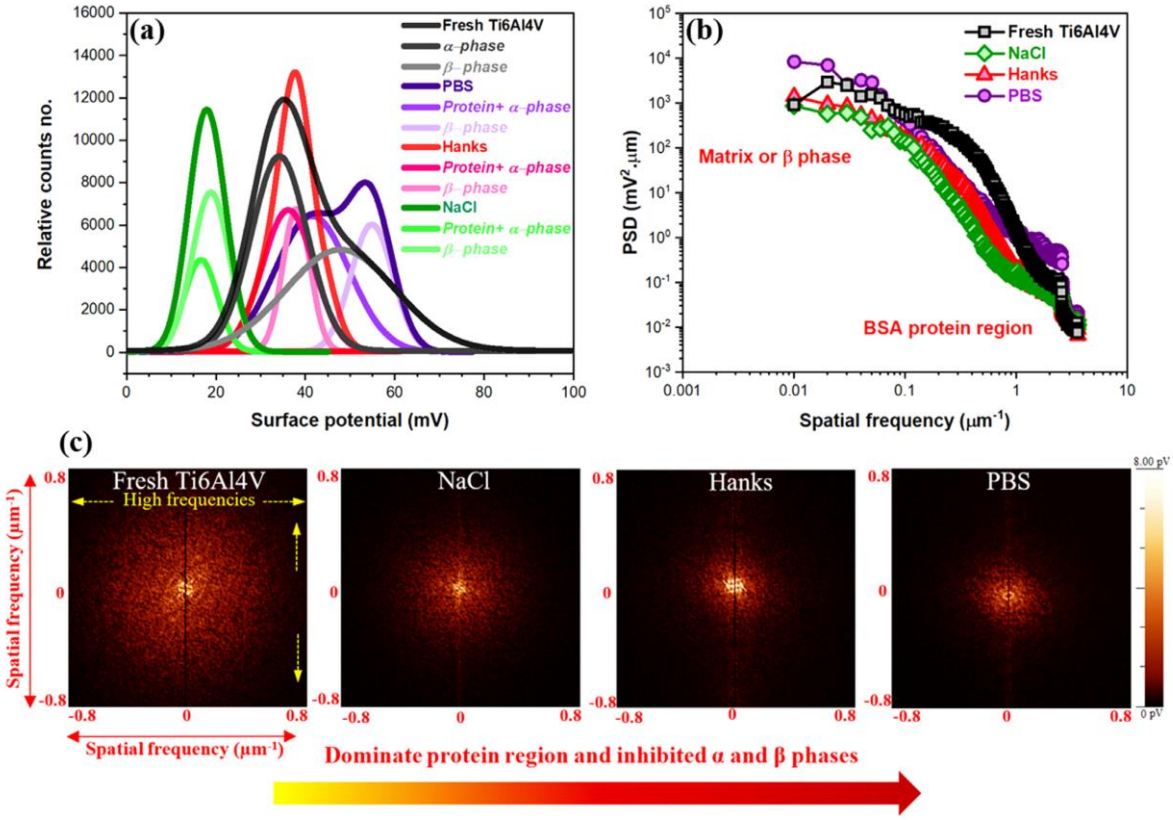

Figure 4.8. (a) Surface potential histogram based in MGD, (b) PSD plots related to **Figure 4.7** and (c) 2D PSD maps of surface potential related to **Figure 4.7**.

The electrostatic surface potential of proteins and DNA molecules is governed by the surrounding surface charge and isoelectric point (IEP) [222, 223]. The IEP is defined as the degree of the relative proton affinity of a molecule, which has an opposite correlation with the electronegativity. Additionally, the pH value, which is a measure of the protein surface charge, has a minimum value that can be defined as IEP [137]. Consequently, it can be said that the BSA protein with a fibrillar or network morphology has a low surface potential, which represents a low isoelectric point (~5.4 and ~5.2 for theoretical estimated and bulk measured, respectively [110, 137]), which can affect the concentration of the charge carriers at the atomic and molecular levels of the BSA structure. The conformational or structural pattern changes of a protein molecule from globular to a network morphology is related to

the chemical properties of the substrate, and migratory parameters lead to a suitable adhesiveness level for improving fibroblast motility [224, 225]. The molecular shape of the BSA protein is ellipsoidal, with dimensions of 4 nm × 4 nm × 14 nm [226]. Depending on the protein features and surface properties, the adsorption type of the BSA monolayer is side-on and end-on [164]. Stobiecka et al. [227] indicated that BSA on highly ordered pyrolytic graphite (HOPG) has a network morphology in comparison to a globular shape on Au because of the free diffusion and association into large assemblies with high self-interaction energies. Previous studies have shown that depending on the solid surface properties and environmental conditions, protein molecules can adsorb into co-operative adsorption with the growth of two-dimensional surface clusters that are densely ordered, leaving some uncovered regions, which is consistent with our SKPFM results [119, 228].

The BSA protein in the Hanks' solution showed a finer network morphology in comparison with PBS media, whereas small regions with higher Volta potential correspond to the underlying β-phase grains that remain distinguishable. Based on image analysis, BSA proteins in PBS and Hanks' solution covered approximately 50% and 56% of the Ti6Al4V surface, respectively. Nevertheless, the BSA protein network in the Hanks' solution represented a smaller net size in the range from 200 nm to 5 µm, whereas the net size in the PBS solution was much larger, between 2 and 20 µm. Moreover, the protein regions in the PBS solution presented a higher surface potential (40.5 mV) than in those in Hanks' solution (32.4 mV), as reported in **Table 4.2**.

The PSD analysis (**Figure 4.8b**) showed the heterogeneous distribution of the surface potential with respect to the spatial frequencies. The lowest and highest spatial frequencies were related to higher surface potential constituents (matrix, α-, and β-phases) and BSA proteins with lower surface potential distribution, respectively [88]. Two-dimensional PSD

mappings (Figure 4.8c) showed the surface potential distribution of various constituents (protein, α-, and β-phases) versus spatial frequencies in the *x–y* direction. By sweeping from fresh Ti6Al4V up to PBS, the homogeneous distribution on the surface potential at all frequencies, especially at high frequencies, decreased owing to the formation of large and dominant protein regions [229]. Indeed, the large circle in fresh Ti6Al4V represents the homogenous distribution of α- and β-phases with various surface potentials at different spatial frequencies. In the NaCl condition, a wider and more uniform distribution of surface potential of all constituents was detected compared to the Hanks' solution and PBS with a small circle and semi-homogenous distribution of surface potential owing to the dominant BSA protein region that covered the matrix.

4.4.3 Effect of the polarisation in the different environment containing BSA+H_2O_2

The SKPFM maps of Ti6Al4V specimens after 1-h polarisation at 0.2 V vs. Ag/AgCl in the three base solutions containing BSA protein and H_2O_2 at 37 °C are shown in Figure 4.9.

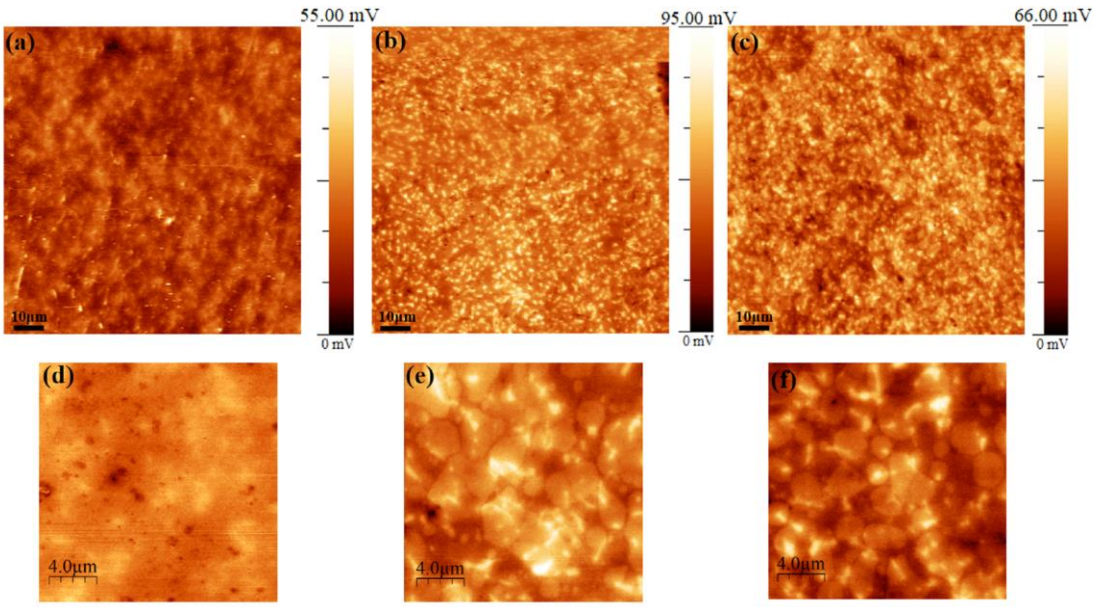

Figure 4.9. Low and high magnification maps of surface potential of Ti6Al4V alloy polarized for 1-h at 0.2 V vs. Ag/AgCl in (a, d) NaCl, (b, e) PBS and (c, f) Hanks physiological solutions with 1 g L^{-1} BSA protein and 100 μM H_2O_2.

The H_2O_2 agent significantly hindered the adsorption of BSA protein molecules on the surface, forming thick films in all environments to clearly detect the individual α- and β-phase grains. The surface potential values were slightly higher than those detected in solutions containing only BSA. Likewise, the total surface potential differences on the Ti6Al4V surface in the BSA+ H_2O_2 solutions followed the trend NaCl < Hanks' < PBS. To better observe the BSA features on the Ti6Al4V passivated surface, higher-magnification SKPFM images are shown in **Figures 4.9d, e, and f.**

As presented in the higher-magnification SKPFM images, higher surface coverage with BSA protein was noticed in Hanks' solution as compared to that in PBS solution, 51% and 40%, respectively. In addition, the morphology of the protein on the surface was different; in NaCl solution, the protein was in the form of aggregates (dark regions in **Figure 4.9d**), whereas in PBS and Hanks' solutions, the protein presented a network morphology. As mentioned above, the primary adsorbed thin layer of phosphate and calcium-phosphate complex can provide appropriate conditions for BSA protein adsorption and control the migration and conformational arrangement of protein molecules. In comparison with the Volta potential maps obtained in solutions without H_2O_2, the adsorbed film seemed to be thinner as the β-phase regions with higher surface potential were still distinguishable.

As shown in **Table 4.2**, the α- and β-phases showed higher surface potentials in PBS solution (46.5 mV_{α} and 54.1 mV_{β}, respectively) than in the Hanks' and NaCl solutions, with values of 34.7 $mV_{\alpha/Hanks}$, 45.6 $mV_{\beta/Hanks}$ and 15.5 $mV_{\alpha/NaCl}$, 19.8 $mV_{\beta/NaCl}$, respectively.

4.5 Degradation occurrence on complex oxide layer

The particular morphological distribution of BSA protein and the differences in the surface potential could trigger localised corrosion. To investigate this, SEM micrographs at higher magnification of the marked areas in **Figure 4.7e** are shown in **Figures 4.10a and b**.

Localised corrosion attacks (arrows) are observed at the interface protein/substrate interface owing to the formed crevices and the differences in the surface potential. This can be explained by various degradation mechanisms considering the metal ions releasing of metallic implants during interaction with proteins, especially human serum albumin (HSA) and BSA proteins as a consequence of (1) shielding effect or inhibiting the cathodic reaction, (2) attracting counterions, (3) a complexation process with the various oxide constituents, and (4) the Vroman effect, as presented schematically in **Figure 4.10c**.

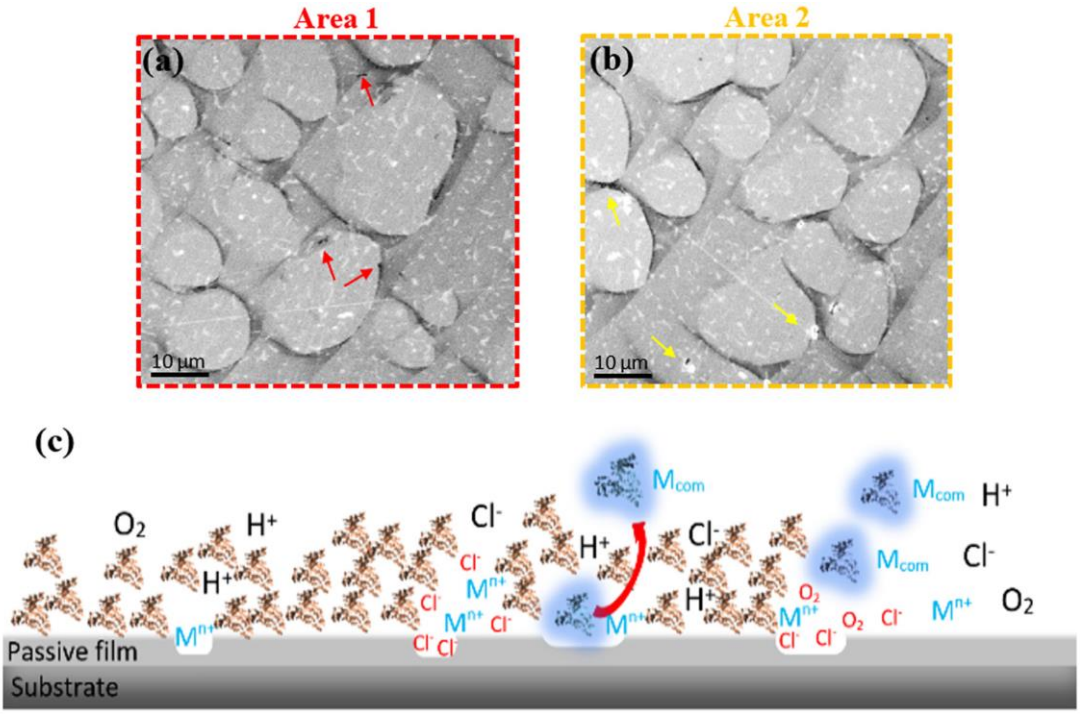

Figure 4.10. (a and b) SEM images of adsorbed BSA protein on Ti6Al4V detected after 1-h polarisation at 0.2 V vs. Ag/AgCl in PBS solution containing 1 g L^{-1} BSA protein at 37 °C (marked areas in **Figure 4.7e**, (c) Schematic representation of localized corrosion mechanism on passive metal in presence of BSA protein.

Some properties, such as the physiological environment and surface chemistry, have a direct effect on the degradation mechanism time. The shielding effect explains that the BSA protein initially decreases the release of metal ions by inhibiting the cathodic reactions on the passive film. However, with time (milliseconds to years), it provides a suitable

condition for increasing the metal ion release process [111, 117]. The BSA protein or BSA micronetwork/passive film interface is an attractive site for easier adsorption of the counterions (aggressive ions such as Cl^-). This can lead to penetration within the BSA protein layer and then into the BSA protein/passive film interface and finally promote localised corrosion of the passive layer [222]. The BSA protein can create complexes with metal or metal–oxide species on passive films, which in turn triggers more degradation and formation of metal–protein conjugates [61]. The Vroman effect indicates that the detachment of metal–protein bounds is under the control of the exchange process of adsorbed proteins, which finally leads to enhancing the corrosion rate.

4.6 Partial conclusions

The electrochemical measurement results indicated that the alloy is more resistant to corrosion in PBS solution in comparison to Hank's and NaCl. The addition of BSA leads to a slight increase of the corrosion current density and the passive current density in all tested solutions, whereas a more marked increase is observed by adding H_2O_2 or both BSA and H_2O_2. These results are correlated to the semiconductive characters of the formed passive film. Indeed, Mott-Schottky analyses demonstrated that under inflammatory conditions (BSA+H_2O_2) an increase of the donor density of the passive film formed was noticed in all environments. XPS analyses and SKPFM maps revealed that specimens polarized in the NaCl environment containing BSA+H_2O_2 presented the highest protein covering, the lowest Ti and Al contents in the passive film, and the lower surface potential compared with the other solutions. The morphology of the adsorbed protein changed from globular to a large micronetwork (PBS) to fine micro-nanonetworks (Hanks'), along with increasing the surface potential. According to the SKPFM and SEM images, the different interfaces including protein/α- or β-phases and the top surface of BSA protein were the susceptible sites for

corrosion initiation owing to different surface potentials and suitable places for the adsorption of counter ions, e.g., Cl^-.

Summarizing the results of the electrochemical and surface analyses techniques it could be stated that the adsorption of protein on the surface of Ti6Al4V increases the degradation rate in all human body simulating solution and this effect is more intense in inflammatory conditions (presence of H_2O_2). On the other hand, the presence of phosphate and calcium species contributes to the formation of a more protective layer due to their adsorption on the alloy surface. This hinders the adsorption of BSA protein, decreasing the corrosion rate.

Chapter 5: A visualizing on Albumin protein adsorption, electrochemical and surface potential evaluation on oxide layer of CoCrMo implant alloy

In this chapter, the conformation and morphology changes of BSA protein during adsorption on the CoCrMo oxide layer at different overpotential conditions, including OCP, 0.1V, and 0.3V vs. Ag/AgCl in phosphate-buffered saline (PBS) solution containing different concentrations of BSA protein are presented. A multi-technique procedure was used, including electrochemical measurements, AFM/SKPFM, XPS, and field-emission scanning electron microscopy (FE-SEM) to reveal the BSA protein conformation arrangement and its surface potential distribution on the corrosion initiation sites in the CoCrMo alloy surface.

5.1 OCP, PDP and EIS measurements of the complex surface layer

To characterize BSA protein molecules' role on the electrochemical response, during adsorption on the complex oxide layer of CoCrMo alloy in PBS solution, OCP, PDP, and EIS measurements were used. As can be observed in the OCP curves obtained in solutions with different BSA concentrations (**Figure 5.1a)**, CoCrMo presents a gradual increase in the OCP value, which is mainly related to the passive film growth during immersion for 1 hour. Adding BSA protein to PBS solution from 0 up to 2g.L^{-1}, generally led to a potential decrease from -190 (0 g.L^{-1} BSA) to -280 vs. Ag/AgCl (2 g.L^{-1} BSA). As stated previously, [70, 230], this can be attributed to the cathodic inhibitor character of BSA. BSA acts as an inhibitor and controls the kinetics of metal ions release and the reduction reactions, including oxygen and hydrogen reactions.

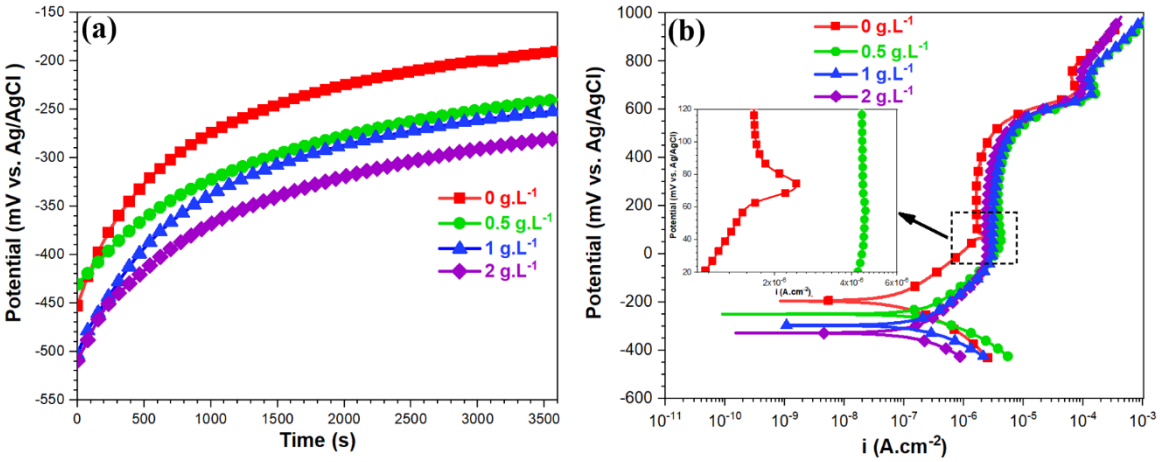

Figure 5.1. (a) OCP and (b) the potentiodynamic polarization measurements of CoCrMo alloy in PBS solution with various concentrations of BSA protein at 37C°, pH 7.4, and aerated conditions.

Figure 5.1b illustrates the PDP curves of CoCrMo alloy after OCP measurements in PBS solution for 1 hour with the different BSA protein concentrations. The significant electrochemical parameters of the PDP curves such as corrosion potential (E_{corr}) and corrosion current density (i_{corr}) calculated using Tafel extrapolation as well as the passive

current density (i_{pass}) are reported in **Table 5.1**. As reported before, by increasing the BSA protein concentration from 0 up to 2 g.L^{-1}, a decrease of the E_{corr} value ($-195_{0\ g/L} > -250_{0.5g/L} > -292_{1g/L} > -330_{2g/L}$ mV vs. Ag/AgCl) can be observed due to the BSA protein effect on the cathodic reaction [231, 232]. Moreover, a small peak appears on the anodic branch of the CoCrMo sample (inserted image) in the absence of BSA protein during sweeping to passivity region at about 72 mV vs. Ag/AgCl. This peak has been attributed to an intense chromium (Cr) contribution to the growth and compaction of the passive layer with two different forms, including Cr_2O_3 and $CrOH_3$ [81]. Moreover, the presence of BSA cause an increase of the i_{corr} and i_{pass} values, as presented in **Table 5.1**. It has to be noticed that by increasing gradually the BSA protein concentration from 0.5 to 2g.L^{-1} there is a decrease on the i_{pass}. It could, therefore, be assumed that at low concentration the complexing effect of BSA molecules with the metal substrate has a major role leading to a higher dissolution rate or metal-protein complex detachment, while at higher BSA concentrations, higher amounts of protein are absorbed on the surface providing a shielding effect [2].

Table 5.1. i_{corr}, E_{corr} and i_{pass} values obtained from the PDP curves in **Figure 5.1b**.

BSA concentration (g.L^{-1})	i_{corr} (A.cm^{-2})	E_{corr} (mV vs. Ag/AgCl)	i_{pass} (A.cm^{-2})
0	$0.7\pm0.3\times10^{-7}$	-195±15	$1.6\pm0.3\times10^{-6}$
0.5	$2.4\pm0.5\times10^{-7}$	-250±30	$4.2\pm0.4\times10^{-6}$
1	$1.9\pm0.4\times10^{-7}$	-292±20	$3\pm0.2\times10^{-6}$
2	$1.2\pm0.2\times10^{-7}$	-330±25	$2.5\pm0.2\times10^{-6}$

It has to be considered that in real conditions in the human body, the inflammatory cells have the ability to release reactive oxygen species (ROS) thus increasing the degradation process of implant materials [76]. Based on previous studies, in the simulated inflammatory conditions, the electrochemical potential of CoCrMo alloy can present a positive shift from -0.1V up to 0.65V due to hydrogen peroxide (H_2O_2) and Fenton reaction

[74]. On this account, we polarized CoCrMo samples for 1-hour at two different anodic potentials, namely 0.1V and 0.3V vs. Ag/AgCl (comparing to OCP as reference) in all tested solutions. Then, EIS was used to visualize the simultaneous influence of passive film growing, protein adsorption on passive film with a positive charge, and degradation process (e.g., resistance to charge transfer) on CoCrMo samples, as shown in **Figure 5.2.** The EIS spectra have been fitted using the two equivalent circuits reported in **Figure 5.2 (d)and (e).** The fitting has been carried out using the Zview software package and the results are listed in **Table 5.2**.

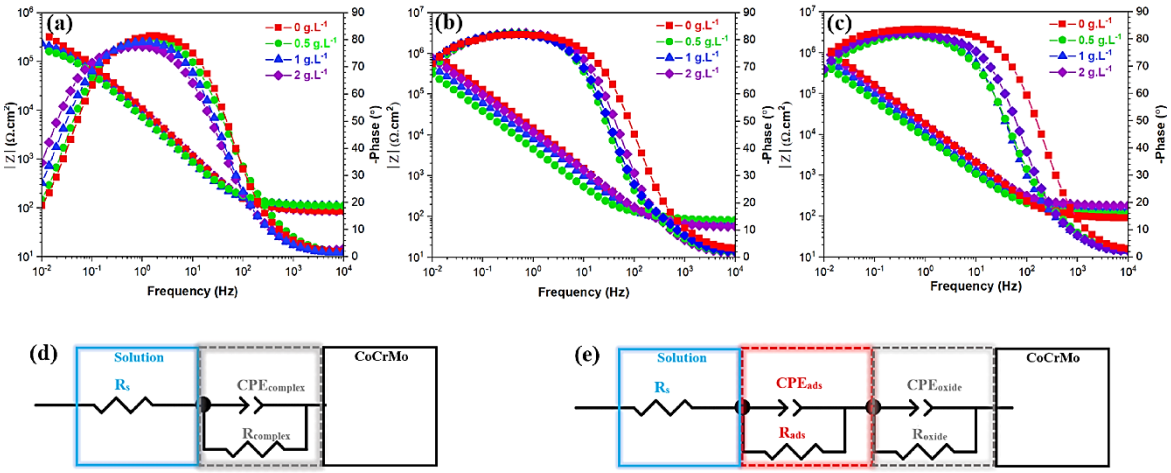

Figure 5.2. Bode phase and Bode magnitude diagrams of CoCrMo alloy in the PBS solution with the various concentrations of BSA protein at 37Cº, pH 7.4, and aerated condition, after 1-hour polarization at (a) in OCP, (b) 0.1V vs. Ag/AgCl, (c) 0.3V vs. Ag/AgCl, equivalent electrical circuits of EIS measurements into (d) one time constant (e) two-time constants.

Table 5.2. EIS extracted parameters for CoCrMo alloy in the presence of different BSA protein concentrations and overpotential conditions in Figure 5.2.

Condition (g.L^{-1} BSA)	R_s (Ω.cm^2)	R_{ads} (kΩ.cm^2)	CPE_{ads} (μF.S^{-1}.cm^{-2})	n_{ads}	$R_{complex/oxide}$ (MΩ.cm^2)	$CPE_{complex/oxide}$ (μF.S^{-1}.cm^{-2})	$n_{complex/oxide}$
OCP							
0	90±4				0.41±0.02	52±2	0.92±0.03
0.5	123±10				0.18±0.06	60±2	0.91±0.02
1	127±5				0.24±0.05	82±2	0.91±0.01
2	88±6				0.26±0.05	108±2	0.90±0.02
0.1V							
0	112±6	0.45±0.3	238±40	0.82±0.01	1.02±0.04	50±10	0.96±0.02
0.5	96±5	0.32±0.5	254±40	0.80±0.02	0.34±0.05	66±7	0.94±0.01
1	79±5	0.32±0.3	260±50	0.83±0.01	0.56±0.09	72±3	0.94±0.01
2	76±5	0.37±0.4	270±70	0.84±0.02	0.94±0.08	78±2	0.97±0.03
0.3V							
0	123±3	0.49±0.4	250±50	0.80±0.01	1.15±0.06	54±5	0.92±0.02
0.5	128±5	0.33±0.2	265±60	0.81±0.02	0.54±0.05	71±4	0.92±0.03
1	145±7	0.42±0.3	280±30	0.81±0.01	0.95±0.07	76±6	0.94±0.02
2	214±4	0.40±0.6	290±50	0.85±0.02	1.04±0.1	87±5	0.95±0.01

For the non-polarized samples (OCP condition), only an one-time constant was detected, referred to a complex layer composed by the thin passive film, phosphate species, and adsorbed protein layer [232]. In this case, the equivalent electrical circuit (EEC) parameters can describe as follows: solution resistance (R_s), metal/complex layer resistance, and constant phase element ($R_{complex}$ and $CPE_{complex}$).

Two-time constants were detected for the polarized samples, thus it could be assumed that the response at low frequencies corresponds to the metal/oxide film (R_{oxide} and CPE_{oxide}) and the response at high frequencies to the oxide film/adsorbed layer (R_{ads} and CPE_{ads}) [114]. Therefore, in this case, the adsorbed layer is composed of phosphate species, metal-protein complexes and a thin layer of adsorbed BSA protein [232]. The impedance values of *CPEs* were calculated using the following equation[233]:

$$Z_{CPE}=\frac{1}{Y_0(j\omega)^n} \tag{5.1}$$

where Y_0 is the modulus, j is the imaginary unit, ω is the angular frequency, and n is the CPE exponent ($-1 \leq n \leq 1$).

The impedance magnitude at 10mHz was used to compare all tested samples and the results are reported in **Figure 5.3.** As indicated in **Figure 5.2 and Figure 5.3**, the CoCrMo samples polarized at 0.3V vs. Ag/AgCl in the solutions with different BSA protein concentrations exhibited a higher absolute impedance value at 10mHz or total resistance ($R_{Total}= R_s+R_{ads}+R_{oxide}$) than the ones polarized at 0.1V vs. Ag/AgCl and OCP conditions ($Z_{0.3V}> Z_{0.1V} > Z_{OCP}$). The increase of the R_{Total} by increasing the applied overpotential is due to the increased thickness and compactness of the passive layer, particularly impacting on the R_{oxide} [95, 232].

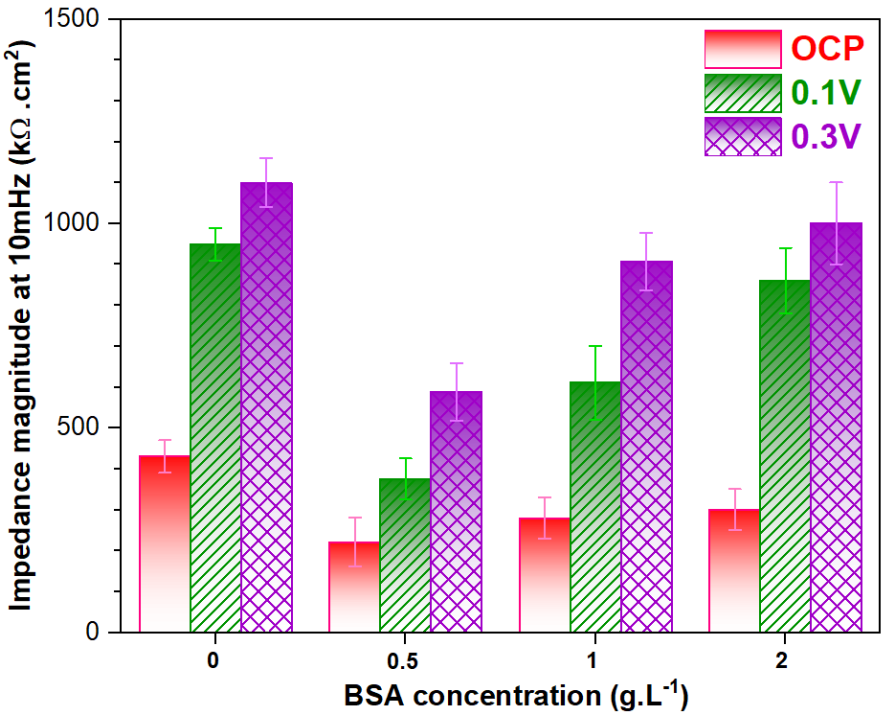

Figure 5.3. Impedance magnitude at 10 mHz $|Z_{10\ mHz}|$ for all CoCrMo specimens at different applied overpotentials and protein concentrations.

The CoCrMo alloy exposed to the blank PBS solution in all applied overpotential conditions (OCP, 0.1V, and 0.3V vs. Ag/AgCl) indicated a higher impedance than that in all BSA protein concentrations. This is attributed to the adsorption of phosphate species

(HPO_4^{-2} and $H_2PO_4^-$) on the oxide layer which block the active sites providing a higher shielding effect in comparison to the adsorption of protein molecules and/or proteins-metal complexes [2]. Likewise, the formation of metal phosphate complexes such as orthophosphate ($CrPO_4$) and metaphosphate ($Mo(PO_3)_3$) could occur, which have a direct effect on absolute impedance value [2]. The EEC elements values in **Table 5.2** show that the resistance of both adsorbed layer (R_{ads}) and oxide film (R_{oxide}) in the polarized samples decrease by the BSA protein. Nevertheless, by increasing the protein concentration from 0.5 to 2 $g.L^{-1}$ a slight increase is observed, which in turn, has a direct relationship on increasing the absolute impedance value at 10mHz (**Figure 5.3**). This could be due to the fact that when BSA is present at high concentration in the solution, strongly adsorbs on the metal or oxide surfaces by electrostatic or hydrophobicity (chemisorption through carboxylate/amino group) interactions and then inhibit the electrochemical reactions [70, 111]. On the other hand, when BSA present at low concentrations can act as a competitor to phosphates species to be adsorbed on the surface, weakening thus the protective effect of adsorbed phosphates species on the passive thin film [114].

5.2 Protein–oxide surface complex analysis by XPS

XPS surface analysis was used to reveal the influence of the different applied overpotential (OCP and 0.3 V vs. Ag/AgCl) on the chemical distribution and BSA protein adsorption on the complex oxide layer of CoCrMo alloy. To interpret the synergistic effect of applied overpotential and BSA protein on the metal ions releasing process, the individual high-resolution spectra of the main elements are shown in **Figure 5.4,** including Co2p, Cr2p, Mo3d, P2p, C1s, N1s, and O1s. Furthermore, the element distribution in the surface oxide layer of CoCrMo calculated from XPS results is shown in **Figure 5.4h.** As shown, the Co spectrum presents two metallic peaks including Co $2p_{3/2}$ and $2p_{1/2}$ at binding energies of

777.9 eV and 792.5 eV respectively, alongside one cobalt hydroxide ($Co(OH)_2$) peak at 781.5 eV [196]. Moreover, four separate Cr peaks were detected on the Cr spectrum including Cr_2O_3 $2p_{3/2}$ and $2p_{1/2}$ at binding energies of 576.4 ± 0.1 eV and 586.1± 0.1 eV, respectively, and the two Cr metallic peaks at binding energies of 573.5 ± 0.6 eV ($Cr^0 2p_{3/2}$) and 582.5± 0.6 eV ($Cr^0 2p_{1/2}$) [81]. The Mo spectrum exhibits the three main peaks including two Mo metal states at 227.8 eV (Mo $3d_{5/2}$) and 231.0 eV (Mo $3d_{3/2}$), one MoO_3 $3d_{5/2}$ oxide at binding energy 232.5 eV, respectively [69, 81, 196]. In the C spectrum, the main C peaks are originated from airborne carbon or contamination. However, it is known that the BSA protein is included in CO–NH peptides and in amino ($–NH_2$) and carboxyl (–COOH) groups [234].

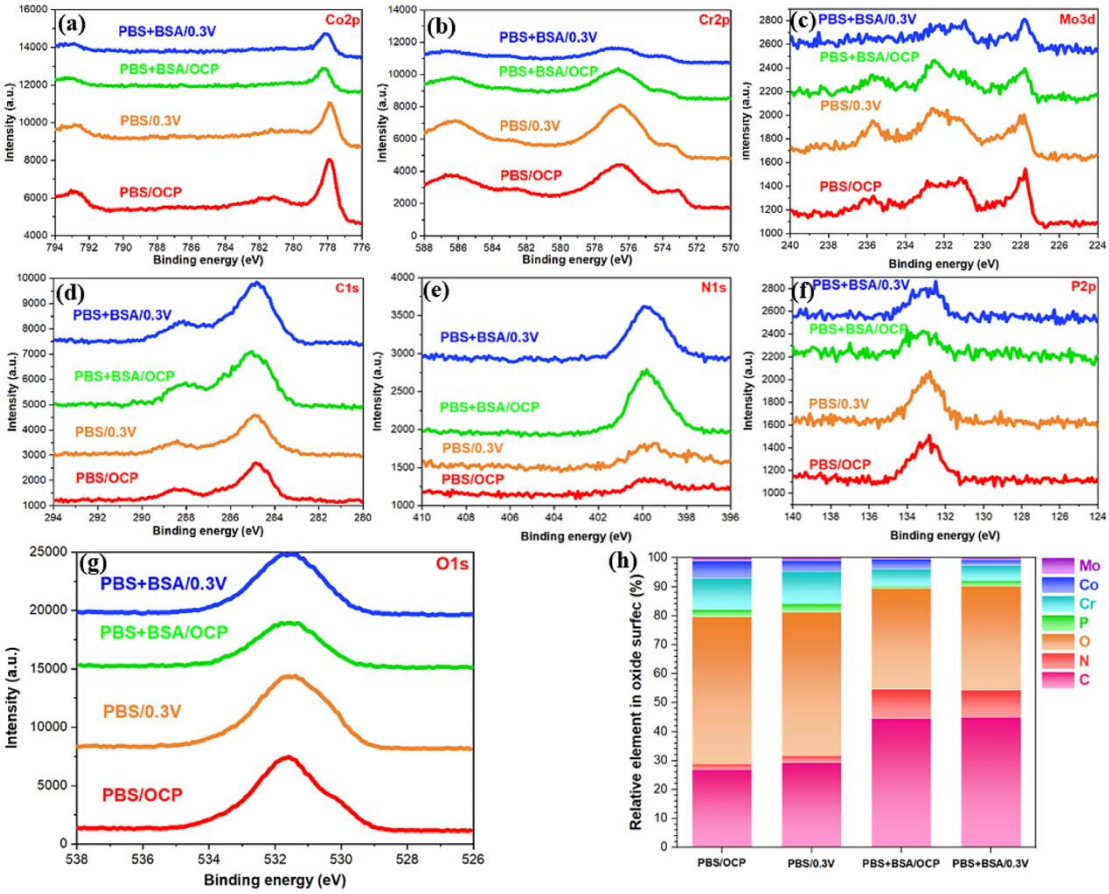

Figure 5.4. XPS spectra of (a) Co2p, (b) Cr2p, (c) Mo3d, (d) C1s, (e) N1s, (f) P2p, and (g) O 1s electron energy regions on CoCrMo alloy after exposing to PBS solution for 1 hour at OCP and 0.3 V vs. Ag/AgCl with and without 2 $g.L^{-1}$ BSA, (h) Relative element in surface oxide obtained from XPS spectra.

Thus, the C 1s peaks can be deconvoluted into three peaks at 284.8 ± 0.2 eV, 286.0 ± 0.1 eV, and 287.8 ± 0.2 eV, which are related to mainly C–C and C–H bonds, peptidic residues or C–O and C–N bonds, and N–C=O bonds, respectively [145, 212]. Therefore, we can conclude that the higher C and N intensity peaks on the CoCrMo surface layer in the BSA solution are attributed to BSA protein adsorption on the oxide surface. Likewise, the P spectrum peak (P 2p3) was distinguished between binding energies of 133.2 and 134.1 [232]. The O 1s spectrum indicated two dominant individual peaks that originated from oxide (O^{2-}) at 530.4 ± 0.5 eV and hydroxide or hydroxyl groups at 531.8 ± 0.3 eV arising from metal oxides and oxidized surface carbon [196]. As shown in **Figure 5.4**, only at OCP and 0.3V vs. Ag/AgCl conditions in PBS solution, the surface oxide layer of CoCrMo is highly enriched in Co, Cr, and Mo oxides. However, with the addition of BSA protein to PBS solution, the surface oxide layer shows the lower value distribution of Co, Cr, and Mo elements at both OCP and 0.3V vs. Ag/AgCl overpotential conditions. Likewise, the BSA protein environment significantly inhibited the formation and growing process of the complex oxide layer on CoCrMo, which is obviously accompanied by a declining O spectrum signal [232] (**Figure 5.4g and h**). Although, it is important to notice that the covered layer of BSA protein (approximate thickness layer 6-8 nm) on the oxide layer slightly affected the Co, Cr, and Mo content within the passive film (vide infra).

By adding the BSA protein in PBS solution, the P element distribution on the oxide layer of CoCrMo alloy remarkably decreased at both OCP and 0.3V vs. Ag/AgCl conditions, as shown in **Figure 5.4f and h**. Therefore, the BSA molecules with an inhibiting action can control the adsorption of phosphate species' on the complex oxide layer of CoCrMo. This is in accordance with a previous study, showing that BSA protein can remarkably slow down the ionic diffusion of calcium and phosphate species to adsorption and then to the formation

of the surface crystal [232, 235]. Indeed, by increasing the BSA concentration, a higher inhibition action can be detected on nuclei and crystal growth of calcium-phosphate species, affecting especially their morphology. In the PBS environment, HPO_4^{2-} and $H_2PO_4^-$ are dominant species that can easily adsorb onto CoO, Cr_2O_3, and MoO_3 oxides to form a thin phosphate-complex film [2]. Based on the P spectrum, P 2p3 at a binding energy of 133.4 eV originates from $CrPO_4$ [230]. The thin and rich layer of phosphate species formed in the PBS solution on the CoCrMo complex oxide offers better protection, hindering the release of Co, Cr, and Mo ions or blocking the mass transport compared to the PBS+BSA environment.

A precise correlation can be established between the lowest Co, Cr, and Mo elements amounts and the highest C and N contents on the surface oxide layer of CoCrMo when samples are polarized at 0.3V vs. Ag/AgCl in the PBS+BSA environment. Indeed, by applying the positive surface charge (0.3V vs. Ag/AgCl), BSA molecule with negative zeta potential [137] tend to adsorb strongly due to an electrostatic interaction with the complex oxide layer, which finally triggers higher protein adsorption (higher C and N amount). This has been confirmed by FE-SEM and AFM/SKPFM surface analyses which will be discussed in the next section. Finally, a schematic representation of the BSA protein impact on the metal ion releasing process in the CoCrMo surface at different overpotentials is shown in **Figure 5.5**.

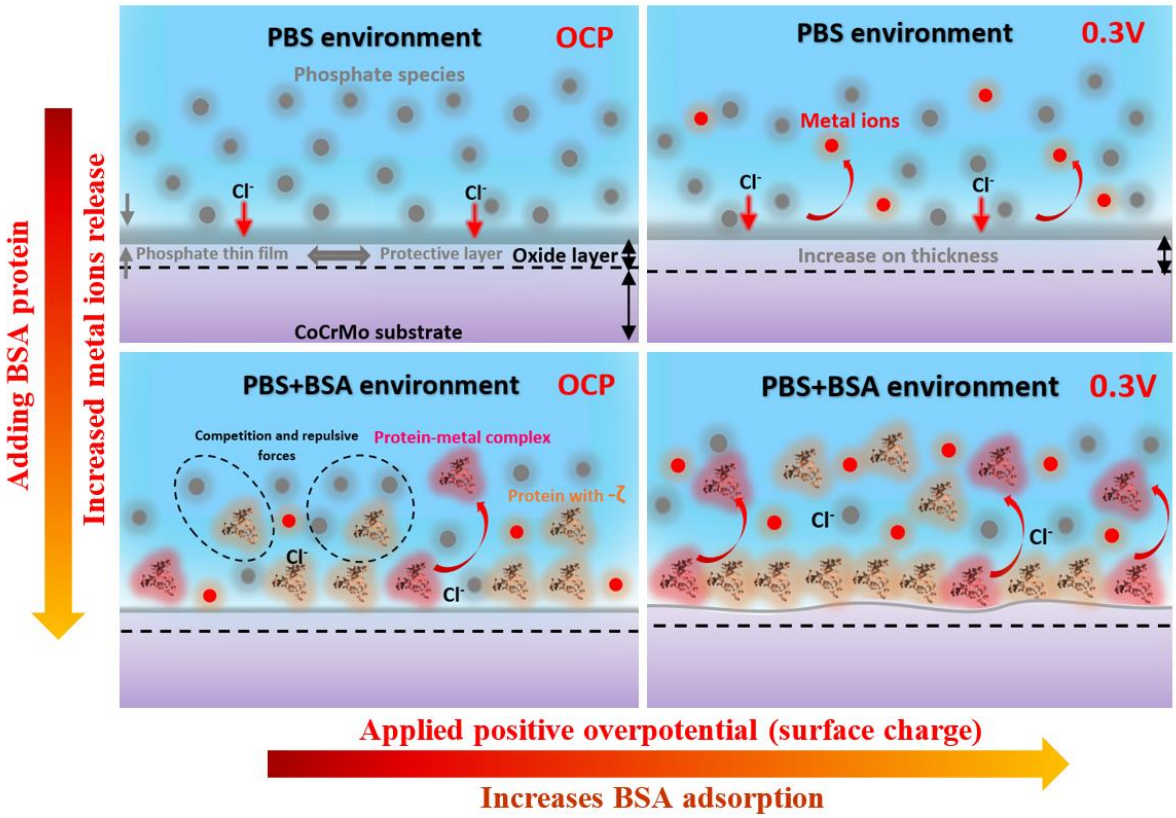

Figure 5.5. Schematic representation of the role of the applied overpotentials on the BSA protein adsorption and metal ion release on the surface of CoCrMo alloy.

5.3 Surface potential and protein conformational arrangements

The CoCrMo alloy with heterogenous oxide components during exposure to the simulated physiological environment can show different adsorption mechanisms of the various ions and protein species, protein conformations, and metal ion release processes. By applying the positive overpotential, the parameters mentioned above can change due to new evolutions on the surface oxide layer, including chemical compositions (as stated by XPS), nanometric roughness, and WFEs with occupied and unoccupied densities of state [193]. Figure 5.6 presents the AFM and SKPFM maps of the CoCrMo specimens immersed in PBS+ 0.5g.L^{-1} BSA for 1-hour at different applied overpotential, including OCP, 0.1 V, and

0.3 V vs. Ag/AgCl. In addition, AFM and SKPFM maps of a polished or fresh surface of CoCrMo alloy are reported in Figure 5.7 as reference.

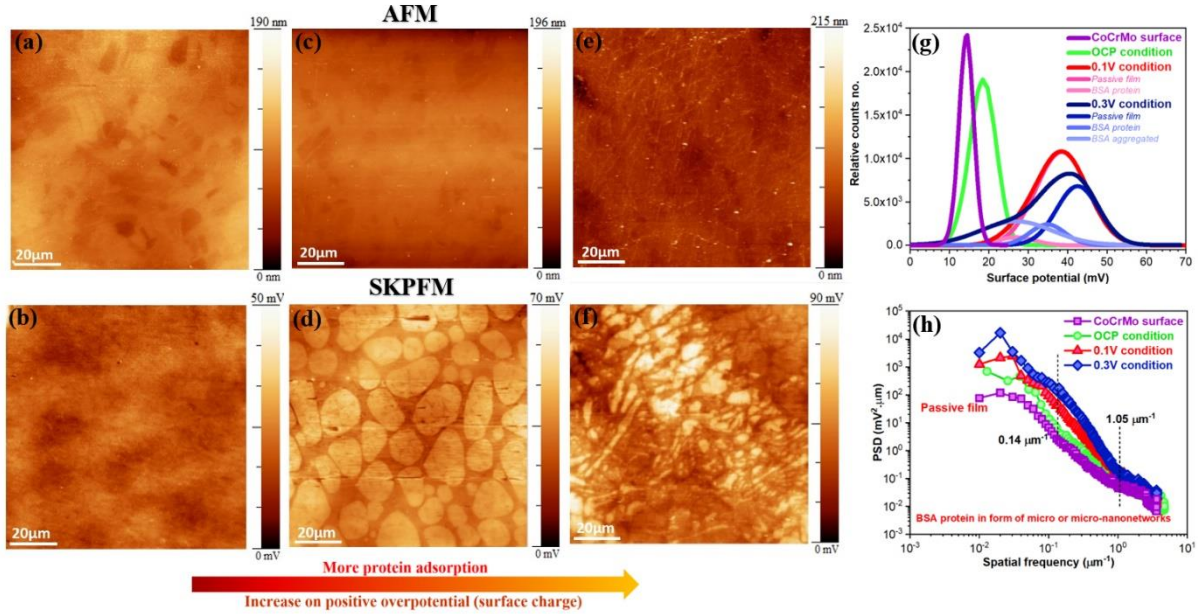

Figure 5.6. AFM (first row) and SKPFM (second row) images of CoCrMo alloy polarized for 1 hour at different overpotentials (a, b) OCP, (c, d) 0.1V vs. Ag/AgCl, (e, f) 0.3V vs. Ag/AgCl, in PBS+ 0.5g.L^{-1} BSA protein environment (g) The surface potential histogram and (h) PSD plots related to SKPFM maps.

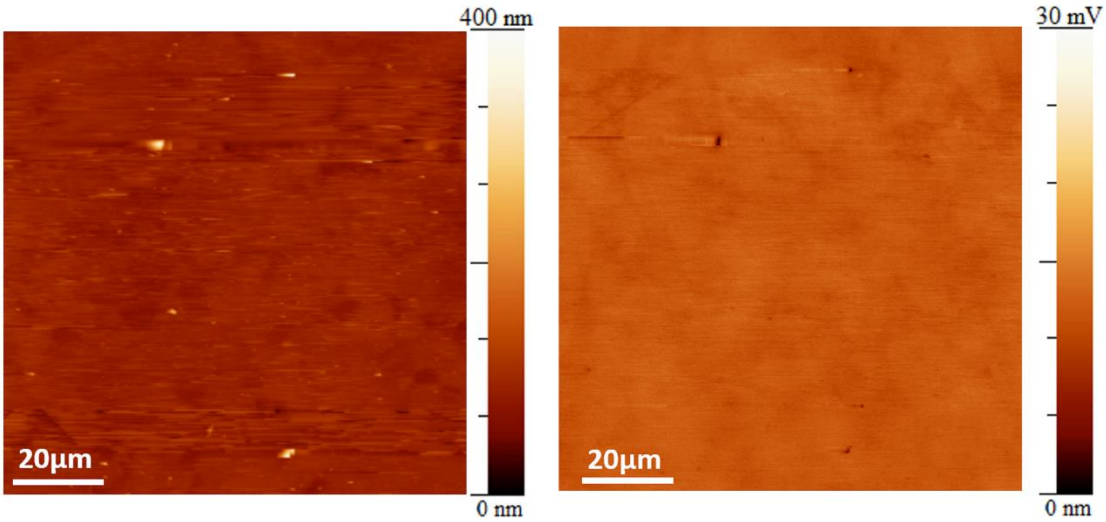

Figure 5.7. (a) AFM and (b) SKPFM images of the CoCrMo polished surface.

The AFM topography map of the sample at OCP (**Figure 5.6a**) obviously reflects the microstructure of the CoCrMo alloy where different grains and twins are visible (without protein evidence). However, by applying a positive overpotential at 0.1V and then at 0.3V vs. Ag/AgCl, the features of the alloy microstructure gradually disappeared and the BSA protein forming micro and nanonetworks on the CoCrMo surface gradually appear (**Figure 5.6c and 5e**). Since the SKPFM is very sensitive to the surface evolutions, the corresponding surface potential maps demonstrate a homogenous distribution of surface potential at OCP condition (**Figure 5.6b**). In contrast, at 0.1V and 0.3V vs. Ag/AgCl, a heterogeneous distribution of BSA protein with micro and nanonetworks is noticed in the surface potential images (**Figure 5.6d and 5f**). A closer look at the CoCrMo surface at OCP in the resolution of 1×1μm^2 and 500×500nm^2 (**Figure 5.8**) shows the uniform adsorption of BSA protein in the form of denatured and aggregated shape. Hence, we can figure out that the applied positive overpotential significantly affected the shape and amount of protein adsorption and in turn the surface potential distribution. Albumin protein is known as the strongest metal binder among human blood proteins and it is also present with a high concentration in the synovial fluid [117]. BSA molecule has an ellipsoidal shape with dimensions of 4 nm ×4 nm ×14nm [226].

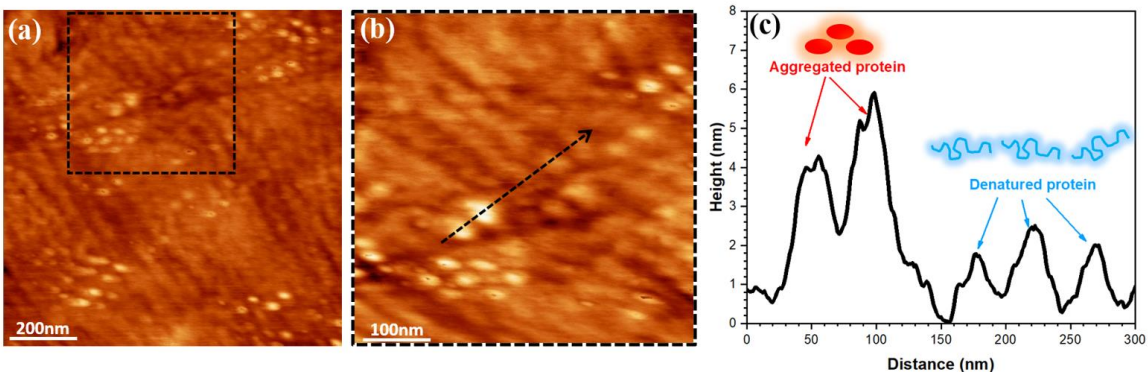

Figure 5.8. (a) Topography image of adsorbed BSA protein on CoCrMo alloy after 1 hour immersion in PBS+0.5g.L^{-1} BSA solution at OCP, 37 ºC, pH 7.4, and aerated conditions, (b) Higher magnification image of marked region in (a), (c) The topography line profile in (b).

The aggregated BSA proteins in **Figure 5.8c** present a height value in the range of 4 to 6 nm, while the height value in denatured proteins is close to 3 nm. Moreover, the wide value (or length) of both denatured and aggregated BSA proteins is about 20-40 nm which is longer than the real size of this molecular structure, as stated above . However, this deviation is due to the AFM tip-sample interaction, the correction being approximately close to ~10-20 nm, based on a prior study [164]. The conformational or structural pattern changes of a protein molecule from uniform to heterogenous or network morphology is related to the surface properties of the substrate and migratory parameters [236]. These properties could have a synergistic effect on protein adsorption mechanisms, including Langmuir-isotherm and cooperative adsorptions.

Regarding the surface potential image obtained at OCP (**Figure 5.6b**), we can suggest that BSA protein molecules' main adsorption mechanism on the oxide layer of CoCrMo alloy is based on the Langmuir-adsorption model. In this model, BSA proteins tend to fill the available unoccupied surface sites, with some fluctuations in the density of adsorbed proteins due to the oxide layer's heterogeneity. However, polarization at 0.1V and 0.3V vs. Ag/AgCl, change the BSA protein molecules' adsorption mechanism into cooperative adsorption which is dominated by the electrostatic force due to the positive surface charge more than the hydrophobic protein-surface interactions. According to the cooperative adsorption mechanism, the BSA protein molecules prefer to adsorb in the vicinity of other preabsorbed proteins, and then self-migration and lateral movements lead to a special morphology distribution [237]. This network or cluster morphology has been reported in a previous research using FE-SEM and AFM-peak force deformation maps on a CoCrMo alloy after -0.9 V cathodic polarization in PBS+15 $g.L^{-1}$ BSA media at 37 ºC [143].

As shown in surface potential maps in **Figure 5.6 (b, d, and f)**, the BSA protein regions exhibited a lower surface potential with respect to the substate. It must be noticed that the electrostatic surface potential on biologic molecules strongly depends on the isoelectric point (IEP) and on the surrounded surface charge of the substrate [223]. The IEP defines a degree of the relative proton-affinity of a molecule with opposite behaviour than electronegativity [238]. Moreover, the pH value indicates that the protein surface charge has a minimum value defined as IEP [137]. The IEP value of BSA protein based on theoretical calculation and experimental measurements is between 4.7 and 5.4 [110, 137]. At pH 7.4, BSA protein presents negative zeta potential and the positive surface charge on the oxide layer during anodic polarization leads to a strong adsorption of BSA protein with electrostatic attraction [137]. Therefore, 0.3V vs. Ag/AgCl polarization induces the high BSA protein adsorption with higher heterogeneity of both surface potential and conformational arrangement (**Figure 5.6e and 5.6f**). In fact, the degree of protein unfolding or denaturation at 0.3V vs. Ag/AgCl is higher than at 0.1V vs. Ag/AgCl and OCP condition.

The histograms of the surface potential in **Figure 5.6 g** under different conditions show one uniform peak on polished CoCrMo and OCP condition, a bimodal distribution when polarized at 0.1V (substrate and BSA protein) and a three modal one (substrate, BSA protein and aggregated BSA protein) when polarized at 0.3V vs. Ag/AgCl. The results of histogram deconvolution and the extracted Gaussian distribution parameters are reported in **Table 5.3.**

Table 6.3. Extracted Gaussian distribution parameters from the surface potential histograms in Figure 5.6 and Figure 5.9.

Region label	Constituents	Mean value of surface potential (μ,mV) and standard deviation (σ,mV)
CoCrMo alloy	Substrate	14.3±3.4
0.5g.L^{-1} BSA protein		
OCP	Substrate+BSA protein	18.4±4.7
0.1V	Substrate	38.5±10.1
	BSA protein	26.8±9.6
0.3V	Substrate	42.5±10.7
	BSA protein	34.8±8.7
	BSA aggregated	28.7±16.2
2 g.L^{-1} BSA protein		
OCP	Substrate	37.5±6.4
	BSA protein	30.7±12.5
0.1V	Substrate	53.1±30.4
	BSA protein	37.3±26.5
0.3V	Substrate	56.3±16.4
	BSA protein	42.1±15.1

As shown, by changing the condition from the fresh CoCrMo alloy (AFM and SKPFM presented in Figure 5.7) to OCP and finally to polarized at 0.3V vs. Ag/AgCl, the total surface potential increases or all peaks are shifted towards higher values due to a synergistic effect of oxide film growing and BSA protein adsorption. Moreover, from the SKPFM maps it is possible to observe changes on the morphology of the adsorbed protein clusters. When the specimens are polarized at 0.1 V vs. Ag/AgCl, the protein forms large clusters in the range of 2 to 15 μm (Figure 5.6(d)), while when polarized at 0.3V vs. Ag/AgCl, a fibrillar morphology with more narrow clusters of about 200 nm to 4 μm(Figure 5.6(f)). Based on the PSD profiles of surface potential images in Figure 5.6h, in the total range of spatial frequencies, all features on CoCrMo (substrate and BSA protein) at 0.3V vs. Ag/AgCl polarization show the higher PSD value (mV^2. μm) with respect to the other conditions. In addition, the higher spatial frequencies in PSD profiles in Figure 5.6h display the presence of BSA protein regions with the lowest surface potential. Moreover, the lower

spatial frequencies with the highest PSD magnitude attributed the substrate (oxide layer) with the highest surface potential, that are higher when the specimens are polarized at 0.3V vs. Ag/AgCl compared to the ones of the specimens in OCP [88].

By changing the BSA protein concentration from 0.5 to 2 g.L^{-1} in PBS solution, a higher surface covering of BSA protein on CoCrMo surface can be distinguished with fibrillar morphology at OCP and micro and nano-networks at both 0.1V and 0.3V vs. Ag/AgCl polarizations, as shown in **Figure 5.9**. As mentioned above, only the surface potential map at OCP+0.5 g.L^{-1} (**Figure 5.6b**) BSA presented the uniform surface potential distribution, without any evidence of BSA protein, whereas in 2 g.L^{-1} BSA, a fibrillar morphology of BSA protein is detectable at OCP conditions (**Figure 5.9b**).

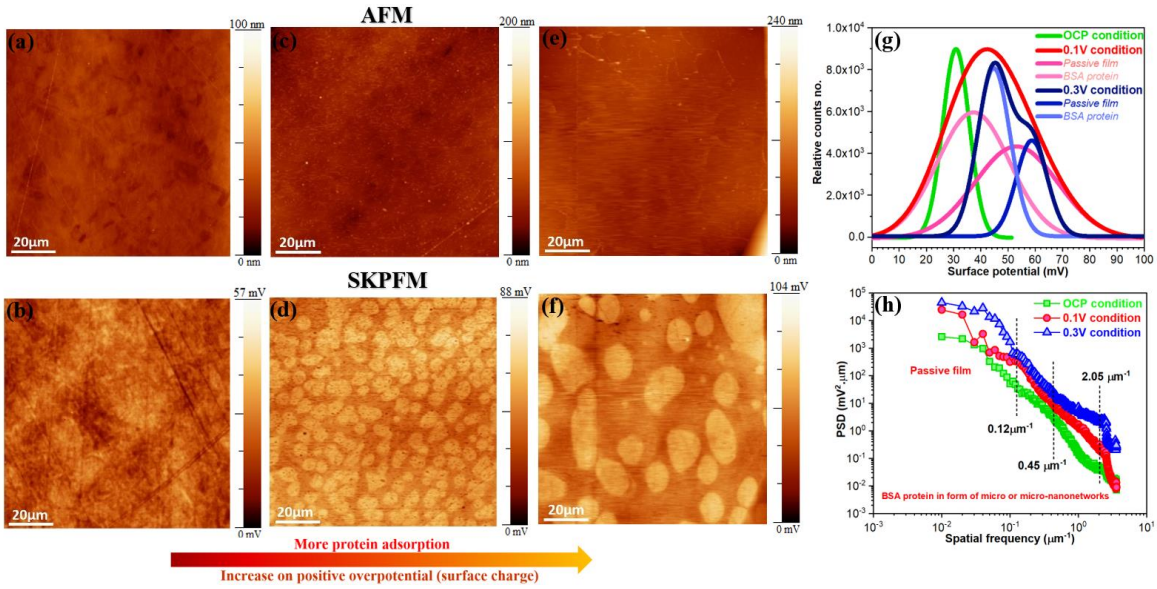

Figure 5.9. AFM (first row) and SKPFM (second row) images of CoCrMo alloy polarized for 1 hour at different overpotentials (a, b) OCP, (c, d) 0.1V vs. Ag/AgCl, (e, f) 0.3V vs. Ag/AgCl, in PBS+ 2g.L^{-1} BSA protein environment (g) The surface potential histogram and (h) PSD plots related to SKPFM maps.

The noticeable point is the large domain size or micro-networks of BSA protein in the range values of 5-20 µm at 0.3V vs. Ag/AgCl condition. According to the histogram of surface potential maps in **Figure 5.9g and Table 5.3**, 2 $g.L^{-1}$ BSA protein significantly increased the total surface potential of surface features, including protein regions and substrate respect to 0.5 $g.L^{-1}$ BSA protein in all applied overpotential conditions. The PSD curves of CoCrMo samples (**Figure 5.9h**) at all overpotential conditions reveal the different slopes (2.05, 0.45, and 0.12 μm^{-1}), and the heterogeneous distribution of PSD magnitude in all spatial frequencies; this is consistent with higher standard deviation based on histogram analysis (**Table 5.3**).

5.4 Degradation phenomena on the complex oxide layer

As reported in the previous sections, both BSA protein concentration and applied overpotential values controlled significantly the type and amount of BSA adsorption, its morphology, the elemental distribution on CoCrMo oxide layer, and the metal ion releasing process. To visualize the synergistic effect of both BSA protein concentration and applied overpotential on the degradation process of CoCrMo, the alloy surface has been observed by FE-SEM and representative micrographs are shown in **Figure 5.10**. A meaningful correlation can be established between the surface potential maps (**Figure 5.6 and Figure 5.9**) and FE-SEM images based on the BSA protein morphology distribution. However, different regions with an intense localized corrosion attack are clearly visible on the polarized at 0.3V vs. Ag/AgCl samples in 0.5$g.L^{-1}$ BSA. These attacks are mainly localized at protein/substrate interface (**Figure 5.10g**), which is consistent with our prior work [232].

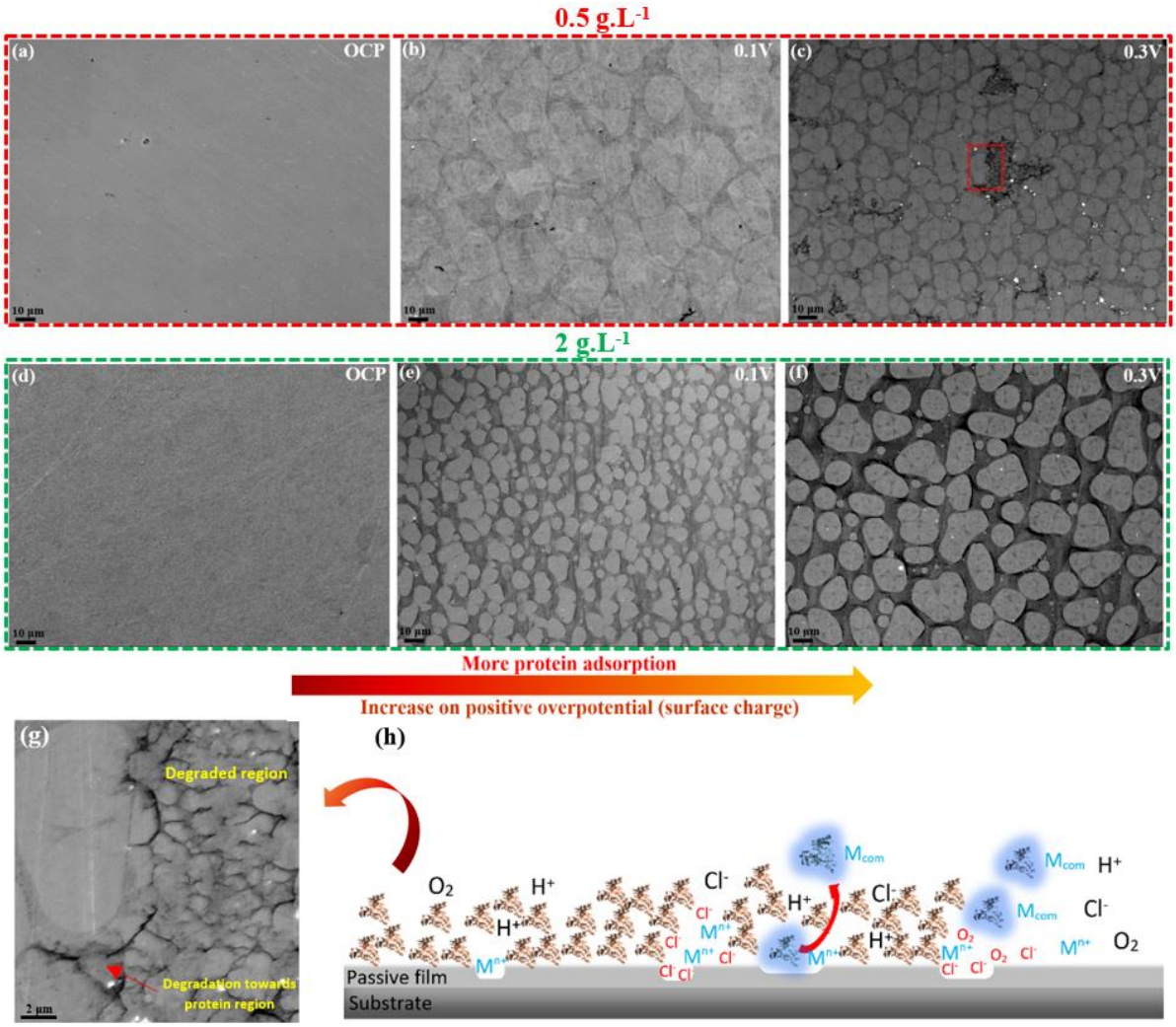

Figure 5.10. SEM images of CoCrMo alloy after 1 hour polarization at OCP, 0.1V, and 0.3V vs. Ag/AgCl, 37Cº, pH 7.4, and aerated conditions in PBS plus (a, b, and c) 0.5g.L^{-1} and (d, e, and f) 2g.L^{-1} BSA solution; (g) SEM image of the marked region in (c), (h) a schematic representation for degradation process on CoCrMo alloy in the presence of BSA protein with different mechanisms after passing time (short or long-term).

As presented, the CoCrMo surface layer is intensively degraded (passive film breakdown), especially close to the BSA protein region. Nevertheless, these types of corrosion attacks were not observed in 2g.L^{-1} BSA solution polarized at 0.3V vs. Ag/AgCl condition. This could be attributed to the fact that the higher protein concentrations can strongly hinder the initiation of localized corrosion attacks, as stated in the previous sections by electrochemical measurements. The different degradation mechanisms of metallic

implants during interaction with various protein molecules such as human serum albumin (HSA), fibronectin, and BSA proteins can be described thus as follows: (1) shielding effect or inhibiting the cathodic reaction, (2) attraction of counterions, (3) a complexation process with the various oxide constituents, and (4) the Vroman effect, as presented schematically in **Figure 5.10h**.

It should consider that the physiological environment and the surface chemistry directly influence the degradation mechanism with time. The BSA protein initially decreases the release of metal ions due to the shielding effect by inhibiting the passive film's cathodic reactions. However, depending on the time (milliseconds to years), it can trigger an increase in the metal ion release process [111, 117]. On the other hand, the interface between BSA covered regions and un-covered regions are attractive sites for the counterions (such as Cl^-). Thus, in these regions, counterions can penetrate within the adsorbed protein layer, reach the passive film region, and eventually promote localized corrosion as shown in **Figure 5.10c**. The metal–protein conjugates due to the BSA protein complexation with metal or metal–oxide species on passive films is another reason for the degradation process of metallic implants [61]. Moreover, the Vroman effect intensifies the metallic implants' corrosion in the protein environment due to the detachment of metal–protein bounds under the control of the exchange process of adsorbed proteins.

5.5 Partial Conclusions

In this chapter, the influence of both BSA protein concentrations and applied overpotentials on protein adsorption mechanism, distribution/morphology, and surface potential on CoCrMo alloy has been reported. To this aim AFM, SKPFM, XPS, FE-SEM, and electrochemical measurements have been used.

An improved resistance to the metal ion release was detected on CoCrMo alloy in high BSA protein ($2g.L^{-1}$) solution with respect to lower concentration ($0.5g.L^{-1}$), whereas the highest resistance was achieved in only PBS media. XPS analyses results of CoCrMo specimens that exposed to PBS+BSA environment in both OCP and under anodic polarization indicated an increase on the intensity of C and N peaks (due to BSA protein adsorption) and a decrease of the Co, Cr, and Mo content within the passive film. The FE-SEM and SKPFM images showed that by changing the overpotential on the CoCrMo surface from OCP to 0.1V and finally 0.3V vs. Ag/AgCl for 1-hour polarization, the morphology of adsorbed BSA protein changed from a uniform protein layer to large micro-nanonetworks with a heterogeneous distribution. Moreover, a higher protein covering based on electrostatic interaction was disclosed on the CoCrMo surface by increasing both surface overpotential and protein concentration from OCP up to 0.3V vs. Ag/AgCl and from $0.5g.L^{-1}$ up to $2g.L^{-1}$, respectively. SKPFM images showed a lower surface potential distribution in covered BSA protein regions. The histogram and power spectral density analyses of the surface potential maps presented an increase on total surface potential distribution on the CoCrMo surface by increasing the BSA protein concentration from $0.5g.L^{-1}$ to $2g.L^{-1}$. Finally, FE-SEM micrographs indicated the initiation of localized corrosion attacks at the BSA protein/substrate interface due to the adsorption of counterions and the surface potential difference.

Chapter 6: Degradation mechanisms of magnetic microrobotic platforms in protein media

In this chapter an insight into the degradation mechanisms of magnetic microrobots consisting of NiCo micropillars (NiCo-MPs), both uncoated and Au-coated, in simulated human body fluids is given, using both electrochemical and surface analysis techniques for the first time. NiCo alloys have been widely used for small-scale robotic designs due to their superior mechanical properties as well as their optimal soft magnetic features. Because of their potential cytotoxicity, these alloys are usually coated with Au. However, the presence of defects on small-scale structures can accelerate their corrosion by galvanic coupling. To understand the role of defects in the degradation of microscale structures, the corrosion resistance and corrosion mechanisms, both uncoated and Au-coated magnetic microstructures were tested after short and long-time immersion in phosphate-buffered saline (PBS) solution with and without the addition of bovine serum albumin (BSA) protein. A combination of large-scale electrochemical techniques, field-emission scanning electron microscopy (FE-SEM), atomic force microscopy (AFM), and scanning Kelvin probe force microscopy (SKPFM), were used to understand the degradation of the swimmers. The long-term degradation was also evaluated through inductively coupled plasma-atomic emission spectrometry (ICP-AES) analyses of the media, where the MPs were immersed for varying periods of time.

6.1 Microstructure and electronic properties of NiCo and NiCo/Au-MPs

SEM micrographs of a NiCo and NiCo/Au single micropillar, together with elementary EDXS maps, are reported in **Figure 6.1a and 6.1b**, while lower magnification micrographs showing different MPs are reported in **Figure 6.2**. The surface of NiCo-MPs was very smooth (**Figure 6.1a**), and the elementary EDXS maps reveal a uniform distribution of Ni and Co. The semi-quantitative EDXS analyses demonstrate that the pillars are composed of 78% Ni and 22% Co (at%). The presence of O reveals that the surface of the pillar is covered by the native passive film (NiO and CoO oxides [239]). NiCo/Au-MPs present a rougher surface and the elementary EDXS maps shows that the O signal differences disappear (no contrast between the MPs and the glassy carbon plate), while Ni and Co can still be detected as the thickness of the Au layer is very low.

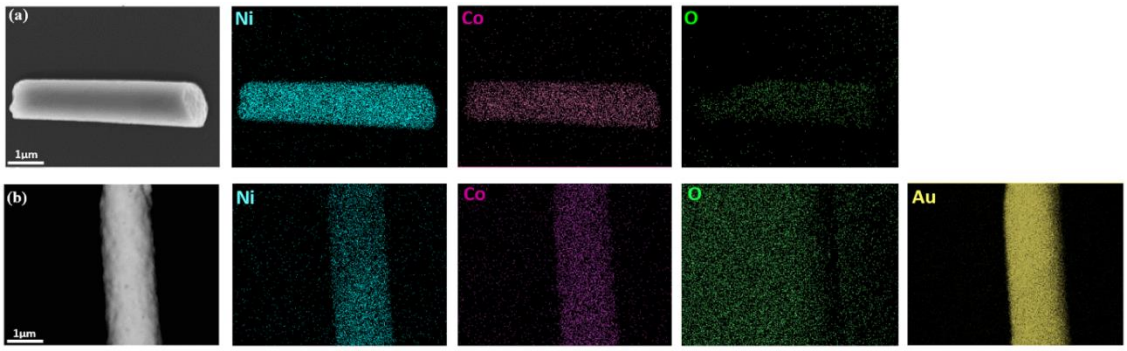

Figure 6.1. SEM and EDXS elemental maps of (a) NiCo and (b) NiCo/Au-MPs.

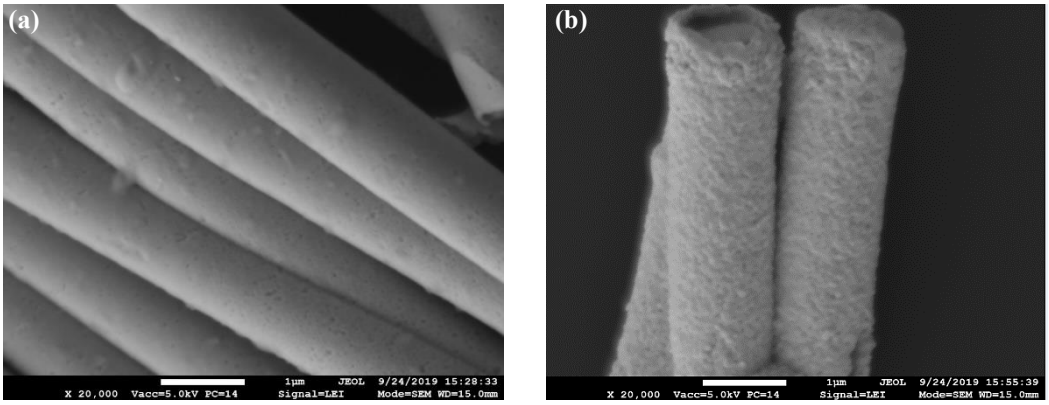

Figure 6.2. low magnification FESEM micrographs of (a) NiCo and (b) NiCo/Au MPs.

From a closer look at the top surface of NiCo-MP in **Figure 6.3a**, we can discern some nano-pores and nano-defects mainly due to hydrogen evolution during the deposition and to the intrinsic roughness of the membrane walls. The surface roughness of the NiCo micropillars, measured by AFM, is about 10-30nm. The high magnification image of NiCo/Au-MP in **Figure 6.3b** shows that the Au coating presents a cauliflower morphology. However, the Au layer does not uniformly cover all the observed micropillars. Uncovered regions, micro, and nano-sized defects are present, as indicated in **Figures 6.3c, 6.3d,** and **6.3e.**

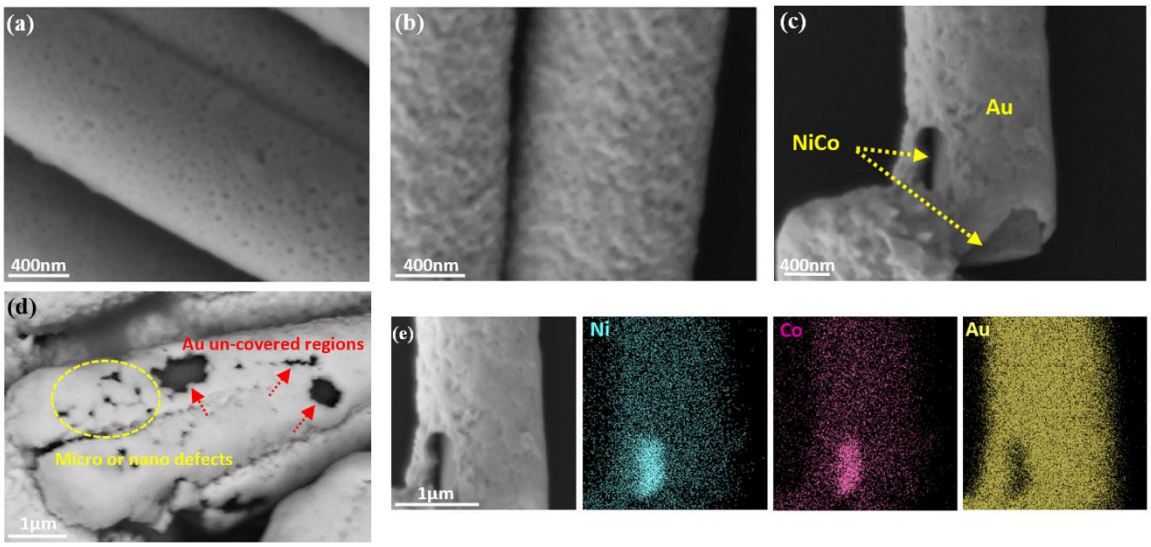

Figure 6.3. High magnification images of (a) NiCo and (b, c, d) NiCo/Au-MPs, (e) SEM and EDXS elemental maps of an NiCo/Au-MP, which exhibits the presence of an NiCo/Au un-covered interface.

We can distinguish two main types: areas where part of the coating has been detached (**Figure 6.3c and 6.3e**), perhaps during the post-deposition and/or cleaning procedure, and uncovered areas (**Figure 6.3d**) where the deposit has not grown over the NiCo substrate. In both cases, the NiCo substrate is in direct contact with the environment. These types of defects are very common on low thickness immersion deposits and are linked to the deposition process. Such defects are negligible over large-scale objects but in the case of the

micro-sized pillars, these defects can significantly accelerate the metal ions' release from the substrate due to galvanic coupling (*vide infra*). AFM topographic images of NiCo and NiCo/Au-MPs are shown in **Figure 6.4a and b**, respectively, together with the height line profiles (**Figure 6.4c**). The NiCo/Au-MPs has slightly increased height and diameter values than the NiCo-MP. Based on the difference in height measured by AFM (about 0.18µm on measurements made by FE-SEM in the places where the Au coating has been detached (**Figure 6.3c**)), the thickness of the Au layer can be estimated at about 90-100 nm.

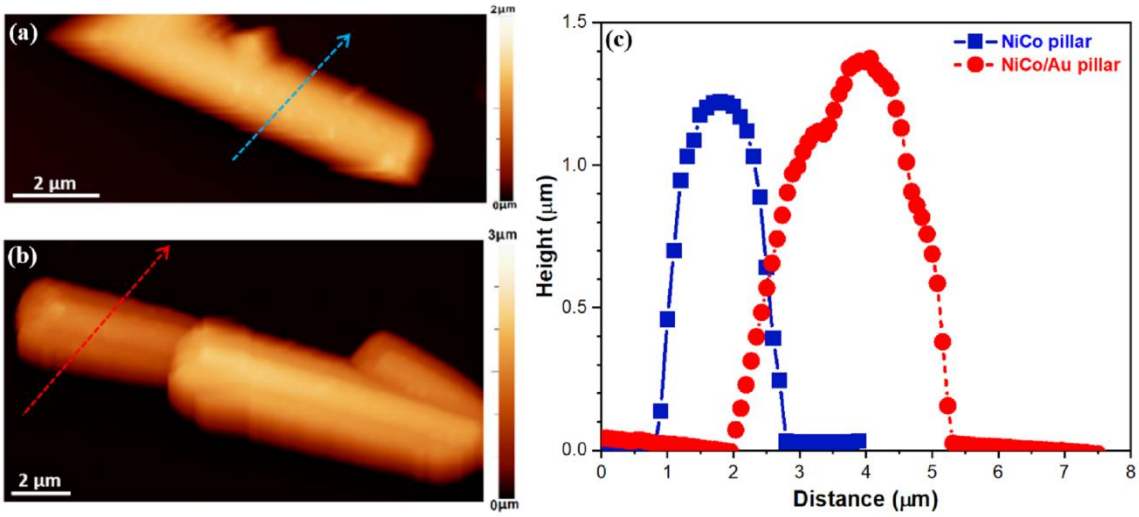

Figure 6.4. Topography images of (a) NiCo and (b) NiCo/Au-MPs on glassy carbon, (c) Topography line profiles of both NiCo and NiCo/Au-MPs.

In order to verify if the defects present on the Au layer can accelerate the NiCo dissolution due to galvanic coupling, surface Volta potential maps were obtained on areas presenting defects. Indeed, the differences in the surface electronic properties of materials can be used as a criterion to determine the surface conductivity, which plays a significant role on the electrochemical interactions [240, 241]. According to previous studies [242-244], materials with high surface Volta potential or *WFE* values present higher stability of valance electrons or a more stable electronic state, inhibiting valence electrons from participating in

electrochemical reactions. Consequently, materials with higher surface Volta potential behave with higher electrochemical nobility [88, 245, 246].

High magnification topographic and Volta potential maps of a NiCo/Au-MP on a defected zone as the one indicated by the yellow circle in **Figure 6.3d** are reported in **Figure 6.5a and 6.5b,** respectively, together with the corresponding line profiles in **Figure 6.5c**. Comparing the topographic and the Volta potential maps, it is clear that in the areas with low height, the NiCo is uncovered (lower Volta potential). The potential difference between the Au coating and the uncovered NiCo substrate is approximately 120 mV (**Figure 6.5c**). As this difference appears quite high considering the passive layer of NiCo, the same measurements were also performed on large scale specimens produced by partially covering with an Au thin layer electroformed NiCo alloy with the same composition as the NiCo-MP. The results are presented in **Figure 6.6**. The measured Volta potential difference in this case was about 150 mV, confirming the results obtained on the MP surface. It is hence fair to predict a marked galvanic coupling between the Au coating and the NiCo substrate with a localization of the cathodic reactions on the Au and the anodic reactions on the NiCo.

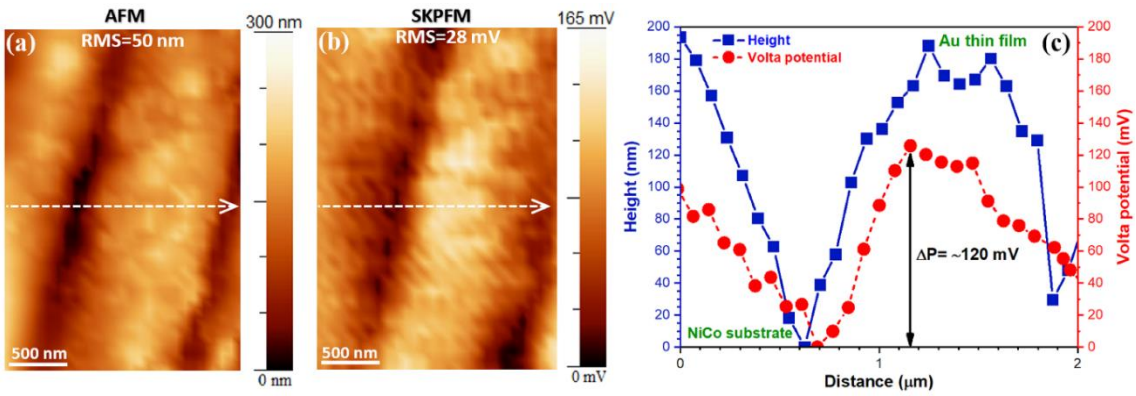

Figure 6.5. (a) Topography and (b) surface Volta potential images of NiCo/Au-MP with small porosities,(d) Topography and surface Volta potential line profiles from (a and b).

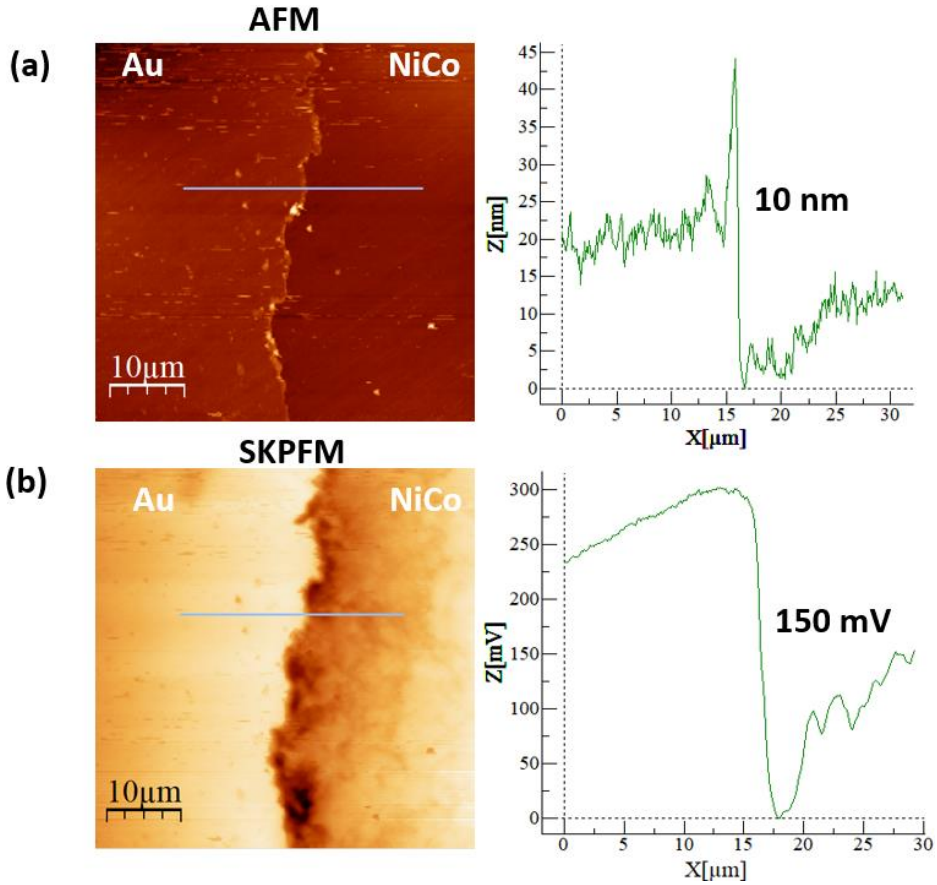

Figure 6.6. (a) Topography and (b) surface Volta potential maps of electroformed-NiCo surface half-coated by Au thin film, together with corresponding topography and Volta potential lines.

6.2 Electrochemical study of NiCo and NiCo/Au-MPs in PBS with and without BSA

Figure 6.7a shows the OCP curves of NiCo and NiCo/Au-MP samples immersed in the PBS solution with and without 1 $g.L^{-1}$ BSA protein for 1 hour at 25 ºC in aerated conditions, together with the curves corresponding to ITO glass and ITO glass+Nafion® samples immersed in PBS and used as references. The OCP curves of all samples showed a relatively fast stabilization. The measurements performed in PBS electrolyte showed that the deposition of a Nafion® layer onto the ITO glass leads to a marked ennoblement of the

potential (~390 mV vs. Ag/AgCl against -68 mV vs. Ag/AgCl of the bare ITO glass). This is due to the hydrophobic behaviour of Nafion®, which acts as a barrier to diffuse the oxygen, water molecules, and other ions to the conductive surface of ITO glass [247].

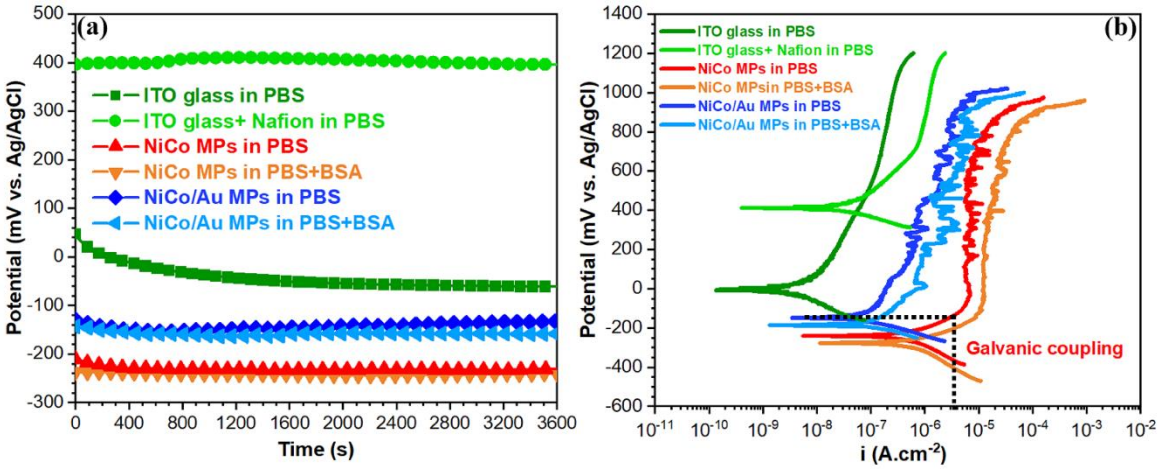

Figure 6.7. (a) OCP and (b) PDP curves of NiCo and NiCo/Au-MPs coated with Nafion® on ITO glass in PBS and PBS+BSA solutions at 25 °C and pH 7.4.

Instead, the dispersion of both MPs types in the conductive polymer led to a decrease in the OCP, and was more evident in the samples prepared with NiCo MPs. It should also be noted that, due to the nature of the analysed specimens, the measured potential is always a mixed potential of all the components of the specimens. Considering the preparation procedure, we can assume that the same content of MPs is present on the specimens' surface in all cases, and thus a comparison between the different types of MPs can be done quite safely. The deposition of an Au layer on the NiCo-MPs led, as anticipated, to an increase of the OCP of about 105 mV vs Ag/AgCl. Nevertheless, the registered value is much lower than Au's potential in the same environment. As the ITO glass+Nafion® presents a higher OCP, the difference can be solely attributed to the defects present on the Au coating, which expose the underlying NiCo to the electrolyte. The addition of BSA protein into the PBS

solution led to a decrease in the OCP in both cases by inhibiting the cathodic reactions and covering the active sites on the heterogeneous surface by chemisorbed bonds [70, 232].

Figure 6.7b shows representative PDP curves of NiCo and NiCo/Au-MP in PBS and PBS+1 $g.L^{-1}$BSA solutions at 25ºC and aerated conditions, together with the curves corresponding to ITO glass and ITO glass+Nafion® in PBS solution. The corrosion potential (E_{corr}) and the corrosion current density (i_{corr}), extrapolated using the Tafel equations, and together with the passive current density (i_{pass}), are reported in Table 6.1.

Table 6.1. i_{corr}, E_{corr} and i_{pass} data obtained from PDP curves in Figure 7.8b.

Samples	i_{corr} ($A.cm^{-2}$)	E_{corr} (mV vs. Ag/AgCl)	i_{pass} ($A.cm^{-2}$)
ITO glass in PBS	$1\pm0.2\times10^{-8}$	-10±2	
ITO glass+Nafion® in PBS	$6\pm0.5\times10^{-8}$	415±50	
NiCo MPs in PBS	$5\pm0.5\times10^{-7}$	-240±15	$7\pm0.3\times10^{-6}$
NiCo MPs in PBS+BSA	$7\pm1\times10^{-7}$	-285±25	$1.2\pm0.2\times10^{-5}$
NiCo/Au MPs in PBS	$6\pm0.6\times10^{-8}$	-140±20	$4\pm0.5\times10^{-7}$
NiCo/Au MPs in PBS+BSA	$9\pm0.8\times10^{-8}$	-180±20	$9\pm0.5\times10^{-7}$

The E_{corr} values of the different analysed specimens, extrapolated from the PDP curves, confirmed the galvanic series observed in the OCP measurements. Prior discussing on the current density evolution of the different PDP curves, it is fair to point out that, considering the different materials that compose the samples, under anodic polarization in the investigated range of potential, on the surface of the ITO glass (stable conductive oxide in a wide potential range), the Nafion® (conductive polymer, stable in a wide potential range) and the Au (inert metal in a wide potential range and environments), the anodic reactions can only concern the oxidation of the components present in the electrolyte, such as phosphate species (HPO_4^{2-} and $H_2PO_4^-$) [2]. Based on this statement, the anodic branches of the PDP curves of both ITO glass and ITO glass+Nafion® show a progressive increase

of the anodic current by increasing the potential due to the oxidation of the components in the solution. The higher the driving force, the higher the oxidation rate of the species in the solution and hence the measured current.

The optimization of the sample production method containing the two types of MPs substantiates the fact that the metallic area exposed to the electrolyte is essentially the same. By considering that up to 400mV vs. Ag/AgCl (E_{corr} of the ITO glass+Nafion®) the Nafion® is under cathodic polarization, the anodic currents of the samples containing MPs are attributable only to the reactions that take place on the exposed metallic surfaces. Due to the active-passive behaviour of the NiCo alloy, the anodic reactions can be mainly attributed to its oxidation under anodic polarization. The anodic branch of the PDP curves of the sample containing the NiCo-MPs showed a passive behaviour of up to around 200mV vs. Ag/AgCl. Nevertheless, above a value of around 200mV vs. Ag/AgCl, fluctuations of the anodic current suggest triggering of metastable pits [248]. Moreover, the NiCo-MPs anodic current was higher in comparison to all other types of samples due to the contribution of the metal oxidation. The anodic current measured on the specimens containing NiCo/Au-MPs is the sum of two distinguished phenomena: the oxidation of the species present in the electrolyte on the surface of the Au coating, and the oxidation of the NiCo alloy through the pores or defects of the Au coating [75, 248], similar to the measured E_{corr} being a mixed potential of the Au and the uncovered NiCo substrate through the coating defects.

In order to confirm this hypothesis, PDP curves were obtained, under the same conditions, on a pure Au sheet and on a 1mm thick electroformed NiCo alloy with a chemical composition similar to that of the MPs, as shown in **Figure 6.8**. The obtained curves have a similar form to those obtained on the MPs, but the E_{corr} of the pure Au is much higher than that of the NiCo/Au-MPs, confirming the hypothesis of measuring a mixed potential.

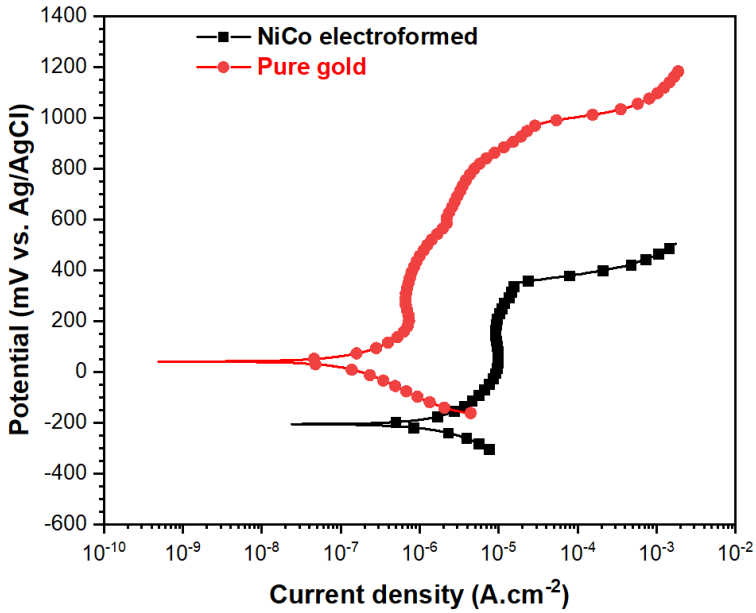

Figure 6.8. PDP curves of pure Au sheet and 1mm thick electroformed Ni-Co alloy at 25 °C and pH 7.4.

Considering that the area of the Au coating largely exceeds the exposed area of NiCo substrate, it is fair to assume that in free corrosion conditions, the galvanic potential ($E_{galvanic(NiCo)/(Au)}$) due to the coupling between different materials is near to the E_{corr} of the NiCo/Au-MPs sample revealed by the PDP measurements. Therefore, the exposed NiCo substrate will be oxidized with a corrosion rate that corresponds to the anodic current of the NiCo-MPs at the same potential (vertical dashed line in **Figure 6.7b**), and higher than the corrosion current density of the NiCo-MPs. Nevertheless, relying only on the PDP measurements, it is difficult to establish if this relatively small over-potential ($E_{galv(NiCo)/(Au)} \approx E_{corr\ NiCo/Au} - E_{corr\ NiCo} \approx 100$ mV) caused by the galvanic coupling is high enough to trigger the localized corrosion of the NiCo alloy and a significant release of Ni and Co ions to the electrolyte. The fluctuations of the anodic current above 200 mV vs. Ag/AgCl for the NiCo/Au-MPs also indicates the formation of metastable pits [75].

The addition of BSA in the PBS electrolyte leads to a decrease in the E_{corr} and an increase of both i_{corr} and anodic current density of both samples containing MPs, suggesting

an increase in the aggressiveness of the electrolyte. The BSA, known as the strongest metal binder among human blood proteins with a high concentration in synovial fluid [249], is a strong promoter of metal ions release for a wide range of biomedical alloys [2, 122, 144, 230]. Although it takes time to express its aggressiveness, as it interacts slowly following different mechanisms (adsorption, protein-metal binding, metal ion detachment [249]), in our experiments, the effect on the decrease of the corrosion resistance is already demonstrated after 1 hour of immersion by the PDPs. The shape of the PDP curves showed a similar effect on the addition of BSA proteins for both types of MPs, but the difference in the anodic currents was much more evident with the NiCo-MPs with respect to the NiCo/Au-MPs. Assuming that the Au is essentially inert to the presence of BSA in the solution, with the exception of the possible adsorption phenomena, the higher the NiCo surface exposed to the electrolyte, the higher the oxidation phenomena and hence the anodic current measured during the potential scan.

As a consequence, the SKPFM analyses and the PDP measurements revealed the galvanic coupling between the Au and the uncovered areas of the NiCo substrate through the Au layer defects. However, it does not give an indication of the long-term corrosion in simulated body fluids and the metal ions release. To this aim, long-term immersion tests were considered necessary and will be discussed in the next section.

6.3 Long-term immersion tests

6.3.1 EIS measurements

As reported in the experimental section, ITO glass with a Nafion® coating containing either NiCo or NiCo/Au-MPs were immersed in either PBS or PBS+BSA solutions for 30

days, then OCP and EIS measurements were performed at regular intervals. Bode magnitude and phase diagrams of the EIS measurements can be found in **Figure 6.9.** From the Bode plots, it is clear that the NiCo-MPs present a lower impedance than the NiCo/Au-MPs immediately after immersion and that the addition of BSA in the electrolyte lowers the impedance of both systems. However, by increasing the immersion time, an increase of the impedance magnitude was observed in all tested systems, along with a flattening of the phase diagram, indicating a transition from a single time constant system to a two-time constant system. This increase was much more evident in BSA-containing electrolytes, which presented the lowest values immediately after immersion. Assuming that Nafion® has a similar effect on all studied systems, the main contribution to the charge transfer resistance corresponds to the metal elements (Ni, Co and Au). For this reason, the impedance modulus at 10mHz was used to compare all specimens' performances. The results together with the OCP values monitored during the 30 days of immersion are reported in **Figures 6.10a and 6.10b**.

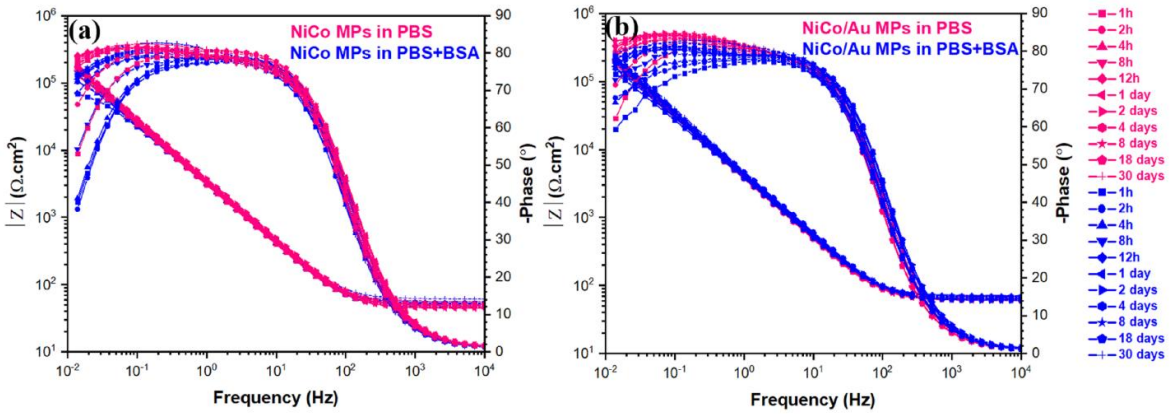

Figure 6.9. Bode phase, and absolute impedance of (a) NiCo and and (b) NiCo/Au-MPs for long-term immersion in PBS and PBS+BSA at 25 °C and pH 7.4.

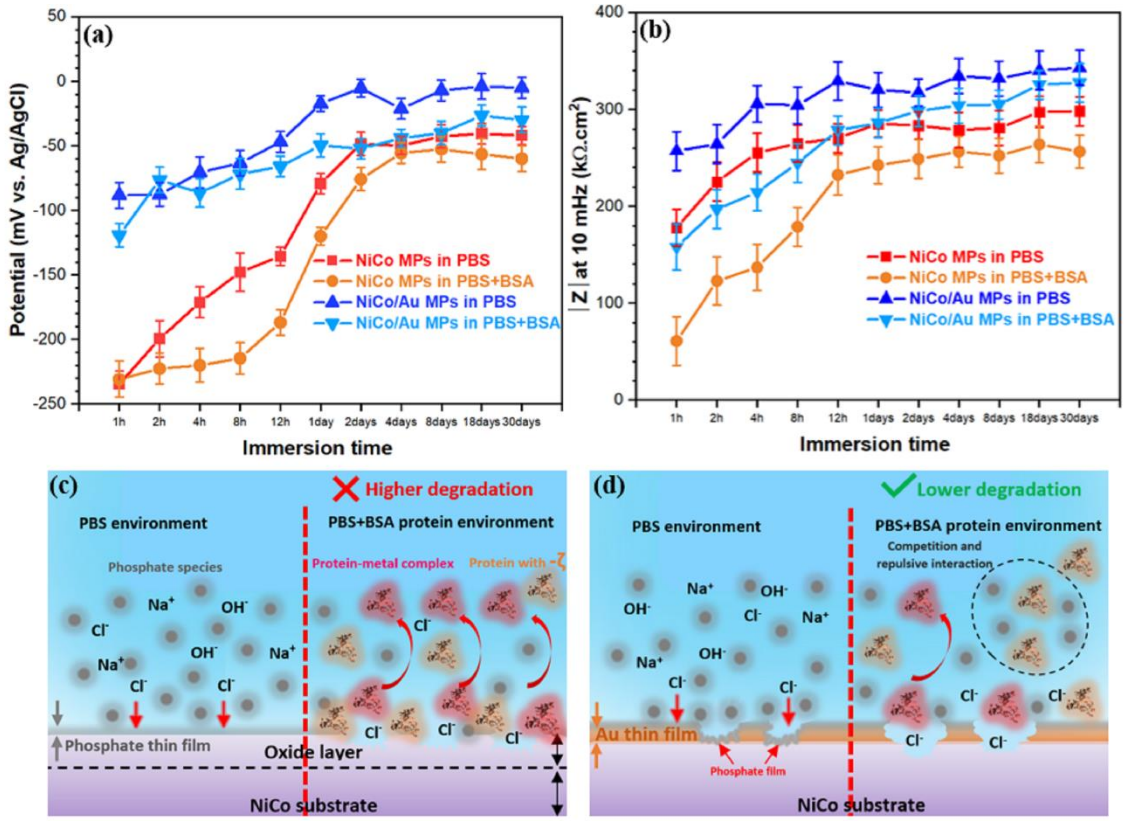

Figure 6.10. (a) OCP and (b) |Z| at 10mHz during long-term immersion tests of NiCo and NiCo/Au-MPs immersed in PBS and PBS+BSA at 25 °C and pH 7.4, Schematic presentation of phosphate species adsorption and BSA protein interaction and its role on metal ion releasing on (c) NiCo and (d) NiCo/Au-MPs in the different environments.

From Figure 6.10a, it is evident that all samples showed a marked increase of the OCP during the first two days of immersion and then reach a virtual steady state. The NiCo/Au-MPs consistently showed higher potential values in both environments due to the presence of an Au coated layer. The increase of the OCP was, however, more evident on the NiCo-MPs, so that all samples reached values of the same order of magnitude after long immersion times, always maintaining the order NiCo/Au in PBS>NiCo/Au in PBS+BSA>NiCo in PBS>NiCo in PBS+BSA. The same behaviour was observed by the impedance modulus at 10mHz (Figure 6.10b). In addition, an increase was shown during the first two days followed by a stabilization of up to 30 days. The presence of the Au layer

increased the impedance values, while the addition of the BSA protein led to lower values. This was due to the formation of a thin film of phosphates on the MPs' surface after the immersion in the electrolyte [232], which offered a barrier protection for the metal ion release. After longer immersion times, the stability of the phosphates film increased, and both OCP and $|Z|$ values reached a steady state. The BSA protein was also adsorbed on the specimens' surface as it exhibited a negative ζ potential at pH 7.4 [232]. The BSA molecules competed with the phosphate species to form the adsorbed film, lowering both the OCP and $|Z|$ values. The adsorbed layers provided a shielding effect to the aggressive Cl^- attack and the corrosion of the NiCo/Au-MPs due to galvanic coupling. However, the BSA proteins can exhibit detrimental effects towards the NiCo passive film. Indeed, BSA interacts with the metal atoms in the oxide layer and, if the metal-protein bonds are stronger than the metal-oxygen bonds, leads to the detachment of protein-metal complexes, increasing the metal ions release and hence the degradation phenomena [249]. The process is schematically represented in **Figure 6.10c and 6.10d.**

6.3.2 Metal ions release and morphological evaluation of the degradation

To clarify if the adsorbed phosphates layer slows down the metal ion release due to the presence of Cl^- or galvanic coupling between the NiCo substrate and the Au coating, and to confirm that the presence of BSA enhances the corrosion of the MPs, NiCo and NiCo/Au-MPs non-supported on Nafion®, were immersed in PBS and PBS+BSA solutions for a total time of 140 days. Both solutions and immersed MPs were characterized at different intervals to evaluate the degradation.

The Ni and Co ions concentration in the two solutions after 7, 56, and 140 days of immersion, as measured by ICP-AES, are reported in **Figures 6.11a and 6.11b**. The results

demonstrated that higher amounts of both Ni and Co were released from the NiCo-MPs with respect to the NiCo/Au-MPs, proving the protection offered by the Au, despite the defects. The Ni release was around three times higher in comparison to the Co, respecting the alloy chemical composition. Finally, the addition of BSA protein increased the electrolyte's aggressiveness due to the protein-metal bonding effect, leading to an increase of around 200% and 80% (after 140 days of immersion) in the Ni ion release for the NiCo and NiCo/Au-MPs, respectively. This difference is mainly due to the different NiCo exposed areas in the two cases and the fact that the detrimental effect of BSA concerns only the NiCo.

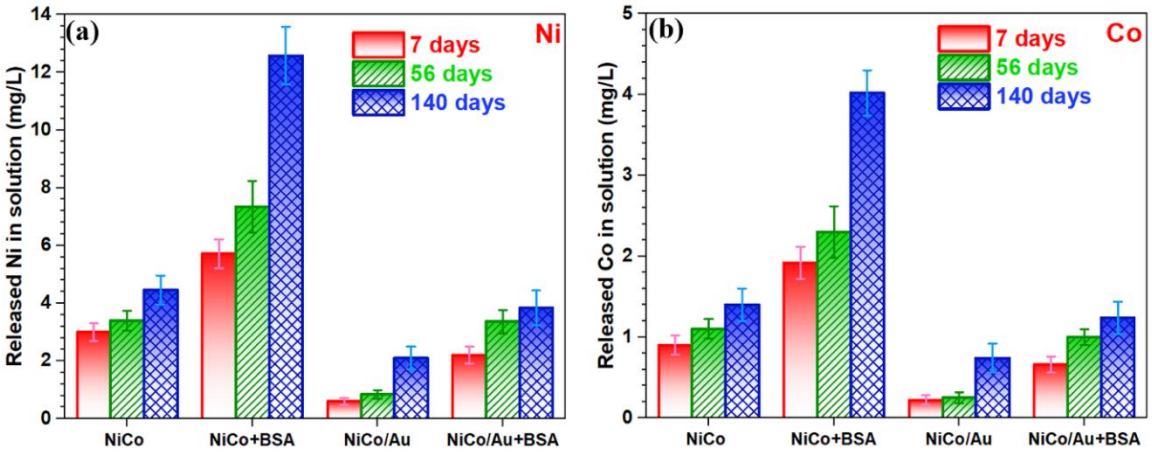

Figure 6.11. The total amounts of (a) Ni and (b) Co released from NiCo and NiCo/Au-MPs after immersion for 7, 56 and 140 days in PBS and PBS+BSA at 25 °C and with a pH 7.4.

FE-SEM images of both types of MPs after 56 days of immersion in both PBS and PBS+BSA solutions are reported in **Figure 6.12** and **Figure 6.13**. The surface of the NiCo-MPs immersed in PBS solution was relatively uniform and was covered by a thick oxide-phosphates layer, where small dimension pits (red arrows **Figure 6.12b**) could be attributed to the Cl^- attack. The corrosion attack in the presence of BSA was much more intense and led to a severely grooved surface (**Figures 6.12c and 6.12d**). This is due to the protein-metal bonding and the detachment of the protein-metal complexes [249, 250]. The immersion of

NiCo/Au-MPs in PBS solution for 56 days led to an intense corrosive attack on the NiCo through the Au layer defects (Figure 6.13a), proving the galvanic coupling. The dissolution of the NiCo through the defects was striking compared to that of NiCo-MPs immersed in the same solution (Figures 6.12a and 6.12b).

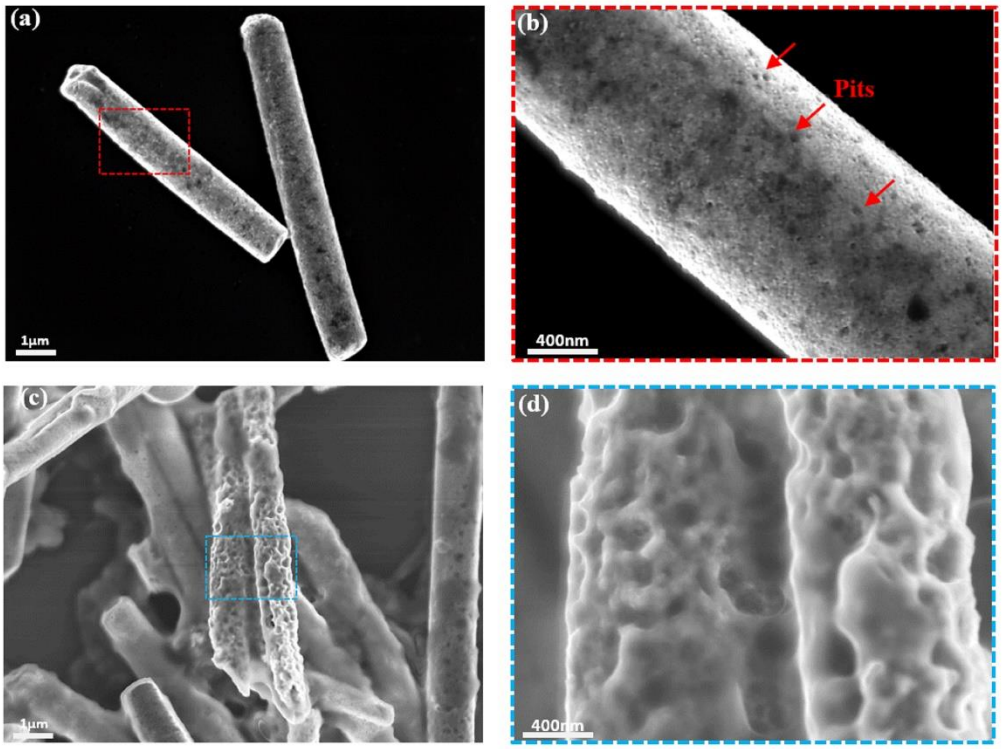

Figure 6.12. Low and high magnification FE-SEM images of NiCo-MPs after immersion in (a and b) PBS and (c and d) PBS+BSA solution for 56 days.

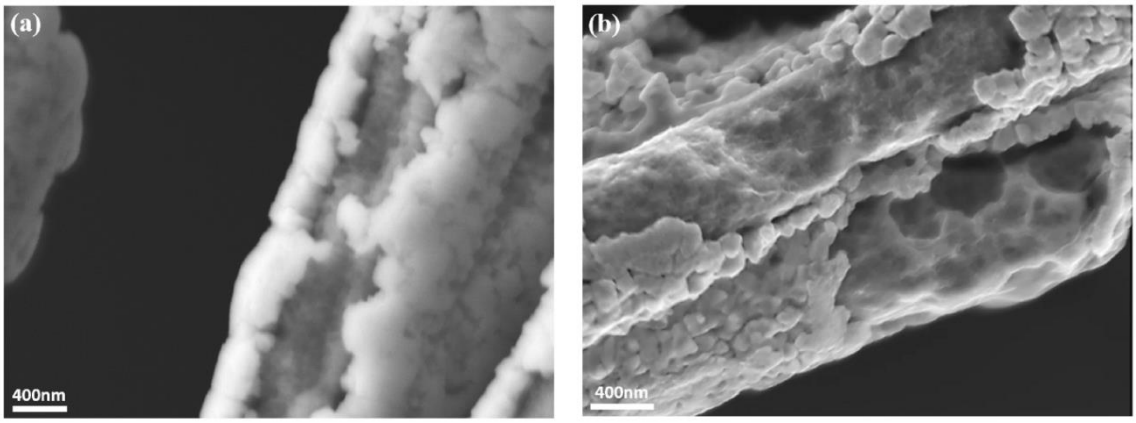

Figure 6.13. FE-SEM images of NiCo/Au-MPs after immersion in (a) PBS and (b) PBS+BSA solutions for 56 days.

The presence of BSA protein intensified the corrosion attack and the uncovered NiCo surface appeared highly degraded, with the same morphology observed in the NiCo-MPs immersed in the same environment. The effect of the BSA protein also had an indirect impact on the morphology of the Au coating. The more intensive dissolution of the NiCo, not only as a result of the defects but also from the Au grain-boundaries, makes the Au layer appear as not continuous but as isolated grains (**Figure 6.13b**).

However, the dissolution of NiCo through the Au defects was not as severe as expected from the galvanic coupling, observed by the PDP curves and SKPFM measurements. After long-immersion times, the formation of a phosphates film, as observed in the increase of both OCP and $|Z|$, could attenuate this difference. To confirm this hypothesis, AFM and SKPFM maps from a defective area of NiCo/Au-MP immersed for 56 days in PBS+BSA solution were obtained and reported in **Figure 6.14**, together with the Volta potential line profile. In the SKPFM map, the potential difference between the NiCo and the Au is clearly visible (**Figure 6.14b**), but as demonstrated by the line profile, this difference is around 40mV, which is much lower than that observed before immersion (~120mV, **Figure 6.5c**). The SKPFM analyses proved that during long-immersion times, the potential difference between NiCo and Au, a driving force for the galvanic coupling, is significantly decreased due to the formation of the phosphates-oxides film [230] on the whole surface, as presented in **Figure 6.15**.

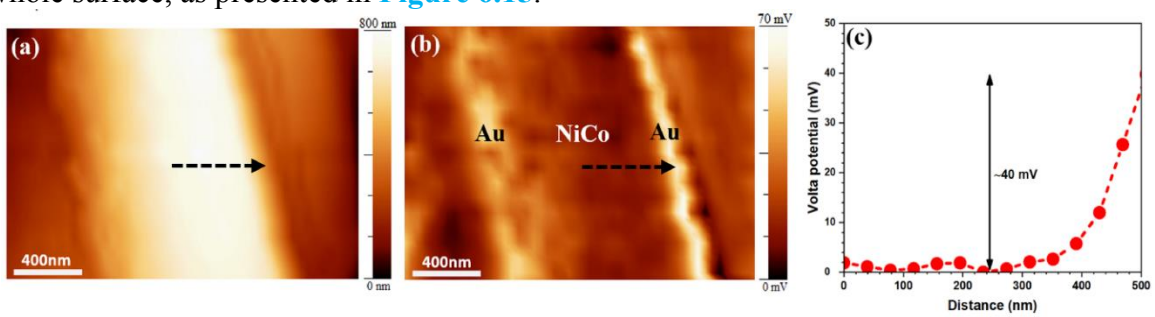

Figure 6.14. (a) AFM and (b) SKPFM images of NiCo/Au-MPs after immersion in PBS+BSA solution for 56 days, (c) surface Volta potential line profile in (b).

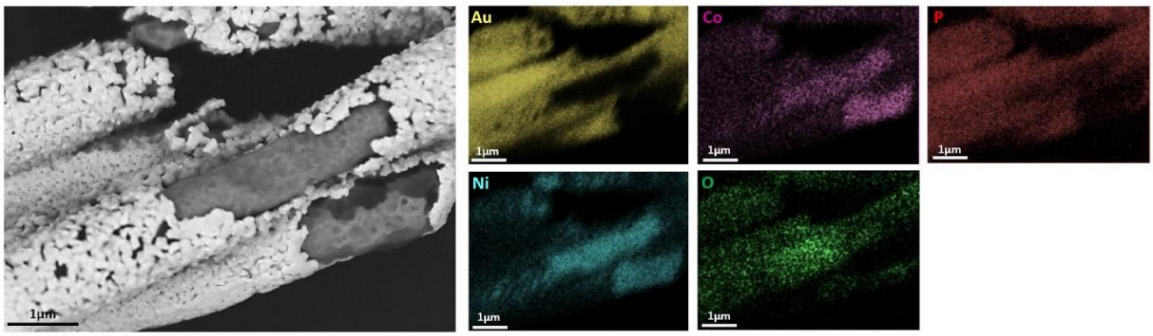

Figure 6.15. (a) The SEM and EDXS elemental maps of NiCo/Au-MPs after immersion in PBS+BSA solution for 56 days.

6.4 Partial Conclusions

In this chapter, the degradation of NiCo-micropillars (NiCo-MPs), both uncoated and Au-coated, during immersion in phosphate-buffered solution containing bovine serum albumin was studied, for the first time, using a combination of electrochemical and surface analyses techniques. The resultant NiCo-MPs present a smooth surface and a uniform chemical composition. However, the Au coating on the NiCo/Au-MPs did not uniformly cover the MPs surface, presenting uncovered regions and micro- and nano-sized defects. SKPFM and potentiodynamic polarization measurements revealed the galvanic coupling between the Au and the uncovered areas of the NiCo substrate as a result of the Au layer defects, which could increase the dissolution rate of the NiCo. Conversely, long-term EIS measurements showed that a phosphate-based layer was formed on the MPs' surface, which became more stable after longer immersion times, providing a shielding effect from the aggressive Cl^- attack and the corrosion of the NiCo/Au-MPs due to galvanic coupling. The formation of the phosphates film after long immersion times decreased the Volta potential difference between the Au layer and the NiCo substrate exposed by the defects as demonstrated by the SKPFM measurements. Metal ions release measurements performed

for 140 days demonstrated that, despite its defects, the Au coating provided certain protection, lowering the Ni and Co release in the electrolyte of around 60% and 50%, respectively.

The presence of BSA increased the aggressiveness of the electrolyte, as demonstrated by all electrochemical measurements. The BSA molecules competed with the phosphate species to form the adsorbed film on the MPs' surface and increased the corrosion rate due to the protein-metal bonding and the detachment of the protein-metal complexes. This was confirmed by the metal ions' release measurements and the observation of the corrosion attack morphology on the different pillars after long-term immersion tests. BSA's presence led to an increase in the Ni release of about 200% and 80% after 140 days of immersion for the NiCo and NiCo/Au-MPs, respectively. The NiCo corroded surface, in BSA's presence, was much rougher in both cases when compared to immersion in only PBS solution. In addition, the Au coating offered certain protection, despite the defects, due to the fact that the BSA detrimental effect only had an impact on the NiCo, and the exposed area through the defects was significantly lower in comparison with the non-coated NiCo-MPs.

Chapter 7: apoferritin protein impact on the electrochemical behaviour and degradation process of $CoFe_2O_4$ and $CoFe_2O_4$-$BiFeO_3$ nanoparticles

Magnetic nanoparticles such as cobalt ferrite ($CoFe_2O_4$, CFO) and surface functionalized cobalt ferrite-bismuth ferrite ($BiFeO_3$, BFO) core-shell ($BiFeO_3$, CFO@BFO) are widely used for biomedical applications due to unique magnetic properties, chemical stability, and surface electrocatalyst activity. Nevertheless, in the human body they can undergo degradation mainly when in contact with metal storage proteins. In this chapter, the electrochemical behavior and electronic properties of CFO and CFO@BFO magnetic nanoparticles during interaction with apoferritin protein in a phosphate-buffered saline (PBS) solution were investigated by a multi-technique characterization. Both localized (SKPFM) and large-scale electrochemical techniques (OCP, electrochemical polarization measurements and Mott-Schottky analysis) were used to this aim.

7.1 Surface potential of nanoparticles oxide surface by SKPFM

To determine the local surface potential as a criterion for electronic properties (e.g. WFE) of both CFO and CFO@BFO nanoparticles, AFM/SKPFM surface analysis was used. Topography and surface potential maps together with the line-profiles are reported in **Figure 7.1**.

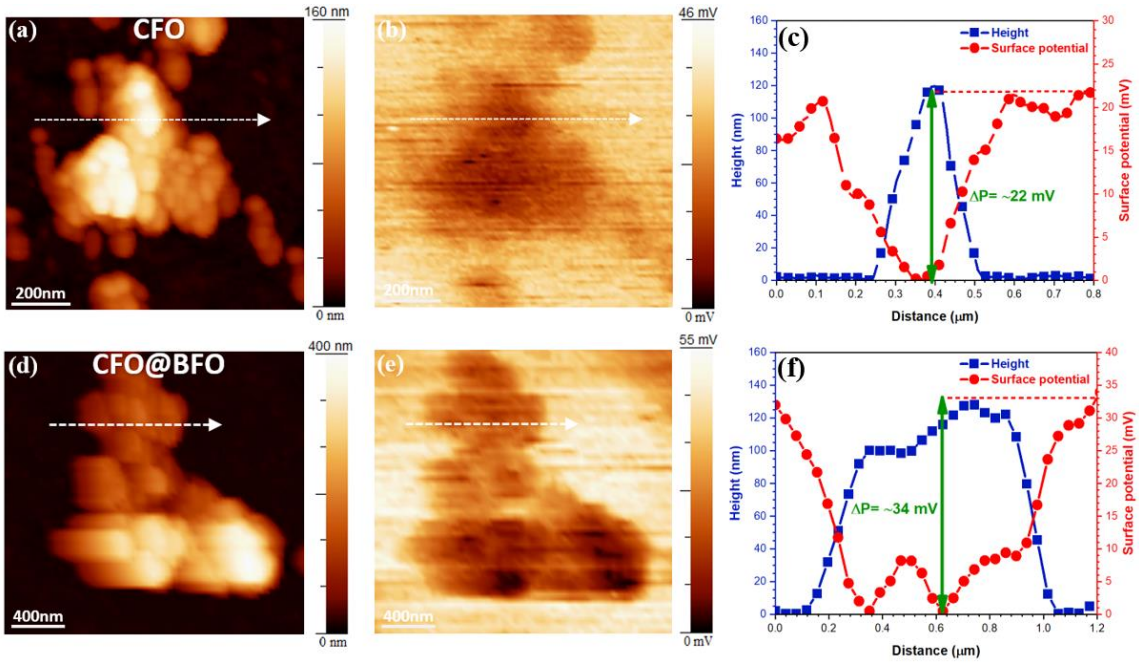

Figure 7.1. Topography, surface potential, and line profiles of (a, b, and c) CFO and (b, c, and d) CFO@BFO nanoparticles distributed on glassy carbon at 25 °C and RH 28%, respectively.

In order to interpret the results, we need to consider that in non-conducting materials such as dielectrics, semiconductors, and ferroelectrics, the additional Columbic forces during scanning by SKPFM are related to static surface charge and polarizability [251]. The total electrostatic forces or signal detected by SKPFM analysis can be divided into two separate parts including Columbic forces due to static charges and multipoles, capacitance forces due to surface potential, and dielectric properties. According to the surface potential scale bar on both SKPFM images of CFO and CFO@BFO nanoparticles, we can figure out that both CFO and CFO@BFO nanoparticles exhibit a lower response to electrostatic interactions (lower surface potential) between tip and oxide surface of nanoparticles in

comparison with glassy carbon matrix with higher surface potential (bright region). The presence of the low local surface potential or weak electrostatic interactions on both nanoparticles is attributed to a combination of the local changes on polarization and bandgap energy values alongside the density of states distribution [252]. Previous studies on polyaniline nanoparticles on silicon (Si) substrate by SKPFM showed that polyaniline nanoparticles have a lower surface potential than Si substrate and the doping process with etchant solution can increase difference value in the WFE of nanoparticles [253].

Considering that both samples have a similar roughness as demonstrated by **Figure. 71. (a and b) and (d and e)**, the surface potential line profiles clearly show that the CFO@BFO nanoparticles exhibit a higher surface potential difference (ΔP= ~34 mV) with respect to glassy carbon than the CFO nanoparticles with value ΔP= ~22 mV (**Figure 7.1c and 7.1f**). Accordingly, the CFO nanoparticles exhibit a higher semiconductive behaviour in comparison to the CFO@BFO in agreement with other research group's results on current sensing AFM [254]. In addition, since the bandgap energy value of CFO@BFO core-shell nanoparticles (E_g = ~1.8 eV) is higher than that of CFO nanoparticles (E_g = ~1.45 eV) [255], the CFO nanoparticles behave with a lower barrier to the transfer of electrons from valance band energy (E_v) to conduction band energy (E_c). The electron transfer mechanism on both nanoparticles is based on electron hopping between iron or cobalt ions due to the smaller activation energy and lower bandgap energy for the transfer process [256].

It has to be noticed that the interface between CFO and BFO shell can provide a special density of states and electronic structure due to atomic or lattice discontinuity and modification of chemical bonds which, in turn, triggers to different WFE and surface potential at the interface [252]. This explanation is consistent with previous works which demonstrated that the CFO/BFO interface with special electronic structure (population of

additional states at the interface) and low energy barrier leads to enhanced local conduction as characterized by conductive AFM (CAFM) [252, 257]. Likewise, the presence of high oxygen vacancies at CFO/BFO or perovskites/spinels interface can act as donors to transfer electrons to the conduction band. On the other side, the segregation of Fe^{3+} ions in the regions close to the interface can significantly reduce the interfacial energy and increase the conductivity or electron transfer [257]. Moreover, crystal defects, cation distribution, grain size, porosity, and sintering method can influence the dielectric behaviour of ferrite materials[192].

Therefore, the surface potential or electrostatic force signal detected by SKPFM on the CFO@BFO oxide surface is a combination of the surface potential of the BFO shell (a thin layer with an approximate thickness 7 nm [57]) and of the CFO/BFO interface with new bandgap energy and WFE which are close to CFO nanoparticles. According to previous studies [57, 255], the bandgap energies of CFO, BFO, and CFO@BFO nanoparticles were calculated using the Kubelka-Munc function into values of 1.45, 2.2, and 1.8 eV considering approximate CFO core diameter 20 nm and BFO shell thickness 7 nm. Thus, the BFO used as a coating over CFO presents lower values with respect to bulk BFO. These results are supported by a previous study which explained that by doping the elements on the oxide structure leads to a decrease of the bandgap energy by reducing the conduction band and enhancing the electron affinity [258]. In this regard, the difference in surface potential of CFO and CFO@BFO nanoparticles, $\Delta P_{difference} = \Delta P_{CFO\text{-}BFO} - \Delta P_{CFO} = 12mV$, is not significant because of the close Fermi level values.

According to the above elucidations, we can assume that the charge carrier mobilities (electron/holes and oxygen vacancies) on the surface oxide of CFO nanoparticles with semiconductor behavior is higher than that of CFO@BFO core-shell and BFO nanoparticles

in the order CFO> CFO-BFO > BFO. However, we should take to account the relationship between WFE and bandgap energy and especially the influence of the WFE value of both nanoparticles on the surface potential difference signal. Due to this influence, the local surface potential difference between WFE of PtIr probe (Φ_{PtIr} = 4.28 eV [259]) and sample (Φ_{sample}) was described into [142]:

$$\Delta P = \Phi_{PtIr} - \Phi_{sample}/e \quad (7.1)$$

Where e is an elementary charge (1.60217×10^{-19} coulombs).

According to the above equation, considering the $\Delta P_{CFO/PtIr}$ = 22 mV and $\Delta P_{CFO-BFO/PtIr}$ = 34 mV, it can be estimated that CFO@BFO nanoparticles indicate the higher WFE than CFO nanoparticles which is related to significant influence of the BFO shell and CFO-BFO interface structure electronic properties. In the electrochemical interactions in an environment with various ions and species (complexes, proteins, and cells), materials with high surface potential or WFE present higher stability of valance electrons or a more stable electronic state which inhibit the valence electrons from participating in electrochemical reactions [240, 241, 245]. On this account, materials with high surface potential or WFE value are more noble in comparison to those exhibiting lower values of WFE, and this can be used as a criterion to predict the metal ion release or degradation [246, 260].

7.2. Electrochemical behaviour of nanoparticles in PBS at different pH and apoferritin concentrations

The OCP curves of CFO and CFO@BFO nanoparticle samples monitored during immersion in the PBS solution with three different pH values (pH 3, 5 and 7) and apoferritin concentrations (0, 10μg.mL^{-1} and 100μg.mL^{-1}) for 1 hour at 25ºC and aerated conditions are reported in **Figure 7.2a and 7.2b**. The working electrodes were prepared by embedding the

nanoparticles in Nafion® and spread on ITO glass as described in 4.3.2. Curves related to the ITO glass and ITO glass+Nafion® are also reported for comparison.

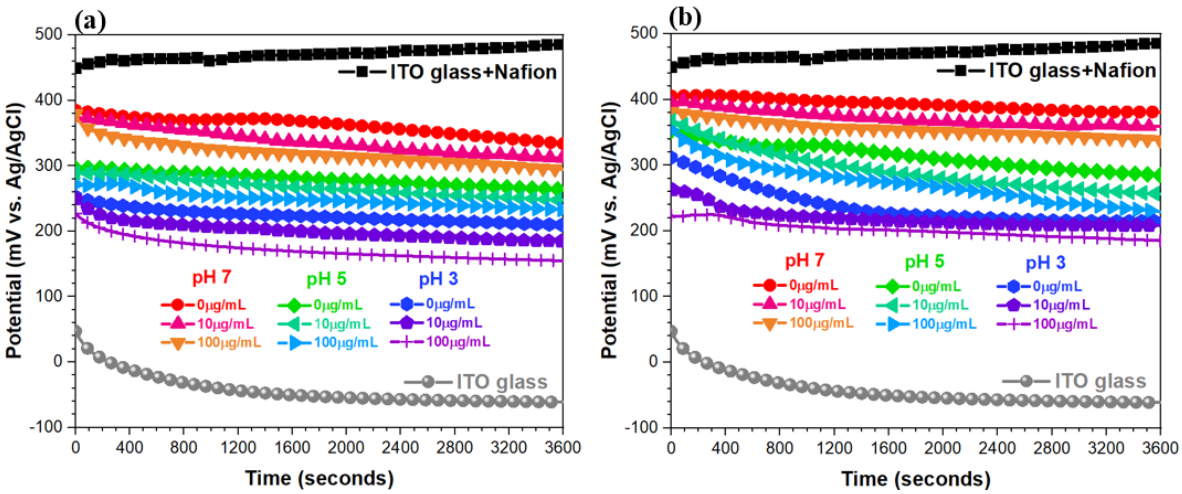

Figure 7.2. Open-circuit potential (OCP) curves of (a) CFO and (b) CFO@BFO nanoparticles coated with Nafion® on ITO glass and exposed in PBS solution at 25 °C with different pH values 7, 5, and 3 alongside the various apoferritin protein concentrations (0, 10 and 100μg/mL).

As presented on OCP curves, the ITO glass+Nafion® sample presents the higher OCP in PBS solution (~480 mV vs. Ag/AgCl) and the ITO glass the lowest (-68 mV vs. Ag/AgCl). It is very clear that the Nafion® film can act as a barrier to diffuse the oxygen, water molecules, and other ions to the conductive surface of ITO glass [247, 261]. Therefore, this organic layer with hydrophobic behaviour increases the electrochemical potential in turn act as a determined step to control the whole electrochemical reactions e.g. oxidation-reduction (redox) reactions on solid/organic layer/solution interfaces. All other curves are placed in between. Generally, the CFO@BFO particles present higher values of OCP in comparison to CFO particles in all conditions. A decrease of OCP by decreasing the pH of the solution is always recorded. Within the curves corresponding to solutions with the same pH, a decrease of the OCP is noticed by increasing the apoferritin concentration.

Regarding the role of the apoferritin concentration, a possible explanation is linked to the absorption phenomena on the surface of the particles. The protein adsorption on solid surfaces is a complex process. The adsorption process is defined as a quick event (seconds to hours) [122]. The kinetics of adsorption and conformational arrangement of protein strongly depend on three critical parameters including solid surface properties such as surface energy, roughness, hydrophobicity, chemical composition, and charge; protein properties such as protein size, concentration, charge, and structure; solution properties such as pH, ionic strength, and variety of ions and molecules [249]. According to previous studies, protein molecules during the first interaction with the solid surface (oxides layer on metal, alloy, and ceramic materials) tend to form metal-protein binding and thus act as a cathodic inhibitor on reduction reactions e.g. ($2H^+ + 2e^- \rightarrow H_2$ and/or $O_2 + H_2O + 4e^- \rightarrow 4OH^-$) and decrease the electrochemical potential [2, 197, 262]. Thus, the apoferritin molecules with 100µg/mL provide a higher inhibiting effect than 0 and 10µg/mL which in turn leads to decreasing the OCP during the competition with other ions and species on both nanoparticles. In addition, some H^+ ions have a chance to migrate within the interior oxide surface of CFO and BFO shell especially on defect sites (high energy places) which trigger the formation of the new complexes and in turn enhance the metal ion releasing process. **Figure 7.3 (a, b) and (c, d)** present the I-V curves of CFO and CFO@BFO nanoparticle samples obtained after the OCP measurement (1 hour) in all solutions.

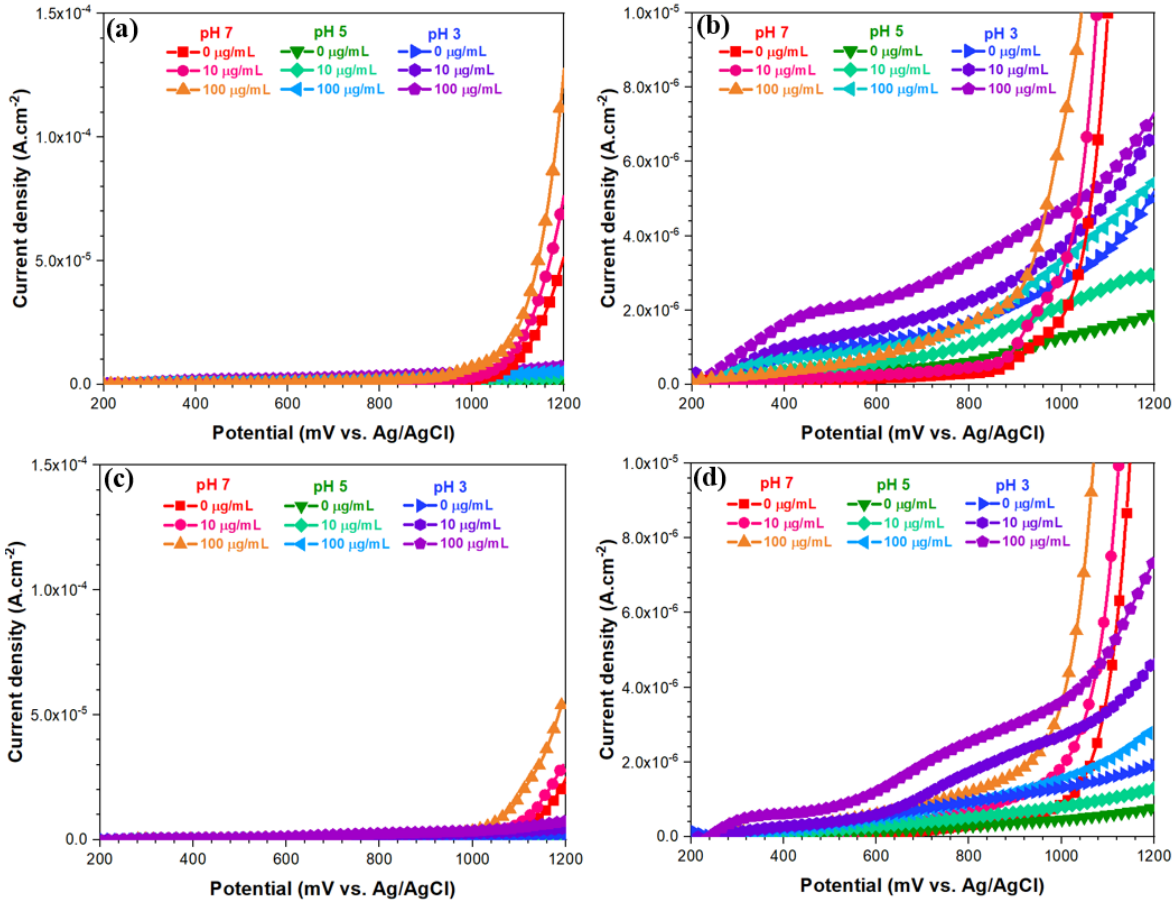

Figure 73. I-V curves (anodic potential) of (a and b) CFO and (c and d) CFO@BFO nanoparticles coated with Nafion® on ITO glass and exposed in PBS solution after 1 hour at 25 °C with the different pH values 7, 5 and 3 alongside the various apoferritin protein concentrations including 0, 10, and 100µg/mL.

On all curves obtained in solutions with pH 7 we can notice a significant increase of the current density for potentials above 1V vs. Ag/AgCl. This is due to the oxygen evolution reactions (OER):

$$2H_2O \rightarrow O_2 + 4H^+ + 4e^- \quad (7.2)$$

Using the following equation, we can estimate the OER potential respect to Ag/AgCl electrode with varieties pH values as follows [263]:

$$E\ (vs.\ RHE) = E\ (vs.\ Ag/AgCl) + 0.210V + 0.059\ pH \quad (7.3)$$

Correspondingly, according to equation (8.3), we can observe that the OER onset potential for CFO is lower than CFO@BFO at pH 7 with values of 900 mV and 1000 mV vs. Ag/AgCl (**Figure 7.3 b and 7.3d**) respectively due to the higher electronic conductivity and facility in charge transfer mechanism in the structure of CFO nanoparticles. In the PBS solution, the presence of phosphate species (HPO_4^{-2} and $H_2PO_4^-$) with quick adsorption and formation of a thin film of phosphate complex on an oxide surface can restrict the electrochemical reactions [2]. According to previous studies [144, 149], a thin and compact adsorbed layer of phosphate on the oxide layer of metallic alloys can act as an anodic inhibitor and control the metal ion release.

The BFO shell in CFO@BFO nanoparticles slightly reduces the total anodic current density. These results are in agreement with SKPFM results which indicated a higher WFE difference of CFO@BFO nanoparticles alongside a higher E_g value with respect to the CFO nanoparticles. By increasing the apoferritin concentration from 0 up to 100μg/mL the anodic current density tends to increase on both CFO and CFO@BFO nanoparticle samples in PBS solution. The role of apoferritin on the metal ion release and the up-taking process is predominant.

Apoferritin and ferritin (or apoferritin filled with a metal complex core) protein are composed of 24 polypeptide subunits that trigger the formation of a hollow sphere with an outer diameter of 120Å and an inner core diameter of 80 Å [264]. The arrangement of apoferritin subunits causes the formation of 6 hydrophobic and 8 hydrophilic channels that have access to the interior of the protein shell [265]. The metal ions up-taking or metal ion releasing can occur by electron transfer mechanism between the protein shell and the oxide surface [266]. It has been explained that iron or other metal ions can enter the protein shell with the hydrophilic 3-fold channel and chelate with regions that are enriched by

carboxylate-terminated residues [139, 267]. Moreover, the adsorption of apoferritin is controlled by electrostatic or hydrophobic interactions on both CFO and CFO@BFO nanoparticles which have a direct relationship with the charge of the protein molecule and the surface charge on the oxide layer.

The electrostatic interaction of proteins with the ceramic particles is strongly dependent on the charge distribution and the polar residues of protein structure (isoelectric point (IEP)) which can be controlled by changing the pH [268, 269]. The IEP value of apoferritin protein is between 4.1-5.1 [270, 271]. Therefore, the apoferritin molecule at pH 3, 5, and 7 exhibits a positive, neutral, and negative zeta potential (ζ) on its molecule structure. Also, the apoferritin molecule can maintain its hollow spherical shape with the same structure in the approximate pH range of 7.3 down to 3 [140]. Taking into account that the oxide surface of both CFO and CFO@BFO nanoparticles during the overpotential in the anodic region has a positive charge, electrostatic adsorption will occur between the protein and the oxide surface at pH 7. However, at pH 5 and 3, the hydrogen bonding and the hydrophobic interactions can play a predominant role [272]. As a result, apoferritin molecules cause an increase of the total anodic current density or facilitate the oxidation reactions on the oxide surface of both nanoparticles. Indeed, the apoferritin molecules adsorbing and binding on the oxide surface could accelerate the metal ions release and create defect sits on the oxide surface of CFO and CFO@BFO. A previous study on the effect of Lithium (Li) doping on electrocatalytic efficiency of CFO nanoparticles indicated that the Li creates a large number of defective domains on CFO structure which significantly reduced the OER onset potential or increasing the charge carriers [189]. We could consider a similar mechanism due to the adsorption of apoferritin.

By polarizing the samples to more noble potentials, we increase the positive surface charge and thus enhance the electrostatic adsorption of apoferritin molecules which in turn enhance the transfer of electrons between the ferritin and the oxide surface [266]. Considering that the metal ions up-taking process and the formation of a mineral core by apoferritin shell are based on the oxidation reaction (e.g. $Fe^{2+} \rightarrow Fe^{3+} + e^{-}$ or other metal oxidation), the observed oxidation peaks on the I-V curves at lower potentials than that of the OER are due to the presence of apoferritin. These peaks can be related to multi-reactions/interaction on the oxide/apoferritin interface [271]. According to the electrochemical results in **Figure 7.3**, both CFO and CFO@BFO nanoparticle samples present the highest anodic current density at pH 3 and 100µg/mL apoferritin in PBS solution. We can state, thus, that the presence of apoferritin and the low pH enhances the anodic oxidation reactions. To evaluate the role of protein on the structure and electronic or semiconductor character of the oxide surface Mott Shottcky measurements have been performed.

7.3. Electronic properties evaluations during interaction with apoferritin protein

We should consider that apoferritin proteins can interact or bind to metal atoms on the oxide surface of CFO and CFO@BFO nanoparticles which is strongly dependent on the properties of the oxide surface [117]. Thus, the detachments process between varieties proteins and metals atom on the oxide surface will occur if the protein-metal bonds at the oxide surface are stronger than metal-oxide (in this case in bulk) or hydroxides bonds. On this account, we conducted the MS analysis to reveal the type of semiconductor character along with the role of pH and apoferritin protein molecules on the C^{-2} magnitude on CFO and CFO@BFO oxide surface in turn influence on metal ion releasing and up-taking process.

As indicated in Figure 7.4, CFO and CFO@BFO nanoparticle samples in PBS solutions with different pH values and apoferritin concentrations showed a positive slope or an increasing trend on C^{-2} value generally for potential values above -0.2 V vs. Ag/AgCl. The positive slope with a linear behavior represents n-type semiconductor character (N_d , donor density) due to the presence of electrons and oxygen vacancies in the oxide surface of both nanoparticles [273].

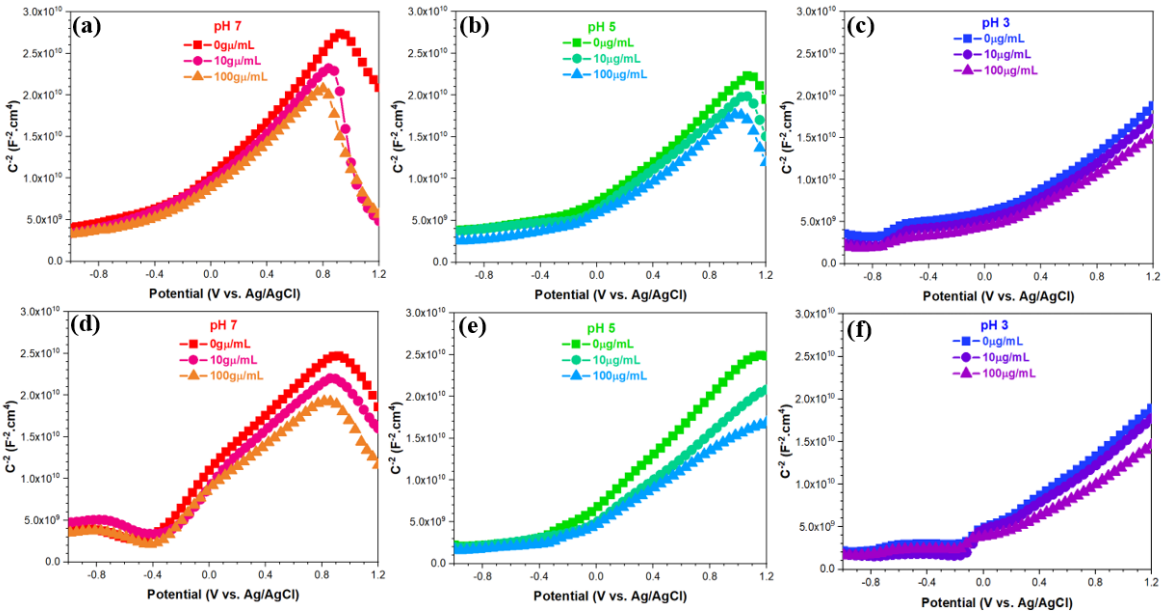

Figure 7.4. Mott-Schottky analysis of (a, b and c) CFO and (d, e and f) CFO@BFO nanoparticles coated with Nafion® on ITO glass and exposed to PBS solution after 1 hour at 25 °C with different pH values of 7, 5, and 3 along with various apoferritin concentrations including 0, 10 and 100μg/mL

In both cases, we notice a decrease in C^{-2} values or a negative slope for the solutions with pH 7 and 5 for potentials above 0.9V vs. Ag/AgCl. This behaviour can be attributed to p-type semiconductor character (acceptor density) which is enriched with hole defects or metal ions vacancies on the oxide surface of nanoparticles. This effect is more intense at pH 7 than at 5. The CFO can act as a semiconductor (electron transfer for conductivity) with n-type or p-type semiconductor characters which can be attributed to Fe^{2+} (electrons) and Co^{3+}

(electron holes), respectively [254]. In the CFO inverse spinel structure, half of the iron ions (Fe^{3+}) locate in tetrahedral sites, and the further half iron ions with cobalt ions (Fe^{3+} and Co^{2+}) are positioned in octahedral sites [188]. The semiconductor property or main predominant conduction mechanism in $CoFe_2O_4$ are related to the presence of Fe^{2+} and Co^{3+} in octahedral sites with a conduction mechanism [172]:

$$Fe^{2+} + Co^{3+} \leftrightarrow Fe^{3+} + Co^{2+} \tag{7.4}$$

In $BiFeO_3$ shell, the presence of Bi^{3+} in eightfold coordination with ferroelectricity property and Fe^{3+} in sixfold coordination with magnetism property provides a condition for transfer of charge carriers [274]. The presence of donor density distribution in both nanoparticles clearly explains the role of oxygen vacancies concentration on semiconductor behaviour and the charge transfer process during electrochemical reactions on the oxide surface. With reducing the pH value in PBS solution from 7 to 5 and then 3, both C^{-2} and the linear regions with positive slopes on CFO and CFO@BFO nanoparticle samples shift to a lower value, slightly more marked on CFO nanoparticle samples. By decreasing the pH to 3, we can notice a decrease in the slope of the positive linear region both for the CFO and CFO@BFO particles. As can be seen in **Figure 7.5**, both for CFO and CFO@BFO particles there is an increase of the E_{fb} with reducing the pH in all apoferritin concentrations. This could be attributed to protonation/deprotonation dissolutions on their oxide surfaces [275, 276].

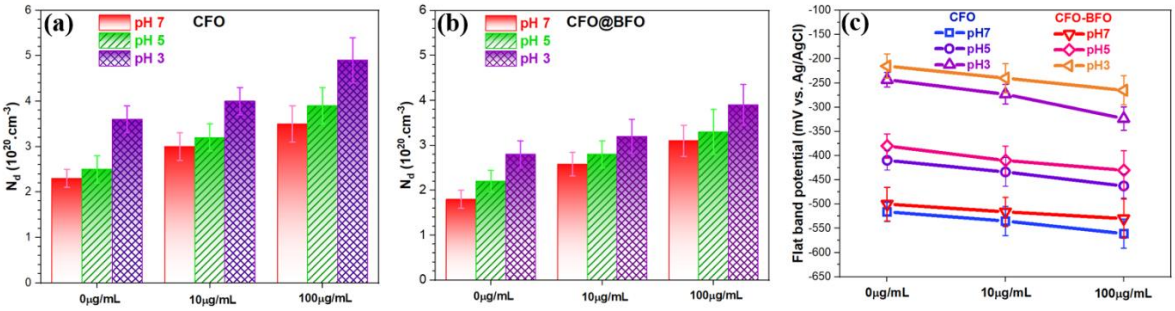

Figure 7.5. Donor charge carriers of (a)CFO and (b)CFO@BFO nanoparticles, (c) flat band potential values on oxide surface of CFO and CFO@BFO nanoparticles, results analyzed from Mott-Schottky analysis in Figure 7.4.

Moreover, the higher apoferritin concentration (100μg/mL) leads to a decrease of the slope of the positive linear region and the p-type semiconductor character onset potential (~0.8 V vs. Ag/AgCl) promoting the formation of defect sites. On the other hand, there is also a decrease in the E_{fb}. In PBS media, we must consider the role of a phosphate-rich layer on the oxide surface of the nanoparticles which acts as a barrier for controlling the kinetics of reactions. With increasing apoferritin concentration from 0 up to 100μg/mL the electrochemical interactions can be enhanced leading to a higher charge transfer, metal-protein detachment and/or metal ion release [193]. By increasing the amount of apoferritin, more protein molecules can interact with the oxide surface and bind with metal atoms on the defects sites. A previous study showed the two main mechanisms can influence on degradation and metal ion releasing process on TiO_2, ZnO, CeO, iron oxides and aluminum oxides by proteins and other organic substance including complex formation with metal atoms at oxide surface or released metal ions and ligand-enhanced dissolution by extracting the metal atoms on oxide surface [193]. As represented in **Figure 7.5**, CFO@BFO nanoparticle samples exhibit a slightly higher E_{fb} than CFO nanoparticle samples in all pH and apoferritin concentration solutions which represent a lower activity with lower charge carrier densities.

As a consequence, the apoferritin molecule can facilitate the charge transfer and mass transport at the oxide/protein interface with binding on active sites of the surface oxide and then up-taking or releasing metals such as Fe, Bi and Co, specially from the surface defects (cation vacancies and/or oxygen defects). The electrochemical reactions on the surface of the oxide are strongly dependant on the electron transfer and in particular on the donor density. By decreasing the donor density, the electron transfer is decreased and thus the electrochemical reactions are inhibited [189].

7.4 ICP-AES analysis

To reveal the significant role of apoferritin molecules on Co, Fe, and Bi ions releasing process of CFO and CFO@BFO during long-term immersion (30 days), ICP-AES analysis has been performed. The reported results indicated that the apoferritin protein environment with respect to PBS solution in both pH 7 and 3 remarkably triggered a higher releasing of Co, Fe, and Bi ions from either CFO and CFO@BFO nanoparticles (**Figure 7.6a and 7.6b**). However, the Co, Fe, and Bi ions releasing process of nanoparticles were more intensive at pH 3 especially in PBS+apoferritin environment, a higher acceleration rate of ions release was detected. The thin layer of BFO coating on CFO nanoparticles in the absence of apoferritin molecules, led to significant decreasing of Bi, Fe (2 times decrease at pH 3), and Co (6 times decrease at pH 3) ions release due to the lower electrochemical activity and corrosion hindering behaviour. However, adding the apoferritin to PBS solution, BFO nano-coated layer gradually starts to degrade, as indicated by the higher concentration of Bi and Fe ions, which reach the highest values at pH 3.

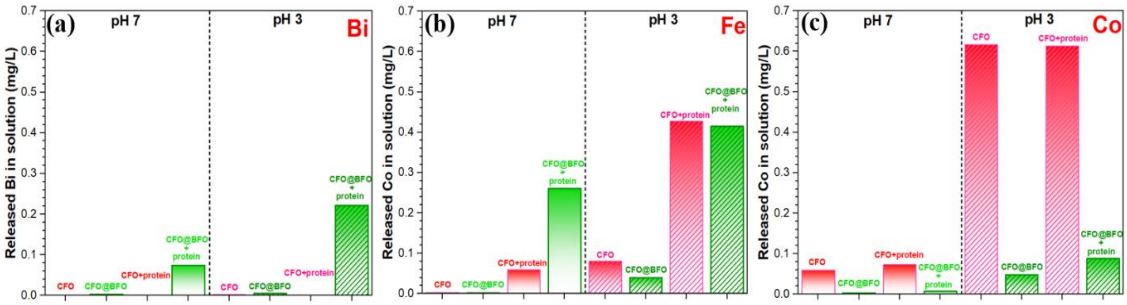

Figure 7.6. Total amounts of (a) Bi, (b) Fe, and (b) Co-released from CFO and CFO@BFO nanoparticles after immersion for 30 days in the two different solutions and pH including PBS and PBS+apoferritin, pH 3 and 7 at 37 °C.

As a consequence, based on electronic properties by SKPFM, all electrochemical analyses, and ICP-AES results, we can achieve to this point that the presence of a nanometre layer of BFO on CFO nanoparticles during exposure to human body media can improve its performance and resistance to metal ion releasing process.

7.5 Partial Conclusions

In summary, we have experimentally studied the electronic properties (at solid/air and solid/electrolyte interfaces by SKPFM and MS analysis, respectively), electrochemical response and metal ion releasing process of $CoFe_2O_4$ (CFO) and $CoFe_2O_4$@ $BiFeO_3$ (CFO@BFO) magnetic nanoparticles in PBS solution containing various concentration of apoferritin protein. Interestingly, the SKPFM results indicated a higher WFE distribution on CFO@BFO nanoparticles surfaces than CFO nanoparticles which could be attributed to the electronic properties of the BFO shell and CFO-BFO interface. Potentiodynamic polarization measurements in different solutions demonstrated higher anodic current densities on both CFO and CFO@BFO nanoparticle samples at pH 3 and 100µg/mL apoferritin in PBS solution. By utilizing Mott-Schottky analysis, we revealed a slightly higher E_{fb} and lower donor density distribution on CFO@BFO nanoparticle samples than on CFO in all pH values and apoferritin concentrations, showing a lower activity with lower

charge carrier densities on CFO@BFO nanoparticle. In absence of protein, a thin film of phosphate species is formed on the surface of the particles increasing their stability in the PBS solutions. The presence of apoferritin, increases the meatal ion release and in particular Fe (2 times increase at pH 3), and Co (6 times increase at pH 3) contributing to the electrochemical reactions and forming metal-protein complexes. These results provide new approaches to mechanistically understanding the chemical stability and biodegradation processes of ceramic nanoparticles as innovative nano-biomaterials in the human physiological media.

Chapter 8: Final Remarks and suggestion for future work

8.1 Final Remarks

In this work the degradation of different materials used in the biomedical field was investigated focusing on the corrosion mechanisms in micro- or nanoscale. The research activities followed two distinct routes: a) Study of the corrosion mechanisms on bulk, passive alloys, namely Ti6Al4V and CoCrMo, commonly used for biomedical implants, with a special focus on the effect of protein adsorption on their surface and its influence on the passive film formation and corrosion; b) Study of the degradation mechanisms of micro- and nano-devices which can be used for targeted drug delivery, cancer therapy and isolation of biological targets. To this aim NiCo and NiCo/Au coated micropillars and cobalt ferrite ($CoFe_2O_4$ (CFO)) and cobalt ferrite@bismuth ferrite ($CoFe_2O_4$@$BiFeO_3$ (CFO@BFO)) ceramic nanoparticles were taken into consideration. A multi-characterisation approach was followed using electrochemical measurements, Mott–Schottky analysis, SEM-EDXS, XPS, AFM, SKPFM and ICP-AES to reveal and establish the protein interactions with the most important ions or inorganic species in different human body simulating solutions and their role in corrosion phenomena occurring on a heterogeneous surface.

Regarding Ti6Al4V, the effect of different simulated physiological solutions, including a 0.9%wt. NaCl solution, phosphate-buffered saline (PBS) solution, and Hanks' solution, along with an inflammatory condition simulated by the addition of hydrogen peroxide (H_2O_2), on bovine serum albumin (BSA) protein adsorption, conformational arrangement, and surface potential distribution were evaluated. Summarizing the main findings, it could be stated that the alloy is more resistant to corrosion in PBS solution in

comparison to Hank's and NaCl. The addition of BSA leads to a slight increase of the corrosion current density and the passive current density in all tested solutions, whereas a more marked increase is observed by adding H_2O_2 or both BSA and H_2O_2. These results are correlated to the semiconductive character of the formed passive film. Indeed, Mott-Schottky analyses demonstrated that under inflammatory conditions (BSA + H_2O_2) an increase of the donor density of the passive film formed was noticed in all environments. The morphology of the adsorbed protein changed from globular to a large micronetwork (PBS) to fine micro-nanonetworks (Hanks'), along with increasing the surface potential. According to the SKPFM and SEM images, the adsorbed protein/passive film interfaces and the top surface of BSA protein were the susceptible sites for corrosion initiation. Summarizing the results of the electrochemical and surface analyses techniques it could be stated that the adsorption of protein on the surface of Ti6Al4V increases the degradation rate in all human body simulating solutions and this effect is more intense in inflammatory conditions. On the other hand, the presence of phosphate and calcium species contributes to the formation of a more protective layer due to their adsorption on the alloy surface. This hinders the adsorption of BSA protein, decreasing the corrosion rate.

The effect of both BSA concentration and applied overpotential on the adsorption of protein and their influence on the corrosion resistance were evaluated on CoCrMo alloy in PBS base solution. Similar results to those obtained on Ti6Al4V were observed, with the BSA protein increasing generally the degradation rate of the alloy and providing favourable sites for localized corrosion attack when adsorbed on the alloy surface. Moreover, by increasing the BSA concentration and the applied overpotential the morphology of the adsorbed protein changed providing a higher covering of the surface and decreasing the corrosion rate.

With regard to the second part of the work, the degradation mechanisms of micro- and nano-devices in human body simulating solutions was deeply studied for the first time using a combination of electrochemical and surface analysis techniques. The first system studied were NiCo magnetic micropillars (MPs) immersed in PBS solution containing BSA protein. These pillars were protected by an Au layer aimed to increase the biocompatibility and decrease the metal ion release in the human body. However, the Au coating on the NiCo/Au-MPs did not uniformly cover the MPs surface, presenting uncovered regions and micro- and nano-sized defects. SKPFM and PDP measurements revealed the galvanic coupling between the Au and the uncovered areas of the NiCo substrate as a result of the Au layer defects, which could increase the dissolution rate of the NiCo. Conversely, long-term EIS measurements showed that a phosphate-based layer was formed on the MPs' surface, which became more stable after longer immersion times, providing a shielding effect from the aggressive Cl^- attack and the corrosion of the NiCo/Au-MPs due to galvanic coupling. The presence of BSA increased the aggressiveness of the electrolyte, as demonstrated by all electrochemical measurements in a similar way as observed for the Ti6Al4V and CoCrMo bulk alloys. The BSA molecules competed with the phosphate species to form the adsorbed film on the MPs' surface and increased the corrosion rate due to the protein-metal bonding and the detachment of the protein-metal complexes. However, the Au coating offered certain protection, despite the defects, due to the fact that the BSA detrimental effect only had an impact on the NiCo, and the exposed area through the defects was significantly lower in comparison with the non-coated NiCo-MPs.

The second system studied was composed by CFO and cobalt ferrite-bismuth ferrite core shell nanoparticles. As these ceramic particles present a high stability in biological media, apoferritin protein was added to PBS solution at different concentrations and

solutions pH to study the degradation mechanism as it should be able to detach Fe ions even from stable structures. The SKPFM results indicated a higher WFE distribution on CFO@BFO nanoparticles surfaces than CFO nanoparticles which could be attributed to the electronic properties of the BFO shell and CFO-BFO interface. In absence of protein, a thin film of phosphate species is formed on the surface of the particles increasing their stability in the PBS solutions. The presence of apoferritin, increases the metal ion release and in particular Fe (2 times increase at pH 3), and Co (6 times increase at pH 3) contributing to the electrochemical reactions and forming metal-protein complexes.

From all the above it was demonstrated that the combination of electrochemical both large-scale and localized techniques with surface analyses can be a useful tool contributing in understanding the degradation mechanisms in micro- and nano-scale both on the surface of bulk alloys and micro- or nano-devices. The interactions of different proteins present in different environments simulating body fluids on the surface of biomaterials are strongly impacting the biodegradation processes.

8.2 Suggestions for future work

The field of biomedical small-scale swimmers has made impressive strides during the last decade. Yet, their translation to the clinics remains a daunting challenge because several aspects have been often overlooked, mainly because of lack of established methodologies. A clear example of this is the durability and corrosion resistance of micro- and nanoswimmers. In this work we establish for the first time an approach to investigate the corrosion mechanism on metallic small-scale structures by combining electrochemical and surface analysis techniques, which shed light on the degradation mechanisms of these systems in simulated body fluids using NiCo micropillars and CFO particles as models.

However, this is still an unexplored field as different systems with a variety of shapes and consisting of different materials have been developed and their degradation in the human body has been often overlooked. Another aspect to be explored is how the degradation of these tiny structures can influence both their functionality and their biocompatibility during a long-term exposure to human physiological media.

List of publications and conferences:

Publications

1**. Ehsan Rahimi** , Ruben Offoiach , Kitty Baert , Herman Terryn , Maria Lekka , Lorenzo Fedrizzi, "Role of phosphate, calcium species and hydrogen peroxide on albumin protein adsorption on surface oxide of Ti6Al4V alloy", *Materialia 15 (2021): 100988, (DOI: 10.1016/j.mtla.2020.100988).*

2. **Ehsan Rahimi**, Ruben Offoiach, Saman Hosseinpour, Ali Davoodi, Kitty Baert, Alexander Lutz, Herman Terryn, Maria Lekka, and Lorenzo Fedrizzi. "Effect of hydrogen peroxide on bovine serum albumin adsorption on Ti6Al4V alloy: A scanning Kelvin probe force microscopy study". *Applied Surface Science (2021): 150364, (DOI: 10.1016/j.apsusc.2021.150364).*

3**. Ehsan Rahimi**, Ruben Offoiach, Siyu Deng, Xiangzhong Chen, Salvador Pané, Lorenzo Fedrizzi, Maria Lekka "Corrosion mechanisms of magnetic microrobotic platforms in protein media". *Applied Materials Today (2021): 101135, (DOI: 10.1016/j.apmt.2021.101135)*

4**.** Bruno Ribeiro, Ruben Offoiach, **Ehsan Rahimi**, Elisa Salatin, Maria Lekka, and Lorenzo Fedrizzi. "On Growth and Morphology of TiO_2 Nanotubes on Ti6Al4V by Anodic Oxidation in Ethylene Glycol Electrolyte: Influence of Microstructure and Anodization Parameters." *Materials 14, no. 10 (2021): 2540. (DOI: 10.3390/ma14102540).*

5**.** Ivan Spajic, **Ehsan Rahimi**, Maria Lekka, Ruben Offoiach, Lorenzo Fedrizzi, Ingrid Milosev, "Al_2O_3 and HfO_2 atomic layers deposited in single and multilayer configurations on titanium and on stainless steel for biomedical applications", *Journal of The Electrochemical society 168.7 (2021): 071510, , (DOI: 10.1149/1945-7111/ac131b)*

Conferences

1**. Ehsan Rahimi**, Ruben Offoiach, Lorenzo Fedrizzi, Maria Lekka, "Evaluation of electronic properties and Volta potential distribution of CoCrMo alloy in presence of albumin protein molecule by SKPFM and electrochemical measurements", Electrochem-2019, 26th-28th August, Glasgow/Scotland.

2. **Ehsan Rahimi,** (Localized corrosion mechanism on micro-and nano devices in biomedical Field)**,** 2nd mCBEEs training school event, " Structural, mechanical and surface analytical techniques", 06th-09th November, Jönköping University, Sweden.

3. **Ehsan Rahimi**, "Localized corrosion mechanisms on micro- and nano-devices in the biomedical field" in 4nd mCBEEs training school event," Corrosion protection at micro-scale - application fields" UAB University, Spain

4. **Ehsan Rahimi**, Ruben Offoiach, Siyu Deng, Salvador Pané, Lorenzo Fedrizzi, Maria Lekka "A comprehensive insight on the degradation of NiCo and NiCo/Au coated micro-

robots during immersion in simulated body fluids" Oral presentation in EUROCORR 2020, Brussels/Belgium.

5. Donghoon Kim, **Ehsan Rahimi**, Ruben Offoiach, Xiangzhong Chen, Maria Lekka, Salvador Pané "Electrochemical monitoring of the corrosion behavior of functional oxide nanoparticles under biological environments" Oral presentation in EUROCORR 2020, Brussels/Belgium.

6. Ivan Spajić, **Ehsan Rahimi**, Maria Lekka, Lorenzo Fedrizzi, Ingrid Milošev "Protection of biomedical stainless steel and titanium by ALD single and multi-layered thin films made of Al_2O_3 and HfO_2" Oral presentation in EUROCORR 2020, Brussels/Belgium.

7. **Ehsan Rahimi**, Ruben Offoiach, Kitty Baert, Herman Terryn, Maria Lekka, Lorenzo Fedrizzi "Albumin protein adsorption on surface oxide of titanium alloy in various simulated body fluids containing H_2O_2 agent", Oral presentation in EUROCORR 2021, Budapest, Hungary.

Acknowledgment

The research presented in this thesis was carried out at the University of Udine, Italy in Department of Engineering and Architecture under the supervision of Dr. Maria Lekka and Prof. Lorenzo Fedrizzi. This project has received funding from the European Union's Horizon 2020 research and innovation program under the Marie Sklodowska-Curie grant agreements No 764977, mCBEEs (Localized corrosion mechanisms on micro and nano-devices in the biomedical field). I would like to dedicate my extreme appreciation to Italian, Switzerland, Belgium, and Netherlands research groups for their supporting and attempts during this project. I would like to thank Dr. Ruben Offoiach, who actively took part in SEM-EDXS and electrochemical measurements in all parts of this thesis.

References

[1] S.H. Teoh, Engineering materials for biomedical applications, World scientific2004.
[2] I. Milošev, CoCrMo alloy for biomedical applications, Biomedical Applications, Springer2012, pp. 1-72.
[3] R. Narayan, Biomedical materials, Springer Science & Business Media2009.
[4] Y. Rosen, N. Elman, Biomaterials science: an integrated clinical and engineering approach, CRC Press2012.
[5] J. Wilson, 1 - Metallic biomaterials: State of the art and new challenges, in: P. Balakrishnan, S. M S, S. Thomas (Eds.), Fundamental Biomaterials: Metals, Woodhead Publishing2018, pp. 1-33.
[6] B.D. Ratner, A.S. Hoffman, F.J. Schoen, J.E. Lemons, Biomaterials science: an introduction to materials in medicine, Elsevier2004.
[7] D.F. Williams, On the mechanisms of biocompatibility, Biomaterials 29(20) (2008) 2941-2953.
[8] M.M. Stevens, J.H. George, Exploring and engineering the cell surface interface, Science 310(5751) (2005) 1135-1138.
[9] J.J. Ramsden, D.M. Allen, D.J. Stephenson, J.R. Alcock, G. Peggs, G. Fuller, G. Goch, The design and manufacture of biomedical surfaces, CIRP annals 56(2) (2007) 687-711.
[10] W. Suchanek, M. Yoshimura, Processing and properties of hydroxyapatite-based biomaterials for use as hard tissue replacement implants, Journal of Materials Research 13(1) (1998) 94-117.
[11] M. Geetha, A.K. Singh, R. Asokamani, A.K. Gogia, Ti based biomaterials, the ultimate choice for orthopaedic implants–a review, Progress in materials science 54(3) (2009) 397-425.
[12] M. Viceconti, R. Muccini, M. Bernakiewicz, M. Baleani, L. Cristofolini, Large-sliding contact elements accurately predict levels of bone–implant micromotion relevant to osseointegration, Journal of biomechanics 33(12) (2000) 1611-1618.
[13] J.N. Meyer, M.T. Mathew, M.A. Wimmer, R.J. LeSuer, Effect of tribolayer formation on corrosion of CoCrMo alloys investigated using scanning electrochemical microscopy, Analytical chemistry 85(15) (2013) 7159-7166.
[14] M. Koronfel, A. Goode, M. Gomez-Gonzalez, J.N. Weker, T. Simoes, R. Brydson, P. Quinn, M. Toney, A. Hart, A. Porter, Chemical Evolution of CoCrMo Wear Particles: An in Situ Characterization Study, The Journal of Physical Chemistry C 123(15) (2019) 9894-9901.
[15] Y.S. Hedberg, M. Pettersson, S. Pradhan, I. Odnevall Wallinder, M.W. Rutland, C. Persson, Can cobalt (II) and chromium (III) ions released from joint prostheses influence the friction coefficient?, ACS Biomaterials Science & Engineering 1(8) (2015) 617-620.
[16] J.G.S. Moo, C.C. Mayorga-Martinez, H. Wang, B. Khezri, W.Z. Teo, M. Pumera, Nano/microrobots meet electrochemistry, Advanced Functional Materials 27(12) (2017) 1604759.

[17] D. Xu, Y. Wang, C. Liang, Y. You, S. Sanchez, X. Ma, Self-Propelled Micro/Nanomotors for On-Demand Biomedical Cargo Transportation, Small (2019) 1902464.
[18] J. Katuri, X. Ma, M.M. Stanton, S. Sánchez, Designing micro-and nanoswimmers for specific applications, Accounts of chemical research 50(1) (2017) 2-11.
[19] W. Gao, J. Wang, Synthetic micro/nanomotors in drug delivery, Nanoscale 6(18) (2014) 10486-10494.
[20] F. Alouges, A. DeSimone, A. Lefebvre, Optimal Strokes for Low Reynolds Number Swimmers: An Example, Journal of Nonlinear Science 18(3) (2008) 277-302.
[21] P. Fischer, A. Ghosh, Magnetically actuated propulsion at low Reynolds numbers: towards nanoscale control, Nanoscale 3(2) (2011) 557-563.
[22] M. You, C. Chen, L. Xu, F. Mou, J. Guan, Intelligent micro/nanomotors with Taxis, Accounts of chemical research 51(12) (2018) 3006-3014.
[23] M. Guix, C.C. Mayorga-Martinez, A. Merkoçi, Nano/micromotors in (bio) chemical science applications, Chemical reviews 114(12) (2014) 6285-6322.
[24] R. Liu, A. Sen, Autonomous nanomotor based on copper–platinum segmented nanobattery, Journal of the American Chemical Society 133(50) (2011) 20064-20067.
[25] J. Li, B.E.-F. de Ávila, W. Gao, L. Zhang, J. Wang, Micro/nanorobots for biomedicine: Delivery, surgery, sensing, and detoxification, Science Robotics 2(4) (2017).
[26] J. Li, I. Rozen, J. Wang, Rocket science at the nanoscale, ACS nano 10(6) (2016) 5619-5634.
[27] X.Z. Chen, B. Jang, D. Ahmed, C. Hu, C. De Marco, M. Hoop, F. Mushtaq, B.J. Nelson, S. Pané, Small-scale machines driven by external power sources, Advanced Materials 30(15) (2018) 1705061.
[28] J. Li, T. Li, T. Xu, M. Kiristi, W. Liu, Z. Wu, J. Wang, Magneto–acoustic hybrid nanomotor, Nano letters 15(7) (2015) 4814-4821.
[29] H. Wang, M. Pumera, Fabrication of micro/nanoscale motors, Chemical reviews 115(16) (2015) 8704-8735.
[30] X.-Z. Chen, M. Hoop, F. Mushtaq, E. Siringil, C. Hu, B.J. Nelson, S. Pané, Recent developments in magnetically driven micro-and nanorobots, Applied Materials Today 9 (2017) 37-48.
[31] S. Pané, J. Puigmartí-Luis, C. Bergeles, X.Z. Chen, E. Pellicer, J. Sort, V. Počepcová, A. Ferreira, B.J. Nelson, Imaging Technologies for Biomedical Micro-and Nanoswimmers, Advanced Materials Technologies 4(4) (2019) 1800575.
[32] C.C. Alcântara, S. Kim, S. Lee, B. Jang, P. Thakolkaran, J.Y. Kim, H. Choi, B.J. Nelson, S. Pané, 3D Fabrication of fully iron magnetic microrobots, Small 15(16) (2019) 1805006.
[33] C. Hu, F. Aeschlimann, G. Chatzipirpiridis, J. Pokki, X. Chen, J. Puigmarti-Luis, B.J. Nelson, S. Pané, Spatiotemporally controlled electrodeposition of magnetically driven micromachines based on the inverse opal architecture, Electrochemistry Communications 81 (2017) 97-101.

[34] F. Mushtaq, H. Torlakcik, M. Hoop, B. Jang, F. Carlson, T. Grunow, N. Läubli, A. Ferreira, X.Z. Chen, B.J. Nelson, Motile piezoelectric nanoeels for targeted drug delivery, Advanced Functional Materials 29(12) (2019) 1808135.
[35] S. Schuerle, I.A. Vizcarra, J. Moeller, M.S. Sakar, B. Özkale, A.M. Lindo, F. Mushtaq, I. Schoen, S. Pané, V. Vogel, Robotically controlled microprey to resolve initial attack modes preceding phagocytosis, Sci. Robot 2 (2017) eaah6094.
[36] J. Wang, Template electrodeposition of catalytic nanomotors, Faraday discussions 164 (2013) 9-18.
[37] V. Georgiadou, G. Makris, D. Papagiannopoulou, G. Vourlias, C. Dendrinou-Samara, Octadecylamine-mediated versatile coating of CoFe2O4 NPs for the sustained release of anti-inflammatory drug naproxen and in vivo target selectivity, ACS applied materials & interfaces 8(14) (2016) 9345-9360.
[38] N. Sanpo, C.C. Berndt, C. Wen, J. Wang, Transition metal-substituted cobalt ferrite nanoparticles for biomedical applications, Acta Biomaterialia 9(3) (2013) 5830-5837.
[39] A.M. Matos, A.I. Gonçalves, A.J. El Haj, M.E. Gomes, Magnetic biomaterials and nano-instructive tools as mediators of tendon mechanotransduction, Nanoscale Advances 2(1) (2020) 140-148.
[40] L.J. Santos, R.L. Reis, M.E. Gomes, Harnessing magnetic-mechano actuation in regenerative medicine and tissue engineering, Trends in Biotechnology 33(8) (2015) 471-479.
[41] Z.W. Tay, P. Chandrasekharan, A. Chiu-Lam, D.W. Hensley, R. Dhavalikar, X.Y. Zhou, E.Y. Yu, P.W. Goodwill, B. Zheng, C. Rinaldi, Magnetic particle imaging-guided heating in vivo using gradient fields for arbitrary localization of magnetic hyperthermia therapy, ACS nano 12(4) (2018) 3699-3713.
[42] K.E. Scarberry, E.B. Dickerson, J.F. McDonald, Z.J. Zhang, Magnetic nanoparticle−peptide conjugates for in vitro and in vivo targeting and extraction of cancer cells, Journal of the American Chemical Society 130(31) (2008) 10258-10262.
[43] C. Zhang, W. Bu, D. Ni, S. Zhang, Q. Li, Z. Yao, J. Zhang, H. Yao, Z. Wang, J. Shi, Synthesis of iron nanometallic glasses and their application in cancer therapy by a localized Fenton reaction, Angewandte Chemie 128(6) (2016) 2141-2146.
[44] M. Bañobre-López, A. Teijeiro, J. Rivas, Magnetic nanoparticle-based hyperthermia for cancer treatment, Reports of Practical Oncology & Radiotherapy 18(6) (2013) 397-400.
[45] Q. Zhang, T. Yin, G. Gao, J.G. Shapter, W. Lai, P. Huang, W. Qi, J. Song, D. Cui, Multifunctional core@ shell magnetic nanoprobes for enhancing targeted magnetic resonance imaging and fluorescent labeling in vitro and in vivo, ACS applied materials & interfaces 9(21) (2017) 17777-17785.
[46] B.R. Smith, S.S. Gambhir, Nanomaterials for In Vivo Imaging, Chemical Reviews 117(3) (2017) 901-986.
[47] F. Zan, Y. Ma, Q. Ma, Y. Xu, Z. Dai, G. Zheng, M. Wu, G. Li, Magnetic and Impedance Properties of Nanocomposite CoFe 2 O 4/Co 0.7 Fe 0.3 and Single-Phase CoFe 2 O 4 Prepared Via a One-Step Hydrothermal Synthesis, Journal of the American Ceramic Society 96(10) (2013) 3100-3107.

[48] D. Chen, X. Yi, Z. Chen, Y. Zhang, B. Chen, Z. Kang, Synthesis of C o F e2 O 4 Nanoparticles by a Low Temperature Microwave-Assisted Ball-Milling Technique, International Journal of Applied Ceramic Technology 11(5) (2014) 954-959.
[49] C.P. Fernández Perdomo, F.L. Zabotto, D. Garcia, R.H. Kiminami, Effect of the CoFe2O4 initial particle size when sintered by microwave on the microstructural, dielectric, and magnetic properties, International Journal of Applied Ceramic Technology 16(5) (2019) 2073-2084.
[50] S. Ayyappan, J. Philip, B. Raj, Effect of digestion time on size and magnetic properties of spinel CoFe2O4 nanoparticles, The Journal of Physical Chemistry C 113(2) (2009) 590-596.
[51] S. Ayyappan, S. Mahadevan, P. Chandramohan, M. Srinivasan, J. Philip, B. Raj, Influence of Co2+ ion concentration on the size, magnetic properties, and purity of CoFe2O4 spinel ferrite nanoparticles, The Journal of Physical Chemistry C 114(14) (2010) 6334-6341.
[52] X. Fu, D. Chen, M. Wang, Y. Yang, Q. Wu, J. Ma, X. Zhao, Synthesis of porous CoFe2O4 octahedral structures and studies on electrochemical Li storage behavior, Electrochimica Acta 116 (2014) 164-169.
[53] M.A.E. Aleem Ali El-Remaily, A.M. Abu-Dief, R.M. El-Khatib, A robust synthesis and characterization of superparamagnetic CoFe2O4 nanoparticles as an efficient and reusable catalyst for green synthesis of some heterocyclic rings, Applied Organometallic Chemistry 30(12) (2016) 1022-1029.
[54] S. Fan, W. Wang, H. Ke, Y. Zhou, Facile Synthesis of Morphology Controllable CoFe2O4 Particles as High-Performance Electrode Materials, Particle & Particle Systems Characterization 35(10) (2018) 1800223.
[55] D. Erdem, N.S. Bingham, F.J. Heiligtag, N. Pilet, P. Warnicke, L.J. Heyderman, M. Niederberger, CoFe2O4 and CoFe2O4-SiO2 Nanoparticle Thin Films with Perpendicular Magnetic Anisotropy for Magnetic and Magneto-Optical Applications, Advanced Functional Materials 26(12) (2016) 1954-1963.
[56] A. El Arrassi, Z. Liu, M.V. Evers, N. Blanc, G. Bendt, S. Saddeler, D. Tetzlaff, D. Pohl, C. Damm, S. Schulz, Intrinsic activity of oxygen evolution catalysts probed at single CoFe2O4 nanoparticles, Journal of the American Chemical Society 141(23) (2019) 9197-9201.
[57] F. Mushtaq, X. Chen, H. Torlakcik, C. Steuer, M. Hoop, E.C. Siringil, X. Marti, G. Limburg, P. Stipp, B.J. Nelson, Magnetoelectrically driven catalytic degradation of organics, Advanced Materials 31(28) (2019) 1901378.
[58] X.-M. Liu, S.-Y. Fu, C.-J. Huang, Synthesis and magnetic characterization of novel CoFe2O4–BiFeO3 nanocomposites, Materials Science and Engineering: B 121(3) (2005) 255-260.
[59] F. Qiu, B.J. Nelson, Magnetic Helical Micro- and Nanorobots: Toward Their Biomedical Applications, Engineering 1(1) (2015) 021-026.
[60] M. Koleoso, X. Feng, Y. Xue, Q. Li, T. Munshi, X. Chen, Micro/nanoscale magnetic robots for biomedical applications, Materials Today Bio 8 (2020) 100085.

[61] A.I. Muñoz, S. Mischler, Interactive effects of albumin and phosphate ions on the corrosion of CoCrMo implant alloy, Journal of the Electrochemical Society 154(10) (2007) C562-C570.
[62] K. Yamanaka, M. Mori, I. Kartika, M.S. Anwar, K. Kuramoto, S. Sato, A. Chiba, Effect of multipass thermomechanical processing on the corrosion behaviour of biomedical Co–Cr–Mo alloys, Corrosion Science (2018).
[63] Y. Bai, X. Gai, S. Li, L.-C. Zhang, Y. Liu, Y. Hao, X. Zhang, R. Yang, Y. Gao, Improved corrosion behaviour of electron beam melted Ti-6Al–4V alloy in phosphate buffered saline, Corrosion Science 123 (2017) 289-296.
[64] X. Gong, Y. Li, Y. Nie, Z. Huang, F. Liu, L. Huang, L. Jiang, H. Mei, Corrosion behaviour of CoCrMo alloy fabricated by electron beam melting, Corrosion Science 139 (2018) 68-75.
[65] Z. Duan, C. Man, C. Dong, Z. Cui, D. Kong, L. wang, X. Wang, Pitting behavior of SLM 316L stainless steel exposed to chloride environments with different aggressiveness: Pitting mechanism induced by gas pores, Corrosion Science 167 (2020) 108520.
[66] M. Romedenne, R. Pillai, M. Kirka, S. Dryepondt, High temperature air oxidation behavior of Hastelloy X processed by Electron Beam Melting (EBM) and Selective Laser Melting (SLM), Corrosion Science 171 (2020) 108647.
[67] A. Safdar, L.-Y. Wei, A. Snis, Z. Lai, Evaluation of microstructural development in electron beam melted Ti-6Al-4V, Materials Characterization 65 (2012) 8-15.
[68] J. Fojt, M. Fousova, E. Jablonska, L. Joska, V. Hybasek, E. Pruchova, D. Vojtech, T. Ruml, Corrosion behaviour and cell interaction of Ti-6Al-4V alloy prepared by two techniques of 3D printing, Materials Science and Engineering: C 93 (2018) 911-920.
[69] S. Karimi, T. Nickchi, A.M. Alfantazi, Long-term corrosion investigation of AISI 316L, Co–28Cr–6Mo, and Ti–6Al–4V alloys in simulated body solutions, Applied Surface Science 258(16) (2012) 6087-6096.
[70] S. Karimi, T. Nickchi, A. Alfantazi, Effects of bovine serum albumin on the corrosion behaviour of AISI 316L, Co–28Cr–6Mo, and Ti–6Al–4V alloys in phosphate buffered saline solutions, Corrosion science 53(10) (2011) 3262-3272.
[71] L. Chang, Z. Zhifeng, L. Kwok-Yan, Improved corrosion resistance of CoCrMo alloy with self-passivation ability facilitated by carbon ion implantation, Electrochimica Acta 241 (2017) 331-340.
[72] D.D. Macdonald, A. Sun, An electrochemical impedance spectroscopic study of the passive state on Alloy-22, Electrochimica Acta 51(8-9) (2006) 1767-1779.
[73] E. McCafferty, Introduction to corrosion science, Springer Science & Business Media2010.
[74] Y. Liu, J.L. Gilbert, Effect of simulated inflammatory conditions and potential on dissolution and surface oxide of CoCrMo alloy: In situ electrochemical atomic force microscopy study, Electrochimica Acta 262 (2018) 252-263.
[75] G.S. Frankel, T. Li, J.R. Scully, Perspective—localized corrosion: passive film breakdown vs pit growth stability, Journal of the Electrochemical Society 164(4) (2017) C180.

[76] W. Xu, F. Yu, L. Yang, B. Zhang, B. Hou, Y. Li, Accelerated corrosion of 316L stainless steel in simulated body fluids in the presence of H2O2 and albumin, Materials Science and Engineering: C 92 (2018) 11-19.
[77] S. Huth, 10 - Metallic materials for tribocorrosion systems, in: D. Landolt, S. Mischler (Eds.), Tribocorrosion of Passive Metals and Coatings, Woodhead Publishing2011, pp. 265-295.
[78] Y. Okazaki, 2 - Material selection, in: M. Niinomi (Ed.), Metals for Biomedical Devices, Woodhead Publishing2010, pp. 25-67.
[79] M. Talha, C. Behera, O. Sinha, In-vitro long term and electrochemical corrosion resistance of cold deformed nitrogen containing austenitic stainless steels in simulated body fluid, Materials Science and Engineering: C 40 (2014) 455-466.
[80] M. Lei, X. Zhu, In vitro corrosion resistance of plasma source ion nitrided austenitic stainless steels, Biomaterials 22(7) (2001) 641-647.
[81] I. Milošev, H.-H. Strehblow, The composition of the surface passive film formed on CoCrMo alloy in simulated physiological solution, Electrochimica Acta 48(19) (2003) 2767-2774.
[82] P. Panigrahi, Y. Liao, M.T. Mathew, A. Fischer, M.A. Wimmer, J.J. Jacobs, L.D. Marks, Intergranular pitting corrosion of CoCrMo biomedical implant alloy, Journal of Biomedical Materials Research Part B: Applied Biomaterials 102(4) (2014) 850-859.
[83] A. Fattah-Alhosseini, O. Imantalab, G. Ansari, The role of grain refinement and film formation potential on the electrochemical behavior of commercial pure titanium in Hank's physiological solution, Materials Science and Engineering: C 71 (2017) 827-834.
[84] G. Ansari, A. Fattah-alhosseini, On the passive and semiconducting behavior of severely deformed pure titanium in Ringer's physiological solution at 37° C: A trial of the point defect model, Materials Science and Engineering: C 75 (2017) 64-71.
[85] R.W.-W. Hsu, C.-C. Yang, C.-A. Huang, Y.-S. Chen, Investigation on the corrosion behavior of Ti–6Al–4V implant alloy by electrochemical techniques, Materials Chemistry and Physics 86(2-3) (2004) 269-278.
[86] N.T.C. Oliveira, E.A. Ferreira, L.T. Duarte, S.R. Biaggio, R.C. Rocha-Filho, N. Bocchi, Corrosion resistance of anodic oxides on the Ti–50Zr and Ti–13Nb–13Zr alloys, Electrochimica Acta 51(10) (2006) 2068-2075.
[87] D. Velten, V. Biehl, F. Aubertin, B. Valeske, W. Possart, J. Breme, Preparation of TiO2 layers on cp-Ti and Ti6Al4V by thermal and anodic oxidation and by sol-gel coating techniques and their characterization, Journal of Biomedical Materials Research: An Official Journal of The Society for Biomaterials and The Japanese Society for Biomaterials 59(1) (2002) 18-28.
[88] Z. Esfahani, E. Rahimi, M. Sarvghad, A. Rafsanjani-Abbasi, A. Davoodi, Correlation between the histogram and power spectral density analysis of AFM and SKPFM images in an AA7023/AA5083 FSW joint, Journal of Alloys and Compounds 744 (2018) 174-181.
[89] E. Rahimi, A. Rafsanjani-Abbasi, A. Davoodi, S. Hosseinpour, Characterization of the Native Passive Film on Ferrite and Austenite Phases of Sensitized 2205 Duplex Stainless Steel, Journal of The Electrochemical Society 166(16) (2019) C609-C616.

[90] C.D. Griffin, R. Buchanan, J. Lemons, In vitro electrochemical corrosion study of coupled surgical implant materials, Journal of Biomedical Materials Research 17(3) (1983) 489-500.
[91] D. Royhman, R. Radhakrishnan, J.C.-C. Yuan, M.T. Mathew, L.G. Mercuri, C. Sukotjo, An electrochemical investigation of TMJ implant metal alloys in an artificial joint fluid environment: the influence of pH variation, Journal of Cranio-Maxillofacial Surgery 42(7) (2014) 1052-1061.
[92] A. Mellado-Valero, A.I. Muñoz, V.G. Pina, M.F. Sola-Ruiz, Electrochemical behaviour and galvanic effects of titanium implants coupled to metallic suprastructures in artificial saliva, Materials 11(1) (2018) 171.
[93] A. Lanzutti, F. Andreatta, L. Rossi, P. Di Benedetto, A. Causero, M. Magnan, L. Fedrizzi, Corrosion fatigue failure of a high carbon CoCrMo modular hip prosthesis: Failure analysis and electrochemical study, Engineering Failure Analysis 105 (2019) 856-868.
[94] D. Upadhyay, M.A. Panchal, R.S. Dubey, V.K. Srivastava, Corrosion of alloys used in dentistry: A review, Materials Science and Engineering: A 432(1) (2006) 1-11.
[95] C.V. Vidal, A.I. Muñoz, Effect of thermal treatment and applied potential on the electrochemical behaviour of CoCrMo biomedical alloy, Electrochimica Acta 54(6) (2009) 1798-1809.
[96] E.E. Hoffman, A. Lin, Y. Liao, L.D. Marks, Grain Boundary Assisted Crevice Corrosion in CoCrMo Alloys, CORROSION 72(11) (2016) 1445-1461.
[97] A. Lewis, M. Kilburn, I. Papageorgiou, G. Allen, C. Case, Effect of synovial fluid, phosphate-buffered saline solution, and water on the dissolution and corrosion properties of CoCrMo alloys as used in orthopedic implants, Journal of Biomedical Materials Research Part A: An Official Journal of The Society for Biomaterials, The Japanese Society for Biomaterials, and The Australian Society for Biomaterials and the Korean Society for Biomaterials 73(4) (2005) 456-467.
[98] A. Lin, E.E. Hoffman, L.D. Marks, Effects of grain boundary misorientation and chromium segregation on corrosion of CoCrMo alloys, Corrosion 73(3) (2017) 256-267.
[99] R.H. Oskouei, M.R. Barati, H. Farhoudi, M. Taylor, L.B. Solomon, A new finding on the in-vivo crevice corrosion damage in a CoCrMo hip implant, Materials Science and Engineering: C 79 (2017) 390-398.
[100] T.M. Zink, B.J. McGrory, Mechanically Assisted Crevice Corrosion in a Metal-on-Polyethylene Total Hip Presenting With Lower Extremity Vascular Compromise, Arthroplasty Today 6(3) (2020) 445-450.
[101] T. Devine, J. Wulff, The comparative crevice corrosion resistance of Co-Cr base surgical implant alloys, Journal of the Electrochemical Society 123(10) (1976) 1433.
[102] S.A. Mali, V. Singh, J.L. Gilbert, Effect of mixed alloy combinations on fretting corrosion performance of spinal screw and rod implants, Journal of Biomedical Materials Research Part B: Applied Biomaterials 105(5) (2017) 1169-1177.
[103] J.P. Collire, V.A. Surprenant, R.E. Jensen, M.B. Mayor, Corrosion at the Interface of Cobalt-Alloy Heads on Titanium-Alloy Stems, Clinical Orthopaedics and Related Research® 271 (1991).

[104] S.A. Mali, Mechanically assisted crevice corrosion in metallic biomaterials: a review, Materials Technology 31(12) (2016) 732-739.
[105] X. Chen, K. Shah, S. Dong, L. Peterson, E. Callagon La Plante, G. Sant, Elucidating the corrosion-related degradation mechanisms of a Ti-6Al-4V dental implant, Dental Materials 36(3) (2020) 431-441.
[106] M. Nganbe, U. Khan, H. Louati, A. Speirs, P.E. Beaulé, In vitro assessment of strength, fatigue durability, and disassembly of Ti6Al4V and CoCrMo necks in modular total hip replacements, Journal of Biomedical Materials Research Part B: Applied Biomaterials 97(1) (2011) 132-138.
[107] Y. Liu, J.L. Gilbert, The effect of simulated inflammatory conditions and pH on fretting corrosion of CoCrMo alloy surfaces, Wear 390 (2017) 302-311.
[108] J. Dufils, M.A. Wimmer, J. Kunze, M.T. Mathew, M.P. Laurent, Influence of molybdate ion and pH on the fretting corrosion of a CoCrMo – Titanium alloy couple, Biotribology 11 (2017) 20-28.
[109] V. Swaminathan, J.L. Gilbert, Fretting corrosion of CoCrMo and Ti6Al4V interfaces, Biomaterials 33(22) (2012) 5487-5503.
[110] Y. Yan, H. Yang, Y. Su, L. Qiao, Albumin adsorption on CoCrMo alloy surfaces, Scientific reports 5 (2015) 18403.
[111] M. Talha, Y. Ma, P. Kumar, Y. Lin, A. Singh, Role of protein adsorption in the bio corrosion of metallic implants–A review, Colloids and Surfaces B: Biointerfaces (2019).
[112] Y. Li, K.G. Neoh, E.-T. Kang, Plasma protein adsorption and thrombus formation on surface functionalized polypyrrole with and without electrical stimulation, Journal of Colloid and Interface Science 275(2) (2004) 488-495.
[113] M.L.W. Knetsch, Y.B.J. Aldenhoff, L.H. Koole, The effect of high-density-lipoprotein on thrombus formation on and endothelial cell attachement to biomaterial surfaces, Biomaterials 27(14) (2006) 2813-2819.
[114] C.V. Vidal, A.I. Muñoz, Study of the adsorption process of bovine serum albumin on passivated surfaces of CoCrMo biomedical alloy, Electrochimica Acta 55(28) (2010) 8445-8452.
[115] M. Tagaya, T. Ikoma, N. Hanagata, J. Tanaka, Analytical investigation of protein mediation between biomaterials and cells, Materials Express 2(1) (2012) 1-22.
[116] S. Guo, D. Pranantyo, E.-T. Kang, X.J. Loh, X. Zhu, D. Jańczewski, K.G. Neoh, Dominant Albumin–Surface Interactions under Independent Control of Surface Charge and Wettability, Langmuir 34(5) (2018) 1953-1966.
[117] Y.S. Hedberg, Role of proteins in the degradation of relatively inert alloys in the human body, npj Materials Degradation 2(1) (2018) 26.
[118] C. Pradier, F. Karman, J. Telegdi, E. Kalman, P. Marcus, Adsorption of Bovine Serum Albumin on Chromium and Molybdenum Surfaces Investigated by Fourier-Transform Infrared Reflection− Absorption Spectroscopy (FT-IRRAS) and X-ray Photoelectron Spectroscopy, The Journal of Physical Chemistry B 107(28) (2003) 6766-6773.
[119] M. Rabe, D. Verdes, S. Seeger, Understanding protein adsorption phenomena at solid surfaces, Advances in colloid and interface science 162(1-2) (2011) 87-106.

[120] G. Dalkas, S.R. Euston, Molecular Simulation of Protein Adsorption and Conformation at Gas-Liquid, Liquid-Liquid and Solid-Liquid Interfaces, Current Opinion in Colloid & Interface Science (2018).
[121] X. Quan, J. Liu, J. Zhou, Multiscale modeling and simulations of protein adsorption: progresses and perspectives, Current Opinion in Colloid & Interface Science (2018).
[122] M.H. Wood, C.G. Payagalage, T. Geue, Bovine serum albumin and fibrinogen adsorption at the 316L stainless steel/aqueous interface, The Journal of Physical Chemistry B 122(19) (2018) 5057-5065.
[123] T. Sakiyama, J. Tomura, K. Imamura, K. Nakanishi, Adsorption characteristics of bovine serum albumin and its peptide fragments on a stainless steel surface, Colloids and Surfaces B: Biointerfaces 33(2) (2004) 77-84.
[124] C. Valero Vidal, A. Olmo Juan, A. Igual Muñoz, Adsorption of bovine serum albumin on CoCrMo surface: Effect of temperature and protein concentration, Colloids and Surfaces B: Biointerfaces 80(1) (2010) 1-11.
[125] T. Kopac, K. Bozgeyik, J. Yener, Effect of pH and temperature on the adsorption of bovine serum albumin onto titanium dioxide, Colloids and Surfaces A: Physicochemical and Engineering Aspects 322(1-3) (2008) 19-28.
[126] T. Byrne, L. Lohstreter, M. Filiaggi, Z. Bai, J. Dahn, Quantifying protein adsorption on combinatorially sputtered Al-, Nb-, Ta-and Ti-containing films with electron microprobe and spectroscopic ellipsometry, Surface science 603(7) (2009) 992-1001.
[127] Z. Bai, M. Filiaggi, J. Dahn, Fibrinogen adsorption onto 316L stainless steel, Nitinol and titanium, Surface Science 603(6) (2009) 839-846.
[128] P. Roach, D. Farrar, C.C. Perry, Interpretation of protein adsorption: surface-induced conformational changes, Journal of the American Chemical Society 127(22) (2005) 8168-8173.
[129] M. Rabe, D. Verdes, S. Seeger, Understanding cooperative protein adsorption events at the microscopic scale: a comparison between experimental data and Monte Carlo simulations, The Journal of Physical Chemistry B 114(17) (2010) 5862-5869.
[130] M. Rabe, D. Verdes, J. Zimmermann, S. Seeger, Surface organization and cooperativity during nonspecific protein adsorption events, The Journal of Physical Chemistry B 112(44) (2008) 13971-13980.
[131] K. Anselme, L. Ploux, A. Ponche, Cell/material interfaces: influence of surface chemistry and surface topography on cell adhesion, Journal of Adhesion Science and Technology 24(5) (2010) 831-852.
[132] A. Carré, V. Lacarrière, How substrate properties control cell adhesion. A physical–chemical approach, Journal of Adhesion Science and Technology 24(5) (2010) 815-830.
[133] S. Sousa, P. Moradas-Ferreira, B. Saramago, L. Viseu Melo, M. Barbosa, Human serum albumin adsorption on TiO2 from single protein solutions and from plasma, Langmuir 20(22) (2004) 9745-9754.
[134] M. ORATZ, M.A. ROTHSCHILD, S.S. SCHREIBER, Albumin-osmotic function, Albumin: Structure, Function and Uses, Elsevier1977, pp. 275-282.

[135] B. Ahmad, S. Parveen, R.H. Khan, Effect of albumin conformation on the binding of ciprofloxacin to human serum albumin: a novel approach directly assigning binding site, Biomacromolecules 7(4) (2006) 1350-1356.
[136] Y. Jeyachandran, E. Mielczarski, B. Rai, J. Mielczarski, Quantitative and qualitative evaluation of adsorption/desorption of bovine serum albumin on hydrophilic and hydrophobic surfaces, Langmuir 25(19) (2009) 11614-11620.
[137] T. Guckeisen, S. Hosseinpour, W. Peukert, Isoelectric points of proteins at the air/liquid interface and in solution, Langmuir (2019).
[138] K. Kubiak-Ossowska, K. Tokarczyk, B. Jachimska, P.A. Mulheran, Bovine serum albumin adsorption at a silica surface explored by simulation and experiment, The Journal of Physical Chemistry B 121(16) (2017) 3975-3986.
[139] M.-S. Pyon, R.J. Cherry, A.J. Bjornsen, D.C. Zapien, Uptake and release of iron by ferritin adsorbed at tin-doped indium oxide electrodes, Langmuir 15(20) (1999) 7040-7046.
[140] M. Kim, Y. Rho, K.S. Jin, B. Ahn, S. Jung, H. Kim, M. Ree, pH-dependent structures of ferritin and apoferritin in solution: disassembly and reassembly, Biomacromolecules 12(5) (2011) 1629-1640.
[141] P. Silva-Bermudez, S. Rodil, An overview of protein adsorption on metal oxide coatings for biomedical implants, Surface and Coatings Technology 233 (2013) 147-158.
[142] A. Liscio, V. Palermo, P. Samorì, Nanoscale quantitative measurement of the potential of charged nanostructures by electrostatic and Kelvin probe force microscopy: unraveling electronic processes in complex materials, Accounts of chemical research 43(4) (2010) 541-550.
[143] R. Namus, J. Nutter, J. Qi, W.M. Rainforth, The influence of protein concentration, temperature and cathodic polarization on the surface status of CoCrMo biomedical grade alloys, Applied Surface Science 499 (2020) 143908.
[144] F. Yu, O. Addison, A.J. Davenport, A synergistic effect of albumin and H2O2 accelerates corrosion of Ti6Al4V, Acta biomaterialia 26 (2015) 355-365.
[145] Y.S. Hedberg, I. Dobryden, H. Chaudhary, Z. Wei, P.M. Claesson, C. Lendel, Synergistic effects of metal-induced aggregation of human serum albumin, Colloids and Surfaces B: Biointerfaces 173 (2019) 751-758.
[146] P. Silva-Bermudez, S. Rodil, S. Muhl, Albumin adsorption on oxide thin films studied by spectroscopic ellipsometry, Applied Surface Science 258(5) (2011) 1711-1718.
[147] Y. Liao, R. Pourzal, M. Wimmer, J. Jacobs, A. Fischer, L. Marks, Graphitic tribological layers in metal-on-metal hip replacements, Science 334(6063) (2011) 1687-1690.
[148] N. Espallargas, A. Fischer, A.I. Muñoz, S. Mischler, M. Wimmer, In-situ generated tribomaterial in metal/metal contacts: current understanding and future implications for implants, Biotribology 10 (2017) 42-50.
[149] S. Karimi, A. Alfantazi, Electrochemical corrosion behavior of orthopedic biomaterials in presence of human serum albumin, Journal of the Electrochemical Society 160(6) (2013) C206-C214.

[150] S.L. Hirsh, D.R. McKenzie, N.J. Nosworthy, J.A. Denman, O.U. Sezerman, M.M.M. Bilek, The Vroman effect: Competitive protein exchange with dynamic multilayer protein aggregates, Colloids and Surfaces B: Biointerfaces 103 (2013) 395-404.
[151] M. Runa, M. Mathew, M.H. Fernandes, L. Rocha, First insight on the impact of an osteoblastic layer on the bio-tribocorrosion performance of Ti6Al4V hip implants, Acta biomaterialia 12 (2015) 341-351.
[152] M.A. Wimmer, A. Fischer, R. Büscher, R. Pourzal, C. Sprecher, R. Hauert, J.J. Jacobs, Wear mechanisms in metal-on-metal bearings: The importance of tribochemical reaction layers, Journal of Orthopaedic Research 28(4) (2010) 436-443.
[153] M. Mathew, C. Nagelli, R. Pourzal, A. Fischer, M. Laurent, J. Jacobs, M. Wimmer, Tribolayer formation in a metal-on-metal (MoM) hip joint: an electrochemical investigation, Journal of the mechanical behavior of biomedical materials 29 (2014) 199-212.
[154] S. Hiromoto, S. Mischler, The influence of proteins on the fretting–corrosion behaviour of a Ti6Al4V alloy, Wear 261(9) (2006) 1002-1011.
[155] J. Geringer, D.D. Macdonald, Friction/fretting-corrosion mechanisms: Current trends and outlooks for implants, Materials Letters 134 (2014) 152-157.
[156] S. Sugio, A. Kashima, S. Mochizuki, M. Noda, K. Kobayashi, Crystal structure of human serum albumin at 2.5 Å resolution, Protein engineering 12(6) (1999) 439-446.
[157] D.C. Carter, J.X. Ho, Structure of serum albumin, Advances in protein chemistry, Elsevier1994, pp. 153-203.
[158] D.C. Carter, B. Chang, J.X. Ho, K. Keeling, Z. Krishnasami, Preliminary crystallographic studies of four crystal forms of serum albumin, European Journal of Biochemistry 226(3) (1994) 1049-1052.
[159] M. Lundin, Y. Hedberg, T. Jiang, G. Herting, X. Wang, E. Thormann, E. Blomberg, I.O. Wallinder, Adsorption and protein-induced metal release from chromium metal and stainless steel, Journal of colloid and interface science 366(1) (2012) 155-164.
[160] M. Talha, Y. Ma, Y. Lin, A. Singh, W. Liu, X. Kong, Corrosion behaviour of austenitic stainless steels in phosphate buffer saline solution: synergistic effects of protein concentration, time and nitrogen, New Journal of Chemistry 43(4) (2019) 1943-1955.
[161] A. Lewis, P. Heard, The effects of calcium phosphate deposition upon corrosion of CoCr alloys and the potential for implant failure, Journal of Biomedical Materials Research Part A: An Official Journal of The Society for Biomaterials, The Japanese Society for Biomaterials, and The Australian Society for Biomaterials and the Korean Society for Biomaterials 75(2) (2005) 365-373.
[162] S. Omanovic, S.G. Roscoe, Electrochemical studies of the adsorption behavior of bovine serum albumin on stainless steel, Langmuir 15(23) (1999) 8315-8321.
[163] M.L.C.A. Afonso, R.F.V. Villamil Jaimes, E.P.G. Arêas, M.R. Capri, E. Oliveira, S.M.L. Agostinho, The influence of albumin on the anodic dissolution of chromium present in UNS S31254 stainless steel in chloride environment, Colloids and Surfaces A: Physicochemical and Engineering Aspects 317(1) (2008) 760-763.

[164] I. Ron, L. Sepunaru, S. Itzhakov, T. Belenkova, N. Friedman, I. Pecht, M. Sheves, D. Cahen, Proteins as electronic materials: Electron transport through solid-state protein monolayer junctions, Journal of the American Chemical Society 132(12) (2010) 4131-4140.
[165] Y. Zhang, O. Addison, F. Yu, B.C.R. Troconis, J.R. Scully, A.J. Davenport, Time-dependent enhanced corrosion of Ti6Al4V in the presence of H 2 O 2 and albumin, Scientific reports 8(1) (2018) 3185.
[166] Y.S. Hedberg, M. Žnidaršič, G. Herting, I. Milošev, I. Odnevall Wallinder, Mechanistic insight on the combined effect of albumin and hydrogen peroxide on surface oxide composition and extent of metal release from Ti6Al4V, Journal of Biomedical Materials Research Part B: Applied Biomaterials 107(3) (2019) 858-867.
[167] S. Takemoto, M. Hattori, M. Yoshinari, E. Kawada, Y. Oda, Corrosion behavior and surface characterization of titanium in solution containing fluoride and albumin, Biomaterials 26(8) (2005) 829-837.
[168] D. Ling, T. Hyeon, Chemical Design of Biocompatible Iron Oxide Nanoparticles for Medical Applications, Small 9(9-10) (2013) 1450-1466.
[169] X. He, P. Hahn, J. Iacovelli, R. Wong, C. King, R. Bhisitkul, M. Massaro-Giordano, J.L. Dunaief, Iron homeostasis and toxicity in retinal degeneration, Prog Retin Eye Res 26(6) (2007) 649-673.
[170] Y. Okazaki, E. Gotoh, Comparison of metal release from various metallic biomaterials in vitro, Biomaterials 26(1) (2005) 11-21.
[171] F. Mou, C. Chen, H. Ma, Y. Yin, Q. Wu, J. Guan, Self-Propelled Micromotors Driven by the Magnesium–Water Reaction and Their Hemolytic Properties, Angewandte Chemie International Edition 52(28) (2013) 7208-7212.
[172] (!!! INVALID CITATION !!! {}).
[173] W. Gao, A. Pei, J. Wang, Water-driven micromotors, ACS nano 6(9) (2012) 8432-8438.
[174] H.H. Jeong, M. Alarcón-Correa, A.G. Mark, K. Son, T.C. Lee, P. Fischer, Corrosion-Protected Hybrid Nanoparticles, Advanced Science 4(12) (2017) 1700234.
[175] S.K. Srivastava, B. Ghosh, 5 - Metallic biomaterials for dental implant systems, in: P. Balakrishnan, S. M S, S. Thomas (Eds.), Fundamental Biomaterials: Metals, Woodhead Publishing2018, pp. 111-137.
[176] G. Zhao, B. Khezri, S. Sanchez, O.G. Schmidt, R.D. Webster, M. Pumera, Corrosion of self-propelled catalytic microengines, Chemical Communications 49(80) (2013) 9125-9127.
[177] T. Maric, M.Z.M. Nasir, M. Budanovic, O. Alduhaish, R.D. Webster, M. Pumera, Corrosion of light powered Pt/TiO2 microrobots, Applied Materials Today 20 (2020) 100659.
[178] F. Wong, A. Sen, Progress toward light-harvesting self-electrophoretic motors: Highly efficient bimetallic nanomotors and micropumps in halogen media, ACS nano 10(7) (2016) 7172-7179.

[179] A. F-06, Standard test method for conducting cyclic potentiodynamic polarization measurements to determine the corrosion susceptibility of small implant devices, ASTM International West Conshohocken, PA, 2001.
[180] R. Ovarfort, New electrochemical cell for pitting corrosion testing, Corrosion Science 28(2) (1988) 135-140.
[181] P. Dash, P. Mallick, H. Rath, A. Tripathi, J. Prakash, D. Avasthi, S. Mazumder, S. Varma, P. Satyam, N. Mishra, Surface roughness and power spectral density study of SHI irradiated ultra-thin gold films, Applied Surface Science 256(2) (2009) 558-561.
[182] M. Flemming, L. Coriand, A. Duparré, Ultra-hydrophobicity through stochastic surface roughness, Journal of Adhesion science and technology 23(3) (2009) 381-400.
[183] X. Xu, L. Xiao, Y. Jia, Z. Wu, F. Wang, Y. Wang, N.O. Haugen, H. Huang, Pyro-catalytic hydrogen evolution by Ba 0.7 Sr 0.3 TiO 3 nanoparticles: harvesting cold–hot alternation energy near room-temperature, Energy & Environmental Science 11(8) (2018) 2198-2207.
[184] X. Yang, Q. Yang, J. Xu, C.-S. Lee, Bimetallic PtPd nanoparticles on Nafion–graphene film as catalyst for ethanol electro-oxidation, Journal of Materials Chemistry 22(16) (2012) 8057-8062.
[185] H. Park, W. Choi, Photocatalytic reactivities of nafion-coated TiO2 for the degradation of charged organic compounds under UV or visible light, The Journal of Physical Chemistry B 109(23) (2005) 11667-11674.
[186] J. Hong, H. Ghourchian, A.A. Moosavi–Movahedi, Direct electron transfer of redox proteins on a Nafion-cysteine modified gold electrode, Electrochemistry communications 8(10) (2006) 1572-1576.
[187] S.A. Bhakta, E. Evans, T.E. Benavidez, C.D. Garcia, Protein adsorption onto nanomaterials for the development of biosensors and analytical devices: A review, Analytica chimica acta 872 (2015) 7-25.
[188] X. Zhao, Y. Fu, J. Wang, Y. Xu, J.-H. Tian, R. Yang, Ni-doped CoFe2O4 hollow nanospheres as efficient Bi-functional catalysts, Electrochimica Acta 201 (2016) 172-178.
[189] G. Ou, F. Wu, K. Huang, N. Hussain, D. Zu, H. Wei, B. Ge, H. Yao, L. Liu, H. Li, Boosting the Electrocatalytic Water Oxidation Performance of CoFe2O4 Nanoparticles by Surface Defect Engineering, ACS applied materials & interfaces 11(4) (2019) 3978-3983.
[190] C.A. Schneider, W.S. Rasband, K.W. Eliceiri, NIH Image to ImageJ: 25 years of image analysis, Nature methods 9(7) (2012) 671-675.
[191] X. Cheng, Y. Wang, C. Dong, X. Li, The beneficial galvanic effect of the constituent phases in 2205 duplex stainless steel on the passive films formed in a 3.5% NaCl solution, Corrosion Science 134 (2018) 122-130.
[192] N. Sheoran, V. Kumar, A. Kumar, Comparative study of structural, magnetic and dielectric properties of CoFe2O4@ BiFeO3 and BiFeO3@ CoFe2O4 core-shell nanocomposites, Journal of Magnetism and Magnetic Materials 475 (2019) 30-37.
[193] A.E. Nel, L. Mädler, D. Velegol, T. Xia, E.M. Hoek, P. Somasundaran, F. Klaessig, V. Castranova, M. Thompson, Understanding biophysicochemical interactions at the nano–bio interface, Nature materials 8(7) (2009) 543-557.

[194] F.Y. Oliva, O.R. Cámara, L.B. Avalle, Adsorption of human serum albumin on electrochemical titanium dioxide electrodes: Protein–oxide surface interaction effects studied by electrochemical techniques, Journal of Electroanalytical Chemistry 633(1) (2009) 19-34.
[195] M. Aziz-Kerrzo, K.G. Conroy, A.M. Fenelon, S.T. Farrell, C.B. Breslin, Electrochemical studies on the stability and corrosion resistance of titanium-based implant materials, Biomaterials 22(12) (2001) 1531-1539.
[196] T. Hanawa, S. Hiromoto, K. Asami, Characterization of the surface oxide film of a Co–Cr–Mo alloy after being located in quasi-biological environments using XPS, Applied Surface Science 183(1-2) (2001) 68-75.
[197] H.-H. Huang, Effect of fluoride and albumin concentration on the corrosion behavior of Ti–6Al–4V alloy, Biomaterials 24(2) (2003) 275-282.
[198] J.E. Ellingsen, A study on the mechanism of protein adsorption to TiO2, Biomaterials 12(6) (1991) 593-596.
[199] J. Pan, D. Thierry, C. Leygraf, Electrochemical impedance spectroscopy study of the passive oxide film on titanium for implant application, Electrochimica Acta 41(7-8) (1996) 1143-1153.
[200] J. Pan, D. Thierry, C. Leygraf, Hydrogen peroxide toward enhanced oxide growth on titanium in PBS solution: blue coloration and clinical relevance, Journal of Biomedical Materials Research: An Official Journal of The Society for Biomaterials and The Japanese Society for Biomaterials 30(3) (1996) 393-402.
[201] C. Fonseca, M. Barbosa, Corrosion behaviour of titanium in biofluids containing H2O2 studied by electrochemical impedance spectroscopy, Corrosion Science 43(3) (2001) 547-559.
[202] N. Hakiki, M.D.C. Belo, A. Simoes, M. Ferreira, Semiconducting properties of passive films formed on stainless steels influence of the alloying elements, Journal of the Electrochemical Society 145(11) (1998) 3821-3829.
[203] S.L. de Assis, S. Wolynec, I. Costa, Corrosion characterization of titanium alloys by electrochemical techniques, Electrochimica Acta 51(8-9) (2006) 1815-1819.
[204] G. Ansari, A. Fattah-alhosseini, On the passive and semiconducting behavior of severely deformed pure titanium in Ringer's physiological solution at 37 C: a trial of the point defect model, Materials Science and Engineering: C 75 (2017) 64-71.
[205] D.D. Macdonald, The point defect model for the passive state, Journal of the Electrochemical Society 139(12) (1992) 3434.
[206] H. Krawiec, V. Vignal, E. Schwarzenboeck, J. Banas, Role of plastic deformation and microstructure in the micro-electrochemical behaviour of Ti–6Al–4V in sodium chloride solution, Electrochimica Acta 104 (2013) 400-406.
[207] L.N. Wang, A. Shinbine, J.L. Luo, Electrochemical behavior of CoCrMo implant in Ringer's solution, Surface and Interface Analysis 45(9) (2013) 1323-1328.
[208] R. Tsaryk, M. Kalbacova, U. Hempel, D. Scharnweber, R.E. Unger, P. Dieter, C.J. Kirkpatrick, K. Peters, Response of human endothelial cells to oxidative stress on Ti6Al4V alloy, Biomaterials 28(5) (2007) 806-813.

[209] O.R. Cámara, L.B. Avalle, F.Y. Oliva, Protein adsorption on titanium dioxide: Effects on double layer and semiconductor space charge region studied by EIS, Electrochimica acta 55(15) (2010) 4519-4528.
[210] X. Cheng, S.G. Roscoe, Corrosion behavior of titanium in the presence of calcium phosphate and serum proteins, Biomaterials 26(35) (2005) 7350-7356.
[211] Y. Tsutsumi, D. Nishimura, H. Doi, N. Nomura, T. Hanawa, Difference in surface reactions between titanium and zirconium in Hanks' solution to elucidate mechanism of calcium phosphate formation on titanium using XPS and cathodic polarization, Materials Science and Engineering: C 29(5) (2009) 1702-1708.
[212] B. Wu, C. Mu, G. Zhang, W. Lin, Effects of Cr3+ on the structure of collagen fiber, Langmuir 25(19) (2009) 11905-11910.
[213] K. Hamada, M. Kon, T. Hanawa, K.i. Yokoyama, Y. Miyamoto, K. Asaoka, Hydrothermal modification of titanium surface in calcium solutions, Biomaterials 23(10) (2002) 2265-2272.
[214] E. Chang, T.-M. Lee, Effect of surface chemistries and characteristics of Ti6Al4V on the Ca and P adsorption and ion dissolution in Hank's ethylene diamine tetra-acetic acid solution, Biomaterials 23(14) (2002) 2917-2925.
[215] P. Tengvall, H. Elwing, I. Lundström, Titanium gel made from metallic titanium and hydrogen peroxide, Journal of colloid and interface science 130(2) (1989) 405-413.
[216] Y.-S. Hsu, E. Chang, H.-S. Liu, Hydrothermally-grown monetite (CaHPO4) on hydroxyapatite, Ceramics international 24(4) (1998) 249-254.
[217] D. Briggs, Practical surface analysis, Auger and X-Ray Photoelecton Spectroscory 1 (1990) 151-152.
[218] D. Nakhaie, A. Davoodi, G.R. Ebrahimi, The Influence of cold plastic deformation on passivity of Ti-6Al-4V alloy studied by electrochemical and local probing techniques, Corrosion 72(1) (2015) 110-118.
[219] P. Davis, K. Robles, K. Livingston, S. Johns, V. Ravi, E. Graugnard, M. Hurley, Phase Separation in Ti-6Al-4V Alloys with Boron Additions for Biomedical Applications: Scanning Kelvin Probe Force Microscopy Investigation of Microgalvanic Couples and Corrosion Initiation, JOM 69(8) (2017) 1446-1454.
[220] H.B. Michaelson, The work function of the elements and its periodicity, Journal of applied physics 48(11) (1977) 4729-4733.
[221] J.-W. Park, K.-B. Park, J.-Y. Suh, Effects of calcium ion incorporation on bone healing of Ti6Al4V alloy implants in rabbit tibiae, Biomaterials 28(22) (2007) 3306-3313.
[222] C. Leung, H. Kinns, B.W. Hoogenboom, S. Howorka, P. Mesquida, Imaging surface charges of individual biomolecules, Nano letters 9(7) (2009) 2769-2773.
[223] M. Salerno, S. Dante, Scanning Kelvin Probe Microscopy: Challenges and Perspectives towards Increased Application on Biomaterials and Biological Samples, Materials 11(6) (2018) 951.
[224] F. Bathawab, M. Bennett, M. Cantini, J. Reboud, M.J. Dalby, M. Salmerón-Sánchez, Lateral chain length in polyalkyl acrylates determines the mobility of fibronectin at the cell/material interface, Langmuir 32(3) (2016) 800-809.

[225] N.B. Guerra, C. González-García, V. Llopis, J.C. Rodríguez-Hernández, D. Moratal, P. Rico, M. Salmerón-Sánchez, Subtle variations in polymer chemistry modulate substrate stiffness and fibronectin activity, Soft Matter 6(19) (2010) 4748-4755.
[226] B. Jachimska, K. Tokarczyk, M. Łapczyńska, A. Puciul-Malinowska, S. Zapotoczny, Structure of bovine serum albumin adsorbed on silica investigated by quartz crystal microbalance, Colloids and Surfaces A: Physicochemical and Engineering Aspects 489 (2016) 163-172.
[227] M. Stobiecka, M. Hepel, J. Radecki, Transient conformation changes of albumin adsorbed on gold piezoelectrodes, Electrochimica acta 50(25-26) (2005) 4873-4887.
[228] A.P. Minton, Effects of excluded surface area and adsorbate clustering on surface adsorption of proteins. II. Kinetic models, Biophysical journal 80(4) (2001) 1641-1648.
[229] H.-G. Park, H.-C. Jeong, Y.H. Jung, D.-S. Seo, Control of the wrinkle structure on surface-reformed poly (dimethylsiloxane) via ion-beam bombardment, Scientific reports 5 (2015) 12356.
[230] I. Milošev, The effect of biomolecules on the behaviour of CoCrMo alloy in various simulated physiological solutions, Electrochimica Acta 78 (2012) 259-273.
[231] C.V. Vidal, A.I. Muñoz, Effect of physico-chemical properties of simulated body fluids on the electrochemical behaviour of CoCrMo alloy, Electrochimica Acta 56(24) (2011) 8239-8248.
[232] E. Rahimi, R. Offoiach, K. Baert, H. Terryn, M. Lekka, L. Fedrizzi, Role of phosphate, calcium species and hydrogen peroxide on albumin protein adsorption on surface oxide of Ti6Al4V alloy, Materialia 15 (2021) 100988.
[233] E. Rahimi, A. Rafsanjani-Abbasi, A. Kiani-Rashid, H. Jafari, A. Davoodi, Morphology modification of electrodeposited superhydrophobic nickel coating for enhanced corrosion performance studied by AFM, SEM-EDS and electrochemical measurements, Colloids and Surfaces A: Physicochemical and Engineering Aspects 547 (2018) 81-94.
[234] S. Karimi, A.M. Alfantazi, Ion release and surface oxide composition of AISI 316L, Co–28Cr–6Mo, and Ti–6Al–4V alloys immersed in human serum albumin solutions, Materials Science and Engineering: C 40 (2014) 435-444.
[235] C. Combes, C. Rey, Adsorption of proteins and calcium phosphate materials bioactivity, Biomaterials 23(13) (2002) 2817-2823.
[236] E. Grigoriou, M. Cantini, M. Dalby, A. Petersen, M. Salmeron-Sanchez, Cell migration on material-driven fibronectin microenvironments, Biomaterials science 5(7) (2017) 1326-1333.
[237] H. Min, E. Freeman, W. Zhang, C. Ashraf, D. Allara, A.C. Van Duin, S. Tadigadapa, Modified Random Sequential Adsorption Model for Understanding Kinetics of Proteins Adsorption at a Liquid–Solid Interface, Langmuir 33(29) (2017) 7215-7224.
[238] A.K. Sinensky, A.M. Belcher, Label-free and high-resolution protein/DNA nanoarray analysis using Kelvin probe force microscopy, nature nanotechnology 2(10) (2007) 653.
[239] C. Ma, S. Wang, F. Walsh, Electrodeposition of nanocrystalline nickel–cobalt binary alloy coatings: a review, Transactions of the IMF 93(2) (2015) 104-112.

[240] E. Rahimi, A. Rafsanjani-Abbasi, A. Imani, A. Davoodi, TiO2/Cu2O coupled oxide films in Cl− ion containing solution: Volta potential and electronic properties characterization by scanning probe microscopy, Materials Chemistry and Physics 212 (2018) 403-407.
[241] M. Rohwerder, F. Turcu, High-resolution Kelvin probe microscopy in corrosion science: scanning Kelvin probe force microscopy (SKPFM) versus classical scanning Kelvin probe (SKP), Electrochimica Acta 53(2) (2007) 290-299.
[242] P. Schmutz, G. Frankel, Corrosion study of AA2024-T3 by scanning kelvin probe force microscopy and in situ atomic force microscopy scratching, Journal of the Electrochemical Society 145(7) (1998) 2295-2306.
[243] C. Barth, A.S. Foster, C.R. Henry, A.L. Shluger, Recent trends in surface characterization and chemistry with high-resolution scanning force methods, Advanced materials 23(4) (2011) 477-501.
[244] A. Cook, Z. Barrett, S. Lyon, H. McMurray, J. Walton, G. Williams, Calibration of the scanning Kelvin probe force microscope under controlled environmental conditions, Electrochimica acta 66 (2012) 100-105.
[245] C. Örnek, C. Leygraf, J. Pan, On the Volta potential measured by SKPFM–fundamental and practical aspects with relevance to corrosion science, Corrosion Engineering, Science and Technology 54(3) (2019) 185-198.
[246] E. Rahimi, A. Rafsanjani-Abbasi, A. Imani, S. Hosseinpour, A. Davoodi, Correlation of surface Volta potential with galvanic corrosion initiation sites in solid-state welded Ti-Cu bimetal using AFM-SKPFM, Corrosion Science 140 (2018) 30-39.
[247] T. Mashio, K. Malek, M. Eikerling, A. Ohma, H. Kanesaka, K. Shinohara, Molecular Dynamics Study of Ionomer and Water Adsorption at Carbon Support Materials, The Journal of Physical Chemistry C 114(32) (2010) 13739-13745.
[248] D.A. Shores, Corrosion and metal release rates of Ni substrates under a porous gold coating, Corrosion science 50(2) (2008) 372-383.
[249] Y.S. Hedberg, Role of proteins in the degradation of relatively inert alloys in the human body, npj Materials Degradation 2(1) (2018) 1-5.
[250] M. Talha, Y. Ma, P. Kumar, Y. Lin, A. Singh, Role of protein adsorption in the bio corrosion of metallic implants–A review, Colloids and Surfaces B: Biointerfaces 176 (2019) 494-506.
[251] O. Cherniavskaya, L. Chen, V. Weng, L. Yuditsky, L.E. Brus, Quantitative noncontact electrostatic force imaging of nanocrystal polarizability, The Journal of Physical Chemistry B 107(7) (2003) 1525-1531.
[252] Y. Zhao, J. Li, Z. Yin, X. Zhang, J. Huang, L. Cao, H. Wang, Interface-mediated local conduction at tubular interfaces in BiFeO3–CoFe2O4 nanocomposites, Journal of Alloys and Compounds (2020) 153699.
[253] J. Park, D. Bang, K. Jang, S. Haam, J. Yang, S. Na, The work function of doped polyaniline nanoparticles observed by Kelvin probe force microscopy, Nanotechnology 23(36) (2012) 365705.

[254] G. Jonker, Analysis of the semiconducting properties of cobalt ferrite, Journal of Physics and Chemistry of Solids 9(2) (1959) 165-175.
[255] F. Mushtaq, X. Chen, H. Torlakcik, B.J. Nelson, S. Pané, Enhanced catalytic degradation of organic pollutants by multi-stimuli activated multiferroic nanoarchitectures, Nano Research (2020) 1-9.
[256] R. Panda, D. Behera, Investigation of electric transport behavior of bulk CoFe2O4 by complex impedance spectroscopy, Journal of alloys and compounds 587 (2014) 481-486.
[257] Y.H. Hsieh, J.M. Liou, B.C. Huang, C.W. Liang, Q. He, Q. Zhan, Y.P. Chiu, Y.C. Chen, Y.H. Chu, Local conduction at the BiFeO3-CoFe2O4 tubular oxide interface, Advanced Materials 24(33) (2012) 4564-4568.
[258] A.M. Ganose, D.O. Scanlon, Band gap and work function tailoring of SnO 2 for improved transparent conducting ability in photovoltaics, Journal of Materials Chemistry C 4(7) (2016) 1467-1475.
[259] S. Sadewasser, T. Glatzel, M. Rusu, A. Jäger-Waldau, M.C. Lux-Steiner, High-resolution work function imaging of single grains of semiconductor surfaces, Applied Physics Letters 80(16) (2002) 2979-2981.
[260] E. Rahimi, A. Kosari, S. Hosseinpour, A. Davoodi, H. Zandbergen, J.M.C. Mol, Characterization of the passive layer on ferrite and austenite phases of super duplex stainless steel, Applied Surface Science 496 (2019) 143634.
[261] D.K. Paul, K. Karan, A. Docoslis, J.B. Giorgi, J. Pearce, Characteristics of self-assembled ultrathin Nafion films, Macromolecules 46(9) (2013) 3461-3475.
[262] Y. Yan, H. Yang, Y. Su, L. Qiao, Albumin adsorption on CoCrMo alloy surfaces, Scientific reports 5(1) (2015) 1-10.
[263] K. Chakrapani, G. Bendt, H. Hajiyani, I. Schwarzrock, T. Lunkenbein, S. Salamon, J. Landers, H. Wende, R. Schlögl, R. Pentcheva, Role of composition and size of cobalt ferrite nanocrystals in the oxygen evolution reaction, ChemCatChem 9(15) (2017) 2988-2995.
[264] T. Rakshit, R. Mukhopadhyay, Tuning band gap of holoferritin by metal core reconstitution with Cu, Co, and Mn, Langmuir 27(16) (2011) 9681-9686.
[265] G. Bakker, R. Boyer, Iron incorporation into apoferritin. The role of apoferritin as a ferroxidase, Journal of Biological Chemistry 261(28) (1986) 13182-13185.
[266] R.J. Cherry, A.J. Bjornsen, D.C. Zapien, Direct electron transfer of ferritin adsorbed at tin-doped indium oxide electrodes, Langmuir 14(8) (1998) 1971-1973.
[267] J. Kolay, S. Bera, T. Rakshit, R. Mukhopadhyay, Negative Differential Resistance Behavior of the Iron Storage Protein Ferritin, Langmuir 34(9) (2018) 3126-3135.
[268] K. Rezwan, L.P. Meier, M. Rezwan, J. Vörös, M. Textor, L.J. Gauckler, Bovine serum albumin adsorption onto colloidal Al2O3 particles: a new model based on zeta potential and UV− Vis measurements, Langmuir 20(23) (2004) 10055-10061.
[269] T. Guckeisen, S. Hosseinpour, W. Peukert, Isoelectric points of proteins at the air/liquid interface and in solution, Langmuir 35(14) (2019) 5004-5012.
[270] L. Stühn, J. Auernhammer, C. Dietz, pH-depended protein shell dis-and reassembly of ferritin nanoparticles revealed by atomic force microscopy, Scientific reports 9(1) (2019) 1-9.

[271] M. Tominaga, A. Ohira, Y. Yamaguchi, M. Kunitake, Electrochemical, AFM and QCM studies on ferritin immobilized onto a self-assembled monolayer-modified gold electrode, Journal of Electroanalytical Chemistry 566(2) (2004) 323-329.
[272] A.G. Hemmersam, K. Rechendorff, F. Besenbacher, B. Kasemo, D.S. Sutherland, pH-dependent adsorption and conformational change of ferritin studied on metal oxide surfaces by a combination of QCM-D and AFM, The Journal of Physical Chemistry C 112(11) (2008) 4180-4186.
[273] E. Rahimi, A. Kosari, S. Hosseinpour, A. Davoodi, H. Zandbergen, J.M. Mol, Characterization of the passive layer on ferrite and austenite phases of super duplex stainless steel, Applied Surface Science 496 (2019) 143634.
[274] G. Catalan, J.F. Scott, Physics and applications of bismuth ferrite, Advanced materials 21(24) (2009) 2463-2485.
[275] J.M. Bolts, M.S. Wrighton, Correlation of photocurrent-voltage curves with flat-band potential for stable photoelectrodes for the photoelectrolysis of water, The Journal of Physical Chemistry 80(24) (1976) 2641-2645.
[276] J. Bandara, R.A.S.S. Ranasinghe, The effect of MgO coating on photocatalytic activity of SnO2 for the degradation of chlorophenol and textile colorants; the correlation between the photocatalytic activity and the negative shift of flatband potential of SnO2, Applied Catalysis A: General 319 (2007) 58-63.